

Christoph Martin Eigenwillig

**New rapidly wavelength-swept light sources
for optical coherence tomography and
picosecond pulse generation**



München 2012

**New rapidly wavelength-swept light sources
for optical coherence tomography and
picosecond pulse generation**

Dissertation
an der Fakultät für Physik
der Ludwig-Maximilians-Universität
München

vorgelegt von
Christoph Martin Eigenwillig
aus Landsberg am Lech

München, den 14.08.2012

Erstgutachter: Dr. Robert Huber

Zweitgutachter: Prof. Dr. Ulf Kleineberg

Tag der mündlichen Prüfung: 11.10.2012

Abstract

This thesis deals with research on novel, semiconductor-based, ultrafast and widely tunable wavelength-swept light sources with respect to different applications. The main focus was on the young technology of Fourier domain mode locked (FDML) lasers, where the insertion of a kilometer-long fiber delay line enables to tune a narrowband spectral filter synchronously to the roundtrip time of light in the resonator. In this way, very high sweep speeds become feasible. A very successful application in the field of biomedical imaging is optical coherence tomography (OCT), where FDML lasers allow for very large image acquisition rates.

One important part of the research work was the development and characterization of novel concepts of wavelength-swept light sources improving performance and applicability in OCT. In this context, two novel modes of operation of FDML lasers have been demonstrated. On the one hand, an FDML laser with a highly linear time-frequency sweep characteristic was realized for the first time and allowed for OCT imaging at 1300 nm based on simplified numerical image processing. On the other hand, the first subharmonic FDML laser was implemented and successfully used for OCT imaging at 1300 nm. Here, light passes the same fiber delay line several times during each laser cavity roundtrip. In case of reduced sweep range, subharmonic FDML operation enabled an inherent multiplication of the effective sweep rate by a factor of ten, reaching 570 kHz. Another important achievement was the demonstration of a new type of ultrafast wavelength-swept light sources, where superluminescent light alternately passes a cascade of different gain elements and spectral filters which have to be tuned out of phase in order to compensate for the transit time of light. Different implementations operated at 1300 nm and at 1060 nm enabled effective sweep rates of up to 340 kHz. Ultrafast OCT imaging of the human retina was shown.

The second part of the research work focused on the demonstration and investigation of a novel approach of short pulse generation, where light within the wavelength sweeps of an FDML laser is temporally compressed by a subsequent pass through 15 km of highly dispersive fiber. The achievable temporal pulse width was an indicator for the coherence properties and the quality of mode-locking of the FDML laser. This became evident in the very critical dependence on the FDML sweep frequency as well as due to the results of comparable pulse generation experiments based on using an incoherent wavelength-swept light source. With a dispersion compensated FDML laser, operated at 1560 nm, pulse durations of 60-70 ps at a repetition rate of 390 kHz were achieved. Although the generation of bandwidth-limited pulses was not feasible, it was shown that the electric field within the wavelength sweeps of the FDML laser must at least be partially coherent. Due to remaining uncompensated higher order chirp, the optical bandwidth was limited to 6 nm and the pulse energy was restricted. Pulse energies of 5.6 nJ have been achieved using erbium-doped fiber amplification prior to temporal compression.

Zusammenfassung

Die vorliegende Arbeit befasst sich mit der Erforschung neuartiger, spektral sehr schnell und weit abstimmbarer, halbleiterbasierter Lichtquellen in Bezug auf deren unterschiedliche Anwendungen. Das Hauptaugenmerk lag hierbei auf der jungen Technologie der Fourier-Domänen modengekoppelten (FDML) Laser, bei denen durch das Einfügen einer kilometerlangen Glasfaserstrecke ein schmalbandiger spektraler Filter synchron zur Lichtumlaufzeit im Resonator abgestimmt werden kann und somit sehr große Abstimmgeschwindigkeiten möglich werden. Ein sehr erfolgreiches Einsatzfeld ist das biomedizinische Bildgebungsverfahren der optischen Kohärenztomographie (OCT), bei dem auf diese Weise sehr große Bildaufnahmezeiten realisierbar sind.

Ein wichtiger Bestandteil der Forschungsarbeit war die Erschließung und Charakterisierung neuer Konzepte zur verbesserten Anwendung schnell abstimmbarer Lichtquellen für die OCT. Hierbei konnten zwei neue Operationsmodi von FDML-Lasern realisiert werden. Zum einen gelang erstmals die Umsetzung eines FDML-Lasers mit einer hochgradig linearen Zeit-Frequenz Abstimmcharakteristik, welche OCT-Bildgebung bei 1300 nm mit vereinfachter numerischer Bilderzeugung ermöglichte. Zum anderen wurde erstmalig ein subharmonisch betriebener FDML-Laser verwirklicht und für OCT-Bildgebung bei 1300 nm verwendet. Dabei durchläuft Licht dieselbe Faserstrecke mehrmals pro Resonator-Umlauf. Bei reduziertem Abstimmbereich konnte die Abstimmrate des FDML-Lasers auf diese Weise inhärent um ein Zehnfaches auf 570 kHz gesteigert werden. Weiterhin gelang die Demonstration eines neuen Typs ultraschnell abstimmbarer Lichtquellen, bei dem superlumineszentes Licht abwechselnd verschiedene verstärkende Elemente und spektrale Filter durchläuft, welche zum Ausgleich der Lichtlaufzeit phasenversetzt abgestimmt werden müssen. Verschiedene Umsetzungen bei 1300 nm und bei 1060 nm ermöglichten effektive Abstimmraten von bis zu 340 kHz. Ultraschnelle OCT-Bildgebung am menschlichen Augenhintergrund wurde realisiert.

Der zweite Teil der Forschungsarbeit bestand in der Demonstration und Untersuchung einer neuen Methode zur Erzeugung kurzer Lichtpulse, bei der das Licht der Abstimmzyklen eines FDML-Lasers durch eine 15 km lange, dispersive Faser nachträglich zeitlich komprimiert wird. Die erreichbare Pulsdauer war hierbei ein Indikator für die Kohärenz und die Güte der Modenkopplung des FDML-Lasers. Dies zeigte sich in einer sehr kritischen Abhängigkeit von der FDML-Abstimmfrequenz sowie aufgrund der Ergebnisse von Vergleichsexperimenten mit einer inkohärenten abstimmbaren Lichtquelle. Mit einem dispersionskompensierten FDML-Laser bei 1560 nm wurden Pulsdauern von 60-70 ps bei einer Repetitionsrate von 390 kHz ermöglicht. Obwohl diese nicht Bandbreite-begrenzt waren, konnte gezeigt werden, dass das elektrische Feld innerhalb der Abstimmzyklen des FDML-Lasers mindestens partielle Kohärenz aufweisen muss. Aufgrund von ungenügend kompensiertem Chirp höherer Ordnung war die Bandbreite auf 6 nm limitiert und die Pulsenergie beschränkt. Mittels eines Erbium-dotierten Faserverstärkers vor der Komprimierung konnten Pulsenergien von 5.6 nJ erzeugt werden.

Contents

<i>Abstract</i>	<i>v</i>
<i>Zusammenfassung</i>	<i>vii</i>
1 Introduction and outline	1
2 Overview of the research field	5
2.1 Optical coherence tomography	5
2.1.1 Introduction and principle	5
2.1.1.1 On the way to OCT	6
2.1.1.2 OCT and other biomedical imaging techniques	7
2.1.1.3 Suitable wavelength ranges for OCT	8
2.1.1.4 Basic setup and principle of OCT	9
2.1.2 Different implementations of OCT.....	12
2.1.2.1 Overview.....	12
2.1.2.2 Time domain OCT (TD-OCT).....	13
2.1.2.3 Frequency domain OCT (FD-OCT).....	14
2.1.2.4 Practical aspects in FD-OCT.....	16
2.1.2.5 Dual balanced detection	17
2.1.2.6 Comparison of different implementation techniques	17
2.1.3 Point spread function and optical resolution.....	19
2.1.3.1 Axial resolution.....	19
2.1.3.2 Transversal resolution.....	20
2.1.4 Sensitivity and dynamic range	21
2.1.4.1 Sensitivity	21
2.1.4.2 Sensitivity roll-off with increasing depth.....	23
2.1.4.3 Dynamic range	24
2.1.5 Shot noise limit and other noise contributions.....	24
2.1.5.1 Shot noise.....	24
2.1.5.2 Shot noise limit in TD-OCT	25
2.1.5.3 Shot noise limit in FD-OCT.....	26
2.1.5.4 Sensitivity advantage of FD-OCT compared to TD-OCT	27
2.1.5.5 Shot noise limit, imaging speed and maximum allowed optical power	28
2.1.5.6 Other noise contributions and dependence on heterodyne gain	28

2.1.6	<i>Typical swept source OCT setup</i>	30
2.1.6.1	Experimental setup.....	31
2.1.6.2	Signal processing and numerical resampling	33
2.1.7	<i>Overview of OCT development and applications</i>	34
2.1.7.1	Medical applications	34
2.1.7.2	Functional OCT and different OCT approaches	35
2.1.7.3	Advances in OCT imaging performance.....	36
2.2	Fourier domain mode locked lasers	39
2.2.1	<i>Wavelength-swept light sources for OCT</i>	39
2.2.1.1	Definition, prerequisites for OCT and first implementations	39
2.2.1.2	Wavelength-swept external-cavity semiconductor lasers for OCT	40
2.2.1.3	Fundamental sweep speed limit in wavelength-swept lasers	41
2.2.1.4	Ways to solve the problem of the fundamental sweep speed limit.....	42
2.2.1.5	Alternative approaches	44
2.2.2	<i>Principle, setup and characteristic parameters of FDML lasers</i>	44
2.2.2.1	Principle and functionality of FDML lasers	44
2.2.2.2	Typical components in an FDML setup	48
2.2.2.3	Characteristic parameters of FDML operation.....	51
2.2.3	<i>Different implementations of FDML lasers</i>	53
2.2.3.1	Sigma-ring configuration	53
2.2.3.2	Polarization maintaining FDML (PM FDML) laser	54
2.2.3.3	Optical buffering	55
2.2.3.4	Post-amplification	56
3	<i>New concepts of wavelength-swept light sources in application for OCT</i>	59
3.1	New operation modes of FDML lasers	59
3.1.1	<i>K-space linear FDML laser and applications for OCT</i>	60
3.1.2	<i>Subharmonic Fourier domain mode locking</i>	85
3.2	Fast wavelength-swept ASE sources - a novel approach	91
3.2.1	<i>Fast wavelength-swept ASE source at 1300 nm</i>	92
3.2.2	<i>Fast wavelength-swept ASE source for retinal OCT at 1060 nm</i>	107
4	<i>Picosecond pulse generation with an FDML laser</i>	117
4.1	Motivation and overview of the work	117
4.2	Experimental setup	119
4.2.1	<i>FDML cavity at 390 kHz and optical switching</i>	119
4.2.2	<i>Temporal compressor stage and filter drive parameters</i>	121
4.2.3	<i>Erbium-doped fiber amplification</i>	123
4.2.4	<i>Pulse detection: Sampling oscilloscope or autocorrelation</i>	123

4.3	Results and discussion.....	124
4.3.1	<i>Theoretical model: Achievable pulse width for two special cases.....</i>	<i>124</i>
4.3.1.1	Fully incoherent case	124
4.3.1.2	Fully coherent case	126
4.3.2	<i>Pulse generation with an incoherent wavelength-swept source.....</i>	<i>126</i>
4.3.3	<i>Pulse generation with an FDML laser.....</i>	<i>127</i>
4.3.4	<i>Sensitivity roll-off performance of the FDML laser.....</i>	<i>129</i>
4.3.5	<i>Evaluation of the results: Partially coherent superposition</i>	<i>130</i>
4.3.6	<i>Pulse generation with an FDML laser and EDFA amplification</i>	<i>131</i>
4.3.7	<i>Conclusion</i>	<i>132</i>
5	Conclusion and outlook.....	135
	<i>Bibliography.....</i>	<i>139</i>
	<i>List of publications.....</i>	<i>155</i>
	<i>Curriculum Vitae</i>	<i>159</i>
	<i>Danksagung.....</i>	<i>161</i>

1 Introduction and outline

Optical coherence tomography (OCT), first introduced in 1991 [1], is a non-invasive, biomedical imaging technique providing three-dimensional, depth-resolved information about scattering properties of biological tissue with micrometer scale resolution and millimeter scale depth range. OCT has widespread medical applications in clinical diagnostics, where the most prominent example is retinal imaging in the human eye. In OCT, the optical beam is scanned transversally over the surface of the sample, whereas the intensity depth profile is continuously determined by measuring the time delays of backscattered light, analogously to ultrasound imaging. In OCT, this is realized on the basis of an interferometric measurement using a Michelson interferometer setup with a reference and a sample arm. One crucial parameter which has become increasingly important in the last years is imaging speed, critically depending on the achievable depth scan rate. The reason is that for many medical applications the possibility to acquire large and densely sampled volumes in a minimum recording time is highly desirable. In the original time domain based approach of OCT, a comparably slow depth scanning is realized by repetitively moving the reference arm mirror and shifting the point of zero delay in the sample. Temporal gating is achieved using a spectrally broadband, incoherent light source, comparable to white light interferometry. In contrast to this, the frequency domain based approach, which emerged a few years later, allows for considerably higher imaging speeds and provides an inherently higher sensitivity [2-4]. Here, the reference mirror is static and the interference signal is measured spectrally resolved. A Fourier transformation of the different spectral contributions then yields the desired intensity depth profile. Today, almost all research in the field of OCT focuses on the frequency domain approach, where one possible implementation is to use a spectrally broadband light source in combination with a spectrometer. However, up to now the fastest high-quality OCT imaging has been achieved with a different frequency domain OCT implementation based on wavelength-swept, narrow-band light sources, where the optical frequency is changed repetitively, so that frequency is directly encoded in time. In the last years, a lot of research has been performed in the field of semiconductor-based ultrafast wavelength-swept light sources in order to meet the high requirements in application for OCT. Operated in the near infrared wavelength regime, the wavelength needs to be repetitively swept over a broad wavelength range on the order of ~ 100 nm within a time of a few microseconds or less in order to guarantee sufficiently high axial resolution and imaging speed. Additionally, the swept light source must provide a narrowband instantaneous spectrum to enable a sufficient depth range. Using conventional wavelength-swept lasers, comprising a narrowband tunable bandpass filter

and a broadband gain medium, there exists a fundamental sweep speed limit [5], which is determined by the laser cavity length and usually impedes the achievement of the required performance for OCT. The reason is that every time the filter is tuned to another spectral position several round-trips of light in the resonator are required so that lasing can rebuild from amplified spontaneous emission (ASE).

There are different potential solutions to this problem. Besides approaches aiming to minimize the laser cavity length, a very important step was the introduction of Fourier domain mode locked (FDML) lasers in 2006 [6] which can overcome the fundamental sweep limitation. This technique allows for high-quality OCT imaging at ultra-high depth scan rates exceeding several MHz [7, 8]. The key idea was to insert up to a few km of optical fiber in the laser cavity which enabled to drive the tunable optical filter synchronously to the round-trip time of light in the resonator. In this way, the whole wavelength sweep is stored optically in the cavity. In an ideal case, FDML operation can be seen as a new mode of stationary lasing operation where sequential wavelength sweeps have the same phase evolution of the electric field and are mutually coherent [6]. However, the FDML dynamics given under real operation conditions is not fully understood up to now, making research on this novel type of laser operation particularly interesting.

Apart from the great success in application for OCT, FDML lasers might also become a promising alternative in other fields such as in short pulse generation with semiconductor-based mode locked lasers [9]. Here, temporal compression of the wavelength sweeps from an FDML laser, which are equivalent to very long, highly chirped pulses, could principally allow for the generation of time-bandwidth limited pulses in the future. Contrary to conventional mode locked semiconductor lasers, where the small carrier relaxation time impedes large pulse energies, FDML lasers have the advantage that energy is not stored as population inversion but optically in the long cavity, which can be as high as several 100 nJ per sweep. Therefore, this technique has the potential to enable comparably very high pulse energies at repetition rates of several hundred kHz obtainable directly from the oscillator.

The research work done within the framework of this thesis had two main objectives. On the one hand, a large part of the research focused on the investigation and characterization of new concepts of fast wavelength-swept light sources, including FDML lasers, aiming to improve the performance and applicability in OCT. On the other hand, the goal was to demonstrate the feasibility of short pulse generation using FDML lasers, investigate the dependence of the achievable temporal pulse width on internal FDML parameters and, in this way, learn about the coherence properties of the FDML laser.

In chapter 2, a detailed overview of the research field is given addressing the operation principle and development of OCT and FDML laser technology including also other fast wavelength-swept light sources.

In chapter 3, the initial focus is on the presentation of two different novel operation modes of FDML lasers, which have been demonstrated in the research work presented in this thesis. On the one hand, a k-space space linear FDML laser is introduced [10]

that, unlike almost all other wavelength-swept light sources utilized in OCT, exhibits a highly linear time-frequency sweep characteristic, which is attractive for application in OCT. The main advantage is that numerical resampling, which is required in order to guarantee equidistant frequency sampling prior to Fourier transformation, becomes unnecessary, simplifying numerical data processing. The key to achieve k-space linear FDML operation is a specially chosen, characteristic drive of the utilized piezo-actuated tunable Fabry-Pérot filter. The necessary linearity is quantized and different strategies based on numerical simulations are presented to obtain the optimum filter drive waveform. OCT imaging without the need for numerical resampling is successfully demonstrated.

On the other hand, a subharmonic FDML laser is introduced [11], where light is recirculated an adjustable number of times in the resonator yielding a multiple-pass through the same delay fiber within each cavity round-trip. OCT imaging is successfully demonstrated. The key element of subharmonic FDML operation is a reflective tunable Fabry-Pérot filter which acts as an optical switch. The main advantage for OCT is that this approach provides the inherent possibility to effectively multiply the sweep rate and therefore the OCT imaging speed by extracting a part of the optical power in the delay fiber. Current experimental restrictions are discussed.

Besides advances in FDML technology, chapter 3 also describes a new alternative approach of ultrafast wavelength-swept light sources, which was investigated within the research work reported in this thesis [12] and, in common to FDML lasers, can overcome the fundamental sweep speed limit. These wavelength-swept ASE sources are based on a setup having no optical feedback. The necessary output power is achieved since ASE light alternately passes a cascade of different gain elements and tunable optical filters, which are required to prevent the amplification of unfiltered ASE background. A crucial factor for optimum operation is a phase-shifted drive of the tunable filters compensating for the light transit time between the filters. Unlike FDML lasers, no long delay fiber is required which can be a potential advantage in wavelength ranges where polarization effects, chromatic dispersion or loss in the fiber complicate FDML operation. A theoretical analysis and experimental characterization of important properties of this new concept is given. Different implementations applicable for different wavelength ranges are presented and OCT imaging is demonstrated in each case. At 1060 nm, high speed in-vivo OCT imaging of the human retina was shown [13].

Chapter 4 deals with a completely new approach of short pulse generation using FDML lasers. A detailed description of the first experiments is presented which were performed within the framework of this thesis in a wavelength range close to 1550 nm. The temporal compression of the wavelength sweeps is accomplished by a subsequent pass through at least 15 km of highly dispersive fiber. With regard to the utilized FDML lasers, there are two crucial elements. Besides the fiber delay line, where chromatic dispersion needs to be compensated best possible [14], it is the home-build tunable Fabry-Pérot filter that is of particular importance, allowing for very high tuning speeds. The achievable temporal pulse width is investigated as a function of the internal FDML

laser parameters like the spectral width of the tunable filter or the filter drive frequency. A high dependence on the coherence properties of the FDML laser is observed. Current experimental restrictions on the choice of FDML parameters as well as limitations of the spectral bandwidth and the pulse energy, caused by imperfect temporal compression, are mentioned and discussed.

To enable comparison, equivalent pulse generation experiments were performed using a wavelength-swept ASE source which has no optical feedback and therefore can be seen as a fully incoherent swept light source. Additionally, a theoretical model is introduced describing the results of temporal compression of this type of swept sources. Based on these findings and considering the pulse widths achievable with the FDML laser, a direct insight into the coherence properties of the laser is obtained. Although time-bandwidth limited pulses have not been achieved under given experimental conditions, showing that FDML laser dynamics currently does not provide a fully coherent amplitude and phase evolution of the electric field and optimal mode-locking, it was demonstrated that there must occur at least partially coherent superposition of the different spectral components of the FDML sweep during the temporal compression process.

In order to gain a better understanding in how far different FDML parameters influence pulse generation, numerical simulations have been performed on the basis of a theoretical model of FDML laser dynamics [15]. This was achieved in close collaboration with the research group of Dr. Jirauschek from TUM (Technische Universität München). Chapter 4 also includes a comparison of the experiment with the numerical simulations.

2 Overview of the research field

A large part of the thesis focuses on advances of wavelength-swept light sources, primarily Fourier domain mode locked lasers, improving the applicability for optical coherence tomography (OCT). In each case OCT imaging is demonstrated. Therefore, it is essential to give an introduction to this biomedical imaging technique, which is the topic of the first part of this chapter. In the second part, the goal is to introduce the principle of Fourier domain mode locked lasers, but also address other wavelength-swept light sources which can be applied for OCT.

2.1 Optical coherence tomography

After an introduction to OCT, including the operation principle, different possible implementations are explained and compared. The following part of the section focuses on the explanation of different characteristic OCT parameters, such as optical resolution and sensitivity, which essentially influence OCT image quality. Besides addressing the theoretical background, the experimental determination of the parameters are discussed. After that, a typical OCT setup as used for OCT imaging within the framework of this thesis is presented. This chapter ends with an overview of the development of OCT technology also addressing different medical applications.

2.1.1 Introduction and principle

OCT is a powerful biomedical imaging technique which enables non-invasive, high-resolution, cross-sectional imaging of biological tissue with the possibility to generate three-dimensional data sets containing comprehensive, volumetric information. OCT is a comparably young imaging technique and was first demonstrated in 1991 [1]. OCT is used for various different applications in medicine. Two important examples are the diagnostics of diseases affecting the human retina [16] like glaucoma, age-related macular degeneration or diabetic retinopathy and the imaging of coronary atherosclerosis or vulnerable plaques [17, 18] using endoscopy. The name “optical coherence tomography” already implies that OCT is an optical technique. In OCT, biological tissue is exposed to near-infrared light (NIR) with typical wavelengths from ~ 800 nm to ~ 1400 nm. Light penetrates into the sample and a very small percentage of the photons are backscattered from different depths of the tissue. The time delay of the photons, which return from different layers of the sample, can be determined, as pointed out later

in chapter 2.1.2. In this way, a depth profile of backscattered intensity is obtained. Additionally, the light beam is transversally scanned over the sample (perpendicular to the beam). Therefore, a three-dimensional image, reflecting the internal microstructure of the tissue, can be generated via suitable data processing.

2.1.1.1 On the way to OCT

OCT is often referred to as the optical analogy to ultrasound imaging, which is based on time delay measurement of backscattered sound waves. However, the measurement procedure is different. Whereas in medical ultrasonography the time delay is measured on a direct electronic way, this is not possible for optical imaging. The reason is simply the fact that the speed of light exceeds the speed of sound by a factor of $\sim 10^5$. Thus, in order to obtain an axial resolution of at least $100\ \mu\text{m}$, time durations $< 330\ \text{fs}$ would have to be resolvable, which is impossible with a purely electronic approach. Therefore, alternative methods had to be investigated that circumvent this problem and enable a measurement of optical echoes. In 1971, a fast optical shutter ($\sim 10\ \text{ps}$), which was based on the Kerr effect and triggered by intense ps-light pulses, was presented that enabled photographing of light pulses on their way through scattering liquid [19]. The authors were the first to suggest that high-speed optical gating could be used to see inside biological tissue, rejecting light backscattered from unwanted layers. Based on this technique, measurements of cataract microstructure in rabbit eyes have been performed [20]. The achievable axial resolution of $> 1\ \text{mm}$ was still not satisfying. Another approach, which enabled ranging measurements of the cornea in rabbit eye, was based on using ultra-short optical pulses in combination with a background-free, nonlinear cross-correlation setup (second harmonic generation (SHG)) [21]. Here, gating is realized since superposed pulses returning from reference and sample arm generate an SHG signal only if the two pulses coincide temporally. Due to the pulse duration of $\sim 65\ \text{fs}$, an axial resolution of $\sim 15\ \mu\text{m}$ has been achieved. However, the sensitivity, defined as the ratio of illuminating to the minimum detectable power (see chapter 2.1.4.1), was $\sim 70\ \text{dB}$ which is still too small for high-quality imaging of most biological tissue. Finally, the breakthrough came with the technique of white light interferometry (or low coherence interferometry), which is easier to implement and is based on using a spectrally broadband, temporally incoherent light source, as for example a superluminescent diode (SLD). Therefore, an interference signal can only be measured within very small path length differences that do not exceed the coherence length. In this way, light which is backscattered from different closely spaced layers can be effectively distinguished. The principle is well known since the early 18th century. It has been successfully applied to measure optical echoes in waveguides or optical fiber [22-24], also denoted as optical coherence-domain reflectometry. A first application of this technique in biological tissue was the in-vivo measurement of axial length of the human eye in 1988 [25], followed by different other biological applications [26, 27]. However, it was in 1991 that Huang et al. showed, for the first time, cross sectional images of biological tissue using white light interferometry [1], which was the first demonstration of the new field of

OCT. In this work, ex-vivo OCT images of human retina and coronary artery were presented. The OCT system provided high axial resolution of $\sim 17 \mu\text{m}$ and a high sensitivity of $\sim 93 \text{ dB}$.

2.1.1.2 OCT and other biomedical imaging techniques

Today, there are several different imaging techniques used in medicine such as computer tomography (CT), magnetic resonance tomography (MRT) or positron emission tomography (PET). These techniques enable imaging of large volumes in the human body, but they are comparably expensive and require a lot of space in clinical applications. CT and PET both are based on the use of ionizing radiation, which constrains the applicability for human imaging. Conventional clinical systems provide spatial resolutions from $\sim 0.5 \text{ mm}$ to $\sim 1 \text{ mm}$ (CT and MRT, [28]) and several mm (PET, [29]), which is insufficient for many medical applications. Alternative, less complex approaches, which are based on non-ionizing radiation and provide a better resolution, are medical ultrasonography and optical techniques, such as confocal microscopy [30, 31] or OCT. In Figure 2.1, the typical performance of these three technologies is presented with respect to the achievable resolution and the penetration depth into tissue. In ultrasonography, there has to be made a trade-off between resolution and image penetration depending on the ultrasound frequency [32-34]. High frequency approaches provide resolutions of $\sim 15 \mu\text{m}$, but image penetration is restricted to a few millimeters. The typical resolution of a standard clinical system is a few $100 \mu\text{m}$, whereas penetration depth can achieve several centimeters. The best resolutions are obtained with optical techniques. In confocal microscopy, where transversal and axial resolution are linked by beam diffraction, a resolution approaching $1 \mu\text{m}$ has been realized. However, the disadvantage is the small penetration depth of a few $100 \mu\text{m}$ caused by strong scattering of light in typical, biological tissue. In OCT, transversal and axial resolution are decoupled enabling

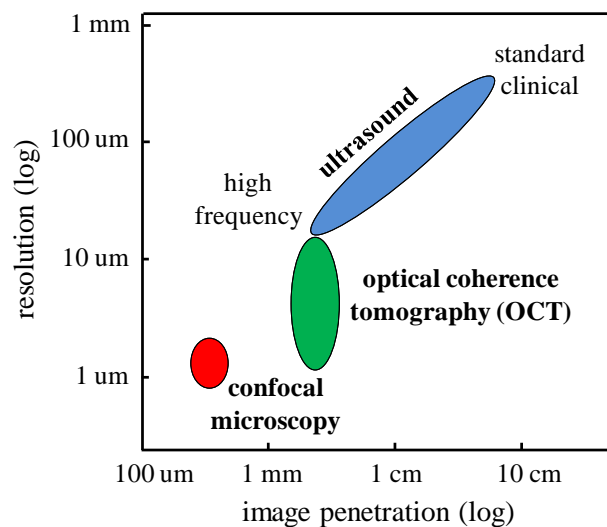


Figure 2.1: Performance of different biomedical imaging techniques with respect to image penetration and achievable resolution (logarithmic representation). Optical coherence tomography (OCT) can fill the gap between confocal microscopy and ultrasound imaging.

low numerical aperture focusing which increases the depth of field (see chapter 2.1.3). Here, the penetration depth is limited to $\sim 2\text{-}3$ mm with typical resolutions of ~ 10 μm . However, ultra-high resolution OCT has been demonstrated providing axial resolutions of $2\text{-}3$ μm [35]. In spite of the small penetration depth and the comparably small imaging volumes, OCT is preferred to ultrasound or CT in several medical applications due to high resolution and fast image acquisition. By means of, for example, endoscopes or catheters internal body imaging can be realized.

2.1.1.3 Suitable wavelength ranges for OCT

When choosing a certain wavelength range for OCT imaging, one important prerequisite is, of course, the availability of appropriate light sources and detection systems in this wavelength range. Moreover, the wavelength can have a considerable impact on image quality, contrast and the achievable penetration depth in the biological tissue depending on the medical application. Principally, there are two main processes which are wavelength dependent and influence OCT imaging: scattering and absorption of photons in the tissue. In the case of retinal OCT imaging, which is the most prominent application in OCT, the absorption in water plays an important role, since light traverses the eye twice, which corresponds to approximately 2×2.5 cm of water. In Figure 2.2, the absorption coefficient of water is shown. If light passes 5 cm of water, absorption results in an attenuation of optical power of $\sim 99.5\%$ at 1300 nm, $\sim 46\%$ at 1060 nm and only $\sim 12\%$ at 800 nm. Therefore, and due to the simple accessibility of light sources and detectors, the first OCT imaging has been carried out exclusively in a wavelength range centered at ~ 800 nm, which is still the dominant wavelength regime used for clinical systems in case of retinal OCT. However, besides absorption, the scattering of photons, which is inherently important for OCT imaging, influences image quality. In the spectral range of $\sim 600\text{-}1500$ nm, the wavelength dependence of the reduced scattering coefficient in many biological tissues can usually be described according to the power

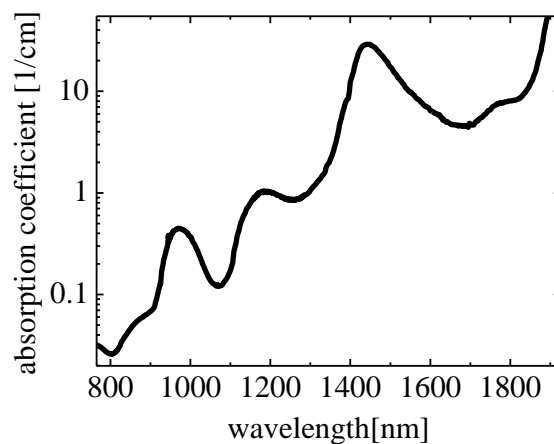


Figure 2.2: Absorption coefficient of water dependent on wavelength in a logarithmic representation, extracted from [36]. The local minimum of the absorption coefficient close to 1060 nm allows for retinal imaging at higher wavelengths, which can facilitate high-quality imaging of structures beneath the retinal pigment epithelium.

law $a\lambda^{-w}$, where typical values of w range from 1-2 [37]. Therefore, OCT imaging of highly scattering tissue can benefit from longer wavelengths, since the scattering probability of photons is reduced and, therefore, larger penetration depths can be realized at the same OCT sensitivity. Except for retinal imaging, almost all OCT applications require imaging in highly scattering, optical dense tissues where absorption due to water or other contents at near infrared wavelengths plays a considerably small role. Consequently, the wavelength region of choice for OCT imaging of tissues other than the posterior eye became ~ 1300 nm, where suitable light sources were available. Increased penetration depths at ~ 1300 nm compared to ~ 800 nm were first demonstrated in different investigations in the mid-1990s [38-40]. In case of even longer wavelengths, water absorption increases strongly complicating OCT imaging of biological tissues. At 1550 nm it has been shown that OCT imaging of biological tissue can yield similar image quality compared to 1300 nm if the proportion of water is not too high [41]. Since the retina consists of rather transparent and low scattering tissue, retinal OCT at ~ 800 nm can result in very good image quality where the major intraretinal layers can be distinguished. For OCT imaging of optically more dense tissue located beneath the retinal pigment epithelium, such as the choroid, longer wavelengths can become desirable enabling a deeper penetration into tissue. However, due to high losses on the way through the eye and back, OCT is not possible for wavelengths exceeding ~ 1150 nm. Nevertheless, as can be seen from Figure 2.2, the absorption in water has a distinctive, local minimum at ~ 1060 nm making retinal OCT imaging highly attractive in this wavelength range. With the availability of suitable light sources, retinal OCT was first demonstrated at 1060 nm in 2003 [42], followed by other comparative studies [43-45] demonstrating an increased penetration depth and high-quality images resolving structures below the RPE. Other advantages of retinal imaging at 1060 nm are the lower dispersion of light in water [45] (zero dispersion ~ 1000 nm) or the fact that the patient is not disturbed by 1060 nm light.

2.1.1.4 Basic setup and principle of OCT

In Figure 2.3, the typical setup for OCT imaging is sketched, which is based on a Michelson interferometer. The electric field originating from the source at a given position z is described as a superposition of monochromatic plane waves $E(t) = \sum_k E(k, t)$. The wavenumber k and the angular frequency ω are linked by the dispersion relation $\omega / k = c/n(\omega)$, where c is the speed of light and $n(\omega)$ is the refractive index of the medium. The monochromatic wave at a defined position z can then be written as:

$$E(k, t) = a(k)\cos(kz - \omega t - \varphi_k) \quad 2.1$$

In the following, the analysis is restricted to a monochromatic wave. Furthermore, the reflection from only one single depth in the sample (distance z_{Sx} to beam splitter) is considered. For the sake of simplicity, the corresponding electric field reflectivity r_{Sx} is assumed to be a real value. This situation is equivalent to replacing the sample with a

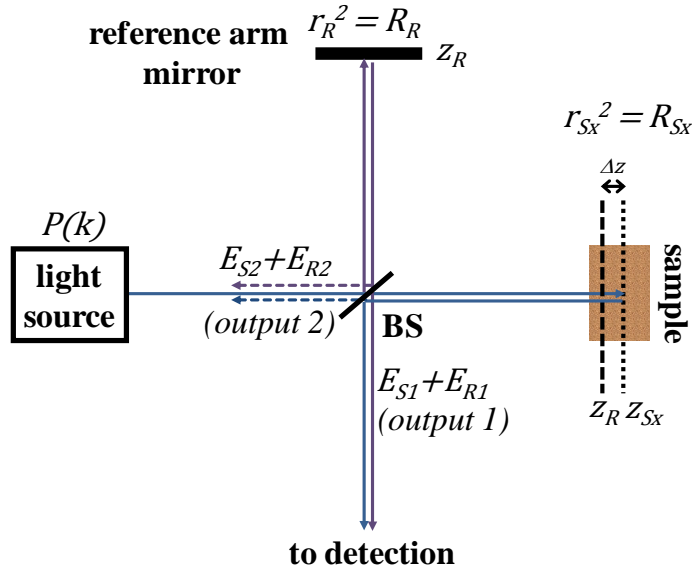


Figure 2.3: Basic setup of OCT imaging using a Michelson interferometer with a 50/50 optical beam splitter (BS) and a mirror placed in the reference arm and the sample in the other arm. Here, r_R , r_{Sx} and R_R , R_{Sx} correspond to the electric field reflectivities and the power reflectivities, respectively.

mirror of electric field reflectivity r_{Sx} located at a distance z_{Sx} from the beam splitter. Analogously, in the reference arm the distance from the beam splitter to the reference mirror is z_R and the electric field reflectivity of the reference mirror is denoted as r_R . Note that the further consideration includes phase jumps of the electric field of π for the reflection at the sample arm mirror (replacing sample) and the reference arm mirror. The optical beam splitter (BS) is assumed to be lossless with an ideal, achromatic power splitting of 1:1. The following derivation considers phase jumps of the electric field of π for reflections at the beam splitter as well as, necessarily, phase shifts of $\pi/2$ for light transmitting the beam splitter. This is a direct consequence of power conservation of the beam splitter and the resulting general expression of the scattering matrix for a lossless 2x2 beam splitter (see [46, 47]). Moreover, $z = 0$ is defined as the location of the beam splitter and the phase φ_k is set to zero. After light passing the interferometer, the electric field directly at output 1 (output leading to detection) is the sum of the electric fields E_{S1} (light returning from sample arm) and E_{R1} (light returning from reference arm), which read:

$$E_{S1}(k, t) = \frac{1}{2} r_{Sx} a(k) \cos\left(2kz_{Sx} - \omega t + \frac{\pi}{2}\right)$$

2.2

$$E_{R1}(k, t) = \frac{1}{2} r_R a(k) \cos\left(2kz_R - \omega t + \frac{\pi}{2}\right)$$

Analogously, the electric field directly at output 2 (output leading back to the light source) is the sum of the electric fields E_{S2} and E_{R2} , which read:

$$E_{S2}(k, t) = \frac{1}{2} r_{Sx} a(k) \cos(2kz_{Sx} - \omega t) \quad 2.3$$

$$E_{R2}(k, t) = \frac{1}{2} r_R a(k) \cos(2kz_R - \omega t - \pi)$$

Assuming an optical detector with an electronic bandwidth B , corresponding to an integration time $T_i = 1/(2B)$, with a detector responsivity ρ , supposed to be independent from k , the detector current $I_D(k)$ can be written as:

$$I_D(k) = \gamma \rho \langle |E_R(k, t) + E_S(k, t)|^2 \rangle_{T_i} \quad 2.4$$

Here, γ is a proportionality factor and $\langle x(t) \rangle_{T_i} = \frac{1}{T_i} \int_0^{T_i} x(t) dt$ is denoted as the average over the time T . In the following, the identities $\cos(a) \cdot \cos(b) = \frac{1}{2} (\cos(a - b) + \cos(a + b))$, $\Delta z = z_R - z_{Sx}$, $\langle \cos^2(kz - \omega t) \rangle_T = \frac{1}{2}$ and $\langle \cos(kz - 2\omega t) \rangle_T = 0$ are used. Under consideration of equations 2.2, 2.3 and 2.4 and by substituting for the power reflectivities $R_R = r_R^2$, $R_{Sx} = r_{Sx}^2$ and the spectral power of the light source $P(k) = \frac{1}{2} \gamma a(k)^2$, the detector current $I_D(k)$ that may be measured at both outputs reads:

$$I_{D1,2}(k) = \frac{\rho}{4} P(k) \left(R_R + R_S \pm 2\sqrt{R_R R_S} \cos(2k\Delta z) \right) \quad 2.5$$

Equation 2.5 shows that the detector current consists of three different contributions. The first two terms only reflect the spectral power of the light source and do not carry any important information for OCT since they are independent on Δz . By contrast, the last interference term depends on Δz and is the basis for the derivation of the intensity depth profile. Since under typical OCT conditions the backscattered power from the sample is very small ($R_S \ll R_R$), the second term can be neglected. Note that the last term is proportional to $\sqrt{R_R R_S}$. This is the reason why OCT is based on heterodyne gain, meaning that the signal gain can be adjusted via control of the power of the returning reference arm light. Therefore, very high sensitivities of >100 dB can be achieved, which is crucial to enable high-quality imaging. So far, the analysis has been restricted to a single reflection from one depth in the sample. An extension of the treatment, considering n reflections with different r_{Sx_n} but neglecting possible autocorrelation terms, yields the interference term $\frac{\rho}{2} P(k) \sqrt{R_R} \sum_n (\sqrt{R_{S_n}} \cos(2k\Delta z_n))$ [32]. Until now, the analysis was based on a monochromatic wave. However, the derivation of the depth profile $R_S(\Delta z)$ of the backscattered intensity requires the use of a light source generating a wide range of frequencies (see chapter 2.1.2 and chapter 2.1.3). There are different approaches in OCT that enable a determination of $R_S(\Delta z)$, which is topic of the next chapter.

2.1.2 Different implementations of OCT

2.1.2.1 Overview

In OCT, one can distinguish between different approaches which differ considerably on the procedure how the intensity depth profile, which is called A-scan, is determined. In Figure 2.4, the basic principle of these implementations is sketched. On the one hand, there is time domain OCT (TD-OCT), which is the traditional technique that was exclusively used during the first years after introduction of OCT and is based on white light interferometry. Here, all spectral components of a broadband light source are measured instantaneously with a photodiode. Due to the small temporal coherence, only light that is backscattered from depths very close to the zero delay point contributes to the signal. Thus, by moving the reference mirror and therefore shifting the point of zero delay in the sample, a whole A-scan can be recorded. The time required for one A-scan is given by the speed of the mirror movement. On the other hand, there is the field of frequency domain OCT (FD-OCT), sometimes also referred to as Fourier domain OCT, which emerged a few years later and where currently almost all research in OCT is focused on since it provides many advantages compared to TD-OCT. In FD-OCT, the reference arm mirror is static and a further differentiation is made between spectral domain OCT (SD-OCT) (also called spectrometer based OCT), and swept source OCT (SS-OCT) (also called optical frequency domain imaging or OFDI). SD-OCT also requires a broadband light source. However, instead of a photodiode, a spectrometer is used meas-

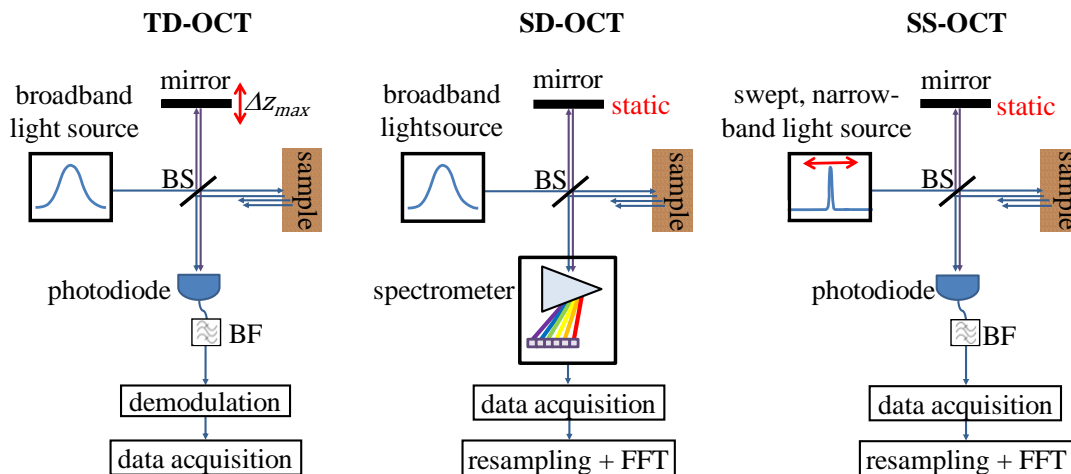


Figure 2.4: Different implementations of OCT: In time domain OCT (TD-OCT), the reference arm mirror is moved to determine the depth profile of backscattered intensity. All spectral components from the broadband light source are monitored instantaneously with a photodiode yielding interference signal only for small path length differences. In frequency domain OCT (FD-OCT), the mirror is static. In FD-OCT, a further differentiation is made between spectral domain OCT (SD-OCT), where a spectrometer determines the interference signal of all spectral components from a broadband light source, and swept source OCT (SS-OCT), where a narrowband light source is swept over a wide wavelength range and the interference signal is recorded with a photodiode. In both cases, a fast Fourier transformation (FFT) yields the desired intensity depth profile. (BF: Electrical band-pass filter)

using the different spectral components of the light after the interferometer. In SS-OCT, the principle is similar. Here, a narrowband light source, where wavelength changes with time and over a large wavelength range, a so called wavelength-swept light source, is used and the light from the output of the interferometer is recorded during this wavelength sweep using a photodiode. However, in both cases the measured interference signal $I(k)$ or $I(t)$ must be Fourier transformed after data acquisition, since the backscattered intensity from each depth $R_s(\Delta z)$ is proportional to a certain frequency component of the signal. Unlike TD-OCT, in FD-OCT the information of backscattered intensity from each depth is contained in the entire A-scan signal.

2.1.2.2 Time domain OCT (TD-OCT)

In TD-OCT, all spectral components are monitored with the photodiode simultaneously. Therefore, for a specific reference mirror position z_R , the detector current is obtained by integration over k ($I_D(z_R) = \int_0^\infty \tilde{I}_D(k) dk$), where $\tilde{I}_D(k)$ is the spectral density of the current. In the following, the spectrally integrated power of the source $P_0 = \int_0^\infty \tilde{P}(k) dk$ is introduced. $\tilde{P}(k)$ is the power spectral density of the light source, which is assumed to have a Gaussian shape where k_0 is the center wavenumber and Δk_{FWHM} is the full-width of half maximum (FWHM) of $\tilde{P}(k)$. Assuming a reflection from a single depth in the sample z_{Sx} , $\tilde{I}_D(k)$ is given by equation 2.5 (replace $P(k)$ with $\tilde{P}(k)$, $z_R = \Delta z + z_{Sx}$). Integrating $\tilde{I}_D(k)$ over k then results in a detector current that reads (see [32]):

$$I_D(z_R) = \frac{\rho}{4} P_0 \left(R_R + R_S + 2\sqrt{R_R}\sqrt{R_S} e^{-\frac{(z_R - z_{Sx})^2 \Delta k_{FWHM}^2}{4 \ln(2)}} \cos(2k_0(z_R - z_{Sx})) \right) \quad 2.6$$

Obviously, the interferometric part includes two terms depending on z_R . The envelope of the signal is proportional to $\sqrt{R_R}\sqrt{R_S}$ and decays with $e^{-(z_R - z_{Sx})^2 \Delta k_{FWHM}^2 / (4 \ln(2))}$. Additionally, the signal is modulated by a cosinusoidal carrier wave modulation with a frequency proportional to the center wavenumber k_0 . Generally, the function describing the decay of the envelope is the so called coherence function $\gamma(\Delta z)$ which is directly linked to the spectral power density of the light source $\tilde{P}(k)$ by Fourier transformation:

$$\gamma(z) \overset{FT}{\leftrightarrow} \tilde{P}(k) \quad 2.7$$

Note that equation 2.6 is a direct consequence of the Wiener–Khinchin theorem, which states that spectral power density and the electric field autocorrelation function are linked by Fourier transformation. Since, in TD-OCT, the reference arm length $z_R(t)$ is scanned over the desired imaging range Δz_{max} in the A-scan time ΔT with a constant speed $v = \frac{\Delta z_{max}}{\Delta T}$, the detector current becomes time-dependent and the carrier modulation frequency reads: $\nu = \frac{1}{\pi} k_0 v$. To ensure optimal sensitivity and resolution, an electrical band-pass filter is used centered at the carrier frequency with an optimal bandwidth B , which equals approximately twice the FWHM power bandwidth of the signal

and therefore is proportional to the spectral width Δk_{FWHM} and the scan speed v [48]. Furthermore, the signal is demodulated before data acquisition. In this way, the DC-offset can be rejected and the signal envelope can be measured allowing for the determination of $R_s(\Delta z)$.

2.1.2.3 Frequency domain OCT (FD-OCT)

In FD-OCT, the reference mirror is static and the backscattered intensity profile is derived by Fourier transformation of the signals generated by measuring the different spectral components. One possibility to apply FD-OCT is spectral domain OCT (SD-OCT), which is based on a spectrometer used for detection after the interferometer output. The first attempts to use this technique enabled the measurement of intraocular distances in 1995 [49]. In 2002, SD-OCT was first demonstrated for in-vivo retinal imaging [50]. Typically, the spectrometer consists of a grating which is dispersing the light and a pixel array integrated in a line scan camera which simultaneously measures the different spectral components. The A-scan time ΔT is given by the time the camera needs to read out all pixels. Since the signal of each pixel is integrated over a time ΔT , the electrical bandwidth is $B = 1/(2\Delta T)$. Assuming a single reflection from the sample and a detection of all spectral components with infinite accuracy, the spectrally dependent current reads as denoted in equation 2.5.

The second technique associated with the field of FD-OCT is swept source OCT (SS-OCT), also referred to as optical frequency domain imaging (OFDI), which is not based on using broadband light sources but on narrowband wavelength-swept light sources. In chapter 2.2, an overview over the development, the principle of operation and different implementations of these types of light sources is given. The principle was already used since the early 1980's for measurements in fiber optics and photonics components [51-53], referred to as optical frequency domain reflectometry (OFDR). The first demonstration of this technique for OCT was presented in 1997 [54, 55]. SS-OCT imaging with improved quality and a considerably higher A-scan rate was shown in 2003 [56]. The wavenumber of the light generated in a wavelength-swept light source changes repetitively and monotonically within a certain range Δk as a function of time. Unlike SD-OCT, where different spectral components are separated in space, in SS-OCT the spectral information is encoded in time. The segment of the light field comprising the spectral width Δk and the temporal width ΔT , which defines the A-scan time, is called a sweep. To simplify things, only a single ascending sweep is considered which is assumed to exhibit a linear time-wavenumber characteristic. The wavenumber then can be written as: $k(t) = k_i + \frac{\Delta k}{\Delta T} t$. Thus, assuming a single reflection from the sample, the detector current, which is measured with the photodiode, can be derived in a similar way as shown in chapter 2.1.1.4 and reads:

$$I_D(t) = \frac{\rho}{4} P[k(t)] \left(R_R + R_S + 2\sqrt{R_R}\sqrt{R_S}\cos(2k(t)\Delta z) \right) \quad 2.8$$

Substituting for $k(t)$, the interferometric term of $I_D(t)$ oscillates with an angular frequency ω_I

$$\omega_I = 2 \frac{\Delta k}{\Delta T} \Delta z \quad 2.9$$

This result can easily be understood if one considers the fact that the optical frequencies of the two light waves which return from both interferometer arms, incident on the photodiode, always differ by an amount that is proportional to the path length difference $2\Delta z$. The detectable signal then simply exhibits a frequency equal to the difference frequency or beat frequency of these two light waves.

Therefore, in SD-OCT as well as in SS-OCT, the signal which is acquired over the A-scan time ΔT , and usually is referred to as fringe signal, oscillates with a frequency that is proportional to the path length difference $2\Delta z$ exhibiting an amplitude that is proportional to $\sqrt{R_S}$ assuming a single reflection. Thus, Fourier transformation is the appropriate mean to determine $R_S(\Delta z)$ in case of multiple reflections since it decomposes the fringe signal in its different frequency components, each representing light reflected from a certain depth in the sample. If one assumes that the spectral components can perfectly be resolved by the FD-OCT system and under consideration of equation 2.5 or equation 2.8, the resulting Fourier transformed signal for a single reflection can be written as follows [2, 32]:

$$i_D(z) = \frac{\rho}{8} \gamma(z) (R_R + R_S) + \frac{\rho}{4} \sqrt{R_R} \sqrt{R_S} (\gamma[z + \Delta z] + \gamma[z - \Delta z]) \quad 2.10$$

Here, $\gamma(z)$ is the coherence function which is the Fourier transformation of the spectral power density $\tilde{P}(k)$ (see equation 2.7). It is important to know that Fourier transformation decomposes the fringe signal with regard to time delay or path length difference \hat{z} between the interferometer arms which is twice the optical distance in the sample ($\hat{z} = 2z$). This has to be considered if one wants to recover single-sided distances, as done in the derivation of equation 2.10. Obviously, the coherence function appears three times in the Fourier transform. It is centered at $z = 0$ representing the DC components (non-interferometric terms), at $z = -\Delta z$ and at $z = \Delta z$ representing the reflection at Δz , where the maximum of the coherence function is proportional to $\sqrt{R_S}$. The fact that $i_D(z)$ is always symmetric with regard to $z = 0$, meaning that the complete information about backscattered intensity is contained twice in the Fourier transform, is called the complex conjugate artifact in FD-OCT. This is a direct consequence of the fact that the detected fringe signal is real and the Fourier transformation therefore must be Hermitian symmetric. Light reflected from the opposite side of the zero delay point in the sample appears as a mirror image. A differentiation between positive and negative Δz (positive or negative frequencies) is not possible.

2.1.2.4 Practical aspects in FD-OCT

So far, several assumptions have been made that do not apply for real FD-OCT setups. On the one hand, the ability to resolve the spectral components is finite and not infinite as assumed up to now. In a SD-OCT setup, the spectral resolution δk is given by the optical resolution of the grating but can also be affected by the finite spacing of the CCD pixels in the line scan camera. In SS-OCT, δk is given by the instantaneous spectral linewidth of the wavelength-swept light source which is typically ~ 1000 times smaller than the sweep range but not negligible. Assuming a spectral resolution function $\psi(k)$ centered at $k = 0$ with a width δk , then equation 2.5 or equation 2.8 have to be convoluted with $\psi(k)$. Due to the convolution theorem, the correct result for $i_D(z)$ is obtained by multiplication of equation 2.10 with the Fourier transform of $\psi(k)$, where the maximum is centered at $z = 0$ and the width that is proportional to $1/\delta k$. Therefore, the signal $i_D(z = \Delta z)$ decreases with increasing imaging depth Δz , even if the reflectivity $R_S(\Delta z)$ is constant. This inherent fact is often referred to as sensitivity roll-off in FD-OCT, which can be reduced by optimizing the spectral resolution δk .

On the other hand, it is important to know that the time dependent photodiode signal is digitized with an analog to digital converter with a sample rate f_s (SS-OCT) and that there are a finite number of pixels in the line scan camera (SD-OCT). In both cases, a discrete number of values are acquired during one A-scan and are processed numerically. Assuming M samples with sampling interval δk_S covering a total range $\Delta k = M\delta k_S$, then a direct consequence of discrete Fourier transformation is that the sampling interval in the z -domain is equal to $\frac{\pi}{\Delta k}$ and the total z range becomes $\frac{\pi M}{\Delta k} = \frac{\pi}{\delta k_S}$. Therefore, the imaging range is limited by (see [2]):

$$\Delta z_{max} = \pm \frac{\pi}{2\delta k_S} \quad 2.11$$

Note that there have been several approaches that can remove the complex conjugate artifact and therefore double the possible imaging range. Besides frequency shifting in SS-OCT systems [57], there were developed several active phase-shifting techniques using piezoelectric actuators or phase modulators [58-62]. Phase shifts can also be generated by pivot offset scanning [63, 64]. Other techniques are based on interferometer designs using $N \times N$ ($N > 2$) fiber couplers [65, 66], where the outputs provide inherently phase shifted signals. An appropriate algorithm to obtain the complex conjugate resolved signal is given in [67]. An alternative approach uses non-matched dispersion between sample and reference arm [68].

In SS-OCT, usually an electrical low-pass filter is used, so that the electrical bandwidth B does not exceed half of the sampling rate $f_s = \frac{M}{T}$ of the analog to digital conversion ($B \leq \frac{f_s}{2}$), in order to avoid aliasing (Nyquist theorem). Additionally, a high-pass filter can suppress remaining DC-components.

Another assumption that has been made and does not apply in practice is a linear wave-number over time (SS-OCT) or linear wavenumber over pixel number characteris-

tic (SD-OCT). In SD-OCT, the grating is dispersing the light approximately linear in wavelength but not in wavenumber. Therefore, the wavenumber difference between adjacent pixels is not equal. The same is true for SS-OCT, where digitizing of the photodiode signal with an even spacing in time results in uneven wavenumber spacing of the samples. The reason is that the wavenumber over time characteristic depends on the wavelength-swept light source, and typically differs considerably from being linear. Consequently, the fringe signal obtained, assuming a single reflection in the sample arm, does not exhibit a single angular frequency ω_l and the peaks in the discrete Fourier transform signal are broadened. There are several ways to solve this problem, which is discussed in chapter 3.1.1. The common approach is to perform numerical resampling prior to discrete Fourier transformation in order to provide data that is evenly sampled in wavenumber (see chapter 2.1.6.2).

2.1.2.5 Dual balanced detection

Interestingly, the interferometric terms of the current signals that result from measuring intensity of the light originating from output 1 and output 2 of the Michelson interferometer (see Figure 2.3) exhibit a phase difference of π (see chapter 2.1.1.4 and equation 2.5). However, the DC terms which do not depend on Δz and carry no relevant information for OCT have no phase difference. Using a setup with an optical circulator (see Figure 2.7), placed between the light source and the input of the interferometer, the light returning from output 2 can be detected with an additional photodiode. In dual balanced detection, as used in coherent optical communication systems [69], the signals of both detectors are subtracted electronically. Therefore, the OCT relevant fringe signal is doubled, whereas the DC terms are cancelled out. Besides a removal of the unwanted DC signal, enabling to use the available dynamic range of the analog to digital conversion more effectively, the main advantage of this approach is that excess intensity noise originating from the light source (see chapter 2.1.5.6) can be suppressed yielding improved sensitivity [70, 71]. Dual balanced detection is commonly used in TD-OCT and SS-OCT. However, in SD-OCT, dual balanced detection would require an additional, identical spectrometer. Up to now, dual balancing in SD-OCT has not been demonstrated.

2.1.2.6 Comparison of different implementation techniques

Today, almost all research in optical coherence tomography focuses on FD-OCT. The reasons for this are two main advantages of FD-OCT compared to TD-OCT. The first point is imaging speed. Since, in TD-OCT, the A-scan time is dependent on the mechanical movement of the reference mirror, A-scan rate and therefore imaging rate is typically limited to a few kHz. In FD-OCT, the A-scan rate is defined by the read-out rate of the CCD camera (SD-OCT) or by the sweep rate of the wavelength-swept light source (SS-OCT). However, in both cases, typical A-scan rates and imaging speeds exceed those of TD-OCT by a factor of 100 or more. Imaging speed is of great importance for OCT, since it provides many advantages like, for example, the possibility of three-

dimensional visualization of fast processes such as in development biology [72] or acquiring large, densely sampled, volumetric datasets in a short time as, for example, in intracoronary, endoscopic OCT [73] or retinal OCT [74]. On the one hand, short imaging times are often highly desirable. In retinal OCT, for example, the patient eye motion and blinking complicate imaging. In intracoronary, endoscopic OCT, blood has to be removed in the artery. Thus, a short imaging time, meaning a rapid pullback speed of the endoscopic probe in the artery, reduces the risk of ischemia. On the other hand, the acquisition of large, densely sampled, volumetric data-sets enables various different possibilities to visualize the data in post-processing, such as cross-sectional images along arbitrary coordinates or depth-resolved en-face fundus images [74] which can be a great advantage for the physician. Furthermore, high imaging speed enables effective use of averaging.

The other main advantage of FD-OCT in comparison to TD-OCT is an inherent sensitivity advantage of ~ 20 dB to 30 dB assuming same power incident on the sample and the same A-scan rate. A derivation of this fact is given in chapter 2.1.5.4. As a direct consequence, FD-OCT can detect considerably smaller signals which are backscattered from the sample improving image quality.

However, there are also some disadvantages of FD-OCT compared to TD-OCT. One example is the sensitivity roll-off with increasing imaging depth, which is appearing only in FD-OCT. Furthermore, numerical resampling is not necessary. Another advantage of TD-OCT is the possibility to dynamically shift the focus in the sample within the imaging range without changing the path length of the sample arm [75]. In this way, it is possible to achieve a situation where the zero delay point (center of coherence gate) and the focus position in the sample are always identical. Therefore, the transversal resolution is almost the same over the whole imaging range and focusing with a higher NA becomes feasible, improving transversal resolution. In OCT without dynamic focus adjustment, this is not possible, since higher NA-focusing results in a decrease in depth of field, reducing the available depth range (see chapter 2.1.3.2). Note that this technique is not applicable for FD-OCT, since here the information about backscattered intensity from each single depth in the sample is encoded in the entire A-scan signal.

Comparing SD-OCT with SS-OCT in terms of imaging speed or sensitivity roll-off requires a closer look at the current availability of fast spectrometers or fast wavelength-swept light sources in the desired wavelength range, which is investigated in chapter 2.1.7.3. However, it is generally true to say that currently the fastest high-quality OCT imaging can be realized with SS-OCT and that SS-OCT can show a considerably less pronounced sensitivity roll-off than SD-OCT. One has to recognize that both FD-OCT techniques have the same sensitivity advantage compared to TD-OCT, however the lack of dual balancing capability in SD-OCT can be a disadvantage. Also worth mentioning is an effect called fringe washout which occurs in FD-OCT due to unwanted, axial motion of the sample during image acquisition degrading sensitivity [76]. The reason is a decrease of the amplitude of the fringe signal due to averaging of the signal over the integration time in each spectral channel of the detector. In SD-OCT, averaging in all

spectral channels (CCD-pixels) happens simultaneously with an integration time of approximately the A-scan time T , whereas, in SS-OCT, it happens sequentially (M samples in A-scan time T) and the integration time therefore is $\sim T/M$. Consequently, in comparison to SD-OCT, SS-OCT systems exhibit fringe washout effects which are negligible small or play a comparable role only for a $\sim M$ times faster axial movement [77]. Generally, fringe washout effects decrease with increasing imaging speed (shorter A-scan time). Note that in SS-OCT, axial motion of the sample give rise to other effects like spatial image distortion caused by Doppler shift or blurring of images caused by degradation of axial resolution [76], which, in the case of very low A-scan rates, can also significantly deteriorate image quality.

2.1.3 Point spread function and optical resolution

2.1.3.1 Axial resolution

The point spread function (PSF) is defined as the OCT signal that is obtained if a mirror is placed in the sample arm representing a single reflection from a certain depth in the sample with $R_S(\Delta z) = 1$. Consequently, measuring the PSF is the measurement of choice for a determination of the axial resolution in an OCT system. In TD-OCT, the PSF is the envelope (after demodulation) of a signal given by equation 2.6. Assuming perfect resampling and neglecting the sensitivity roll-off, the PSF in FD-OCT is given by the last term in equation 2.10, picking only the contribution from one side of the Fourier transform due to complex conjugate artifact. However, for both techniques the peak of the PSF is centered at $z = \Delta z$ and the shape is only defined by the coherence function $\gamma(z)$ (see equation 2.7), which is typically referred to as coherence gating. If one assumes a spectral power density $\tilde{P}(k)$ exhibiting a Gaussian shape, where Δk_{FWHM} is the spectral FWHM, k_0 is the center wavenumber and P is an arbitrary power, $\tilde{P}(k)$ can be written as follows [32]:

$$\tilde{P}(k) = \frac{P}{\Delta k_{FWHM}} \frac{2\sqrt{\ln 2}}{\sqrt{\pi}} \cdot e^{-\frac{4\ln(2)(k-k_0)^2}{(\Delta k_{FWHM})^2}} \quad 2.12$$

Note that for SS-OCT, $\tilde{P}(k)$ is equal to the time-dependent power spectral density $\tilde{P}(t) = \tilde{P}(k(t))$. Fourier transformation then yields the coherence function:

$$\gamma(z) = P \cdot e^{-z^2 \frac{(\Delta k_{FWHM})^2}{4\ln(2)}} \quad 2.13$$

The axial resolution Δz_{FWHM} , defined as the FWHM of $\gamma(z)$, can be determined to:

$$\Delta z_{FWHM} = \frac{4\ln(2)}{\Delta k_{FWHM}} = \frac{2\ln(2)}{\pi} \cdot \frac{\lambda_0^2}{\Delta \lambda_{FWHM}} \quad 2.14$$

Here, λ_0 is the center wavelength and $\Delta \lambda_{FWHM}$ is the FWHM of the spectral power density in terms of wavelength. As expected, the achievable resolution is indirectly propor-

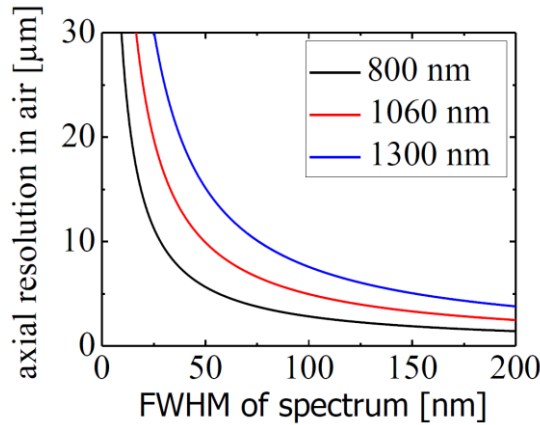


Figure 2.5: Axial resolution in air against the FWHM of the Gaussian shaped spectrum of the utilized light source (in SS-OCT: FWHM of the sweep range) for different center wavelengths.

tional to the spectral width of the light source or, in the case of SS-OCT, the spectral sweep range of the wavelength-swept light source. Interestingly, the resolution does not only depend on $\Delta\lambda_{FWHM}$, but also on the center wavelength λ_0 . Figure 2.5 sketches the axial resolution for the most relevant wavelength regimes in OCT (see chapter 2.1.1.3). Thereby, it is important to know that the derivation of equation 2.14 is based on the assumption that the refractive index n equals 1, defining the resolution in air. Generally, one has to consider the optical path length nz . Therefore, the effective resolution in biological tissue is n times smaller (typically $n \sim 1.35$, see [78]).

2.1.3.2 Transversal resolution

In OCT, axial and transversal resolution are independent from each other unlike confocal microscopy, where axial and transversal resolution are both determined by the diffraction limited focusing of the optical beam in the sample. However, in OCT, this is true only for transversal resolution. Note that OCT is also a confocal technique, which normally is accomplished using optical single mode fiber for beam delivery in the sample arm, acting as a pinhole aperture for illuminating and collecting backscattered light, comparable to a fiber based scanning confocal microscope [31]. For OCT, this is a crucial factor, since, in this way, confocal gating leads to an attenuation of out-of-focus light, which suppresses the detection of multiply scattered photons that would have been detected by coherence gating. Using Gaussian beam optics, the transversal resolution Δx in the focus, defined as twice the beam waist w_0 ($\frac{I(w_0)}{I(0)} = e^{-2}$), is given by (approximation of small angles):

$$\Delta x = \frac{4\lambda f}{\pi D} = \frac{2\lambda}{\pi \cdot NA} \quad 2.15$$

Here, D is the spot size of the beam incident on the objective lens, f is the corresponding focal length and $NA = D/2f$ is the numerical aperture. On the one hand, high-NA focusing minimizes Δx , on the other hand, it restricts the usable depth range due to con-

focal gating. High NA-focusing yields an emphasized degradation of transversal resolution with increasing distance to the focus. This can be expressed by the confocal parameter b (or depth of field), which equals twice the Rayleigh length z_R ($b = 2z_R$). If $z = z_R$ the transversal resolution is increased by a factor of $\sqrt{2}$. The confocal parameter is proportional to Δx^2 :

$$b = \frac{\pi \Delta x^2}{\lambda} \quad 2.16$$

Since the aim of OCT is to image over the maximum possible depth range, typically low-NA focusing is used, tolerating a larger Δx but ensuring an almost constant transversal resolution over the desired depth range. So typically, the confocal parameter considerably exceeds the axial resolution ($b \gg \Delta z_{\text{FWHM}}$). However, if the desired depth range is small, there is an operation modus called optical coherence microscopy (OCM) [79], which is based on high-NA focusing yielding $b \approx \Delta z_{\text{FWHM}}$. Due to combined coherence and confocal gating, OCM can achieve improved imaging depth compared to confocal microscopy.

2.1.4 Sensitivity and dynamic range

In this chapter, several important characteristic parameters for OCT imaging are defined and corresponding measurements determining these parameters are introduced. Since within the research work presented in this thesis all OCT imaging was based on the swept source approach, the following analysis is restricted to SS-OCT. However, the principle easily can be transferred to other OCT techniques.

2.1.4.1 Sensitivity

The sensitivity Σ_{dB} in an OCT system is defined as the ratio of incident power P_S on the sample to the minimum detectable power P_{min} that is backscattered from a certain depth corresponding to a path length difference $2\Delta z$. Sensitivity is given in a logarithmic representation:

$$\Sigma_{\text{dB}} = 10 \cdot \log\left(\frac{P_S}{P_{\text{min}}}\right) = 20 \cdot \log\left(\frac{i_D(\Delta z)}{i_{D,\text{min}}(\Delta z)}\right) = 10 \cdot \log\left(\frac{1}{R_{s,\text{min}}}\right) \quad 2.17$$

The sensitivity can also be defined as the ratio of peak detector current signal in the Fourier transform $i_D(\Delta z)$ (equation 2.10) to the corresponding value of the minimum detectable power $i_{D,\text{min}}(\Delta z)$. Note that the additional factor 2 stems from the fact that $i_D(\Delta z) \sim \sqrt{P_S} \sim \sqrt{R_S}$. Moreover, the sensitivity is directly linked to the smallest possible power reflectivity $R_{s,\text{min}}$ that enables detection of backscattered light. One straightforward approach to measure sensitivity is to use a mirror in the sample arm ($R_S = 1$), determine the PSF and attenuate the light in the sample until the signal in the Fourier transform cannot be detected any more. However, the transition between the condition that a signal can be detected and that it vanishes in the noise background is smooth.

2. Overview of the research field

Therefore, a definition has been introduced, most commonly accepted in the OCT community, that states that this transition occurs when the signal to noise ratio (SNR) is equal to 1. The SNR is defined in terms of electrical power and reads as follows:

$$SNR = \frac{i_D(\Delta z)^2}{\sigma^2(\Delta z)} \quad 2.18$$

Here, $i_D(\Delta z)^2$ is the mean-square peak signal power and $\sigma^2(\Delta z)$ is the variance of the noise background in a small window centered at $z = \Delta z$. With $SNR = 1$, the minimum peak detector current signal $i_{D,min}(\Delta z)$ reads:

$$i_{D,min}(\Delta z) = \sqrt{\sigma^2(\Delta z)} = \sigma(\Delta z) \quad 2.19$$

A typical measurement of sensitivity at $z = \Delta z$, as done during research work presented in this thesis, is performed as follows: Firstly, a mirror is placed in the sample arm yielding a path length difference $2\Delta z$. Since a direct measurement of the PSF aiming to determine $i_D(\Delta z)$ would saturate the detector, a neutral density filter of optical density OD is introduced in the sample arm (attenuation of $(2 \cdot 10 \cdot OD)$ dB) and the peak value of the PSF (after resampling) $i'_D(\Delta z)$ is determined. Secondly, the sample arm is blocked and the standard deviation $\sigma(\Delta z)$ of the noise floor in the Fourier transform in a window centered at $z = \Delta z$ is calculated. Blocking of the sample arm and performing both measurements separately is essential since an additional signal increases the noise floor over the whole z -domain. Using equation 2.17 and 2.19, the sensitivity is then given by:

$$\Sigma_{dB} = 20 \cdot \log\left(\frac{i'_D(\Delta z)}{\sigma(\Delta z)}\right) + 2 \cdot 10 \cdot OD \quad 2.20$$

Since the sensitivity depends on the reflected optical reference arm power (optical power of light returning from the reference arm; see chapter 2.1.5.6), the measurement is repeated for different power reflectivities R_R changing the attenuation in the reference arm. In this way, the optimum reflected reference arm power can be determined. Note that, understandably, the power P_S incident on the sample is limited to avoid potential thermal damages to the tissue. These limits depend on the medical application and were determined by the American national standards institute (ANSI) [80]. Since the power reflectivities R_S from interesting layers in biological tissue can be very small and due to the limitation of optical power on the sample, sensitivity is a very important parameter for OCT imaging. Depending on the OCT application, sensitivities of at least 90 dB or, in many cases, even higher than 100 dB are required to ensure high OCT image quality. Assuming an incident average power of ~ 1 mW, a sensitivity of 100 dB translates to a minimum detectable power of only ~ 100 fW. In chapter 2.1.5, the theoretically achievable maximum sensitivity as a function of incident power and A-scan time is derived.

2.1.4.2 Sensitivity roll-off with increasing depth

As already mentioned in chapter 2.1.4.2, an intrinsic characteristic of FD-OCT is the depth dependent sensitivity roll-off, which, in SS-OCT, is due to the finite instantaneous linewidth δk of the wavelength-swept light source. Typically, the experimental determination of this effect is simply carried out by measuring the PSFs corresponding to different imaging depths Δz . This is realized by recording the fringe signal for different reference mirror positions. The same numerical resampling is applied to all fringe signal traces and the resulting Fourier transformed signals $i_D(z)$ (single sided) are plotted, as shown in Figure 2.6, representing a typical sensitivity roll-off measurement. The sensitivity drop over imaging depth can then directly be derived from the decay of the peaks of the PSFs. Note that the y-axis is representing the sensitivity that was determined a single time for a small Δz as described above (see equation 2.20). Generally, in SS-OCT, a logarithmic representation is preferred using a $20 \cdot \log(i_D(z))$ representation due to the fact that $i_D(\Delta z)$ is proportional to $\sqrt{R_S}$. Optionally, the decay of the corresponding fringe visibilities can be plotted. The fringe visibility is defined as the time averaged amplitude of the interferometric fringe signal envelope (see equation 2.8). A discrepancy between fringe visibility decay and the decay of the PSF peaks, which typically increases for larger Δz , can be caused by non-perfect numerical resampling or/and can be due to phase noise in the fringe signal. The sensitivity roll-off is often specified in different ways in literature. A common way is to name the 6 dB roll-off point which corresponds to halving of $i_D(z)$. Other descriptions, considering a larger imaging range, define the R-number [14] which is given by the slope of a linear fit to the peak maxima of the PSFs (logarithmic representation). There are several applications in OCT that require a large imaging range making an optimum roll-off performance highly desirable like OCT imaging of the anterior segment of the human eye [81]. However, for many applications using FD-OCT, the achievable imaging range is less determined by the sensitivity roll-off than by the penetration depth of the light in the biological tissue ($\sim 2-3$ mm).

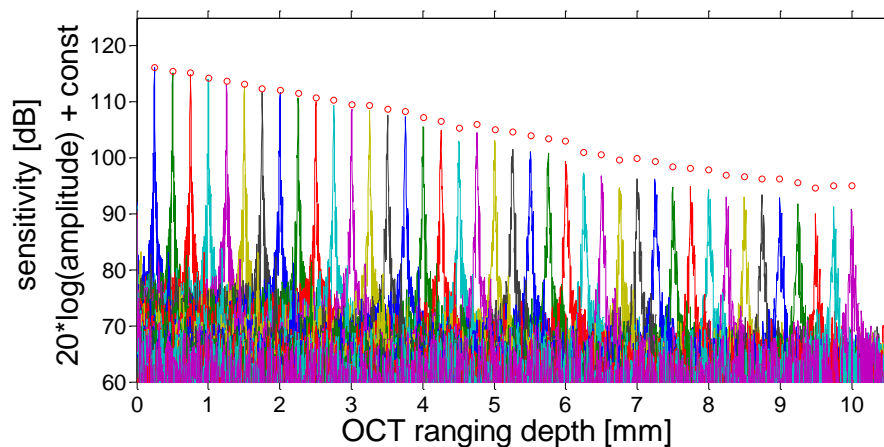


Figure 2.6: Typical sensitivity roll-off measurement, extracted from [11]. The picture shows several PSFs corresponding to different OCT ranging depths Δz . The peaks of the PSFs represent the decay in sensitivity. The red circles are the corresponding fringe visibilities.

2.1.4.3 Dynamic range

The dynamic range in an OCT system is defined as the ratio of maximum to minimum reflected power that can be detected simultaneously. The measurement of dynamic range is performed similarly to a sensitivity measurement. A mirror is placed in the sample arm ($R_S = 1$) and the PSF is determined corresponding to a certain path length difference $2\Delta z$ in the interferometer arms. If necessary, a neutral density filter can be used to attenuate the light in the sample arm. The maximum detected signal then corresponds to the peak value of the PSF $i_D(\Delta z)$. As already mentioned, the minimum detectable signal is equal to the standard deviation of the noise floor $i_{D,min}(\Delta z) = \sigma(\Delta z)$. However, the main difference to the determination of sensitivity is the fact that here both measurements have to be done simultaneously and not separately. The standard deviation of the noise floor typically is determined in a window close to the peak at $z = \Delta z$ where the coherence function $\gamma(z)$ is negligible small. Therefore, the dynamic range in logarithmic representation at $z = \Delta z$ reads as follows:

$$D_{dB} = 10 \cdot \log\left(\frac{P_{max}}{P_{min}}\right) = 20 \cdot \log\left(\frac{i_D(\Delta z)}{\sigma_{next\ to\ max}}\right) \quad 2.21$$

In OCT, the dynamic range is typically several orders of magnitude smaller than the sensitivity. OCT imaging quality and imaging range can be affected if the dynamic range is not sufficiently high to enable simultaneous detection of the weakest and strongest reflections from biological tissue. However, in OCT, the limiting factor is often not dynamic range but rather insufficient sensitivity and the multiple scattering of photons in optical dense tissue.

2.1.5 Shot noise limit and other noise contributions

2.1.5.1 Shot noise

An important noise contribution in optical detection is shot noise, which is exclusively due to the discreteness of the photons (quantum nature of light) and therefore is a noise contribution which exists inherently. In other words, shot noise sets a lower limit to the total noise in a system. This is why calculating the shot noise allows for a determination of the maximum possible sensitivity, which then is only shot noise limited. This is presented in the chapters 2.1.5.2 and 2.1.5.3 for the different OCT implementations. If a light source is shot noise limited, as it is the case for an ideal unimodal laser (monochromatic operation), the arrival of photons at the photo detector is completely uncorrelated. On this basis and assuming that the mean number of photons that hit the detector during a certain time interval equals \bar{N} , the probability of N photons incident on the detector during this time interval can be determined to follow a Poisson distribution, where the variance in photon number is given by $\sigma_N^2 = \bar{N}$ [82, 83]. Assuming a photo detector with quantum efficiency η and considering the uncertainty in the number of photo-generated electrons (binomial distribution with a variance $\eta(1 - \eta)\bar{N}$), the result-

ing variance of the generated electrons is determined to $\sigma_e^2 = \eta(1 - \eta)\bar{N} + \eta^2\bar{N} = \eta\bar{N}$ [82]. In order to specify the variance of the detector current σ^2 , this result can be transformed using the mean detector current $\bar{I} = \rho\bar{P} = \rho\bar{N}\hbar\omega/T_i = \eta\bar{N}e/T_i$ with the detector responsivity $\rho = \eta e/\hbar\omega$, the mean optical power \bar{P} , the photon energy $\hbar\omega$, the elementary charge e and the detector integration time $T_i = 1/(2B)$ with the electronic bandwidth B of the detector. The shot noise limited detector current variance then reads:

$$\sigma_{\text{sh}}^2 = 2e\bar{I}B \quad 2.22$$

2.1.5.2 Shot noise limit in TD-OCT

In the following, only the last interferometric term of equation 2.6 is used, carrying the OCT relevant information. Moreover, P_{TD} is defined as the optical power illuminating the sample $P_{TD} = P_S = P_0/2$ where P_0 is the power of the broadband light source. Therefore, the mean-square peak signal power $\langle I_D^2 \rangle_{TD}$, occurring at $z_R = z_{Sx}$, is calculated to [32]:

$$\langle I_D^2 \rangle_{TD} = \frac{1}{2}\rho^2 P_{TD}^2 R_R R_S \quad 2.23$$

It is assumed that the power of the light reflected from reference arm is considerably larger than the light backscattered from the sample arm ($R_S \ll R_R$), which is neglected as a noise contribution. Thus, the mean detector current is given by $\bar{I} = \frac{1}{2}\rho P_{TD} R_R$. Using equation 2.22, the shot noise limited variance of the detector current therefore equals $\sigma_{TD}^2 = \rho e P_{TD} R_R B_{TD}$ and, with equation 2.23, the signal to noise ratio reads [32, 48]:

$$SNR_{TD} = \frac{\langle I_D^2 \rangle_{TD}}{\sigma_{TD}^2} = \frac{\rho P_{TD} R_S}{2e B_{TD}} \quad 2.24$$

With equation 2.17, using $SNR_{TD} = 1$ and $R_S = R_{S,min}$, the shot noise limited sensitivity Σ_{TD} can be derived:

$$\Sigma_{TD} = 10 \cdot \log \left(\frac{\rho P_{TD}}{2e B_{TD}} \right) \quad 2.25$$

Note that the previous analysis is based on a perfect Michelson interferometer where only one interferometer output is used. Therefore, SNR_{TD} and Σ_{TD} have to be adapted in case of different interferometer layouts. In case of a dual balanced approach, using both outputs of the Michelson interferometer with two detectors, $10 \cdot \log \left(2 \cdot \frac{P_{D1} + P_{D2}}{P_S} \right)$ has to be added in equation 2.25, where P_{D1} and P_{D2} are the powers at both detectors and $P_S = P_{TD}$ is the power on the sample. This results in an increased value of the shot noise limited sensitivity.

2.1.5.3 Shot noise limit in FD-OCT

In the following, a FD-OCT setup is considered exhibiting M spectral channels with wavenumber k_m , corresponding to M samples in SS-OCT and M CCD pixels in SD-OCT, respectively. Sensitivity roll-off with increasing depth is not considered here. Furthermore, for the sake of simplicity, a rectangular shaped spectrum is assumed, so that each spectral channel comprises the same optical power. If one rewrites equation 2.5, substituting for $P_{FD}(k_m)$, which is defined as the incident power on the sample corresponding to each channel $P_{FD}(k_m) = P(k_m)/2$, the interferometric term reads $I_D(k_m) = \rho P_{FD}(k_m) \sqrt{R_R R_S} \cos(2k_m \Delta z)$. It can be shown [2, 32] that discrete Fourier transformation of this fringe signal, representing a single reflection, yields a peak signal of the PSF of $i_D(\Delta z) = \frac{M}{2} \rho P_{FD}(k_m) \sqrt{R_R R_S}$ which is a factor $\frac{M}{2}$ larger than the signal amplitude of $I_D(k_m)$. The interpretation of this fact is that the sinusoidal interference pattern corresponding to each spectral channel adds coherently in the discrete Fourier transformation resulting in an enhancement factor of M in the peak signal. The coherence length of each channel in FD-OCT is much larger than the coherence length of the single channel in TD-OCT. The factor $\frac{1}{2}$ stems from the complex conjugate artifact in FD-OCT. The mean-square peak signal power at $z = \Delta z$ therefore reads:

$$\langle i_D^2 \rangle_{FD} = \frac{M^2}{4} \rho^2 P_{FD}(k_m)^2 R_R R_S \quad 2.26$$

On the other hand, it is necessary to analyze the transformation of noise from k into the z -domain. Here, it makes sense to assume that the detector signal of each channel $I_D(k_m)$ includes an additive, uncorrelated white noise term $\alpha(k_m)$ with a mean of zero and a variance $\sigma_{FD}^2(k_m)$. Again, the power of the light reflected from the sample arm is neglected ($R_S \ll R_R$) and, with equation 2.22, the shot noise limited variance of the signal of each channel is equal to $\sigma_{FD}^2(k_m) = \rho e P_{FD}(k_m) R_R B_{FD}$. Since noise in each spectral channel is uncorrelated, the noise variances add incoherently in Fourier transformation. If $\alpha(k_m)$ is white, the variance in z -domain can be determined to $\sigma_{FD}^2 = \sum_{m=1}^M \sigma_{FD}^2(k_m) = M \rho e P_{FD}(k_m) R_R B_{FD}$ [2, 32]. Therefore, using equation 2.26, the signal to noise ratio of FD-OCT systems can be written as:

$$SNR_{FD} = \frac{\langle i_D^2 \rangle_{FD}}{\sigma_{FD}^2} = M \cdot \frac{\rho S_{FD}(k_m) R_S}{4e B_{FD}} \quad 2.27$$

In case of SS-OCT, it is important to realize that the previous derivation is only correct if the bandwidth $B_{FD} = B_{SS}$ is substituted by the Nyquist frequency which is half of the sampling frequency $f_S/2 = M/(2T)$ (A-scan time T). This is an important consideration since, in SS-OCT, an electrical low-pass filter with a cut-off frequency $f_L < f_S/2$ is often used. However, in this case, $\alpha(k_m(t))$ is not white within the relevant frequency range ($0 \rightarrow f_S/2$), but truncated at f_L , which makes the derivation of σ_{FD}^2 incorrect. Indeed, σ_{FD}^2 is no longer constant over the whole z -range but truncated. Note that decreasing the electronic bandwidth to values smaller than $f_S/2$ reduces the imaging range and

the total amount of noise power. However, close to $z = \Delta z$, the variance σ_{FD}^2 does not decrease assuming sufficient remaining imaging range. Thus, the signal to noise ratio (or the sensitivity) at $z = \Delta z$ is independent of the cut-off frequency f_L of the low-pass filter if $f_L \leq f_S/2$. In case of SD-OCT, the bandwidth $B_{FD} = B_{SD}$ is determined to $1/(2T)$. Substituting $SNR_{FD} = 1$ and $R_S = R_{S,min}$ in equation 2.27 and considering equation 2.17 finally yields the shot noise limited sensitivity for both OCT techniques:

$$\Sigma_{SS} = 10 \cdot \log \left(\frac{\rho T}{2e} P_{SS}(k_m) \right) \quad 2.28$$

$$\Sigma_{SD} = 10 \cdot \log \left(\frac{\rho T}{2e} P_{SD}(k_m) \cdot M \right)$$

In order to compare both shot noise limited sensitivities, the optical power P_S illuminating the sample, the number of channels M and the A-scan time T are assumed to be equal for both techniques. Since, in SD-OCT, the power is divided in all spectral channels, it is worth stating that $P_S = P_{SS}(k_m) = P_{SD}(k_m)M$. Consequently, under given assumptions, the shot noise limited sensitivities are identical ($\Sigma_{SS} = \Sigma_{SD}$) for both techniques.

Again, the analysis so far is based on a Michelson interferometer where only one output is used. Thus, the shot noise limited sensitivities have to be adapted in case of other interferometer designs. Similar to the analysis of shot noise limit in TD-OCT, Σ_{SS} has to be increased by the term $10 \cdot \log \left(2 \cdot \frac{P_{D1} + P_{D2}}{P_S} \right)$ if dual balanced detection is applied.

Furthermore, the derivation of SNR_{FD} is based on a rectangular spectrum $P(k_m)$, assuming the same optical power in each channel. If one considers a more realistic spectral shape, the result can differ from equations 2.27 and 2.28.

2.1.5.4 Sensitivity advantage of FD-OCT compared to TD-OCT

FD-OCT provides an inherent sensitivity advantage in comparison to TD-OCT, which is shown in the following. This fact was first demonstrated by three research groups independently from each other in 2003 [2-4]. In order to perform a reasonable comparison of equations 2.25 and 2.28, one has to assume equal optical power P_S illuminating the sample ($P_S = P_{TD} = P_{SS}(k_m)$). Moreover, in TD-OCT as well as in SS-OCT, the same A-scan time T , the same imaging range z_{max} and the same rectangular spectrum $P_{TD}(k) = P_{SS}(k(t))$ are assumed. The optimum electronic bandwidth in TD-OCT in case of a Gaussian shaped spectrum with a FWHM Δk_{FWHM} is approximately twice the FWHM of the power bandwidth of the signal [48], so that $B_{TD} \approx 2\Delta k_{FWHM} z_{max} / (\pi T)$. In case of a rectangular spectrum of width Δk , the optimum bandwidth can be expected to be approximately the same if $\Delta k = 2\Delta k_{FWHM}$. With $z_{max} = \pi M / 2\Delta k$ (equation 2.11), the electronic bandwidth can be transformed to $B_{TD} \approx M / (2T)$ and one can state:

$$\Sigma_{SS} = \Sigma_{SD} \approx \Sigma_{TD} + 10 \cdot \log \left(\frac{M}{2} \right) \quad 2.29$$

Although the de facto sensitivity advantage of FD-OCT compared to TD-OCT might differ slightly from equation 2.29, which is based on a rectangular spectrum, it typically is within the range of ~20 to 30dB, representing a tremendous advantage compared to TD-OCT.

2.1.5.5 Shot noise limit, imaging speed and maximum allowed optical power

From equations 2.25, 2.28 and considering that the optimum bandwidth in TD-OCT B_{TD} is proportional to $\Delta k \cdot z_{max}/T$, one can draw the following conclusions: In FD-OCT, the shot noise limited sensitivity is solely defined by the detector responsivity ρ , the power illuminated on the sample P_S and the A-scan time T. In TD-OCT, the sensitivity additionally depends on the spectral width Δk and the imaging range z_{max} . In FD-OCT, increasing imaging speed and therefore reducing the A-scan time T inherently leads to a smaller shot noise limited sensitivity, assuming that the power P_S is at the limit defined by ANSI [80] and cannot further be increased. This is also true for TD-OCT if imaging range and axial resolution may not deteriorate. Consequently, there is always an upper limit to a reasonable imaging speed depending on the minimum sensitivity that is acceptable for the corresponding application and the allowed optical power that may be illuminated on the sample. In case of OCT imaging of human skin, as carried out for the research presented in this thesis, the typical maximum allowed optical power is in the order of a few tens of mW at a wavelength of 1310 nm. The optical power applied for skin imaging for this thesis was always below this threshold. For strongly scattering tissue, as for example human skin, a sensitivity of at least 100 dB is desirable to ensure high-quality imaging. From equation 2.28, it follows that, under these conditions, FD-OCT imaging with an A-scan rate ($f = 1/T$) of several MHz can still provide enough sensitivity, as demonstrated in [8] (single spot A-scan rate of 5.2 MHz). In case of retinal imaging, the situation is complicated, since the maximum allowed power is considerably lower (typically $<800 \mu\text{W}$ at 800 nm and $\sim 1.4 \text{ mW}$ at 1060 nm). For retinal OCT at 1060 nm, performed within the research presented in this thesis, the power was below this limit. However, sensitivities of $\geq 90 \text{ dB}$ are often sufficient for good quality retinal imaging. Therefore, the reasonable maximum A-scan rate is a few MHz (experimental demonstration of retinal imaging with single spot A-scan rate of 1.37 MHz in [74] or very recently 3.35 MHz [7]).

2.1.5.6 Other noise contributions and dependence on heterodyne gain

So far, only shot noise has been considered. However, in an OCT system there are other noise contributions which impede shot noise limited operation or can make it impossible. Besides shot noise, there are two main other types of noise [71], which cause fluctuations of the detector current and will be defined in terms of detector current variances in the following. On the one hand, there is receiver noise σ_{Re}^2 which is independent from the incident light. Receiver noise contains dark noise σ_d^2 (dark current in the photo receiver) and thermal noise σ_T^2 (also referred to as Johnson noise or Nyquist noise), which is due to thermal motion of charge carriers in the equivalent resistance R of the photo

receiver circuit. The thermal noise can be specified to $\sigma_T^2 = 4k_B T B / R$ [84] with temperature T , Boltzmann constant k_B and electronic bandwidth B .

On the other hand, there is photon excess noise σ_{ex}^2 . The name already indicates that this is a noise contribution originating from light intensity fluctuations which occur in addition to shot noise. A light source with nonzero excess noise generates photons that do not obey Poissonian statistics. The arrival of photons at the detector is not uncorrelated. Indeed, the photons are emitted in bunches (photon bunching) [85, 86]. The variance of the photon number of the underlying photon counting statistics exceeds the shot noise limited case ($\sigma_N^2 = \bar{N}$) and can be written as follows: $\sigma_N^2 = \bar{N} + \alpha \bar{N}^2$ ($\alpha > 0$, super-Poissonian photon counting statistics). Note that the last term is referred to the photon excess noise, which is proportional to \bar{N}^2 . Assuming fully polarized broadband, thermal light with a Gaussian intensity distribution (following Bose-Einstein statistics, $\alpha = 1$), the variance of the detector current resulting from excess photon noise can be determined to $\sigma_{ex}^2 = \rho^2 \bar{P}^2 B / \Delta\nu$ [71, 86, 87], where \bar{P} is the mean power, B is the electronic bandwidth of the detector and $\Delta\nu$ is the spectral bandwidth of the source. In SD-OCT and in TD-OCT, usually spectrally broadband SLDs are used which are based on amplified spontaneous emission. Typically, the statistics of the polarized output of an SLD can be approximated very well by the statistics of fully polarized thermal light [88, 89], at least for not too high SLD currents [90]. Thus, the excess noise can be calculated as stated above. In the case of SS-OCT, usually wavelength-swept lasers are applied (see chapter 2.2). In case of laser operation (multiple modes), the photon counting statistics can differ from Poissonian and Bose-Einstein statistics and the derivation of σ_{ex}^2 is more complicated [87]. However, generally it can be assumed that the variance of the excess photon noise current is proportional to the square of the mean power $\sigma_{ex}^2 \sim \bar{P}^2$. Quantization noise of the analog to digital converter and $1/f$ noise at typical A-scan rates can normally be neglected in OCT [4].

In the following, the goal is to derive an expression of the overall SNR in OCT with regard to the previously mentioned noise contributions. Therefore, one needs to be aware of the fact that the mean square peak signal power in OCT is proportional to $R_R R_S$ (see equation 2.23 or equation 2.26). Again, it is assumed that $R_R \gg R_S$. Thus, the sample arm light is neglected in terms of noise. Due to uncorrelated noise contributions, the previously derived detector current variances for the different types of noise can be added and, assuming proportionality factors β_1 and β_2 , the overall SNR for OCT can be written as follows:

$$SNR \sim \frac{R_S R_R}{\sigma_{re}^2 + \sigma_{sh}^2 + \sigma_{ex}^2} = \frac{R_S R_R}{\sigma_{re}^2 + \beta_1 R_R + \beta_2 R_R^2} \quad 2.30$$

For a better understanding of OCT performance, it is instructive to show how the signal to noise ratio would look like assuming each noise contribution occurring individually (neglecting the other contributions). Moreover, it is interesting to see in how far these different SNR values depend on the reflected optical reference arm power (optical power of light returning from the reference arm) or simply the power reflectivity R_R . This is

a parameter that is freely adjustable and has not been taken into account yet. Considering exclusively receiver noise σ_{re}^2 , which is independent of the light incident on the detector, the corresponding signal to noise ratio SNR_{re} is proportional to R_R . Regarding solely shot noise σ_{sh}^2 (proportional to R_R), the corresponding signal to noise ratio SNR_{sh} becomes independent of R_R . If one takes into account only photon excess noise σ_{ex}^2 (proportional to R_R^2), the according signal to noise ratio SNR_{ex} is inversely proportional to R_R .

$$SNR_{re} \sim \frac{R_S R_R}{\sigma_{re}^2} \quad SNR_{sh} \sim R_S \quad SNR_{ex} \sim \frac{R_S}{R_R} \quad 2.31$$

The previous findings clearly indicate that the choice of R_R , determining the heterodyne gain in OCT, is important to achieve the best possible sensitivity for OCT imaging. Typically, the light in the reference arm has to be considerably attenuated resulting in an optimum reflected power on the order of $\sim 100 \mu\text{W}$. If the reflected optical reference arm power is too high, excess noise σ_{ex}^2 usually dominates, which reduces the overall SNR. On the other hand, if the reflected optical reference arm power is too low, the receiver noise σ_{re}^2 typically dominates, also worsening the overall SNR. Note that the application of high-speed photo receivers (high electronic bandwidth B) with sufficiently high amplification, which are required for high speed SS-OCT, often results in a poorer receiver noise performance. Hence, in this case, raising the reflected optical reference arm power (larger R_R) may become necessary. Generally, the OCT system can only achieve shot noise limited operation if the overall SNR value at the intersection point of $SNR_{re}(R_R)$ and $SNR_{ex}(R_R)$ is not smaller than SNR_{sh} . If the measured sensitivity (chapter 2.1.4.1) is constant or almost constant over a large range of reference arm attenuation values R_R , this is a clear indication for shot noise limited operation.

Note that dual balanced operation can considerably reduce photon excess noise [70, 71], simplifying the achievement of shot noise limited operation and allowing for higher values of R_R , if necessary. However, dual balancing is not perfect, particularly due to imperfect power balancing over the whole spectral range. Therefore, residual excess noise remains. Furthermore, another noise contribution, that has been neglected so far but which can make a significant contribution in case of dual balancing, is beat noise σ_{be}^2 [71]. Beat noise arises if one takes in account parasitic light that is reflected from the sample arm, due to e.g. spurious reflections from the sample arm optics, with a power reflectivity R_x . Typically, $R_x > R_S$ and the photon excess noise is proportional to $\sigma_{ex}^2 \sim (R_R + R_x)^2$, where the beat noise is the part $\sigma_{be}^2 \sim 2R_R R_x$ of the result which does not cancel out due to a phase difference of π even if one assumes perfect dual balancing.

2.1.6 Typical swept source OCT setup

The aim of this chapter is to demonstrate a typical SS-OCT setup as applied for OCT imaging presented in this thesis. The setup is sketched in Figure 2.7 and is based on a Michelson interferometer using fiber optic components. The investigation and im-

provement of wavelength-swept light sources for OCT application made up a large part of this thesis. Possible operation principles and different implementations of wavelength-swept light sources are discussed in chapter 2.2 and in chapter 3.

2.1.6.1 Experimental setup

Light from the wavelength-swept light source first passes an optical circulator and is then split in the reference and the sample arm using a 50/50 fused fiber coupler. In the reference arm light is collimated, reflected at a mirror with adjustable position, and coupled back into the single mode fiber. Moving the mirror shifts the point of zero delay in the sample. Additionally, the reference arm light has to be attenuated by a reasonable factor, using for example neutral density filters, in order to ensure an optimal sensitivity (see chapter 2.1.5.6). In the sample arm light exiting the fiber core of the single mode fiber is Rayleigh imaged on the sample, passing two galvanometer mirror scanners (galvoscaners). The second fast scanner moves the beam transversally on the sample

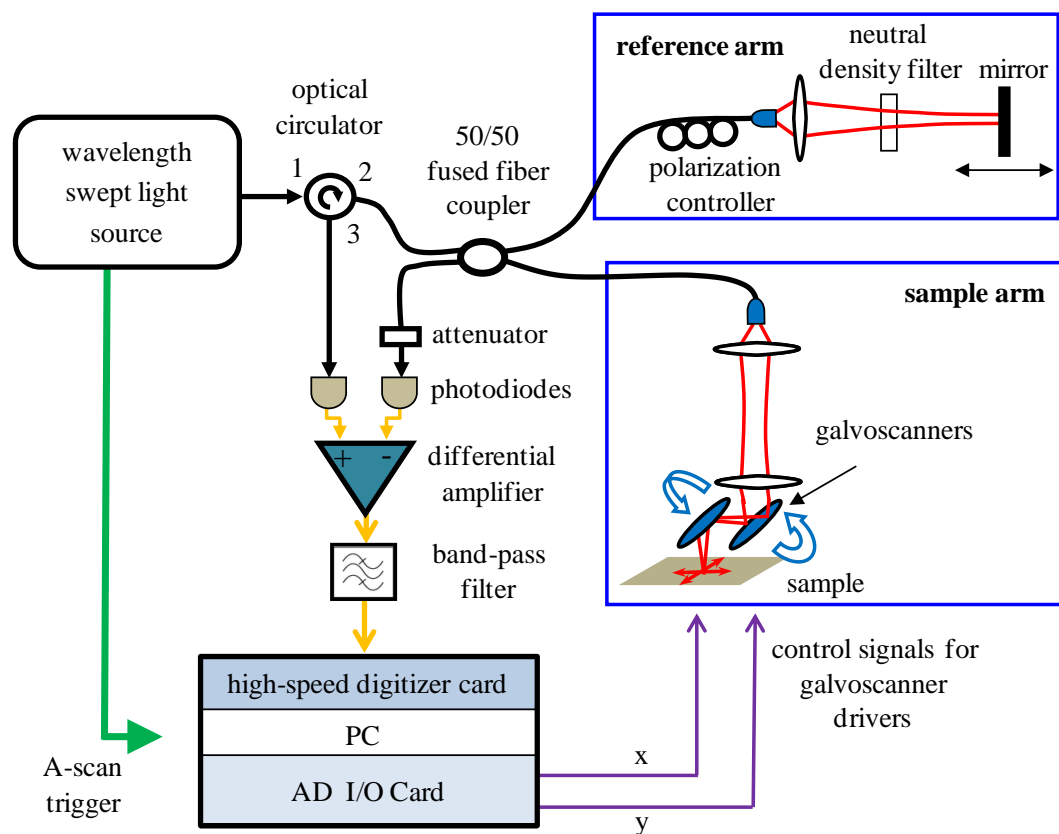


Figure 2.7: Typical SS-OCT setup as used for OCT imaging for this thesis. The interferometer is an optical fiber based Michelson interferometer using dual balanced detection. The two galvanometer mirror scanners (galvoscaners) enable transversal scanning of the light beam on the sample. Data acquisition with the analog to digital converter card, generation of control signals for both galvanometer scanners using an analog/digital input/output card and data processing for real-time display of two-dimensional cross sectional images (B-scans) are synchronized to an A-scan trigger signal from the wavelength-swept light source. A personal computer with LabVIEW software is used.

2. Overview of the research field

(x-direction). For three-dimensional imaging, another slow scanner is scanned in addition to the fast scanner, resulting in a perpendicular, independent movement of the beam on the sample (y-direction). The slow scanner steps to its next position when the fast scanner has completed a B-scan enabling line-by line scanning of the surface. Note that the galvoscaners can be mounted either prior to the last lens (pre-objective-scanning) or after the last lens (post-objective scanning). In case of retinal imaging (see chapter 3.2.2), the arrangement of the lenses has to be adapted. Pre-objective-scanning is used and an additional lens is mounted with a distance to the intermediate focus equal to the focal length (see [74]). In this way, during scanning of the galvoscaner, the OCT light beam ideally pivots around a point which is chosen close to the pupil of the eye and is called the pivot point. Therefore, vignetting of the OCT beam by the pupil can be minimized enabling a wide field of view. Note that fiber lengths in the reference and sample arm are matched.

In order to ensure maximum fringe visibility and therefore a maximum interference signal, a crucial point is that the electric fields returning from both interferometer arms and superposing in the fiber coupler must have the same polarization. Since the polarization state in standard single mode fiber is not preserved and can change considerably, a fiber polarization controller (see chapter 2.2.2.2) has to be used in at least one interferometer arm.

Dual balancing is achieved by detecting light from both outputs of the interferometer with a dual balanced photo detector, which consists of two photo diodes and a differential amplifier. The optical circulator redirects the light that is returning to the light source. A variable attenuator is used in order to guarantee best possible power matching at both photodiodes and therefore enable optimum dual balancing. In case of retinal imaging at 1060 nm (see chapter 3.2.2), two further 50/50 fiber couplers are used. The first is replacing the circulator and the second is inserted prior to the attenuator (see [74]). This solution is preferred to the circulator based approach due to comparably high losses in the circulator at 1060 nm and since it can ensure optimally matched power at both photodiodes over the whole sweep spectrum allowing for better excess noise suppression. The reason is the fact that light is passing components of the same type with almost identical spectral characteristics. Besides equal power levels at the photodiodes, another crucial factor for optimum dual balancing is matching the optical path lengths between the coupler, where light from both interferometer arms superpose, and the two photodiodes.

After the balanced receiver, the signal is low-pass filtered with a cut-off frequency that is chosen depending on the desired imaging range but should not exceed the sampling frequency $f_s/2$ in order to avoid aliasing. The signal is digitized with a high speed digitizer card. For OCT imaging performed for this thesis, an analog to digital converter card with a maximum sample rate of 400 Msamples/s, 12-bit resolution and an onboard memory of 4 Gbyte was used (GaGe Applied Technologies - model CS12400) and a personal computer with LabVIEW software was utilized. The typically saw tooth like shaped control signals for both galvoscaner drivers were generated with an analog and

digital input/output card. The data acquisition with the high-speed digitizer card, numerical processing of the data (in order to generate real-time two-dimensional preview) and the generation of control signals for the galvoscanners were synchronized using an A-scan trigger signal from the wavelength-swept light source.

2.1.6.2 Signal processing and numerical resampling

In order to remove residual DC signal remaining due to imperfect dual balancing, a background trace is typically recorded with the sample arm blocked. This signal is then numerically subtracted from all A-scan fringe traces. Additionally, an electrical high-pass filter can be used to suppress very small frequency components. However, these means cannot improve excess noise suppression.

As already mentioned in chapter 2.1.2.4, the wavenumber over time characteristic of wavelength-swept light sources typically is not linear, which is a problem, since the PSF is broadened if the samples are not equidistantly spaced in frequency. One solution is to develop a swept light source with sufficiently high sweep linearity, as presented in chapter 3.1.1 [10]. Another approach is to apply sampling with uneven time-spacing realized by externally clocking the analog to digital converter [73]. However, the common way is to numerically resample each A-scan data set prior to discrete Fourier transformation. For OCT imaging performed for this thesis, this is accomplished as follows: Firstly, a fringe signal has to be recorded that is corresponding to a single reflection in the sample arm providing not too large fringe frequencies in order to learn about the relative change of optical frequency within the time interval of each A-scan. The change in optical frequency is then directly linked to the change of the phase of the fringe signal. Practically this can be realized by replacing the sample with a mirror. However, normally this procedure has to be repeated occasionally during imaging. Thus, the replacing can become cumbersome. There are alternative solutions which require no removal of the sample, as for example the use of a separate Mach-Zehnder interferometer [73], the utilization of the unused output of a fiber coupler [74] or the application of a beam splitter and an additional mirror in the reference arm, where one optical path can be blocked. In the latter case an autocorrelation signal can be recorded in non-balanced detection [91, 92].

Secondly, the Hilbert transformation of the acquired fringe signal $H(I_D(t))$ is calculated, which corresponds to a rotation of $\pi/2$ in the complex plane. Therefore, the analytical representation of the fringe signal $I_D^A(t)$ reads:

$$I_D^A(t) = I_D(t) + i \cdot H(I_D(t)) \quad 2.32$$

Consequently, the fringe envelope $|I_D^A(t)|$, and, by using proper phase unwrapping, also the time dependent phase of the fringe signal $\phi(t) = \arctan(H(I_D(t))/I_D(t))$ can be derived.

Finally, with the knowledge of $\phi(t)$, each A-scan fringe signal trace acquired during OCT imaging can be numerically resampled with means of interpolation algorithms providing equidistant optical frequency intervals for discrete Fourier transformation.

The time interval after which the determination of $\phi(t)$ has to be repeated, since otherwise axial resolution deteriorates, only depends on the stability and repeatability of the wavelength sweeps from the wavelength-swept light source. In case of the wavelength-swept light sources used in this thesis, this time interval typically exceeded 30 minutes and was usually limited due to thermal drifts in the source (no active feed-back control).

2.1.7 Overview of OCT development and applications

The aim of this chapter is to give a brief overview of the main medical applications of OCT, to mention different OCT approaches that can provide additional contrast information (functional OCT) and to point out the progress of OCT performance in terms of resolution, sensitivity roll-off performance and imaging speed.

2.1.7.1 Medical applications

The most prominent medical application of OCT is imaging of the human retina, playing a very important role in the diagnosis of diseases like glaucoma, age-related macular degeneration or diabetic retinopathy [16]. For retinal imaging, OCT is the technique of choice since it provides high axial resolution which is of particular importance due to the stratified organization of the retina. This cannot be achieved using ultrasonography, which can be used for intraocular examinations but requires physical contact to the eye providing a rather poor axial resolution. Scanning laser ophthalmoscopy (SLO), first demonstrated 1980 [93], where a focused laser spot is scanned on the retina measuring the integrated backscattered light, yields en-face fundus images providing high transversal resolution and good contrast. However, the axial resolution is restricted to typically $\sim 300 \mu\text{m}$ due to pupil aperture and ocular aberrations [32]. Two years after the first demonstration of OCT, the first in-vivo retinal imaging was realized in 1993 [94, 95]. It was only two years later that the first commercial OCT device was launched by Carl Zeiss Meditec enabling retinal OCT imaging for clinical use. Today, OCT is a rapidly growing market, where retinal imaging is the most successful clinical application in the field of OCT. In the last years, a lot of research was done investigating the wavelength regime at 1060 nm, first demonstrated in 2003 [42], instead of the conventional 800 nm, which can provide enhanced choroidal visualization and improved OCT performance for cataract patients [44].

Besides retinal imaging, OCT also provides another medical application in the human eye, namely imaging of the anterior segment including the cornea [81, 96-98], where the applied wavelength range is usually centered at 1300 nm. This allows for higher optical powers on the sample and deeper penetration. Typical diagnostic applications are measurements of corneal thickness and corneal refractive power or identification of causes for corneal opacity.

Another very important medical application is intracoronary, endoscopic OCT which can be used for the diagnosis of coronary atherosclerosis [17], distinguishing vulnerable plaques, or for monitoring stent deployment [99]. Since OCT beam delivery in the sam-

ple arm can be accomplished using optical fiber, coronary catheters can be used guiding the fiber. A circumferential, three-dimensional image of the vessel can be acquired by rotating the fiber and the final deflecting element, which can be a prism, and additionally performing a pullback of the catheter. However, one problem is the fact that blood has to be removed during image acquisition by, for example, saline flushing since blood is highly scattering. This limits the possible image acquisition time to a few seconds, making very fast OCT systems highly attractive for large 3D volume imaging. The first demonstration of intravascular OCT ex-vivo, already showing the potential of this technique, was achieved in 1996 [38], followed by various further investigations [17, 18, 73, 100]. Compared to intravascular ultrasound, OCT provides less penetration depth but much higher resolution. Therefore, it is in particular well suited for investigating microscopic features at the surface of the arterial wall.

Besides examination of coronary arteries, there are several other medical fields where endoscopic OCT can be applied, such as in gastrointestinal endoscopy [101, 102], in laryngology [103, 104], in pulmonary medicine [105, 106], in gynecology [107] or in urology [108]. Further fields of medical application of OCT include development biology [109, 110], dentistry [111, 112] and dermatology [113], where OCT imaging of human skin can for example help to identify skin tumors.

2.1.7.2 Functional OCT and different OCT approaches

Functional OCT provides additional information about the biological sample that is investigated, which usually leads to a contrast enhancement. Three important types of functional OCT are Doppler-OCT, polarization sensitive OCT and spectroscopic OCT. Due to the Doppler effect the flow velocity component of moving material in the sample (such as blood in vessels) that is parallel to the incident light (axial velocity) can be determined. The first in-vivo Doppler OCT images have been demonstrated in 1997 [114, 115]. These first time domain Doppler OCT systems were based on the spectrogram method, where the fringe signal of each A-scan is analyzed via for example a short time Fourier transformation in order to determine the z-dependent fringe frequency and thus the depth dependent velocity. However, for faster imaging the velocity sensitivity is not sufficient. Therefore, another method has been investigated, called phase-resolved Doppler OCT, which relies on measurement of the phase change between adjacent A-scans. This approach was first applied for TD-OCT [116-119] and later adapted in FD-OCT [120-125]. Doppler OCT is mainly used to determine the blood flow as, for example, for drug screening or within the choroid or the retinal capillaries. Polarization sensitive OCT enables to learn about polarization dependent properties of the examined sample tissue such as birefringence, optical axis orientation or dichroism. In 1992, the first OCT system capable to measure changes in the polarization state of light was presented [126]. The first two-dimensional images of birefringence were realized in 1997 [127], followed by other investigations based on TD-OCT [128, 129]. In a completely bulk-optic interferometer, the polarization states of light in the sample arm and the reference arm have to be prepared (typically circularly polarized on

the sample) and after the interferometer both polarization components are separated and measured independently with two detectors. In this way, the entire set of Stokes parameters, fully describing the polarization state, can be derived [128]. In a fiber based setup, problems arise due to the unknown polarization change in the fiber and the fact that the polarization state of the light incident on the sample is unclear. However, these problems can be solved using at least two different polarization states incident on the sample and comparing light reflected from the surface to light reflected from deeper depths [130, 131]. Besides in TD-OCT, polarization sensitive OCT was also demonstrated in SD-OCT [132-137] and SS-OCT [138-140]. Polarization sensitive OCT can for example be used to determine polarization properties in the retinal nerve fiber layer. In spectroscopic OCT [141-143], spectroscopic analysis is combined with standard OCT which enables to identify depth resolved tissue absorption spectra. This is often used for contrast enhancement in OCT by spectral information. Another application is the measurement of localized oxygen saturation.

Besides the usual OCT implementations described so far in this thesis, there have been various other approaches, where two shall be mentioned here. One implementation is linear OCT [144, 145], where the principle is similar to TD-OCT but with no moving parts in the reference arm. Two expanded optical beams originating from the sample and the reference arm are tilted and superpose on a linear line array detector, so that each pixel corresponds to a certain path length difference resulting in an interference pattern. Linear OCT can in principle achieve similar image quality than TD-OCT with no moving parts required. However, disadvantages are in particular high fringe washout and the non-existing sensitivity advantage compared to FD-OCT. Another implementation is full field OCT [146-148], which does not require galvanometer mirrors for transversal scanning of the beam on the sample and is based on homogeneous illumination of the whole field using microscope objectives and a typically, spatially and temporally incoherent light source, such as a halogen lamp. After the interferometer, light is detected using a CCD array. Therefore, during one A-scan, the depth profile at all transversal points on the sample is detected simultaneously. In TD-OCT, this yields an en-face image for every reference arm position. Advantages are that there are no speed limitations due to the beam scanner and that this technique can provide very good axial and transversal resolution. Disadvantages are a rather poor sensitivity, small field of view and considerable fringe washout and pixel cross-talk effects. Recently, full-field OCT was also realized with SS-OCT [149].

2.1.7.3 Advances in OCT imaging performance

Since the invention of OCT in 1991, there have been tremendous advances in OCT image performance in terms of imaging speed, resolution and sensitivity.

Since the axial resolution in OCT is indirectly proportional to the spectral width of the light source (or the sweep range in SS-OCT), there have been lots of investigations using very broadband light sources for OCT in order to minimize the axial resolution. Very successful research in the field of ultra-high resolution OCT was done using

broadband femtosecond mode locked lasers, such as the Ti:Al₂O₃ solid state lasers. The application of this type of laser for OCT has already been studied in 1995 [150] and led to record axial resolutions of $\sim 1 \mu\text{m}$ (at 800 nm), as demonstrated in 1999 [151]. Ultra-high resolution OCT has also been shown in the retina [35, 152] and enabled improved visualization of the intraretinal morphologic features such as detailed structures of the photoreceptors [153, 154].

As already mentioned in chapter 2.1.5.4, the introduction of FD-OCT techniques allowed for a sensitivity advantage of typically 20 dB to 30 dB compared to conventional TD-OCT systems assuming the same illumination power and imaging speed. This has been an important discovery that drove a boom in OCT research and development enabling high-quality imaging in particular at high imaging speeds.

As already pointed out in chapter 2.1.2.6, imaging speed is a very crucial parameter in OCT. The introduction of FD-OCT systems not only led to an increase in sensitivity but also allowed for a considerable increase in imaging speed in contrast to TD-OCT systems, where the A-scan rate typically is limited to a few kHz due to mechanical restrictions concerning movement of the reference mirror.

In SD-OCT, the A-scan rate depends on the available line-scan camera suitable for the desired wavelength range. There has been a considerable progress in terms of read-out rate of line scan cameras in the last years. Before 2008, the read-out rates of CCD line scan cameras used for retinal SD-OCT research at $\sim 800 \text{ nm}$ typically allowed for A-scan rates ranging from 10 kHz to 30 kHz [133, 152, 155, 156] up to maximum rates of 75 kHz [157]. However, the introduction of improved CMOS line scan camera technology enabled a considerable increase in OCT image speed [158, 159] with A-scan rates of up to 312,5 kHz [160]. For applications requiring wavelengths $> 1000 \text{ nm}$, the use of InGaAs line scan cameras becomes necessary. Investigations in this technology enabled SD-OCT imaging at A-scan rates of up to 47 kHz [158, 161-163] and, very recently, 92 kHz [164]. By multiplying two high-speed spectrometers and ensuring a precise control of data-recording and data-reading times, OCT imaging at A-scan rates of 184 kHz [165] at 1310 nm (InGaAs cameras) and 500 kHz [166] at 850 nm (CMOS cameras) have been demonstrated, exploiting the long dead times of the cameras. Another approach was based on optical demultiplexers in combination with parallel signal acquisition using 2×256 photo receivers enabling line sampling rates of up to 60 MHz [167]. However, due to the limited electronic detection bandwidth of 12 MHz, the effective A-scan rate did not exceed 12 MHz. The achievable sensitivity was not sufficient to enable high-quality OCT imaging.

In SS-OCT, the A-scan rate depends on the sweep rate of the utilized wavelength-swept light source. Conventional, SS-OCT suitable external-cavity wavelength-swept lasers, based on a semiconductor gain medium and a tunable wavelength filter, allowed for A-scan rates in the range from $\sim 10 \text{ kHz}$ to $\sim 50 \text{ kHz}$ in the wavelength range of $\sim 1060 \text{ nm}$ [168, 169] and $\sim 800 \text{ nm}$ [170-172] and A-scan rates of up to 115 kHz in the wavelength range of $\sim 1300 \text{ nm}$ [5, 56, 173-175]. In 2006, A-scan rates of 5 MHz were demonstrated with an approach using a stretched pulse supercontinuum source [176].

Nevertheless, OCT imaging was not possible with sufficient quality due to the low sensitivity of 40 dB. A major improvement in OCT imaging speed was the introduction of Fourier domain mode locked lasers (FDML) in 2006, enabling high-quality SS-OCT imaging at A-scan rates of up to 370 kHz at ~ 1300 nm [6, 177] and up to 236 kHz at ~ 1060 nm [178, 179]. A detailed description of FDML laser technology is given in the chapters 2.2.2 and 2.2.3. Within the research work for this thesis, a new wavelength-swept light source has been developed for retinal SS-OCT operating at 1060 nm and allowing for effective A-scan rates of 340 kHz [13], which is introduced in chapter 3.2.2. Recently, the application of a new compact swept source based on a short cavity and micro-electrical-mechanical system (MEMS) technology [180] enabled retinal OCT research at 1060 nm at 200 kHz [120] and 400 kHz in a dual beam approach [181]. A wavelength-swept laser at 1300 nm, based on a polygon scanning filter with a short cavity, allowed for OCT imaging at 403 kHz [182]. However, the introduction of a new generation of FDML lasers in 2010 facilitated a further considerable increase in A-scan rate enabling high-quality Megahertz OCT imaging at 1300 nm with A-scan rates of up to 5.2 MHz with a single beam [8] and, in the same work, the quadruple A-scan rate of 20.8 MHz using a four beam approach. Record voxel rates of 4.5 GVoxels/s were demonstrated [8]. In 2011, ultrawide-field, Megahertz OCT was shown for retinal imaging at 1060 nm using FDML technology with single-spot sweep rates of 1.37 MHz [74] and very recently 3.35 MHz [7]. Using a swept source full-field approach at 850nm, retinal OCT imaging has been demonstrated with an effective sweep rate of 1.5 MHz [149]. Disadvantages of this approach are the low sensitivity of 72 dB, the small field of view and pixel cross talk. Very recently, optically pumped MEMS-tunable vertical-cavity surface-emitting lasers (VCSEL) enabled OCT imaging reaching sweep rates of 1 MHz (single beam) at ~ 1300 nm [183, 184], although the small output power could be a potential drawback.

In conclusion, from a present point of view, SS-OCT can provide considerably faster high-quality imaging than SD-OCT and has high potential to become the OCT implementation of choice for future ultra-high speed applications.

Besides imaging speed, SS-OCT also has the advantage of a potentially increased imaging depth range due to a typically reduced sensitivity roll-off compared to SD-OCT systems, where the roll-off is dominated by the spectrometer resolution or the spacing between adjacent pixels. The 6 dB roll-off point in SD-OCT is typically < 2 mm [181]. A considerably reduced sensitivity roll-off can be observed in SS-OCT applications. There have been several developments in swept laser sources which allowed for a reduction of the instantaneous linewidth and improvements in sensitivity roll-off performance compared to conventional swept sources. A large step was the introduction of FDML lasers [6] and, in particular, the use of dispersion compensated FDML lasers (see chapter 2.2.2.2), where a substantially smaller sensitivity roll-off has been realized at ~ 1550 nm [14] and recently at ~ 1300 nm [185] enabling OCT imaging with a 6 dB roll-off point of ~ 1 cm. Very good roll-off performance was also observed with short cavity, MEMS-based swept lasers [181] (6 dB roll-off point ~ 4 mm). Very recently,

record roll-off performance was demonstrated with an optically pumped single line MEMS-tunable VCSEL laser [184] (6 dB roll-off point exceeding several cm).

2.2 Fourier domain mode locked lasers

Within the scientific work presented in this thesis, two new operation modes of Fourier domain mode locked (FDML) lasers have been investigated and characterized having the potential to improve performance and applicability for OCT imaging (see chapter 3.1). Furthermore, research also focused on a completely new approach of short pulse generation using an FDML laser and temporally compressing the wavelength-swept output, which is the topic of chapter 4. The aim of this chapter is to give an introduction to FDML technology. The section begins with an overview of different approaches of how wavelength-swept light sources have been and can be realized fulfilling the requirements for SS-OCT imaging. Physical limitations to sweep speed in conventional wavelength-swept lasers are mentioned and different approaches how to solve this problem are addressed. Then, the principle of FDML lasers, which exhibit no fundamental sweep speed limit, is introduced. Afterwards, the focus is on the explanation of the different parts in a typical FDML laser setup and on important characteristic FDML parameters. Finally, different implementations of FDML lasers are discussed.

2.2.1 Wavelength-swept light sources for OCT

2.2.1.1 Definition, prerequisites for OCT and first implementations

Wavelength-swept lasers, or more generally wavelength-swept light sources, are characterized by a continuous change of the output wavelength within a certain wavelength sweep range $\Delta\lambda$ as a function of time. This time period ΔT is referred to as a forward sweep (ascending wavelength) or a backward sweep (descending wavelength). The requirements on sweep properties of wavelength-swept light sources capable for application in SS-OCT are quite high. On the one hand, the sweep range $\Delta\lambda$ has to be sufficiently large to guarantee an adequate axial resolution. Typical values of $\Delta\lambda$ in the NIR are ~ 100 nm (see Figure 2.5). On the other hand, the instantaneous linewidth $\Delta\lambda_{inst}$ of the swept source must be small enough to enable a sufficient imaging range. Typical OCT applications require an instantaneous linewidth $\Delta\lambda_{inst}$ which is approximately a factor of 1000 smaller than the wavelength sweep range $\Delta\lambda$ (~ 1000 resolution elements). Thus, typical values for $\Delta\lambda_{inst}$ are on the order of 100 pm. Of course, for particular applications in OCT or for example in profilometry, smaller instantaneous linewidths and a better coherence can become necessary. Both requirements would not be as challenging if, at the same time, the need for a high OCT imaging speed would not result in high demands on sweep rate (A-scan rate) and sweep time ΔT . Today, wavelength-swept light sources in application for OCT should at least provide sweep rates of

a few tens of kHz or better a few hundreds of kHz. However, for several applications this is not fast enough and sweep rates in the order of a few MHz are highly desirable. Assuming a sweep rate of one MHz ($\Delta T = 1 \mu\text{s}$) and a sweep range of 100 nm, this corresponds to a high sweep speed (assuming linear sweep) of 100 nm/ μs . Besides a sufficiently large wavelength sweep rate, a sufficiently narrow instantaneous linewidth and a sufficiently high sweep speed, another important requirement for SS-OCT imaging is that the swept light source provides enough optical output power.

Already in 1965, a continuously tunable coherent pulsed light source was demonstrated allowing for a tuning range of ~ 70 nm at ~ 1000 nm. It was based on a coherent optical parametric oscillation process using frequency doubled light from a pulsed solid state laser [186]. The slow tuning was achieved by changing the temperature of a nonlinear crystal. In the 1970's, the research on tunable dye lasers (pulsed or cw) for spectroscopy played an important role since they provided comparably broad gain spectra. The main focus was the achievement of narrow instantaneous linewidths [187] or wide tuning ranges, as for example realized using an electronically controlled intra-cavity acousto-optic filter [188] (78 nm tuning range in the visible). A disadvantage of this technique was the large spectral filter width of the acousto-optical filter of ~ 1 nm. Though sweep speed did not play a crucial role yet, the utilization of electro optical tuning elements in the dye laser resonator enabled already substantial sweep rates exceeding 100 kHz [189-191]. However, the sweep ranges were restricted to ~ 10 nm.

2.2.1.2 Wavelength-swept external-cavity semiconductor lasers for OCT

The rapidly developing semiconductor technology enabled tunable semiconductor lasers which are more robust, compact and energy-efficient than other lasers. Moreover, due to the short carrier lifetimes (~ 100 ps) of the semiconductor gain medium, these lasers are preferable for fast wavelength tuning, compared to dye laser or other tunable lasers as for example Ti-Sapphire lasers, where the relaxation times are considerably longer. Today, almost all wavelength-swept light sources applicable for OCT are based on semiconductor technology. A prominent type of tunable semiconductor lasers are tunable external-cavity semiconductor lasers [192]. Here, the broadband semiconductor gain chip can be for example a laser diode (LD) with high reflection on one facet and low reflection on the other enabling lasing in a linear external cavity or, alternatively, a semiconductor optical amplifier (SOA) which is anti-reflex coated on both sides enabling lasing in an external ring or a linear cavity. Additionally, there is the need for a wavelength selective, tunable element in the external cavity. This can be realized using acousto-optical filters [193] allowing for large sweep ranges of several tens of nm. However, the drawback is the comparably broad spectral filter width. Typically sweep rates of several tens of kHz are possible. Considerably larger sweep speeds can be achieved with electro-optical filters [194], however, due to a small finesse, sweeping over a sufficiently large sweep range and, at the same time, providing a sufficiently narrow filter width is not possible. In contrast to this, filtering techniques using optical diffraction gratings, optical prisms or Fabry-Pérot filters can provide a sufficiently high

finesse. Typically, these elements are used in combination with mechanically moving parts in order to enable wavelength tuning. One common approach is the application of piezo actuators which rotate a diffraction grating or an optical mirror in the cavity [195]. In this way, SS-OCT imaging was demonstrated, though the sweep rate was still very small [54] (a few Hz). Considerably higher sweep rates have been realized using a diffraction grating mounted on a resonant galvanometer [172] (~ 16 kHz). There have also been investigations to implement wavelength tuning with a grating in an external-cavity semiconductor laser but no moving parts required. Examples are the use of an acousto-optical deflector [196] or a liquid crystal deflector [197]. Apart from these non-mechanical attempts, which did not meet the requirements necessary for high-quality SS-OCT, there are two very successful mechanical approaches. Up to now, these two approaches have been the only filtering techniques used in wavelength-swept external-cavity lasers that allowed for sweep rates of $\gg 50$ kHz, sweep ranges of ~ 100 nm and filter widths of ~ 100 pm enabling high-quality SS-OCT imaging. These are, on the one hand, polygon-based scanning filters [173, 174, 182] typically consisting of a diffraction grating, a telescope and a polygon mirror scanner and, on the other hand, tunable Fabry-Pérot filters [5, 6, 8] which are typically fiber based facilitating the introduction in an all fiber based resonator.

2.2.1.3 Fundamental sweep speed limit in wavelength-swept lasers

One essential point that has to be considered is the fact that the sweep speed in wavelength-swept lasers is not only restricted due to the sweep speed limitations of the optical bandpass filter, but that there are more fundamental physical limitations. Most commonly, in wavelengths swept external-cavity lasers applicable for SS-OCT imaging, a multitude of lasing modes are active at the same time. Note that the spectral width of the filter window usually exceeds the mode spacing by several orders of magnitude. Shifting the spectral filter window over the broadband gain profile (tuning the filter transmission wavelength) therefore results in a generation of new lasing modes at the leading edge of the spectral filter window and suppression of lasing modes at the trailing edge of the filter window. However, one prerequisite for optimum operation is that the time duration the spectral filter transmits a certain wavelength is long enough to enable a sufficiently large number of round-trips of light in the cavity, required to build-up saturated lasing from amplified spontaneous emission (ASE) [5]. Consequently, there is a certain sweep speed (saturation limit) above which the performance of the laser considerably deteriorates, resulting in less output power and a higher noise level. If the sweep speed is increased further, exceeding a certain value (single round-trip limit), light that is filtered once is blocked after the next round-trip in the cavity and the wavelength-swept laser behaves like a single time filtered ASE source. Both limits can be estimated [5] and depend on the spectral filter width, the round-trip time of light in the cavity and the properties of the gain medium. Principally, smaller cavity lengths and spectrally broader filters allow for higher sweep speeds. Interestingly, in conventional wavelength-swept semiconductor lasers, the lasing performance does not only depend

on the sweep speed but also on the sweep direction. Wavelength tuning from short to long wavelengths (forward sweep) allows for higher sweep speeds than tuning from long to short wavelengths (backward sweep). Increasing the sweep speed, the decrease in power is more pronounced within the backward sweep [5, 198]. This can be dedicated to the red shift occurring in semiconductor gain media caused by nonlinear effects supporting the forward sweep. Due to the very short carrier lifetime of semiconductor gain material (~ 100 ps), which usually is considerably smaller than the build-up time of lasing in the resonator, the relaxation dynamics typically has no noticeable influence on the sweep speed limitation. However, in case of gain media with a slower relaxation dynamics, such as for example Yb-doped fibers or Er-doped fibers, relaxation time can play a significant role and fast wavelength sweeping can result in q-switching of the laser. Assuming typical parameters of an SOA based wavelength-swept laser with a cavity length of a few meters and a sweep range of ~ 100 nm, the maximum possible sweep rate does not exceed several tens of kHz [5]. Consequently, there have been lots of investigations to raise the sweep speed limit or, in the best case, completely overcome this limitation.

2.2.1.4 Ways to solve the problem of the fundamental sweep speed limit

One potential approach to solve this problem can be to think of wavelength-swept light sources which do not exhibit an optical feedback and therefore no sweep speed limitations due to the build-up time of lasing. The simplest implementation would then be just a broadband gain medium followed by a tunable bandpass filter. However, due to high-finesse filtering, which is required for SS-OCT, the optical output power is typically clearly too low to enable OCT imaging. Post-amplifying using a second gain element after filtering increases the output power but can be problematic since usually a large part of the power is unfiltered ASE due to the insufficient saturation of the last gain element [5]. Within the research work presented in this thesis, a novel approach using a linear cascade of different alternating gain and filter elements has been investigated which overcomes the fundamental sweep speed limitation [12]. A detailed analysis of this technique is given in chapter 3.2.

Since a narrow filter width is required for SS-OCT, inhibiting the use of much broader filters, the most obvious approach to raise the fundamental sweep speed limit in a wavelength-swept laser is to reduce the cavity length and therefore the round-trip time of light in the cavity. Very short external-cavity wavelength-swept lasers can be realized using micro-electrical-mechanical system (MEMS) technology [199]. In this way, fast swept source OCT imaging was demonstrated using for example a grating and a MEMS scanner mirror [200] or a MEMS-based reflective tunable Fabry-Pérot filter [180]. The latter commercially available wavelength-swept laser provides >100 nm sweep range, narrow instantaneous linewidth and sweep rates of 100kHz (one sweep direction) that can be extended to 200 kHz using optical buffering [120, 181] (see chapter 2.2.3.3). In a wavelength-swept external-cavity laser with a polygon-based scanning filter and considerably reduced cavity length, OCT imaging at sweep rates of ~ 400 kHz and

~100 nm sweep range [182] (using optical buffering) was demonstrated recently. One potential problem of very short cavities can be the fact that reducing the cavity length also reduces the number of active laser modes beneath the spectral window of the filter, which can result in increased mode-beating and noise.

Alternatively to external-cavity semiconductor lasers, wavelength tuning can also be realized using monolithic semiconductor lasers (one chip), such as distributed feedback lasers (DFB), distributed Bragg-reflector lasers (DFB) or vertical-cavity surface-emitting lasers (VCSEL). These lasers exhibit a minimum cavity length and therefore facilitate single-mode operation (single line) during wavelength tuning. In DFB lasers, where two grating structures (Bragg reflectors) are distributed over the whole gain region, wavelength tuning is usually realized by changing the temperature (very slow tuning over several nm) or tuning of the electrical current (very fast tuning over typically less than a nm) [201, 202]. Therefore, DFB lasers are not suitable for SS-OCT. DBR lasers consist of different separated sections, containing the active gain section, the grating sections (Bragg reflectors) and usually an additional phase section (change of cavity length) [201]. Fast wavelength tuning can be realized by appropriate modulation of the electrical currents applied to the different sections. A sweep range of several tens of nm can be achieved using a sampled grating distributed Bragg reflector laser (SG-DBR) in combination with Vernier tuning [203] (or Vernier tunable DBR laser (VT-DBR)). An integrated SOA chip is usually used for post-amplification. Recently, wavelength tuning at 200 kHz sweep rate and a sweep range >100 nm has been announced [204], OCT imaging has not been demonstrated up to now. Though the SG-DBR laser runs in single-mode operation, mode-hops cannot be avoided during wavelength tuning. This method potentially provides very fast and flexible sweeping due to pure electronic tuning without moving parts. However, the complicated current waveforms including discontinuities can be a drawback. Apart from edge-emitting tunable semiconductor lasers, there have been lots of investigations on tunable VCSELs using a MEMS-based dielectric mirror [205], allowing for high sweep speeds due to the low mass. Recent improvements of this technology enabled OCT imaging with an optically pumped, MEMS-tunable VCSEL with sweep rates of up to 1 MHz (bidirectional) and sweep ranges >100 nm [183, 184]. Due to true single mode operation, very good sensitivity roll-off performance was demonstrated with a 6 dB roll-off point exceeding several cm. A drawback of this technique could be the very low output power which requires an additional SOA for post amplification.

Alternatively to minimizing the cavity length, a very successful approach, which can overcome the fundamental sweep speed limit, is the utilization of Fourier domain mode locked (FDML) lasers [6]. Here, the cavity length is extended to several hundreds of meters up to a few kilometers by inserting optical fiber in the cavity. In this way, the tunable bandpass filter can be synchronously tuned to the round-trip time of light in the cavity. Therefore, in an ideal case, the spectral position where the bandpass filter transmits is equal to the wavelength of the light that passes the filter at any time during the sweeps. Consequently, the filter does not dissipate any power and lasing does not have

to build up newly from ASE which is the speed limiting factor in conventional wavelength-swept lasers. In the field of SS-OCT, FDML lasers allow for the fastest high-quality SS-OCT imaging existing at the moment. Record voxel rates of 4.5 GVoxels/s at ultra-high sweep rates of 20.4 MHz (four spot approach) [8] have been demonstrated. A detailed description of the FDML principle and technology is given in chapter 2.2.2 and chapter 2.2.3.

2.2.1.5 Alternative approaches

Apart from the mentioned approaches, there also have been other completely different techniques to implement fast wavelength-swept light sources, which did not prevail in SS-OCT imaging. One example is a semiconductor wavelength-swept laser which is based on dispersion mode-locking. The laser is operated in active mode locked operation generating short pulses. Due to a high dispersion that is introduced in the cavity, harmonic mode locking condition is only fulfilled within a certain wavelength window. Therefore, the tuning of the intensity modulation frequency (changing SOA current modulation frequency) results in sweeping of the output wavelength. In this way, sweep rates of 200 kHz and sweep ranges >100 nm were demonstrated [206, 207]. Problems can arise due the lack of a direct filtering mechanism complicating the achievement of a narrowband output. Another example of a fast wavelength-swept light source is the combination of a spectrally broadband, pulsed source with a dispersive fiber, which results in temporal stretching of the short pulses. With this passive technique, using a sub-nanosecond super-continuum pulsed source, very high sweep rates of 5 MHz and a sweep range >100 nm were easily achieved [176]. However, high-quality OCT imaging was not possible due to a very low sensitivity of only 40 dB. Drawbacks of this approach are the need for a broadband source with low intensity noise and a very large amount of dispersion requiring several 10 km of dispersive fiber.

2.2.2 Principle, setup and characteristic parameters of FDML lasers

2.2.2.1 Principle and functionality of FDML lasers

As already mentioned in chapter 2.2.1.4, the fundamental principle of FDML lasers is a periodic tuning of the transmission wavelength of a tunable optical bandpass filter included in a laser resonator that is synchronous to the round-trip time of light in the cavity. Therefore, assuming ideal conditions, light of one wavelength passes the bandpass filter, propagates through the cavity and returns to the filter at the exact time when the transmission window of the bandpass filter is tuned to the same wavelength. Since, ideally, this is true for all wavelengths within forward and backward sweep, the filter dissipates no power and both sweep directions are optically stored in the cavity. The lasing mechanism can then be seen as a stationary lasing operation. In this way, lasing does not have to build up newly from ASE and the fundamental sweep speed limit, which is present in conventional wavelength-swept lasers and depending on the finite resonator

length, can be overcome. This principle was first demonstrated in 1975, using a cw dye laser and a very fast tuned electro-optical filter [191] (sweep range was restricted to ~ 15 nm). In 2006, this concept was first realized with an external-cavity semiconductor laser [6], allowing for sweep ranges exceeding 100 nm. The main components of this typically all fiber based laser setup (see Figure 2.8) are a fiber based output coupler, the broadband gain medium (usually fiber based semiconductor optical amplifier (SOA)), the tunable bandpass filter (usually a fiber Fabry-Pérot tunable filter) and a typically several 100 to a few 1000 meters long optical fiber delay line (usually standard single mode fiber), which has to be inserted in order to enable the synchronous bandpass filter drive. This laser has been referred to as Fourier domain mode locked laser (FDML) [6]. The reason is that FDML lasers are complementary to standard mode locked laser, comparing the time domain picture in standard mode locked lasers and the frequency domain or Fourier domain picture in FDML lasers. In FDML lasers, the frequency is modulated synchronously to the round-trip time of light rather than the amplitude. Whereas, FDML lasers generate a sequence of frequency sweeps with a narrow instantaneous spectrum providing ideally the same output power (continuous wave operation), standard mode locked lasers generate broadband, very short pulses. The frequency sweeps of FDML lasers can also be seen as long, highly chirped pulses. Under ideal operation, the sequential frequency sweeps, or long highly chirped pulses, exhibit the same phase evolution and are mutually coherent, as it is the case with the short pulses in standard mode-locking. In standard mode locked lasers, the phases of the longitudinal laser modes are locked with a constant phase, whereas in an ideal FDML laser the lon-

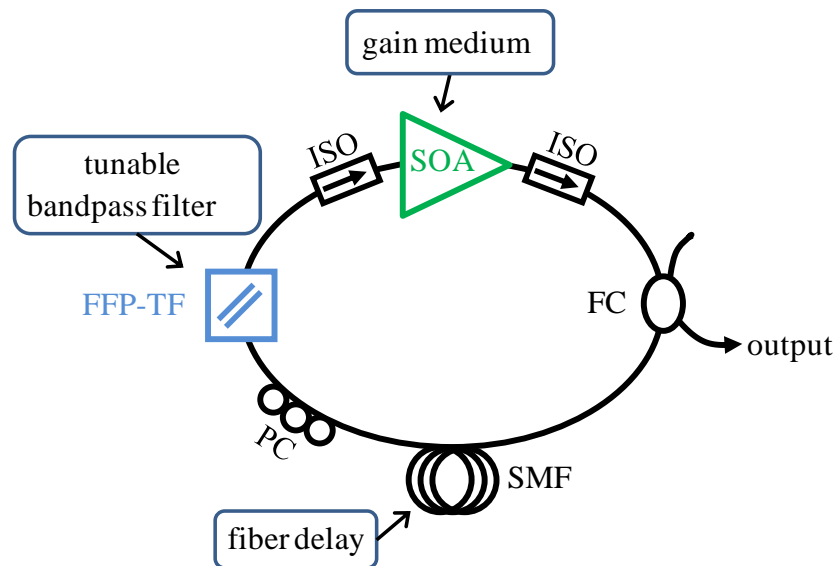


Figure 2.8: Setup of a typical all fiber based Fourier domain mode locked (FDML) laser. Besides the output coupler, the three main elements are the gain medium, which is most commonly a semiconductor optical amplifier (SOA), the tunable bandpass filter, usually a fiber based Fabry-Pérot tunable filter (FFP-TF) and the fiber delay, typically standard single mode fiber (SMF), which has to be inserted in the resonator to enable a filter drive synchronously to the round-trip time of light in the cavity. (PC: Polarization controller, ISO: Optical isolator, FC: Fused fiber coupler)

itudinal laser modes must be locked exhibiting different phases. The spectral, narrow-band filtering in an ideal FDML laser can be compared to an infinite number of narrow-band amplitude modulators that are driven slightly out of phase [6]. Note that FDML lasing operation must not be confused with frequency modulation lasers (FM lasers) [208] or frequency modulation mode locking (FM mode-locking) [209]. In FM lasers, a phase modulator is introduced in the cavity, inducing a phase perturbation at a frequency which approximately equals the inverse round-trip time of light in the resonator. This produces an almost constant intensity trace but a temporal change in output wavelength (sweep with very small sweep range). If the phase perturbation frequency is set nearly synchronous to the round-trip time, this is the transition to FM mode locking, which is used for short pulse generation.

In FDML lasers, the wavelength of the spectral filter is tuned repetitively and continuously (usually sinusoidal drive) with a filter drive frequency f_{Filter} over the filter sweep range $\Delta\lambda_{FilterSweep}$ with alternating sweep directions (bidirectional filter drive, forward and backward sweep). If L is the total length of the cavity, n is the refractive index of the optical fiber, c is the speed of light in vacuum and j is a positive integer ($j \geq 1$), the resonance condition for the filter drive can therefore be expressed by the following equation:

$$f_{Filter}(j) = \frac{c}{L \cdot n} \cdot j \quad 2.33$$

Obviously, FDML operation can only be achieved for discrete filter drive frequencies. Due to the bidirectional filter drive, FDML operation at the fundamental frequency ($j = 1$) means that at any time one pair of forward and backward sweeps is optically stored in the cavity, whereas operation at higher harmonics ($j > 1$) implies that this is true for multiple pairs (j). In order to achieve a sufficient filter tuning range, it can be advantageous to drive the optical bandpass filter with a frequency close to or matching its electro-mechanical resonance [10]. Depending on the filter, typical achievable filter drive frequencies range from several tens to several hundreds of kHz. According to equation 2.33 ($j = 1, n = 1.47$), typical resonator lengths are therefore in the range of several 100 m to a few kilometers, explaining the requirement for an optical fiber delay. Note that the sweep rate ($f_{Sweep} = 1/\Delta T$) or A-scan rate (in OCT) usually exceeds the filter drive frequency f_{Filter} if, for example, forward and backward scans are used simultaneously or if the optical buffering technique is applied (see chapter 2.2.3.3).

One important point that has not been considered yet is chromatic dispersion in the FDML cavity, which results in the fact that the FDML criterion (equation 2.33) can only be fulfilled for one distinct wavelength λ_0 (or several, if dispersion is not constant over wavelength), but is not valid over the entire filter sweep range $\Delta\lambda_{FilterSweep}$. In order to estimate the consequences of this effect, it is helpful to compare two different values [178]. On the one hand, there is the round-trip time mismatch between minimal and maximal wavelengths occurring within the optical bandwidth $\Delta\lambda \leq \Delta\lambda_{FilterSweep}$ (where the FDML laser is lasing), which can be expressed as $\Delta\tau_M = L \cdot \tilde{D} \cdot \Delta\lambda$ assuming a constant dispersion \tilde{D} . On the other hand, there is the gating time

$\Delta\tau_G = \Delta\lambda_{\text{Filter}}/v_{\text{sweep}} \sim (\Delta\lambda_{\text{Filter}} \cdot n \cdot L)/(\Delta\lambda_{\text{FilterSweep}} \cdot c \cdot j)$ of the bandpass filter (spectral width $\Delta\lambda_{\text{Filter}}$), which is the approximate time period within the filter can transmit a certain wavelength or the time where the center frequency is swept over $\Delta\lambda_{\text{Filter}}$. If $\Delta\tau_M \sim \Delta\tau_G$, only a few round-trips of photons in the cavity are possible until lasing has to build up newly from ASE. If the ratio $\Delta\tau_G/\Delta\tau_M$ is increased, this results in a higher number of effective cavity roundtrips. Therefore, $\Delta\tau_M \ll \Delta\tau_G$ is an important prerequisite for optimum FDML operation. Interestingly, under the given assumptions, $\Delta\tau_G/\Delta\tau_M$ is indirect proportional to the dispersion, the filter sweep range, the bandwidth and the number of harmonics ($\tilde{D} \cdot \Delta\lambda_{\text{FilterSweep}} \cdot \Delta\lambda \cdot j$), proportional to the spectral filter width $\Delta\lambda_{\text{Filter}}$ but independent of the resonator length L . Light of a certain wavelength, not fulfilling equation 2.33, passes the optical filter a distinct number of times but each time at a different position within the filter shape approaching gradually the edge of the filter curve. If the loss of the filter exceeds the effective gain in the laser, lasing at this wavelength is suppressed and has to build up newly from ASE. Based on these assumptions, the effective number of roundtrips of light of a certain wavelength can be estimated [14]. Note that there are various other effects influencing FDML operation [15, 210], which are not included in this simple estimation, though they have to be considered for a comprehensive understanding of FDML laser dynamics. Examples are saturation effects, linewidth enhancement and recovery dynamics in the SOA, self phase modulation (SPM) or polarization mode dispersion (PMD) in the delay fiber, or additional effects occurring due to optical filtering. Nevertheless, a minimization of chromatic dispersion in the fiber is an important step to increase the number of effective round-trips and filtering events which, in addition to an appropriate choice of the filter width $\Delta\lambda_{\text{Filter}}$, can considerably improve coherence and minimize the average instantaneous linewidth of the laser over the whole sweep, as demonstrated experimentally [14]. Compared to conventional wavelength-swept lasers, the introduction of FDML lasers enabled, on the one hand, a dramatic increase in available sweep rate and, on the other hand, a considerable reduction of the instantaneous linewidth (increase of instantaneous coherence length) due to multiple filtering [6]. Additionally, FDML lasers also provide an improved phase stability [211], which can be advantageous in, for example, Doppler-OCT. The most successful application of FDML lasers up to date is ultra-high speed SS-OCT. An FDML laser has been used for the fastest high-quality SS-OCT imaging existing at the moment. Record voxel rates of 4.5 GVoxels/s at ultra-high sweep rates of 20.4 MHz (four spot approach) [8] have been demonstrated at 1300 nm. Ultra-fast ultrawide-field retinal SS-OCT imaging was enabled at 3.35 MHz sweep rate (single spot) [7]. However, besides OCT, FDML lasers have the potential to be used in a variety of other applications. Examples are phase sensitive profilometry [211], high-speed spectroscopy [212], optical coherence microscopy (OCM) [213] or fast fiber Bragg grating (FBG) sensing [214-216].

As already mentioned, ideal FDML operation induces longitudinal laser modes which are locked and exhibit a certain well-defined phase relation, making adjacent sweeps mutually coherent. Although there is no doubt that FDML lasers provide improved per-

formance and a stable lasing operation, it is not completely clarified up to now in how far effects occurring in realistic FDML operation (as mentioned in this chapter), influence FDML dynamics. It is not entirely clear if or how these effects interact supporting or impeding a stationary lasing operation. Furthermore, it is not clear in how far the longitudinal laser modes exhibit a definite phase relation or to which extent the modes are locked. Within the framework of this thesis, a completely new approach of short pulse generation has been investigated, which is based on temporal compression of the wavelength-swept output of an FDML laser. Since the achievable minimum pulse width depends on the coherence properties of the laser and on the quality of mode-locking, this approach offered the possibility to gain an insight into these properties and identify parameters which influence the coherence performance. In chapter 4, the results of this approach are presented.

2.2.2.2 Typical components in an FDML setup

In the following, the different elements in the FDML laser will be discussed separately. The most common gain element in FDML lasers are broadband fiber semiconductor optical amplifiers (SOA) (essentially laser diodes with two anti-reflex coated end facets), enabling an external-cavity laser with a ring resonator. The SOAs, as well as typically all other elements required in the FDML cavity, can be purchased with direct fiber coupling simplifying the setup of an all fiber based resonator. The SOAs are available in the telecom windows at ~ 1300 nm and ~ 1550 nm, but also in other wavelength ranges such as ~ 1060 nm or ~ 800 nm. Combining of two SOAs with different gain maxima has been demonstrated to enhance bandwidth [217]. Besides SOAs, other gain media were used to realize FDML operation. Since at 1060nm, compared to 1300 nm, the FDML operation is complicated due to usually lower performance of the SOAs, higher loss of all components and considerably higher dispersion in the resonator, there have been different approaches to use other gain media. Ytterbium-doped fiber amplification (YDFA) has successfully been introduced in the resonator in addition to an SOA [74] enabling very good FDML performance and high output power at 1060 nm. FDML operation based on solely YDFA has been demonstrated at 1060 nm, but enabled only a small sweep range of 15 nm [218]. A tapered amplifier (in addition to an SOA) integrated in the resonator by free space coupling allowed for a high output power FDML laser [179]. At 1550 nm, FDML operation was demonstrated using Raman gain in a Raman fiber (high Raman gain) [92, 219]. This is in particular interesting due to the ultra-fast relaxation times of \sim ps and the very small absorption in the gain medium when the pump is switched off, allowing for cavity ring-down experiments. Furthermore, at 1550 nm, there were investigations using optical parametric amplification in combination with erbium-doped fiber amplification (EDFA) for FDML operation [220].

The fiber delay used in FDML lasers typically consists of several hundred meters to a few kilometers long standard single mode fiber (SMF) (as for example Corning SMF28). The fiber is very cheap (~ 0.01 - 0.02 €/m) and provides very low loss (≤ 0.22 dB/km at 1550 nm and ≤ 0.35 dB/km at 1300 nm). For wavelengths shorter than

~ 1260 nm, single transversal mode operation is not possible any more. However, as recently demonstrated, FDML operation at 1060 nm using standard single mode fiber (~ -0.7 dB/km) is perfectly feasible despite the oligo-mode operation [74] and can therefore be preferable to Hi1060 fiber, which enables single transversal mode operation at 1060 nm but is more expensive (~ 1.2 €/m) and exhibits a higher loss (~ -1.5 dB/km). In Figure 2.9, the measured chromatic dispersion is shown for several types of fibers in the wavelength range from ~ 1300 nm to ~ 1600 nm. In case of standard single mode fiber (SMF), the zero dispersion wavelength is ~ 1315 nm. Therefore, in an FDML cavity designed for a center wavelength close to 1315 nm, the overall dispersion is already considerably low and allows for very high performance in applications such as SS-OCT. The situation is more difficult in the wavelength range close to 1550 nm where dispersion is ~ 16.5 ps/(nm·km) and in particular around 1060 nm where the magnitude of dispersion is even higher. Here, a lower dispersion is highly desirable to improve and facilitate FDML operation. Using a dispersion shifted fiber (DSF) (here: zero dispersion wavelength at ~ 1543 nm as can be seen in Figure 2.9) instead of SMF fiber, the performance of an 1550 nm FDML laser can be improved. Under certain circumstances, where a very high coherence and a considerably improved sensitivity roll-off performance are required, the chromatic dispersion has to be further reduced. At 1550 nm, a very effective method to compensate for the positive chromatic dispersion in the FDML cavity is to substitute a part of the SMF fiber by dispersion compensation fiber (DCF) providing a very high negative dispersion (see Figure 2.9) [14]. If the ratio is properly chosen, chromatic dispersion at ~ 1550 nm is compensated to a large extent over a wavelength range of several tens of nm. Recently, the insertion of a positive and a negative chirped fiber Bragg grating in the cavity allowed for very good dispersion compensation at 1300 nm [185]. Both methods enabled a considerably improved sensitivity

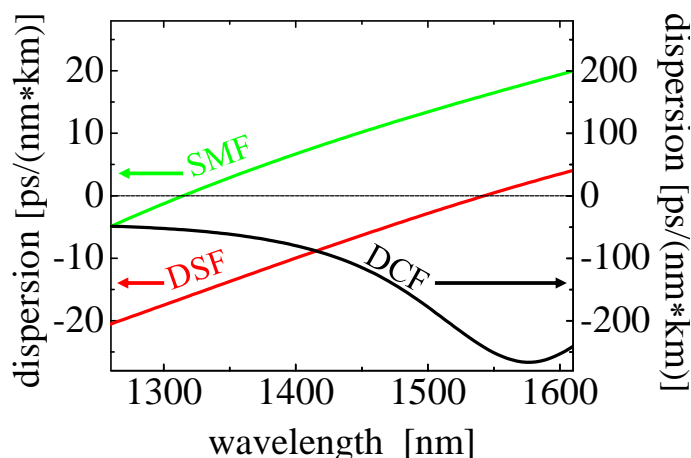


Figure 2.9: Chromatic dispersion of standard single mode fiber (SMF, Corning SMF28, left y-axis), dispersion shifted fiber (DSF, Fujikura FutureGuide-DS, left y-axis) and dispersion compensation fiber (DCF, OFS-HFDK, right y-axis). The dispersion curves have been measured according to a principle described in [221]. Based on two measurement windows (1250 nm-1360 nm and 1480 nm-1615 nm), the complete curves were obtained by polynomial fit for each fiber.

roll-off performance.

Another crucial element of the FDML resonator is the tunable bandpass filter, which has to meet several requirements to enable optimum FDML operation. Firstly, the finesse has to be sufficiently high in order to allow for a large free spectral range (>100 nm) and at the same time enable a narrow filter width (~ 100 pm). Secondly, the reproducibility and stability of the wavelength sweep operation has to be very high and finally, the filter should allow for high sweep rates at large sweep ranges. The bandpass filters, which are best suitable for FDML operation with regard to the mentioned requirements, are fiber based Fabry-Pérot tunable filters (FFP-TF). In commercially available FFP-TFs, as used for this thesis (Lambda Quest, LLC), the end facets of two optical fibers are located very close to each other (typically a distance of a few μm). With a micro concave polycarbonate lens at one facet and suitable coatings on both sides, a Fabry-Pérot cavity can build up between both fiber ends. The distance is periodically changed using a piezo actuator enabling tunable wavelength filtering. Usually, the piezo is driven with a sinusoidal voltage signal, resulting from superposition of an AC and a DC voltage signal, which enables the adjustment of the wavelength sweep range and the sweep center wavelength, respectively. Generally, the electro-mechanical response of FFP-TFs, which are commercially available today, is negligible for frequencies exceeding ~ 250 kHz, preventing a sufficient sweep operation at those frequencies. In case of the purchased filters used for this thesis, the best sweep operation was observed close to the dominant electro-mechanical resonance, typically located around ~ 50 kHz, and, in case of higher frequencies, close to a less pronounced resonance typically located around ~ 170 kHz [10]. In order to push the filter frequency and filter sweep speed performance, a novel Fabry-Pérot tunable filter design has been developed [8, 74, 222] within our research group, allowing for large sweep ranges at filter frequencies exceeding 400 kHz. Note that, apart from using tunable Fabry-Pérot filters, there have also been investigations on FDML operation with polygon scanning filters [223, 224].

The polarization in conventional FDML lasers, which are based on standard single mode fiber, is not preserved. This can be attributed to the fact that the polarization state changes gradually along the fiber due to random birefringence fluctuations and coupling between polarization axes. Reasons are stress induced birefringence or asymmetries in the refractive index profile geometry of the fibers. These effects are inevitably due to random imperfections occurring in the manufacturing process of the fibers. However, the by far largest contribution to birefringence in the fiber is due to externally induced stress which results from bending the fiber due to spooling. Assuming a fiber of length L that is wound up on a spool of diameter D , the phase difference between light polarized parallel to the spool plane (fast axes) and light polarized perpendicular to the spool plane (slow axes) is inverse proportional to the wavelength and inverse proportional to D [225]. A typical fiber spool (~ 20 cm diameter) used to wind up a few kilometers of SMF fiber acts as multiple λ waveplate. Consequently, the polarization state after the fiber can vary over the entire wavelength sweep [226]. Since, usually, high power SOAs

exhibit a highly polarization dependent gain and amplify only the projection of the electric field vector on one distinct axis, the insertion of a fiber polarization controller (PC) in the cavity is essential in order to be able to adjust the polarization state and maximize the output power within the whole lasing range. Typically, the manual fiber polarization controller consists of three fiber paddles (coils with diameter of several cm including several windings). Each paddle can be rotated in order to change the orientation of the optical axis. Usually, the numbers of windings and the coil diameters are chosen in a way yielding two $\lambda/4$ waveplates and one $\lambda/2$ waveplate [225]. Polarization effects can become a problem for FDML operation if sufficient adjustment over the entire wavelength range is not possible resulting in for example partially suppression of lasing within distinct wavelength ranges of the sweep. This is primarily a problem in case of operation at smaller wavelengths (1060 nm) due to the fact that the polarization effects are more dominant. One method to reduce the polarization effects is the enlargement of the fiber coil diameter [74]. Other implementations that considerably reduce or prevent polarization problems are mentioned in chapter 2.2.3.1 and chapter 2.2.3.2. Generally, it is reasonable to utilize a polarization controller, even if an almost polarization independent SOA is used. In order to ensure unidirectional lasing and prevent the amplification of light back reflected from the FFP-TF, two optical isolators are inserted prior to and after the SOA. A fused fiber coupler is introduced, usually after the SOA, in order to enable the extraction of a certain percentage of the optical power. The average output power of typical FDML lasers (without boosting) typically ranges from ~ 10 mW to ~ 50 mW, depending on the wavelength range and the utilized gain medium.

FDML lasers have been successfully demonstrated in the spectral windows of ~ 1300 nm, ~ 1550 nm and also at ~ 1060 nm, where FDML operation is complicated due to higher losses, higher dispersion or increased polarization effects. At ~ 800 nm, these drawbacks are more pronounced and make FDML operation more difficult. Up to now, FDML operation has not been demonstrated for wavelengths < 1000 nm.

2.2.2.3 Characteristic parameters of FDML operation

In this chapter, some characteristic parameters of FDML lasers are discussed. The parameters which determine the sweep operation are the wavelength sweep range $\Delta\lambda_{\text{FilterSweep}}$, the center sweep wavelength and the filter drive frequency f_{Filter} . Typically, the FDML laser is lasing only during a certain time interval ΔT within the filter drive period $1/f_{\text{Filter}}$, defining the optical bandwidth $\Delta\lambda \leq \Delta\lambda_{\text{FilterSweep}}$, the corresponding center wavelength and the duty cycle ($DC = 2\Delta T f_{\text{Filter}}$). A duty cycle $DC \leq 1$ is a requirement for optical buffering (see chapter 2.2.3.3) and can be realized using SOA current modulation. The optical bandwidth can be restricted due to insufficient gain bandwidth, poor FDML operation, but also due to the finite free spectral range of the optical filter, whereas the sweep range is only limited by the electro-mechanical properties of the filter. A precise setting of the filter drive frequency is necessary in order to ensure maximum output power and optimum FDML operation (a few Hz). The required accuracy is increased in case of dispersion compensated lasers,

2. Overview of the research field

where changes in the order of ~ 0.1 Hz do not influence the output power but do already considerably worsen the coherence properties and the sensitivity roll-off performance [14]. In conventional wavelength-swept external-cavity lasers, a clear disparity between forward and backward sweep performance in terms of output power is observed, caused by the red shift in the semiconductor gain medium. This effect is not determined in FDML lasers, though differences in roll-off performance between both sweep directions exist [6], but typically vanish in case of dispersion compensation [14, 73].

Besides the spectral width of the optical filter $\Delta\lambda_{Filter}$, which typically ranges from ~ 100 pm to ~ 300 pm, there is the instantaneous linewidth $\Delta\lambda_{inst}(t)$ of the laser output defined at each point in time within the sweep. It is a very important parameter, since it is directly linked to the instantaneous coherence length of the FDML laser $\tau_c(t)$ and therefore determines the sensitivity roll-off performance in applications such as SS-OCT. Usually, $\Delta\lambda_{inst}$ is considerably smaller than $\Delta\lambda_{Filter}$ due to multiple filtering. Note that $\Delta\lambda_{inst}$ is typically not constant and can differ within the sweep. Moreover, one must bear in mind that $\Delta\lambda_{inst}$ usually is much larger than the linewidth that is measured (assuming sufficient resolution) if the spectral filter in the FDML laser cavity is not swept (non-swept laser). Consequently, a direct measurement of the instantaneous linewidth $\Delta\lambda_{inst}$ of an FDML laser is complicated. One possible approach has been demonstrated recently [227], utilizing an electro optical modulator which extracts a very short time interval within each sweep. The transmitted light then is analyzed with an optical spectrum analyzer (OSA). Although this method can usually deliver sufficiently accurate results, there are several broadening effects one has to be aware of, which reduce accuracy in particular for very small $\Delta\lambda_{inst}$. Examples are broadening due to the finite optical resolution of the OSA, sweep to sweep jitter, sideband generation due to intensity modulation, the filter sweep during the finite measurement time and eventually time-bandwidth limitations. Except for this approach, there is the possibility to indirectly measure the instantaneous linewidth by acquiring the sensitivity roll-off as commonly done in SS-OCT. However, this method, as described in chapter 2.1.4.2, only allows specifying a mean instantaneous linewidth, which represents an average value over the sweep. A certain wavelength dependence can be obtained if the PSFs are generated by Fourier transforming only small temporal windows within the sweep [227]. Typical values of $\Delta\lambda_{inst}$ of typical FDML lasers range from ~ 50 pm to ~ 100 pm. However, $\Delta\lambda_{inst}$ can further be reduced using dispersion compensated FDML lasers [14].

Besides phase noise, which influences the instantaneous linewidth and sensitivity roll-off performance, there is relative intensity noise (RIN) which is an important parameter in FDML laser performance. Compared to conventional fast swept lasers, where the number of effective roundtrips is very low, and lasing has to rebuild permanently from ASE, FDML lasers provide a considerably reduced RIN. A measurement of RIN in FDML lasers gives insight about the amount of excess noise (the part exceeding shot noise) that is introduced in for example a SS-OCT system, where it can affect dynamic range and sensitivity. If one is interested in the wavelength or time-dependent RIN val-

ue of wavelength-swept light sources, a simple analysis of the power spectral density (FFT of digitized optical power signal) is not suitable [14]. Alternatively, the wavelength dependent relative intensity noise ($RIN = \sigma_P(\lambda)/\bar{P}(\lambda)$) can be determined by digitizing the optical power signal $P(\lambda)$ using a certain electronic detection bandwidth and calculating the standard deviation $\sigma_P(\lambda)$ and the mean power $\bar{P}(\lambda)$ for each wavelength. As demonstrated in [14], there are two ways to allocate the samples for the calculation of the standard deviation $\sigma_P(\lambda)$ and the determination of the RIN value at wavelength λ : On the one hand, there is the sliding-RIN approach (intra-sweep noise), where a distinct number of neighboring samples in vicinity to λ (sliding window) are evaluated. On the other hand, there is the ortho-RIN approach (inter-sweep noise), where samples of many adjacent sweeps corresponding to the same wavelength λ are evaluated. Note that these values provide no information about the frequency dependence of the noise. However, the power spectral density of the noise is usually flat. Therefore, the RIN value is proportional to the detection bandwidth allowing for an easy conversion of the RIN value in case of different electronic bandwidths. As shown in [14], the sliding-RIN value depends on the number of samples in the sliding window, whereas the ortho-RIN approach is the most conservative RIN noise analysis, providing the worst case value for RIN noise. All RIN noise analyses of fast wavelength-swept light sources, which have been made within the research presented in this thesis (chapter 3.2), are based on the ortho-RIN approach. In FDML lasers, minimum wavelength dependent ortho-RIN values down to $\sim 0.15\%$ have been observed at a detection bandwidth of 100 MHz and a power of ~ 1 mW [14]. This value is corresponding to a noise power spectral density of ~ -136 dBc/Hz.

2.2.3 Different implementations of FDML lasers

2.2.3.1 Sigma-ring configuration

Very often, the fiber delay is not inserted in the FDML laser cavity as sketched in Figure 2.9, but instead, a sigma-ring configuration is used, as shown in Figure 2.10a. Here, an optical circulator directs the light in a linear delay line (1 \rightarrow 2), where light passes the fiber delay spool (usually SMF) ones, is reflected by a Faraday rotation mirror (FRM) and passes the fiber delay spool a second time in opposite direction. Afterwards, the circulator redirects the light back in the ring (2 \rightarrow 3). Besides the fact that only half of the delay fiber length is required, there is another clear advantage: The FRM is a mirror that does not only reflect light, but also induces a polarization rotation by -90° (flip of magnitude of the polarization components along two orthogonal axes). In this way, any time delay caused by birefringence and any change of the optical axis orientation occurring during the first pass of the fiber are cancelled after the second pass of the fiber. Therefore, ideally, the polarization state of light exiting the linear delay line equals the polarization state of light entering the delay line but rotated by -90° . A fiber of \sim km length coiled on a fiber spool can induce wavelength dependent polarization changes, where a complete compensation over the whole spectral bandwidth might not be possi-

ble with fiber polarization controllers. However, the described method provides very good compensation over a large spectral range and thus is an effective method to reduce polarization effects and improve FDML performance in particular if an SOA with polarization dependent gain is used [226]. One potential drawback is an increased loss due to the double pass of the circulator which is a problem at 1060 nm due to the generally higher loss of all components.

2.2.3.2 Polarization maintaining FDML (PM FDML) laser

Another possible implementation is the polarization maintaining FDML (PM FDML) laser, which was first investigated and tested within the research presented in this thesis and was utilized in several other investigations [12, 15, 226-229]. The setup (see Figure 2.10b) is also based on a sigma-ring cavity, however, the characteristic feature is that the ring is polarization maintaining (red), whereas the linear delay line (black) is not. An important element in this setup is polarization maintaining single mode fiber (PM fiber). The principle of PM fiber [230] is the introduction of a large amount of stress in the core of the fiber, which can for example be realized by manufacturing fibers including two stress rods in the cladding (rods consist of different material) with the core always centered on the connection line of both rods. In this way, the PM fiber exhibits a very large amount of birefringence resulting in an almost complete suppression of cross-coupling between light polarized parallel to the stress rods (slow axis) and light polarized perpendicular to the stress rods (fast axis). Therefore, the polarization state of light that enters the fiber polarized parallel to one of these two axes is maintained along the PM fiber independent from bending or spooling of the fiber. All components used in the ring are special polarization maintaining components which are

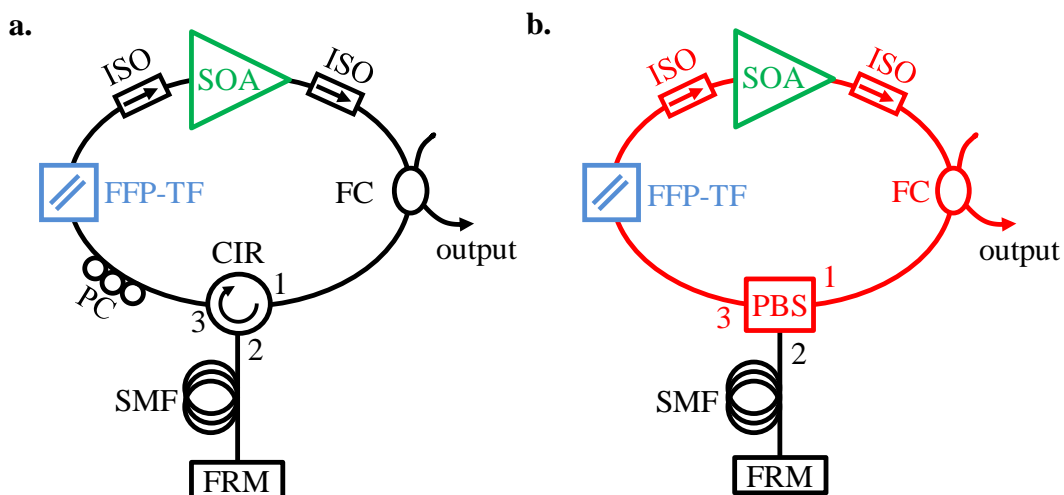


Figure 2.10: Different implementations of FDML lasers. **a.** Sigma-ring configuration using an optical circulator (CIR) and a Faraday rotation mirror (FRM) enabling reduced polarization effects in the fiber delay. **b.** Polarization maintaining FDML laser based on standard single mode fiber (black), polarization maintaining fiber (red) and polarization maintaining components. (FC: Fused fiber coupler, SOA: Semiconductor optical amplifier, ISO: Optical isolator, PC: Polarization controller, FFP-TF: Fiber based Fabry-Pérot tunable filter, PBS: Polarization beam splitter)

based on PM fiber and require special fiber alignment. Typically, light is guided with polarization parallel to the slow axis of the PM fiber. Instead of a circulator, a polarization beam splitter (fiber coupled with one output not connected) is used. Light that is polarized parallel to the slow axis is directed towards the delay line ($1 \rightarrow 2$). Since the light returning to the PBS exhibits a polarization that is rotated by -90° (due to the FRM), the light follows the other path of the PBS ($2 \rightarrow 3$) and finally is coupled to the slow axis of the PM fiber again. In this way, there is no need for PM fiber in the linear delay line. Advantages of PM FDML lasers are, on the one hand, that no polarization controllers are required which facilitates FDML operation and, on the other hand, that the PM FDML laser provides a constant, linear output polarization which is preserved over the entire sweep and is not affected by bending of the output fiber. This could be an attractive feature for applications such as for polarization sensitive OCT. However, the utilization of PM fiber can have a drawback, since the birefringence between the fast and the slow axis is very high. Therefore, already weak cross-coupling between the axes results in spectral power modulations which can yield ghost images in SS-OCT. This cross-coupling occurs when connecting PM fibers or due to imperfect alignment within the components. However, splicing of all PM fibers and the utilization of polarizing components can minimize these effects. Furthermore, reducing the lengths of the PM fiber junctions between the components in the ring can minimize the frequency of remaining spectral modulations and therefore minimize the distance of potential satellite peaks enclosing the main peak in the PSF.

2.2.3.3 Optical buffering

A very important implementation or method used in FDML technology is optical buffering, which allows for sweep rates that exceed the filter drive frequency. Due to the limited frequency-dependent response of the spectral filter, this method is often preferable to just increasing the filter drive frequency. Optical buffering with FDML lasers was first demonstrated shortly after their introduction [177] and enabled record sweep rates [8, 74]. There are essentially two important steps which are necessary to implement this technique. Firstly, the current of the SOA in the cavity is modulated so that the FDML laser is lasing only within a certain time interval $\Delta T < 1/f_{Filter}$, defining the sweep time and the laser bandwidth $\Delta\lambda$. In the remaining dead time the laser is inactive. Secondly, optical copies of the sweep are created, delayed to each other (using optical fiber) and superposed again in a way that the dead time is filled with optical copies of the sweep. Usually, the utilization of sweeps of only one sweep direction is preferable in SS-OCT, although bidirectional sweep operation is possible as well. The reason is that unidirectional sweep operation is beneficial for numerical post-processing (as for example numerical resampling), since all sweeps have identical properties. Furthermore, the FDML performance between forward and backward sweeps can differ [6], thus favoring one distinct sweep direction. An effective approach to double the sweep rate (of one sweep direction) is a 2x buffering scheme, where lasing of one sweep direction is suppressed and the resulting dead time is filled with an optical copy of the other

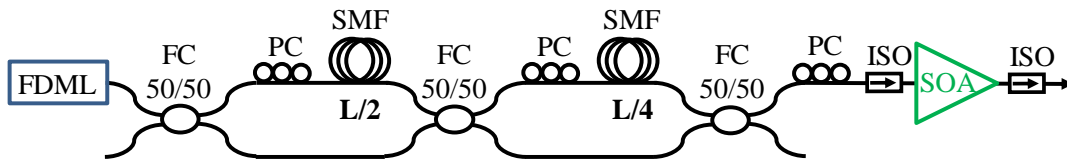


Figure 2.11: Typical setup of an external buffer stage (here: 4x buffering). Generally, this configuration can be extended to obtain a cascade with N fiber spools with length $L/2, L/4 \dots L/2^N$, resulting in an 2^N buffering scheme (L is the cavity length of the FDML laser). Usually the light is post-amplified with an additional semiconductor optical amplifier (SOA) after the buffer stage. Optical isolators (ISO) ensure unidirectional propagation of the light. Several polarization controllers (PC) are required to adjust the polarization of the optical copies. (FC: Fused fiber coupler, SMF: Standard single mode fiber)

sweep direction. However, very often, increasing the sweep rate by more than a factor of two is desirable. In Figure 2.11, a setup of a typical external buffer stage is shown, here for the special case of a 4x buffering scheme. Generally, a setup of an (2^N) x external buffering scheme consists of a cascade of N connected “Mach-Zehnder interferometers” with fiber delays of length $L/2, L/4, \dots, L/2^N$. Using this setup, the sweep rate can be increased by a factor of 2^N ($N \in \mathbb{N}_{>0}$). The current is modulated such that lasing is active only for $1/2^N$ of the time of the filter drive period $1/f_{Filter}$. Then, the resulting dead time is subsequently filled up with $2^N - 1$ optical copies. However, in order to preserve the scan bandwidth of the FDML laser, the filter sweep range has to be increased accordingly by a factor that is proportional to 2^{N-1} . Therefore, optical buffering does only make sense if the bandpass filter supports the required sweep range at the chosen filter drive frequency. Note that 2x buffering has also been implemented without the need for additional fiber, inserting two fiber coils of same length into the FDML cavity separated by an additional output coupler [177]. Within the research presented in this thesis, a new operation mode of FDML lasers has been investigated which inherently provides the possibility of simple up-scaling of the sweep rate with a minimum of optical fiber required in the FDML cavity and with no need for an external buffer stage (see chapter 3.1.2).

2.2.3.4 Post-amplification

Very often, a second SOA is used in addition to the FDML laser in order to post-amplify the light. This is typically applied in case of optical buffering, where the average power is reduced by a factor of $\sim 2^{N+1}$ (see Figure 2.11), but is also used without an optical buffer stage, placing the SOA directly after the output of the FDML laser. Besides a higher optical output power, which is desirable for OCT applications, there is another advantage: Since the current of the second SOA can be actively modulated and controlled, there is the possibility to implement hardware-spectral shaping of the sweeps [231]. Using an iterative optimization process, arbitrary spectral shapes, as for example a Hanning shape, can be realized. Furthermore, in case of optical buffering, hardware-spectral shaping can be applied to the fundamental sweeps and its optical cop-

ies. This ensures that all sweeps have identical spectral shapes and intensities, accurately compensating for the remaining disparities due to different optical paths in the buffer stage.

2. Overview of the research field

3 New concepts of wavelength-swept light sources in application for OCT

In chapter 2, a detailed overview of the research field was given. On the one hand, OCT was introduced and, on the other hand, the principle and functionality of wavelength-swept light sources which can be used for SS-OCT were explained. Most attention was paid to FDML lasers, an important new type of wavelength-swept lasers, enabling record OCT imaging speeds. In this chapter, the focus is on the presentation of novel concepts of fast wavelength-swept light sources, which have been investigated and analyzed during the research presented in this thesis with the aim to improve the performance and applicability in SS-OCT. The chapter is divided into two parts. The first part deals with the investigation of two novel operation modes of FDML lasers and their advantages for SS-OCT. The second part introduces two implementations of a novel type of non-lasing, very fast wavelength-swept light source as an alternative approach for ultrafast SS-OCT.

3.1 New operation modes of FDML lasers

FDML lasers can overcome the fundamental sweep speed limit as given in conventional swept lasers. Since their introduction, great progress in sweep speed and sweep rate has been achieved supported by investigations on the improvement of tunable filter performance. In this way, high-quality SS-OCT has been demonstrated with A-scan rates of several megahertz. This chapter focuses on two novel operation modes of FDML lasers that have first been investigated within research work presented in this thesis. On the one hand, this is the realization of an FDML laser exhibiting wavelength sweeps with a highly linear time-frequency sweep characteristic (k-space linear FDML laser). In contrast to a typical sinusoidal drive of the tunable bandpass filter, the k-space linear operation requires the application of a special waveform comprising several harmonics of the FDML fundamental drive frequency f_{Filter} . In this way, numerical resampling prior to FFT is no longer necessary, which has several advantages in SS-OCT. On the other hand, this chapter addresses subharmonic Fourier domain mode locking (shFDML). Whereas in standard FDML operation light passes the delay fiber a single time or less (higher harmonics) during each filter drive repetition period, in shFDML lasers, light is recirculated repetitively in the FDML cavity inducing multiple passes of the delay fiber within one round-trip. The tunable bandpass filter is used as an optical switch. Besides a

considerable reduction of the required fiber length, the most important advantage of this approach is the inherent and easy possibility to upscale the sweep rate and therefore increase OCT imaging speed without the need for an external buffer stage.

3.1.1 K-space linear FDML laser and applications for OCT

Generally, wavelength-swept light sources providing sweeps with non-linear time-frequency characteristics are not optimal for application in SS-OCT, since the data has to be evenly sampled in frequency prior to Fourier transformation in order to provide the maximum possible axial resolution. There are two possible ways to handle this problem. One possibility is hardware recalibration [73], where the analog to digital converter card is not clocked with a constant sampling rate but with a signal that is generated from the fringe signal acquired with an additional interferometer. In this way, the data samples are unevenly spaced in time but evenly spaced in frequency. Disadvantages are for example the need of complex electronic hardware or higher sampling speed requirements for the analog to digital converter. The other, most commonly used approach is numerical resampling/recalibration, as described in chapter 2.1.6.2. However, this approach can also have drawbacks. Reasons are unwanted, additional software requirements for data processing, but also, for example, inefficient use of system memory caused by oversampling in some parts of the sweep or reduced sensitivity due to overexposure of the sample. Moreover, both numerical as well as hardware recalibration introduce additional noise, which can reduce the dynamic range.

Consequently, a wavelength-swept light source that exhibits a sufficiently linear time-frequency sweep characteristic, making hardware or numerical recalibration obsolete, is highly desirable to overcome the named drawbacks. However, except for wavelength-swept light sources that rely on non-mechanic, pure electrical wavelength tuning, the realization of swept sources with a sufficient sweep linearity is usually not trivial. This is in particular true for swept sources using Fabry-Pérot filters, but also applies to those based on polygon-based scanning filters, where the sweep is linear in wavelength but not linear in optical frequency.

Within the work presented in this thesis, the first implementation of an FDML laser providing a highly linear time-frequency sweep characteristic (k-space linear FDML laser) has been demonstrated in the wavelength range around ~ 1300 nm. A comprehensive description and analysis of the operation principle of k-space linear FDML lasers as well as a detailed analysis of the advantages is given in the reprint¹ of the article

C. M. Eigenwillig, B. R. Biedermann, G. Palte, and R. Huber, "K-space linear Fourier domain mode locked laser and applications for optical coherence tomography", *Optics Express* **16**, 8916-8937 (2008),

which was written by me jointly with B. R. Biedermann, G. Palte and R. Huber and which is attached to this chapter. In order to enable k-space linear operation, the opti-

¹ © 2008 Optical Society of America, Inc.

imum drive signal, that is applied to the piezo-actuated Fabry-Pérot filter and comprises several harmonics of the filter drive frequency f_{Filter} , must be determined. Thereby, the frequency-dependent, electro-mechanical amplitude and phase response of the tunable filter has to be considered. In the following article, different strategies and simulations are presented in order to determine the optimal filter drive waveform. For this purpose, the integrated relative frequency error is introduced as a measure for the linearity of the time-frequency characteristic of the sweep. OCT imaging at 1300 nm with the k-space linear FDML laser is successfully demonstrated without the need for numerical resampling and spectral apodizing. As demonstrated, a prerequisite for this is a very small integrated relative frequency error on the order of 10^{-5} . Moreover, it is shown that a k-space linear FDML laser can be used to compensate for unbalanced dispersion in the OCT interferometer arm within at least a small imaging range by adapting the filter drive waveform.

The k-space linear operation could be a prerequisite for different approaches such as, for example, direct hardware based Fourier transformation, which would reduce the required data transfer bandwidth from the analog digital converter to the system memory or data-storage by a factor of two. One direct application of k-space linear FDML laser, as demonstrated by our group, is real-time en face OCT with direct hardware frequency demodulation [231]. Here, the fringe signal is mixed with an adjustable local oscillator yielding the analytic reflectance signal for one depth. In this way, this technique allows for real-time visualization of en-face images without the need for Fourier transformation. The visualized depth can be chosen via adjustment of the frequency of the local oscillator. Note that a necessary requirement is k-space linear operation since, otherwise, light reflected from one single depth would not yield a fringe signal comprising only one single fringe frequency.

3. New concepts of wavelength-swept light sources in application for OCT

K-space linear Fourier domain mode locked laser and applications for optical coherence tomography

Christoph M. Eigenwillig, Benjamin R. Biedermann,
Gesa Palte, and Robert Huber*

*Lehrstuhl für BioMolekulare Optik, Fakultät für Physik, Ludwig-Maximilians-Universität München,
Oettingenstr. 67, 80538 Munich, Germany*

Corresponding author: Robert.Huber@Physik.Uni-Muenchen.DE

We report on a Fourier Domain Mode Locked (FDML) wavelength swept laser source with a highly linear time-frequency sweep characteristic and demonstrate OCT imaging without k-space resampling prior to Fourier transformation. A detailed theoretical framework is provided and different strategies how to determine the optimum drive waveform of the piezo-electrically actuated optical bandpass-filter in the FDML laser are discussed. An FDML laser with a relative optical frequency deviation $\Delta\nu/\nu$ smaller than $8 \cdot 10^{-5}$ over a 100 nm spectral bandwidth at 1300 nm is presented, enabling high resolution OCT over long ranging depths. Without numerical time-to-frequency resampling and without spectral apodization a sensitivity roll off of 4 dB over 2 mm, 12.5 dB over 4 mm and 26.5 dB over 1 cm at 3.5 μ s sweep duration and 106.6 dB maximum sensitivity at 9.2 mW average power is achieved. The axial resolution in air degrades from 14 to 21 μ m over 4 mm imaging depth. The compensation of unbalanced dispersion in the OCT sample arm by an adapted tuning characteristic of the source is demonstrated. Good stability of the system without feedback-control loops is observed over hours.

©2008 Optical Society of America

OCIS codes: (170.4500) Medical optics and biotechnology: Optical coherence tomography; (110.4500) Imaging systems: Optical coherence tomography; (140.3600) Lasers, tunable. (110.6880) Imaging systems: Three-dimensional image acquisition; (120.3180) Instrumentation, measurement, and metrology: Interferometry; (170.3880) Medical optics and biotechnology: Medical and biological imaging

References and links

1. D. Huang, E. A. Swanson, C. P. Lin, J. S. Schuman, W. G. Stinson, W. Chang, M. R. Hee, T. Flotte, K. Gregory, C. A. Puliafito, and J. G. Fujimoto, "Optical Coherence Tomography," *Science* **254**, 1178-1181 (1991).
2. R. Leitgeb, C. K. Hitzenberger, and A. F. Fercher, "Performance of fourier domain vs. time domain optical coherence tomography," *Opt. Express* **11**, 889-894 (2003).
3. J. F. de Boer, B. Cense, B. H. Park, M. C. Pierce, G. J. Tearney, and B. E. Bouma, "Improved signal-to-noise ratio in spectral-domain compared with time-domain optical coherence tomography," *Opt. Lett.* **28**, 2067-2069 (2003).
4. M. A. Choma, M. V. Sarunic, C. H. Yang, and J. A. Izatt, "Sensitivity advantage of swept source and Fourier domain optical coherence tomography," *Opt. Express* **11**, 2183-2189 (2003).
5. A. F. Fercher, C. K. Hitzenberger, G. Kamp, and S. Y. Elzaiat, "Measurement of Intraocular Distances by Backscattering Spectral Interferometry," *Opt. Commun.* **117**, 43-48 (1995).
6. F. Lexer, C. K. Hitzenberger, A. F. Fercher, and M. Kulhavy, "Wavelength-tuning interferometry of intraocular distances," *Appl. Opt.* **36**, 6548-6553 (1997).
7. G. Häusler, and M. W. Lindner, "'Coherence radar" and "spectral radar"-new tools for dermatological diagnosis," *J. Biomed. Opt.* **3**, 21-31 (1998).
8. S. R. Chinn, E. A. Swanson, and J. G. Fujimoto, "Optical coherence tomography using a frequency-tunable optical source," *Opt. Lett.* **22**, 340-342 (1997).
9. S. H. Yun, G. J. Tearney, J. F. de Boer, N. Iftimia, and B. E. Bouma, "High-speed optical frequency-domain imaging," *Opt. Express* **11**, 2953-2963 (2003).

10. R. Huber, M. Wojtkowski, K. Taira, J. G. Fujimoto, and K. Hsu, "Amplified, frequency swept lasers for frequency domain reflectometry and OCT imaging: design and scaling principles," *Opt. Express* **13**, 3513-3528 (2005).
11. Y. Yasuno, V. D. Madjarova, S. Makita, M. Akiba, A. Morosawa, C. Chong, T. Sakai, K. P. Chan, M. Itoh, and T. Yatagai, "Three-dimensional and high-speed swept-source optical coherence tomography for in vivo investigation of human anterior eye segments," *Opt. Express* **13**, 10652-10664 (2005).
12. R. Huber, M. Wojtkowski, and J. G. Fujimoto, "Fourier Domain Mode Locking (FDML): A new laser operating regime and applications for optical coherence tomography," *Opt. Express* **14**, 3225-3237 (2006).
13. R. Huber, D. C. Adler, and J. G. Fujimoto, "Buffered Fourier domain mode locking: unidirectional swept laser sources for optical coherence tomography imaging at 370,000 lines/s," *Opt. Lett.* **31**, 2975-2977 (2006).
14. D. C. Adler, R. Huber, and J. G. Fujimoto, "Phase-sensitive optical coherence tomography at up to 370,000 lines per second using buffered Fourier domain mode-locked lasers," *Opt. Lett.* **32**, 626-628 (2007).
15. S. W. Huang, A. D. Aguirre, R. A. Huber, D. C. Adler, and J. G. Fujimoto, "Swept source optical coherence microscopy using a Fourier domain mode-locked laser," *Opt. Express* **15**, 6210-6217 (2007).
16. R. Huber, D. C. Adler, V. J. Srinivasan, and J. G. Fujimoto, "Fourier domain mode locking at 1050 nm for ultra-high-speed optical coherence tomography of the human retina at 236,000 axial scans per second," *Opt. Lett.* **32**, 2049-2051 (2007).
17. L. A. Kranendonk, R. Huber, J. G. Fujimoto, and S. T. Sanders, "Wavelength-agile H₂O absorption spectrometer for thermometry of general combustion gases," *Proceedings of the Combustion Institute* **31**, 783-790 (2007).
18. L. A. Kranendonk, X. An, A. W. Caswell, R. E. Herold, S. T. Sanders, R. Huber, J. G. Fujimoto, Y. Okura, and Y. Urata, "High speed engine gas thermometry by Fourier-domain mode-locked laser absorption spectroscopy," *Opt. Express* **15**, 15115-15128 (2007).
19. D. C. Adler, J. Stenger, I. Gorczynska, H. Lie, T. Hensick, R. Spronk, S. Wolohojian, N. Khandekar, J. Y. Jiang, S. Barry, A. E. Cable, R. Huber, and J. G. Fujimoto, "Comparison of three-dimensional optical coherence tomography and high resolution photography for art conservation studies," *Opt. Express* **15**, 15972-15986 (2007).
20. S. H. Yun, C. Boudoux, G. J. Tearney, and B. E. Bouma, "High-speed wavelength-swept semiconductor laser with a polygon-scanner-based wavelength filter," *Opt. Lett.* **28**, 1981-1983 (2003).
21. R. Huber, M. Wojtkowski, J. G. Fujimoto, J. Y. Jiang, and A. E. Cable, "Three-dimensional and C-mode OCT imaging with a compact, frequency swept laser source at 1300 nm," *Opt. Express* **13**, 10523-10538 (2005).
22. M. Y. Jeon, J. Zhang, Q. Wang, and Z. Chen, "High-speed and wide bandwidth Fourier domain mode-locked wavelength swept laser with multiple SOAs," *Opt. Express* **16**, 2547-2554 (2008).
23. S. H. Yun, G. J. Tearney, B. J. Vakoc, M. Shishkov, W. Y. Oh, A. E. Desjardins, M. J. Suter, R. C. Chan, J. A. Evans, I. K. Jang, N. S. Nishioka, J. F. de Boer, and B. E. Bouma, "Comprehensive volumetric optical microscopy in vivo," *Nat. Med.* **12**, 1429-1433 (2006).
24. D. C. Adler, Y. Chen, R. Huber, J. Schmitt, J. Connolly, and J. G. Fujimoto, "Three-dimensional endomicroscopy using optical coherence tomography," *Nat. Photonics* **1**, 709-716 (2007).
25. B. Hofer, B. Povazay, B. Hermann, A. Unterhuber, G. Matz, F. Hlawatsch, and W. Drexler, "Signal post processing in frequency domain OCT and OCM using a filter bank approach - art. no. 644300," *Three-Dimensional and Multidimensional Microscopy: Image Acquisition and Processing Xiv* **6443**, O4430-O4430 (2007).
26. Z. Hu, and A. M. Rollins, "Fourier domain optical coherence tomography with a linear-in-wavenumber spectrometer," *Opt. Lett.* **32**, 3525-3527 (2007).
27. C. Chong, A. Morosawa, and T. Sakai, "High speed wavelength-swept laser source with simple configuration for optical coherence tomography - art. no. 662705," *Proc. SPIE* **6627**, 62705-62705 (2007).
28. V. J. Srinivasan, R. Huber, I. Gorczynska, J. G. Fujimoto, J. Y. Jiang, P. Reisen, and A. E. Cable, "High-speed, high-resolution optical coherence tomography retinal imaging with a frequency-swept laser at 850 nm," *Opt. Lett.* **32**, 361-363 (2007).
29. Y. L. Chen, D. M. de Bruin, C. Kerbage, and J. F. de Boer, "Spectrally balanced detection for optical frequency domain imaging," *Opt. Express* **15**, 16390-16399 (2007).
30. S. Moon, and D. Y. Kim, "Normalization detection scheme for high-speed optical frequency-domain imaging and reflectometry," *Opt. Express* **15**, 15129-15146 (2007).
31. M. Wojtkowski, V. J. Srinivasan, T. H. Ko, J. G. Fujimoto, A. Kowalczyk, and J. S. Duker, "Ultrahigh-resolution, high-speed, Fourier domain optical coherence tomography and methods for dispersion compensation," *Opt. Express* **12**, 2404-2422 (2004).
32. J. A. Izatt, M. R. Hee, G. M. Owen, E. A. Swanson, and J. G. Fujimoto, "Optical Coherence Microscopy in Scattering Media," *Opt. Lett.* **19**, 590-592 (1994).

1. Introduction

Optical coherence tomography (OCT) is a depth resolved biomedical imaging technique, providing high-resolution, cross-sectional and three-dimensional images of tissue microstructure [1]. Recently, the introduction of frequency domain (FD) detection techniques in OCT enabled a dramatic increase in imaging speed, while still maintaining high system

sensitivity [2-4]. In FD-OCT the echo delay time of backscattered light from the sample is measured via spectrally resolved detection of the interference signal between light from the sample and light from a reference arm. Spectrometer based FD-OCT (spectral OCT) systems are already widely used, especially for ophthalmic applications in the 800 nm wavelength range.

Alternatively, the application of FD-OCT systems based on rapidly swept, narrow band light sources (swept source OCT (ss-OCT) / optical frequency domain imaging (OFDI)) [5-11] offers the additional advantages of dual balanced detection, potentially longer ranging depth and higher imaging speeds, compared to spectral OCT. The advent of Fourier domain mode locked (FDML) lasers [12] as light sources for swept source OCT enabled high imaging speeds of up to 370,000 lines/s [13], combined with good phase stability [14] and long ranging depths [12]. Especially because of their high speed, FDML lasers have been applied to numerous applications like optical coherence microscopy (OCM) [15], phase sensitive profilometry [14], retinal imaging in ophthalmology [16], high speed spectroscopy [17, 18] and art conservation studies [19].

However, a general disadvantage of most FD-OCT systems, including FDML based devices, is the requirement to resample or recalibrate the detected OCT interference-fringe signals prior to Fast Fourier transformation (FFT), in order to provide data evenly sampled in optical frequency. Spectrometer based FD-OCT systems and swept source OCT systems based on light sources with polygon scanners [20], exhibit small non-linearity, but they still require correction for the frequency to wavelength relation $\nu = c/\lambda$. Swept source OCT systems based on mechanically resonant filters [21] or typical FDML lasers [12, 22] have an even more pronounced non-linear sweep operation, due to the typically sinusoidal excitation of the piezo controlled fiber Fabry Perot tunable filter (FFP-TF) in the laser cavity.

There are five potential problems in ss-OCT caused by the non-linear time-frequency sweep characteristic. (a) First of all, the numerical recalibration step is usually done in software with the computer by resampling the data after analog-to-digital conversion and it might be challenging to perform this step in real time. OCT with state of the art swept sources generates data rates of more than 0.8 Gbyte/s, a data rate that can hardly be handled with standard personal computers today. Field programmable gate array solutions might solve this problem, but are less flexible and more complex to implement. (b) Second, the oversampled parts towards the edges of the sweep (for a sinusoidal sweep) require system memory but, depending on the recalibration algorithm, carry not proportionally more information. Especially extremely large 3-dimensional datasets, acquired in comprehensive OCT applications [23, 24], are memory critical and efficient use of system memory is desired. (c) A third problem occurs if the recalibration step is performed in hardware. In such systems the recalibration is performed by clocking the analog to digital converter (ADC) with an electronic signal generated by a second interferometer [24], so the sampling is performed with an uneven spacing in time, accounting for the non-linear sweep operation. This avoids the problems mentioned before, however, it requires complex electronic hardware and usually isn't easily adjustable to different operation frequencies of the source. (d) A further problem, common to both, numerical and hardware recalibration, is the noise introduced by the resampling step itself [25] and by phase errors in the recalibration step [10]. The phase errors can lead to a timing jitter, which causes a white noise floor, consequently reducing the dynamic range of the system. (e) Another issue of a non-linear sweep operation is the excess exposure on the tissue. Usually OCT is operated with the maximum permitted power on the sample, in order to achieve the best sensitivity. However, in the oversampled parts of the spectrum, i.e. the parts where the source sweeps slower, the incident light intensity does not increase the sensitivity proportionally, even though it contributes to the total energy per sweep. The power on the sample and with it the sensitivity has to be reduced unnecessarily.

Besides these problems with a non-linear and uncontrolled sweep operation of the source, a highly linear and adaptive time-frequency sweep characteristic may have further advantages. Direct hardware based Fourier transformation of the signal can be envisioned. Such a solution would be faster and at the same time would save a factor of 2 of data transfer bandwidth,

because the amplitude values of the FFT only yield half the number of points. As the transfer speed from the analog-to-digital converter to the system memory or data-storage devices currently limits the OCT performance, such an improvement could be beneficial for future OCT devices. Furthermore an adjustably adaptive time-frequency sweep characteristic can be used to partially compensate sample arm dispersion in real time, without adding material into the reference arm or using complex numerical resampling algorithms. Dispersion compensation by an adaptive time-frequency sweep characteristic will be demonstrated in this paper.

1.2 Quality parameter and error tolerance

In order to analyze and compare the quality of the sweep linearity over a defined temporal range, an appropriate error-parameter has to be defined. The analysis and discussion presented in this work is based on the integrated relative frequency error χ defined as a measure for the sweep linearity:

$$\chi = \sqrt{\sum_{i=1}^N \frac{\Delta v_i(t)^2}{v_i(t)^2 (N-1)}}. \quad (1)$$

Here $\Delta v(t) = v(t) - v_{Lin}(t)$ is the deviation from the perfect linear time-frequency characteristic $v_{Lin}(t)$ that can be calculated by a linear fit to $v(t)$ in the given time interval of interest Δt . Summations are done over all sample points N within Δt .

The main problem with efforts to linearize the time-frequency characteristic of a light source for swept source OCT, or equivalently to linearize the angle dispersion per optical frequency in spectral OCT systems, is the high requirement in linearity. Only very small deviations from a perfectly linear dependence are acceptable, in order to maintain a long ranging depth and a high axial resolution in OCT, if a resampling step should be avoided.

In spectral OCT a concept for linearization of the fringe signals has been demonstrated by correcting the $v = c/\lambda$ relation with an additional prism element [26]. For wavelength swept sources a concept to linearize the sweep characteristic of a laser source based on a polygon mirror filter has been demonstrated, but no OCT imaging without recalibration was performed [27].

Figure 1 shows the linearity requirements. Figure 1 (left) depicts the theoretical optical frequency over time for three different wavelength swept laser sources. We assume three types of frequency swept lasers (sweep rate of 57 kHz each): (i) in the first type, the wavelength filter in the laser is swept perfectly linear in time (black line); (ii) in the second case, an optical bandpass filter is applied with a linear time-wavelength dependence, resulting in a hyperbolic time-frequency characteristic due to the $v = c/\lambda$ relation. Such a situation would represent a grating-polygon scanner type of laser as described in [20]; (iii) the third case would represent a laser with a sinusoidally driven filter in wavelength, as found in swept lasers with mechanical resonant filters [21], sources with piezo actuated fiber based Fabry Perot filters [10] or typical FDML lasers [12, 22]. In all three cases, the filters are assumed to be swept over a range of 175 nm from 1231 nm to 1406 nm. The blue hatched area indicates the region with lasing operation, we assume a range of 100 nm from 1260 to 1360 nm.

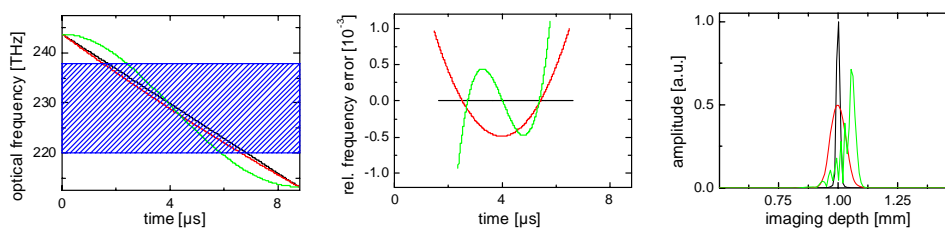


Fig. 1. Left: Temporal evolution of optical frequency for three different sweeps: Linear in frequency (black), linear in wavelength (red) and sinusoidal in wavelength (green). The highlighted, blue region represents the frequency interval of laser activity. Center: Corresponding relative frequency error $\Delta\nu/\nu$, relative to a linear fit in the frequency region where the laser is active. Right: Calculated point spread functions for a spectrum spanning from 1260 nm to 1360 nm and an imaging depth of 1 mm (apodized with a Hanning window).

It should be noticed that the duty cycle (in this example: 175 nm scan range compared to 100 nm lasing) does not influence the linearity of the *wavelength-linear* laser source in contrast to the source that is *sinusoidal in wavelength*. Only for the latter one, a smaller duty cycle can yield better linearity. The lasing range is centered at 1308 nm, the sweep range of the filter is centered at 1318 nm. The chosen 10 nm offset minimizes the non-linearity in case of the sinusoidal sweep, because the slightly non-linear part of the sine can be used to partially cancel the $1/\lambda$ dependence. The sweep duration of the sinusoidal drive waveform equals 3.4 μs . Figure 1 (center) displays the relative frequency error $\Delta\nu/\nu$ for these three sources relative to a perfectly linear evolution over the time range where the laser source is active (1260 nm to 1360 nm - see hatched area). All three curves from Fig. 1 (left) were fitted linearly in the 100 nm lasing range (blue area) and the relative frequency error was plotted. Because the effective sweep speed of the sinusoidal source is higher, the sweep duration is shorter. Naturally, for the perfectly linear evolution (black line) the relative frequency error is zero. Remarkably, for this specific example, the sinusoidally driven source (green) already exhibits a deviation comparable to the wavelength-linear source, as a direct result of the large drive amplitude of the filter (175 nm) compared to the lasing range. The integrated relative frequency error of the sinusoidal driven source (green line) is $\chi_{\text{sine}} = 3.9 \cdot 10^{-4}$, for the wavelength-linear source (red line) $\chi_{\text{lin_lambda}} = 4.3 \cdot 10^{-4}$ respectively.

These values suggest a high degree of linearity. However, considering the point spread functions (PSF) in OCT application (Fig. 1 (right)) at a ranging depth of 1 mm (Hanning window spectral shape), both, the wavelength-linear as well as the sinusoidally driven source, exhibit significant degradation in peak values and in full width at half maximum (axial OCT resolution). This implies that an even better linearity than $4 \cdot 10^{-4}$ is required and an extremely high accuracy and repeatability of the filter is needed.

The approach followed in this paper is to theoretically determine an optimum electronic drive waveform for the piezo actuated fiber Fabry Perot tunable filter, accounting for the mechanical response of the filter, the electronic response of the drive circuit and limitations given by the experimental setup. Constraints and boundary conditions set by the experiment are maximum sweep rate in frequency per second due to electronic bandwidth limitations, maximum permissible power for the filter etc. An experimental setup will be described to measure the frequency dependent mechanical response of the filter. We will discuss and quantify interfering effects, like the mechanical non-linear response of the piezo-electric transducer of the FFP-TF and the repeatability of its mechanical oscillatory motion. The effect of these effects on OCT image quality will be discussed.

2. Experimental setup

2.1 Laser and interferometer setup

Figure 2 (left) shows the experimental setup of the FDML laser used for this study. A semiconductor optical amplifier (SOA, Covega Corp.) with a gain maximum centered at 1310 nm is used as a broadband gain medium. Two isolators (ISO) ensure uni-directional lasing. A fiber based tunable Fabry-Perot-filter (FFP-TF, Lambda Quest, LLC.) provides spectral filtering. The filter is driven periodically with a sweep rate of 56.902 kHz. Arbitrary waveforms can be applied to the filter by a digital function generator and a power amplifier as waveform driver. The AC-signal from the programmable function generator is amplified and superimposed to an adjustable DC-voltage to set the sweep's center wavelength. In order to synchronize the second harmonic of the optical roundtrip time of the light circulating in the laser cavity with the FFP-TF tuning frequency, a 3.6 km long fiber is used in the resonator. The design is based on a sigma-ring configuration. The circulator (CIR) couples light from the ring into the linear part and returns it back into the ring. After forward propagation through the 3.6 km length of fiber, light is backreflected by a Faraday mirror (FRM) and the polarization state is rotated by 90°. Thus, birefringence effects in the 3.6 km fiber are cancelled during back-propagation. Overall 75% of the laser power is coupled out of the laser resonator by two 50/50 couplers. One output is used for analyzing the laser with a Mach-Zehnder interferometer (MZI) in a dual balanced configuration with a detection bandwidth of 350 MHz. The other output is post-amplified with a second SOA and is used for OCT imaging. The two outputs were not used simultaneously. During imaging it was not necessary to monitor the laser with the MZI. Polarization controller paddles (PC) are used to control the polarization state of light entering the SOA (~16dB polarization dependent gain).

2.2 Filter response

One major issue in applying non-sinusoidal drive waveforms at high frequencies (several 10 kHz) to the FFP-TF is the non-flat phase and amplitude response of the filter and the electronic drive circuitry. For low frequencies (<1 kHz) far away from mechanical or electronic resonances, this response function is flat, which means, a certain applied electronic drive waveform will cause the filter to tune in exactly the same time evolution as the applied voltage. However, at higher frequencies near mechanical resonances, the higher harmonics of the drive waveform exhibit a different amplitude and phase response. This means, the mechanical response of the filter will dramatically deviate from the applied drive waveform. The frequency dependent response function of the filter has to be accounted for.

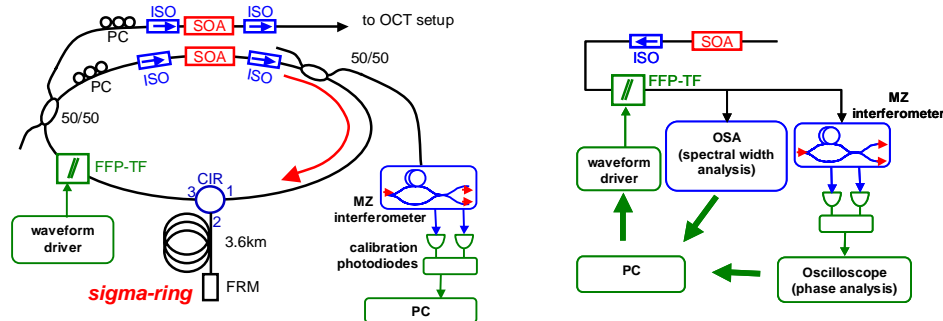


Fig. 2. Left: Schematic diagram of the FDML laser. Right: Experimental setup of the automated measurement of the FFP-filter response function.

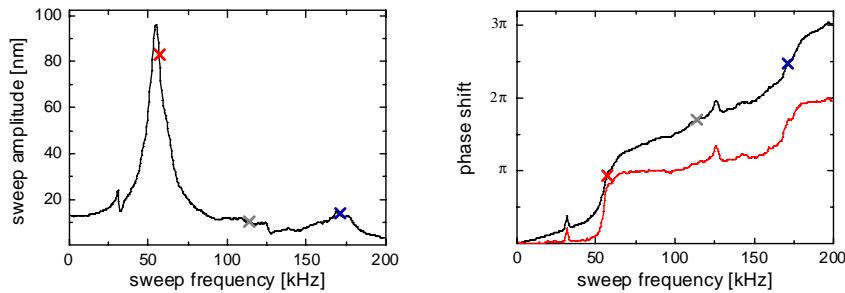


Fig. 3. Left: Measured optical sweep amplitude versus sweep frequency for a sinusoidal excitation of the filter with a constant drive amplitude and DC-offset. Right: Phase shift versus sweep frequency for the same excitation. The black curve represents the phase shift due to the response of both, electrical circuitry and the FFP-filter. The red curve shows the phase shift as a result of the mechanical and electrical response of the FFP-filter only. The crosses in both plots indicate the measured data values for the first (red), second (grey) and third (blue) harmonic of the sweep frequency in the chosen FDML configuration.

In Fig. 2 (right) a setup for the computer controlled measurement of the response is presented. A sinusoidal drive waveform with an amplitude of approximately 2.4 V (after power amplifier) is applied to the filter. The drive frequency is successively increased from 1 kHz to 199 kHz with a 500 Hz increment. In order to analyze (a) the amplitude response of the filter (including electrical circuitry), the amplified stimulated emission (ASE) of an SOA is used as light source and the spectral width of the transmitted intensity is analyzed with an optical spectrum analyzer (OSA). The result is read out with a personal computer (PC) and the measurement is repeated for the next drive frequency. The frequency dependent amplitude response is plotted in Fig. 3 (left).

To analyze (b) the phase response of the filter, the transmitted light is coupled into a MZI and the interference signal is measured with a differential detector. The signal is digitized with a high speed ADC and a Hilbert transformation enables the localization of the turning points of the filter in time. Thus, the phase shift of the mechanical oscillatory motion of the filter with respect to the applied sine wave can be obtained for each scan frequency automatically (black curve in Fig. 3 (right)). The phase response of the electronic circuits is directly measured by comparing the phase shift of the electronic drive waveform from the function generator with the voltage measured directly at the filter. The phase shift value is directly read out from the oscilloscope. From these two measurements, the response of the filter itself can be extracted. In Fig. 3 (right) the red curve indicates the phase shift due to the phase response of the filter only.

In the amplitude and the phase plot, two distinct resonances can be identified at 55 kHz and at its third harmonic at 169 kHz (resonance peaks in Fig. 3 (left) and phase jumps in Fig. 3 (right)). The pronounced peak around 55 kHz represents the fundamental axial resonance of the filter and an amplitude gain of a factor of 8 can be observed. It is also interesting to note that the third harmonic at about 169 kHz exhibits an amplitude response similar to the response at very low frequencies. To limit the amount of electric power to drive the filter, the fiber length in the FDML resonator was adjusted such that the first order FDML sweep frequency of 56.902 kHz (red crosses in Fig. 3) is close to the main resonance peak. Furthermore the third order harmonic (170.706 kHz, blue crosses in Fig. 3) lies in the vicinity of the second resonance peak. The relatively fast roll off for frequencies above 180 kHz suggests that the harmonics of the applied drive waveform should be limited to <180 kHz for this filter. Thus, driving the filter with the fourth or even higher harmonic is hardly practicable for a fundamental of 55 kHz and this type of filter. The different amplitude response values of 40 nm/V, 4.9 nm/V and 6.8 nm/V as well as the phase shift of 0.93π , 1.70π and 0.46π for first, second and third harmonic have to be accounted for when an optimized drive waveform is applied. Once an optimum drive waveform is determined, the amplitudes for the harmonics

are divided by the respective amplitude values of the response function, the phases are subtracted.

3. Semi-analytical / non-iterative approach

3.1 General considerations

With the known filter response function, an optimized drive waveform has to be found within the physical constraints.

A first simple approach to realize a linear time-frequency characteristic could be to apply a periodic AC-voltage with a triangle or sawtooth waveform to the filter. Obviously, this would be a poor solution, due to the frequency dependent response function of the filter. If the waveform would be corrected for the filter response, the excitation of the high harmonics would result in excessive thermal load to the filter. Furthermore, even a perfectly linearly driven PZT would not yield a linear time-frequency characteristic because the elongation of the FFP-resonator is proportional to wavelength, so due to the $v=c/\lambda$ relation only a sweep, linear in wavelength, would be generated.

In order to find the optimum drive waveform and quantify the error, we will choose several parameters typical for FDML lasers in OCT. First, the wavelength interval where the laser is active has to be determined. The spectral bandwidth should be 100 nm, where the interval of laser operation ranges from 1260 nm to 1360 nm (centered around the gain maximum of the SOA at 1310 nm).

Second, we will choose an appropriate sweep range of the filter. On the one hand, it makes sense to choose a sweep range that exceeds the lasing interval of 100 nm significantly which already improves the linearity in the interval of laser activity. On the other hand, there are several reasons that argue against an excessively increased sweep range. (1) The maximum mechanical stress on the PZT should not be exceeded in order to maintain good long term stability. (2) The non-linear mechanical response will increase at very high drive amplitudes and (3) the duty cycle and the sweep duration become too short, increasing requirements for the ADC. A good compromise for the presented setup is a sweep range of approximately 175 nm. As discussed before, in order to limit the amount of electric energy dissipation in the filter, another necessary restriction is to limit the number of harmonics that should be applied. In our case we focus the analysis to three harmonics.

3.2 Semi-analytical / non-iterative approaches

In this section, a semi-analytical approach to find the optimum waveform is presented. Considering just the first three harmonics, the time-frequency characteristic is given by:

$$v(t) = \frac{c}{\lambda_0 + A_1 \cdot \sin(\omega t - \varphi_1) + A_2 \cdot \sin(2\omega t - \varphi_2) + A_3 \cdot \sin(3\omega t - \varphi_3)} \quad (2)$$

Here, λ_0 is the wavelength offset, i.e. the center wavelength of the sweep, c is the speed of light in vacuum, A_i represent the amplitudes of the respective components in wavelength; φ_i are the different phases of the three harmonics respectively and $\omega = 2\pi \cdot 56.902$ kHz is the drive frequency of the filter.

3.3 Simple Fourier expansions

The most obvious approach to determine the unknown parameters would be to perform a Fourier expansion of a triangular time-frequency characteristic (series of hyperbolic branches in wavelength) $v_{\text{lin}}(t)$ with a wavelength offset λ_0 and a sweep range A . All Fourier-components up to third order will be considered, higher orders are neglected, yielding the A_i s and φ_i s. A_1 is chosen such that $v(t)$ exhibits a sweep range of 175 nm.

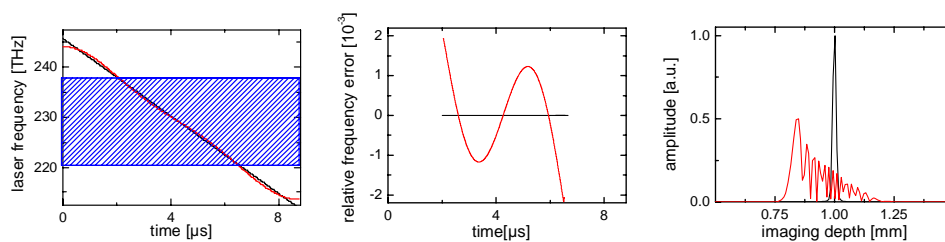


Fig. 4. Left: Temporal evolution of optical frequency. Black: Sweep linear in frequency. Red curve: Waveform with first three Fourier components. The highlighted, blue region represents the frequency interval of laser activity. Middle: Corresponding relative frequency deviation $\Delta v/v$ from a linear fit in the region of laser activity. Right: Calculated PSFs for a spectrum spanning from 1260 nm to 1360 nm and an imaging depth of 1 mm (apodized with a Hanning window).

The wavelength offset λ_0 is chosen analytically such that the inflection point of the time-frequency characteristic $v^{(1)}(t) = c/\lambda^{(1)}(t)$ (case $A_2=0$ and $A_3=0$ in Eq. (2)) is centered in the frequency range of laser activity, reducing non-linearity induced by the $v = c/\lambda$ relation ($\partial^2 v^{(1)}(t_{in})/\partial t^2 = 0$ and $c/v^{(1)}(t_{in}) = 1308$ nm). Figure 4 shows the results of this approach. Figure 4 (left) depicts the triangular linear time-frequency characteristic $v_{lin}(t)$ for a perfectly linear sweep (black curve) and the resulting frequency representation of the discrete Fourier series of $c/v_{lin}(t)$ up to third order with a sweep range of 175 nm (red curve). The inflection point of $v^{(1)}(t)$ has been calculated to be 10 nm below sweep center wavelength. Therefore λ_0 is chosen to be 10 nm larger than 1308 nm, yielding 1318 nm. The two curves were fitted linearly in the 100 nm lasing range (hatched blue area). The relative frequency errors $\Delta v/v$ (relative deviation from fit) are drawn in Fig. 4 (center). The integrated relative frequency error χ as a measure for the non-linearity induced by neglecting the higher order ($n>3$) of Fourier components, has a value of $9.41 \cdot 10^{-4}$. Remarkably, this value of χ even exceeds the integrated relative frequency error resulting from a sinusoidal drive waveform (sweep range 175 nm) by a factor of more than 2 ($\chi_{sine}=3.9 \cdot 10^{-4}$, see section 1). The result for OCT applications is depicted in Fig. 4 (right), where the related PSFs are shown for an imaging depth (delay in Michelson interferometer) of 1 mm (Hanning window spectral shape).

The full width at half maximum (axial OCT resolution) as well as the height of PSF exhibit a considerable degradation compared to the PSF of the perfectly frequency-linear sweep. This means that by simply applying the first 3 harmonics of a perfectly linear waveform in frequency, an unacceptably poor linearity with even higher error than a sine waveform is generated.

A simple explanation for the poor linearity is based on the fact that a Fourier series converges in quadratic mean but not pointwise. This means, the Fourier expansion is an optimization for the waveform over the whole cycle period. However, since high linearity is not required over the entire period, but only during a relative small temporal interval, adding higher orders might even degrade linearity in the desired part of the sweep, though improving the deviation over the whole period in total. Particularly considering the fact that high linearity is only needed for either forward or backward sweep, but not for both, performing a Fourier expansion and skipping higher orders is not a good approach to find the optimum waveform.

4. Numerical methods A: constant sweep duration

As detailed above, the method of a simple Fourier expansion doesn't yield an acceptable solution for a linear time-frequency characteristic. Thus, we will focus on a numerical, iterative optimization process. For the non-linear fit process, an optimization parameter (error parameter) has to be defined that describes the quality of linearity in the predetermined

frequency interval (1260 nm to 1360 nm) of laser activity. We will use the integrated relative frequency error introduced in section 1 as error parameter. To avoid divergence of the optimization algorithm, certain constraints and boundary conditions have to be set, usually given by the experiment.

A very typical situation for OCT applications is a certain desired sweep duration. This could be the case for buffered FDML setups [13], where a defined integer fraction of the roundtrip time is desired. Another example where optimization with a constant sweep duration can make sense, is a condition where the maximum sampling rate of the ADC and the minimum ranging depth set a lower limit for the sweep duration, in order to enable a certain number of sampling points per sweep (A-scan in OCT).

With the method of constant sweep duration, only solutions are considered which provide lasing over a certain time range within each drive cycle. The main advantage implementing an optimization algorithm with the method of constant sweep duration is that the lasing duration during a drive cycle is fixed and known. So the numerical treatment simply integrates the error over a certain time range for a drive cycle.

Including only three harmonics, there are a total of seven parameters that have to be optimized: the amplitudes of the first three orders A_1 , A_2 , A_3 , the phases of the first three orders φ_1 , φ_2 , φ_3 and the wavelength offset λ_0 . Since sweep duration and frequency interval are given, two boundary points in the time-frequency domain can be defined. We can assume a linear sweep from high to low frequency. Hence, the integrated relative frequency error χ can be calculated as described in section 1. χ has to be minimized finding the ideal parameter combination by a non-linear numeric fit procedure.

In order to gain more insight into the optimization problem and the dependence of the error on the parameters, first, second, third order harmonic amplitude and the wavelength offset were kept invariant as fixed parameters during optimization. A nonlinear fit algorithm is applied to optimize the remaining three variables (first, second and third order harmonic phase) for each given parameter combination. This process is repeated for different values of first, second and third harmonic amplitude and the offset in form of a raster scan. With this approach, the minimized χ can be plotted dependent on different parameters in form of error maps.

Figure 5 shows such an error map from the results of an exemplary numerical optimization with a constant sweep duration of 4.385 μ s. The chosen sweep duration equals a quarter of the drive cycle duration for $f_{\text{drive}} \approx 57$ kHz, which would yield a 228 kHz repetition rate for a 4x buffering scheme [13]. In order to ensure that the sweep range is close to the experimentally reasonable value of 175 nm, the amplitude of the first order harmonic is set to 87.5 nm in this example. The amplitude of the second order harmonic and the third order harmonic were stepped with 0.6 % increments (relative to the amplitude of the first order harmonic) ranging from 0 % to 30 % and 0 % to 12 %, respectively. The wavelength offset is changed in steps of 5 nm ranging from 1265 nm to 1355 nm. Figure 5 shows the minima of the integrated relative frequency errors acquired by optimization with different wavelength offsets for each combination of second and third order harmonic amplitudes (Matlab V7.4.0. function "fmincon").

The first interesting feature is that for the given parameter set an absolute minimum of χ can be found for $A_2 = 13.2\% \cdot A_1$ and $A_3 = 0.6\% \cdot A_1$ (Fig. 5, black cross) with the corresponding phases $\varphi_1 = 0.024 \pi$, $\varphi_2 = 0.980 \pi$ and $\varphi_3 = 1.324 \pi$. The minimum of χ corresponds to a wavelength offset $\lambda_0 = 1315$ nm, indicating that the nonlinearity induced by the $v = c/\lambda$ relation is reduced by choosing an offset slightly above the center wavelength of laser activity of 1308 nm (see section 3).

The value of χ in this error map ranges from $3.232 \cdot 10^{-3}$ to the minimum of $3.346 \cdot 10^{-5}$, which is approximately one order of magnitude improvement over wavelength linear sources (see section 1). It should be noted that the result obtained for the chosen parameter set leads to a minimum of χ located in an area of rather high amplitudes of second harmonic, resulting in

relatively high drive voltages due to the weak response of the filter. Solutions with smaller amplitudes of the higher harmonics would be preferred.

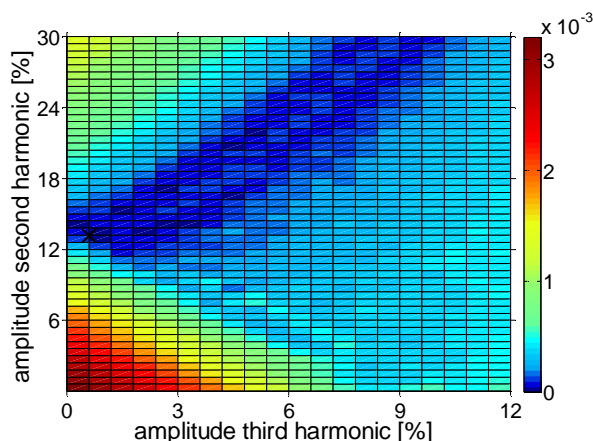


Fig. 5. Results of numerical optimization with a constant sweep duration of 4.385 μs and a first order harmonic amplitude of 87.6 nm. The frequency error is depicted versus the amplitudes of second and third order harmonic (in percent of first order harmonic).

Simulations with differing values of first order amplitude A_1 (from 82.5 nm to 102.5 nm) result in similar error plots. However, higher values of A_1 yield smaller minimum values for χ , so a compromise between electro-mechanical load and required minimum error has to be made.

5. Numerical methods B: arbitrary sweep duration

In cases where the sweep duration is not pre-determined and in order to get a general understanding of the linearization problem, a more flexible approach is applied without the constraint to a constant sweep duration. This method provides full access to sweep duration, wavelength offset and phases for locally optimized solutions.

Again, the integrated relative frequency error χ is used as optimization parameter that has to be minimized adjusting the amplitude and phase parameters of the three harmonics, including wavelength offset. In contrast to the previously presented approach, a predetermined evaluation interval in the time-frequency domain cannot be set.

Therefore, in order to calculate χ , a search algorithm has to evaluate the temporal interval reaching from 1260 nm to 1360 nm (lasing range) and a linear fit to the curve serves as an ideally linear function to determine the error χ . Thus, this optimization approach is computationally more expensive compared to the approach of fixed sweep duration and requires more computing time.

A simultaneous optimization of all parameters at the same time is not performed for the reason described in the previous chapter. Furthermore, here χ is getting arbitrarily small for increasing A_1 as well as for increasing A_2 and A_3 , the problem diverges towards higher amplitudes. So A_1 , A_2 , A_3 and the wavelength offset λ_0 are kept invariant during optimization and are changed in a reasonable raster to plot an error map. ϕ_2 and ϕ_3 are optimized with a nonlinear optimization algorithm (Matlab V7.4.0 function “fminsearch”) for each parameter configuration. Since the time interval of laser activity is found by the search algorithm, the absolute phase is not essential and one can arbitrarily chose the phase of the first harmonic ϕ_1 to 0.

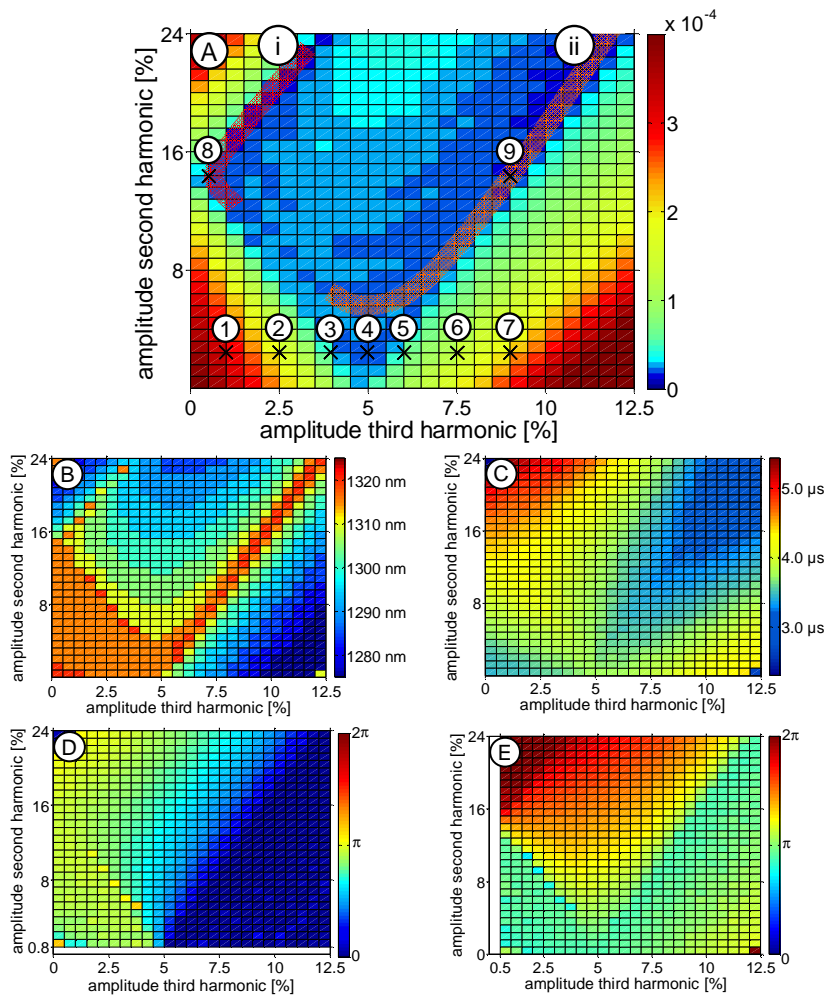


Fig. 6. Results of numerical optimization with arbitrary sweep duration for a first order amplitude of 87.5 nm. A: Frequency error versus the amplitudes of second and third order harmonic (in percent of first order harmonic). The corresponding acquired distributions of the wavelength offset (B), sweep duration (C), second harmonic phase (D) and third harmonic phase (E).

In Fig. 6 the results of the “arbitrary sweep duration” simulation are shown. Just like in the simulation of section 4, A_1 is set to 87.5 nm, consistent with the considerations in section 1. The raster is chosen such that A_3 ranges from 0 % to 12.5 % of A_1 in 0.5 % steps and A_2 is adjusted from 0 % to 24 % of A_1 in 0.8 % steps. The wavelength offset λ_0 is changed from 1275 nm to 1345 nm in 5 nm steps. In Fig. 6(A) the minimum of the integrated relative frequency errors χ acquired by optimization of φ_2 and φ_3 for the different wavelength offsets λ_0 is depicted in a surface plot versus the second and third order harmonic amplitudes. Figure 6(B) shows the related plot illustrating the optimum λ_0 for the same simulation. The corresponding distributions of sweep duration, optimum phase of second harmonic and optimum phase of third harmonic are presented in Fig. 6(C), Fig. 6(D) and Fig. 6(E) respectively.

Figure 6(A) shows that the smallest values for χ are found in a U-shaped “valley of minima”, where the two branches (label “i” and “ii”) are spanning a square of relatively small χ (blue area in the surface plot). Outside this square χ is considerably larger. In contrast to the

approach with fixed sweep duration, here χ is getting smaller for higher amplitudes. The absolute minimum of χ within these parameter-limits is the local minimum at the end of the branch i) with $\chi = 2.373 \cdot 10^{-6}$. Nevertheless, simulations with an extended range of A_2 and A_3 indicate that even smaller values of χ can be achieved in the branch ii). Branch ii) is unlimited towards higher amplitudes and is getting broader for higher A_2 and A_3 . Interestingly, like in the previous section, regions of minimal values of χ correspond to a wavelength offset λ_0 of ~ 1315 nm, indicating that the nonlinearity induced by the $v = c/\lambda$ relation can be reduced by choosing an offset slightly above the center wavelength of laser activity of 1308 nm (1318 nm for $A_1 = 87.5$ nm). Thus, the two branches can also be identified in Fig. 6(B). The plot of the related sweep durations in Fig. 6(C) indicates that the optimum sweep duration in vicinity of the upper branch equals about 4.5 μ s. This fact is consistent with the simulation of constant sweep duration (4.385 μ s), yielding a minimal χ in the same area of the error map. On the other hand, the sweep duration along the lower branch ranges from about 3.6 μ s to 2.9 μ s in the error map and is further decreasing for higher amplitudes (improved linearity, but shorter sweep duration yielding a very asymmetric time-frequency characteristic). By analyzing Fig. 6(C) and Fig. 6(A), one can determine which areas in the error map yield low values of χ for a specific sweep duration. Therefore the ansatz of arbitrary sweep duration offers a more general result than the approach presented in chapter 4. Simulations with differing values of A_1 are resulting in qualitative similar error maps. Nevertheless, the values of χ can be made arbitrarily small by increasing A_1 , the problem diverges towards higher amplitudes.

Using these error maps, the ideal operation point for the filter can be chosen within the experimental constraints. To study the feasibility of OCT with k-space linear FDMML, here a specific sweep duration is not mandatory. We will focus on regions on the map with small values of A_2 and A_3 in order to avoid very high driving voltages for the higher harmonics, preventing excessive electro-mechanical stress on the piezo of the FFP-TF. Hence, the operation point will be set in the lower branch in the region near zero 2nd order amplitude ($A_2 = 2.4$ % and $A_3 = 5$ %; indicated as point 4 in Fig. 6(A)). This solution is a good compromise between having small amplitudes and sufficient linearity. The expected value of χ is $2.307 \cdot 10^{-5}$, this is 20x smaller than the equivalent χ , achieved with a sinusoidal or linear time-wavelength sweep characteristic (see section 1).

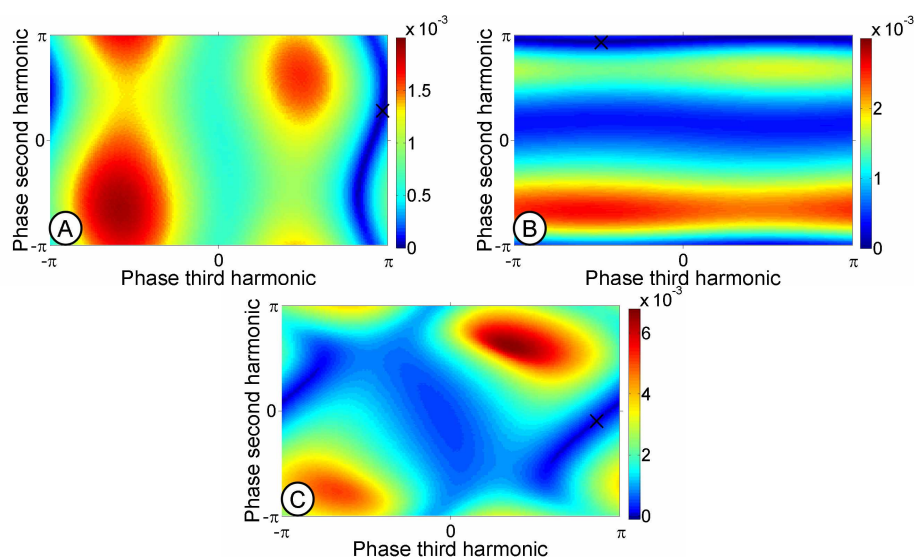


Fig. 7. Frequency error χ versus phase of second and third order harmonic for three characteristic data sets corresponding to point 4 (plot A), point 8 (plot B) and point 9 (plot C) in Fig. 6. The absolute minimum of each plot is indicated with a cross.

In order to understand the dependence of the integrated frequency error on the phases of second and third harmonic, Fig. 7 shows three surface plots where the calculated χ is plotted versus ϕ_2 and ϕ_3 (raster of 2°) for the parameter combinations representing three characteristic points in the error map (Fig. 6(A), points number 4,8,9). The absolute minimum of each plot is indicated with crosses. Figure 7(A) depicts the chosen operation point (point 4) with relative small values for $A_2=2.4\%$, $A_3=5\%$ and an ideal $\lambda_0=1315$ nm. Figure 7(B) is illustrating a case with high $A_2=14.4\%$, small $A_3=0.5\%$ and ideal $\lambda_0=1310$ nm (point 8). Finally Fig. 7(C) demonstrates a case with high $A_2=14.4\%$, high $A_3=9\%$ and ideal $\lambda_0=1320$ nm (point 9). In all three cases the domain of high linearity in the plots is an S-shaped blue curve but the orientations differ. Considering point 4, the range of ϕ_3 yielding small χ is much smaller than the corresponding range of ϕ_2 whereas the situation is inverse at point 8.

There are two conclusions that can be drawn from Fig. 7: On the one hand, it becomes clear that χ is critically dependent on the phases, underlining the benefit of numerical simulation to predetermine the best point of operation. On the other hand, it can be seen that for a given point in the error map, there is more than one good solution yielding a sufficiently small χ , because χ is only slightly varying over the s-shaped curve. For the waveform with the smallest error, the phases are most critical.

6. Experimental results and comparison to theory

6.1 Measurements confirming numerical simulation

In the following paragraph it will be demonstrated that the results obtained with the numerical approach presented before can be used to successfully realize a k-linear FDML laser, i.e. an FDML laser with highly linear time-frequency sweep operation. The experimental data will support the fact that the filter can be driven with sufficient repeatability for OCT without a resampling or recalibration step. Effects like non-linear coupling, parasitic mechanical oscillations and drift are sufficiently small at the demonstrated operation point. A comparison between the experimentally achieved linearity and that predicted by theory will be given.

In order to gain information about the time-frequency characteristic of the FDML-laser, the interference signal obtained from a MZI (dual balanced detection (see Fig. 2 (left))) is analyzed by Hilbert transformation. To adjust the experimental parameters according to the simulation, the wavelength range of laser activity is monitored with an OSA and adjusted by varying the SOA current. In our case, an SOA current of ~ 350 mA is applied, resulting in the desired lasing range from 1260 nm to 1360 nm (10 dB drop in intensity on OSA). The AC-voltage amplitude of the first order harmonic is adjusted such that A_1 equals 87.5 nm. The wavelength offset λ_0 is set to the appropriate value by tuning the applied DC-voltage of the piezo of the FFP-TF. Both, first order harmonic amplitude A_1 and wavelength offset λ_0 , can directly be monitored with the OSA. In order to derive the relative frequency error $\Delta\nu/\nu$ and calculate the integrated frequency error χ , a 100 times averaged interference signal is recorded with the oscilloscope and a Hilbert transformation is performed at the part of the signal where the envelope drop is smaller than 10 dB (≈ 1260 nm to 1360 nm). The accumulative phase evolution of the interference fringes can be extracted and fitted linearly. So $\Delta\nu/\nu$ and χ result from the phase deviation $\Delta\phi$ (phase of the electronic beat signal from the MZI), assuming a wavelength range of the analyzed data from 1260 nm to 1360 nm and setting all ν_i s in Eq. (1) to a center frequency $\nu_M = c/1310$ nm.

In order to verify the numerical simulation in vicinity of the chosen operation point in the error map of Fig. 6(A), an analysis of the interference signal for an arm-length mismatch of the MZI of 2 mm corresponding to the points 1 to 7 was performed. Therefore, the corresponding voltage amplitudes resulting in an A_2 of $2.4\% \cdot A_1$ and the respective values of A_3 have to be applied, accounting for the amplitude response of the filter (see paragraph 2).

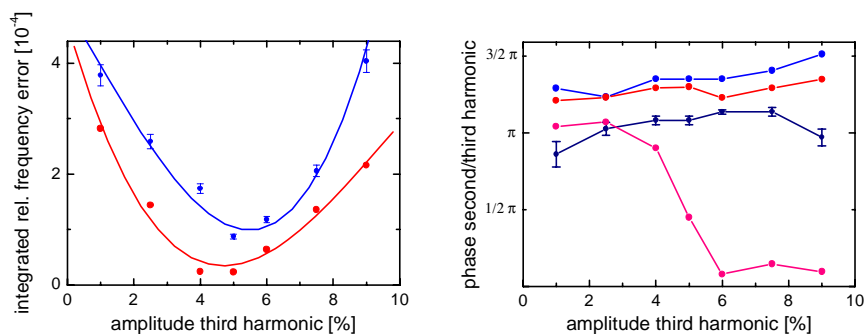


Fig. 8. Left: Frequency error χ from numerical simulation (red, points 1 to 7 in Fig. 6(A)) compared to the measured frequency error for identical parameters (blue). Right: Corresponding phases of second (red points) and third (pink points) harmonic phase from simulation and experimentally determined optimal phases of third order harmonic (blue points) and second order harmonic (dark blue points).

The wavelength offsets are adjusted to the expected values of the theory respectively (1315 nm for point 1 to 4, 1310 nm for point 5, 1295 nm for point 6 and 1285 nm for point 7). In each case, prior to signal acquisition, the phase of second harmonic and third harmonic AC-voltage (with respect to first harmonic) is optimized online by minimizing the width and simultaneously maximizing the height of the Fourier transform of the fringe signal on the oscilloscope.

In Fig. 8 (left) the measured integrated frequency error χ of the corresponding interference signals is plotted versus third order harmonic amplitude A_3 (blue). Here, the dominant error is caused by the inaccuracy in the determination of the wavelength range. The red points indicate the values of χ expected from simulation. Figure 8 (right) presents the expected optimum phases of the second and third order harmonic AC-voltage according to the simulation (red points: third order harmonic phases; pink points: second order harmonic phases). The phases are corrected for the phase shift due to the filter response. The optimum phases for second and third order harmonic found in experiment are plotted as blue line (third order harmonic phase) and as dark blue line (second order harmonic points). The error bars indicate the error for the second order harmonic phase, the third order harmonic error is too small to be drawn.

The qualitative and quantitative good agreement between theory and experiment in Fig. 8 (left) confirm that the filter motion can be predicted theoretically very well. Parasitic mechanical oscillations, drift etc. are small enough to not significantly affect the measured coherence properties of the source. The integrated relative frequency errors χ , obtained from the measurement, are comparable to those predicted by the simulation, the local minimum in the range from 5 % to 6 % of third harmonic amplitude can clearly be identified.

6.2 Discrepancy between theory and experiment – non-linear coupling

However, besides the good agreement in *total errors*, discrepancies in theoretically and experimentally optimized *phase* can be identified in Fig. 8 (right), especially for the last four amplitude points. To understand this observation, one has to recall the phase maps of Fig. 7, demonstrating that for the parameter set of a given point on the error map, there are several phase combinations (S-shaped curve) yielding almost identical error values χ .

In the vicinity of the chosen operation point, the range of second order phase of this S-shaped curve is much larger than the third order phase range. So equivalent χ can be achieved, reducing third order phase as well as second order phase down to the predicted values. Thus, due to small inaccuracies in experimentally chosen parameters, like errors in the phase response measurements of the filter, the true minimum might vary along this S-shaped curve.

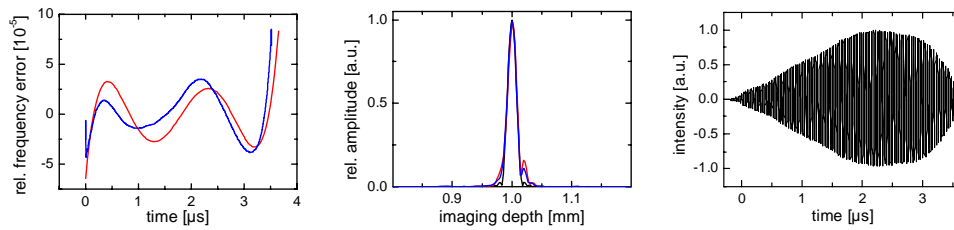


Fig. 9. Left: Optimum relative (instantaneous) frequency error curve theoretically predicted by numerical simulation (red), compared to the measured curve (blue, wavelength of 1260 nm at $t = 0$); Center: Corresponding PSFs (Hanning window) for theoretical solution (blue), measured in the experiment (red) and a perfectly linear time-frequency characteristic (black). Right: Interference signal (original envelope).

In this measurement the wavelength offset was strictly set to the values given by the simulation. However, if λ_0 is slightly increased, the linearity can be improved, yielding smaller values of χ . This particularly applies for the last three points. Here, the predicted decrease of optimum offset from 1310 nm to 1285 nm could only be observed to a minor degree. Furthermore, the two polynomial fits (third order) in Fig. 8 (left) indicate that the minimum of the experimental error curve is shifted to higher amplitudes (absolute deviation of approximately 1 %). This result is also underlined by the following comparison.

In Fig. 9 (left, blue curve) the measured evolution of the relative frequency error $\Delta\nu/\nu$ is plotted for the optimum parameter combination found in the experiment along the points number one to seven from Fig. 6(A). So only the amplitude of the second order harmonic was kept constant, the other parameters were optimized in the experiment. Additionally, the relative frequency error of the optimum parameters expected from the simulation (point 4, red curve) is drawn. In agreement with the findings before, the best solution can be found for a larger amplitude of third order harmonic corresponding to an $A_3 = 6\%$ instead $A_3 = 5\%$. The optimum offset is about 1320 nm instead of 1310 nm. The optimum phase of the second order harmonic is 1.138π , the corresponding phase of the third order harmonic is 1.351π respectively. As can be seen in Fig. 9 (left) the two solutions are in very good agreement, yielding nearly the same characteristic and sweep duration (3.5 μs instead of 3.6 μs expected from simulation). The resulting integrated frequency error of the experimental data is $2.11 \cdot 10^{-5}$ and therefore in very good agreement with the optimal χ of $2.31 \cdot 10^{-5}$ predicted by simulation.

In Fig. 9 (center) the corresponding PSFs are plotted for a Michelson interferometer with 1 mm imbalance in arm lengths (2 mm for a MZI) and a spectral envelope shaped to a Hanning function from 1260 nm to 1360 nm.

Both, the measured PSF (blue) and that calculated from the simulation result (red) are in very good agreement with the PSF of a perfectly linear time-frequency characteristic (black). Comparing the PSFs of Fig. 9 (center) to the PSFs of Fig. 1 (right) for a sinusoidal sweep and a linear time-wavelength characteristic, a dramatic improvement can be seen. Figure 9 (right) shows the corresponding measured fringe signal (no apodization, original envelope) for the presented solution, where the asymmetric envelope of the fringe signal can be seen.

In summary, besides the very good agreement between the absolute error values of theory and experiment, a slight deviation in phase and offset can be observed. The observed discrepancies are probably due to the nonlinearity in the mechanical response of the filter, meaning that the first order harmonic amplitude also leads to contributions in second or third order harmonic amplitude.

6.3 Required accuracy and procedure to set k -space linear FDML

Figure 10 shows the critical dependence of the quality of linearity on the adjusted phase. The interference signal is recorded with a MZI at a 2 mm arm length mismatch (corresponding to 1 mm imaging depth) and the parameter-set of the optimum operation point described above.

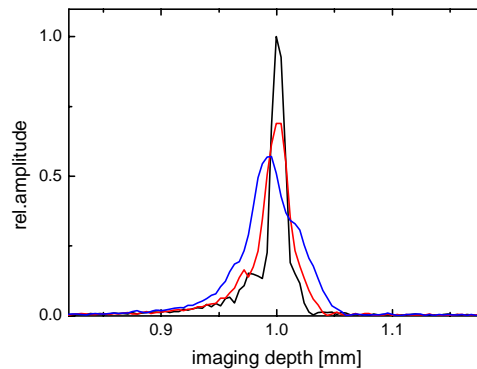


Fig. 10. PSFs calculated directly from the measured fringe signals (no apodization). The black curve represents an optimum parameter adjustment, the red curve was obtained with the phase of third order harmonic detuned by 1.7° with respect to the first order harmonic phase, the blue curve with the phase of the third order harmonic detuned by 3.3° .

The optimum PSF is plotted as black curve and the measured PSFs with slightly detuned phases of 5° (1.7° of first harmonic phase) and 10° (3.3° of first phase) are plotted as red and blue lines respectively. The detuning introduces timing errors of 80 ns and 166 ns respectively. It can be seen in Fig. 10 that width and height of the PSFs significantly degrade, even for such small phase deviations. These findings are again in good agreement with the simulations in Fig. 7(A).

In conclusion, the measurements and comparison to theory in paragraph 6 suggest that a viable approach for a successful linearization of the sweep operation can consist of the following four steps: (1) The complex (amplitude and phase) filter response function of the FFP-TF filter is measured with a setup comparable to the one presented in section 2. (2) Error maps plotting the integrated error dependent on the amplitudes A_i are calculated with a numerical fit procedure. (3) A good operation point within the experimental constraints is chosen on the error map, with an error as small as necessary and drive amplitudes as small as possible. (4) The system is set to amplitude and phase values predicted by the simulation and a fine adjustment of the offset center wavelength and the phases is used for final optimization, using online feedback from an oscilloscope. Possible small discrepancies between theory and experiment due to effects like for example non-linear coupling can be corrected. Usually the width of the PSF generated by the built in FFT-function of an oscilloscope is sufficient. With this method, an integrated frequency error of $\chi = 2.11 \cdot 10^{-5}$ for a sweep duration of $3.5 \mu\text{s}$ was achieved which is about a factor of 20x improvement compared to a wavelength-linear or sinusoidal sweep characteristic (chapter 1). For the online analysis on the oscilloscope a simple, inexpensive fixed MZI, built of two fusion spliced 50/50 couplers, could be applied.

6.4 OCT performance

In order to examine the performance of k-space linear FDML for OCT, we analyze the PSF roll off over imaging depth in OCT application. The optimum waveform presented above is applied to the filter and the interference signal is acquired with the MZI for several delays. In Fig. 11 (left) the resulting PSFs are plotted versus corresponding image depth (image depth = $0.5 \times$ difference in MZI arm lengths). The average output power of the laser is 9.2 mW. It should be noted that here no recalibration or resampling step and also no spectral reshaping or apodization was performed prior to FFT.

Figure 11 (right) shows the logarithmic representation, adjusted such that the peak values of the PSFs represent the measured sensitivity.

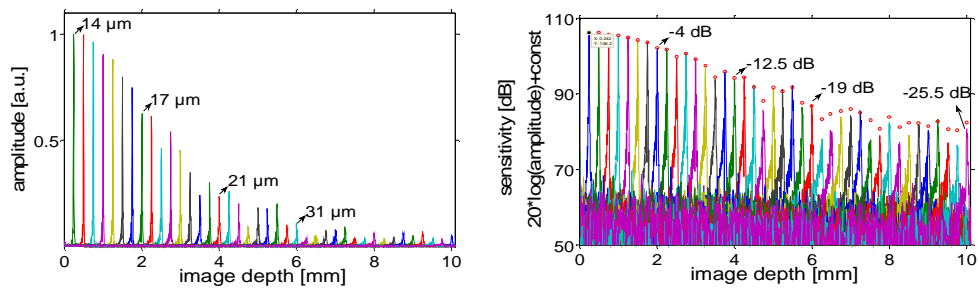


Fig. 11. PSFs at different image depths. No recalibration and no spectral reshaping or apodization step prior to FFT was applied. Left: Linear representation; for some image depths the corresponding axial resolution in air is noted. Right: Logarithmic plot representing sensitivity. The red circles indicate the drop of fringe contrast extracted from measured fringe signals. Numbers for sensitivity roll off values are given for various depths.

The sensitivity values were calibrated with an additional measurement using a neutral density filter with 46.4 dB attenuation in one interferometer arm. The values are adjusted for coupling losses in the interferometer. The values are adjusted for coupling losses in the interferometer. The red circles in Fig. 11 (right) indicate the drop of fringe contrast of the signal extracted from the mean fringe intensity of the acquired intensity envelopes (by Hilbert transformation, see [28]).

The best axial resolution in air (3 dB width of Gaussian fit) was 14.0 μm , in theory the spectrum would support about 13.7 μm in air. For some larger delays, the resolution is labeled in Fig. 11 (left), exhibiting only a 7 μm increase over 4 mm. The maximum sensitivity at short delays is 106.6 dB, about 5 dB below the theoretical shot noise limit of 111.5 dB for 9.2 mW optical power incident on the sample at a detection bandwidth of 350 MHz [4]. The sensitivity is indicated in Fig. 11 (right) for several delays. About 4 dB roll off for 2 mm imaging depth, 12.5 dB for 4 mm and 25.5 dB for 10 mm is measured. Remarkably, the discrepancy between the peaks of the PSFs and the plotted red circles, indicating the drop of fringe contrast, is very small over a wide imaging range. This is an indication that most of the roll off is caused by loss in fringe visibility, rather than added phase error. This means, for the given imaging range, the quality of linearity of the applied waveform is sufficient and the roll off is entirely determined by the coherence properties of the source. This fact supports the assumed model that a possible difference between instantaneous lasing wavelength and the instantaneous center wavelength of the FFP's passband can be neglected here.

Besides the good sensitivity values, the system also exhibits a dynamic range of about 69 dB which can be considered very high for a swept source OCT system [13, 29, 30], especially since the ADC resolution was only 8 bit (digital oscilloscope), again underlining the advantage in dynamic range of FD-OCT [13].

6.5 Imaging with k -space linear FDML without resampling and apodizing

In the following, OCT-imaging with the described k -space linear FDML laser is presented without recalibration step and spectral apodization prior to FFT and a comparison to a conventional sinusoidally driven filter with and without recalibration is given. For that purpose, as described in paragraph 2, the light is coupled out of the laser cavity after the FFP filter and is post amplified to 22 mW by a booster SOA [10] and used in a standard Michelson setup for OCT imaging (dual balanced detection). A pair of galvo-scanner mirrors (Cambridge Technologies, 6215H) is used for transverse scanning on the sample. The calculated transverse spot size on the sample is 22.5 μm . The average incident power on the sample was 10 mW.

The data acquisition was performed using a 400 MSamples/s ADC with a resolution of 12 bit. The real, actual imaging sensitivity was measured with an OD 1.7 neutral density filter and a mirror as sample. The values are not adjusted for losses in the microscope, mirror, coupler and circulator, explaining the reduced numbers compared to the measurement described above. The measured sensitivity is 103 dB for the k -space linear sweep whereas for

a sinusoidal sweep, the sensitivity is with 100 dB slightly smaller, what might be due to the recalibration step.

In Fig. 12 three sets, each consisting of two 2D images of a human finger *in vivo*, are presented for each of three different situations: In Fig. 12(A) and Fig. 12(B) the filter was driven sinusoidally (175 nm scan range) with no recalibration step prior to FFT. For the images in Fig. 12(C) and Fig. 12(D) the same filter drive waveform was used but here a recalibration step was performed. Therefore, an interference signal (single depth) was recorded with the interferometer once and the phase characteristic is extracted and used for recalibration of all lines of the image. Finally, Fig. 12(E) and Fig. 12(F) are demonstrating the case where the k-space linear FDML described in the previous chapters is applied and no recalibration step was used. The presented data sets consist of 4000 lines x 1664 samples (1536 samples for Figs. 12(A), 12(C), and 12(E)), each image was acquired in 0.070s. The transversal scan range is 4.3 mm the axial scan range is 6 mm. The animation in Fig. 12(G) is a rendered 3D representation of the human finger, recorded with the k-space linear FDML and no recalibration step. The movie was created from a 3D data set of 512 frames x 512 lines x 1536 samples, acquired in 4.6 s. The scan range equals 4.3 mm in length, 3.0 mm in width and 6 mm in depth. The images are cropped (3.3 mm x 1.7 mm x 1.9 mm) for better visibility. The three images Fig. 12(A), Fig. 12(C) and Fig. 12(E) as well as Fig. 12(B), Fig. 12(D) and Fig. 12(F) are acquired at the same sample position.

Obviously, the 2D-images acquired with the sinusoidal drive waveform are of considerably poor quality in the case where no recalibration step is performed, as can be seen comparing Fig. 12 (A) with Fig. 12(C) and Fig. 12(B) with Fig. 12(D). This indicates that for FD-OCT with a typical 100 nm bandwidth at 1300 nm wavelength at ~1-2 mm imaging range, an integrated frequency error of $\chi = 4 \cdot 10^{-4}$ is not sufficient to perform OCT without resampling.

Figures 12(E)-12(F) show 2D images acquired with the k-space linear FDML laser and no recalibration. Compared to the images acquired with the standard method (sinusoidal sweep + recalibration) in Figs. 12 (C)-12(D)), no significant difference in image quality can be noticed. The Figs. 12(E)-12(F) might even exhibit slightly higher contrast. However, in the k-space linear case, a more pronounced line artifact can be seen. This artifact originates from an electronic interference signal in the system with a fixed frequency. In the case of recalibration, the signal is washed out over a frequency range, whereas in the k-space linear case (or the sinusoidal case without recalibration), a peak at a certain frequency remains as line artifact. This artifact can be removed by increasing the electronic gain in the system. The 3D image and movie animation shown in Fig. 12(G), again acquired with the k-space linear FDML and no recalibration and apodization, demonstrate the capability of the presented system for high speed 3D imaging. Considering the sweep duration of 3.5 μ s, similar image quality can be expected if the buffering technique is applied in order to multiply the sweep rate [13]. The image quality should be equivalent to a buffered FDML configuration with more than 250 kHz line rate, yielding a 3D acquisition time for the same size of data set of about 1 second.

In view of future clinical imaging applications, the system shows good stability and reproducibility using the presented method of linearization. Once the optimal waveform is found, the linearity performance does not degrade over a period of several hours and parameters do not have to be readjusted during this time. Aging effects of the piezo or drift do not seem to be a dominant effect on this time scale. On a day to day basis it is necessary to slightly change phases of second and third order harmonic and/or the wavelength offset to obtain the required linearity. This might be due to varying external conditions like temperature. So for a potential commercial system an active feedback loop might be required.

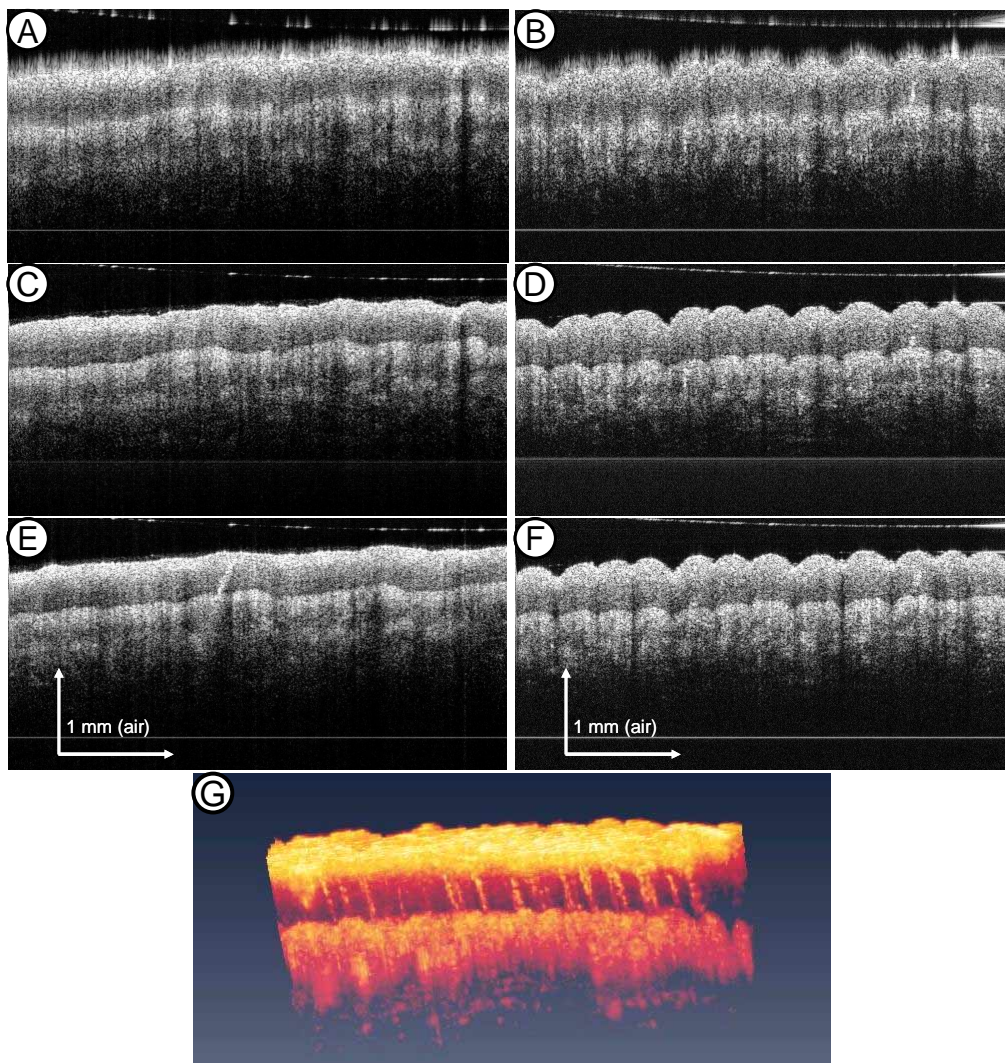


Fig. 12. Three sets of OCT images, each consisting of 2 images of a human finger for three different situations: (A) and (B): sinusoidal sweep with no recalibration step prior to FFT; (C) and (D): sinusoidal sweep with recalibration step prior to FFT; (E) and (F): k-space linear FDML with no recalibration step prior to FFT. The images in each column are acquired at the same sample position. (G): 3D representation acquired with the k-space linear FDML and no recalibration step prior to FFT. No spectral apodization was performed (1MB movie).

6.6 K-space adaptive FDML – Dispersion compensation

Besides the possibility to linearize the optical frequency sweep over time, the control of the filter motion by an arbitrary waveform offers the unique possibility to adaptively adjust the sweep characteristic. So the possibility to actively control and adapt the time-frequency characteristic of the filter waveform by manipulating amplitude and phase of the three harmonics offers more than implementation of a k-space linear swept laser source. One application could be to dynamically compensate unbalanced dispersion in sample and reference arm of an OCT system. For example in ophthalmic applications, perfect dispersion balancing would require to adjust the amount of dispersive material in the reference arm for different eye lengths of each patient. Usually this problem is solved by numerically compensating dispersion [31] in a post-processing step.

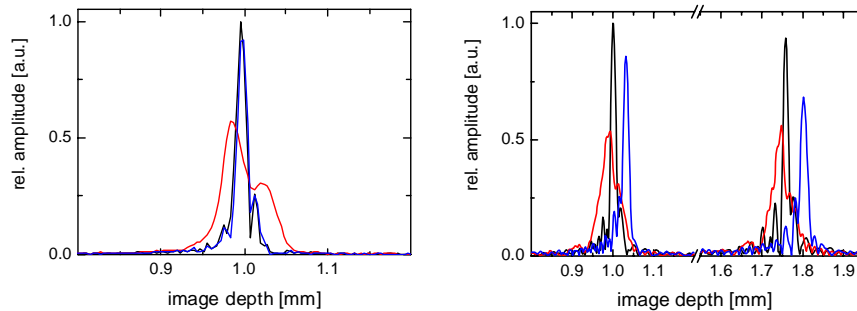


Fig. 13. Measured PSFs at an imaging depth of 1 mm. Black: Ideal waveform with no additional dispersive element. Red: PSF for the same waveform but with three 0.7 mm thick silicon plates inserted into one arm. Blue: PSF for an adjusted waveform correcting for the dispersion introduced by the silicon plates. Left: Almost perfect dispersion correction for only one depth (1 mm). Right: Partial simultaneous dispersion correction for two depths.

However, in the k -space adaptive FDML approach, dispersion compensation is achieved in hardware by manipulating the waveform applied to the filter and real-time compensation with no additional computation time needed becomes possible. The approach is analogous to the “approximate dispersion compensation” described by Wojtkowski, *et al.* [31], where a simple resampling technique is used. This technique only works perfectly at a single depth and compensation over the entire range cannot be achieved. However there are two situations where such a technique can be particularly useful: (1) In cases where only a very small amount of remaining dispersion imbalance has to be compensated, this technique works very effectively. (2) For swept source optical coherence microscopy (OCM) applications [15, 32], where imaging is only performed in one depth, this technique is also perfectly suitable. Especially, since with k -space adaptive FDML the amount of compensation can be dynamically adjusted, it would be feasible to adjust the amount of dispersion compensation synchronous to the image depth. Because OCM is very sensitive to dispersion due to the high resolution, this approach might be very helpful for future swept source OCM systems.

In order to demonstrate that almost perfect dispersion compensation for one imaging depth is possible with k -space adaptive FDML, first of all the amplitude and phase parameters are adjusted to values yielding a k -space linear FDML laser as demonstrated before. The measured PSF from the fringe signal of a Michelson interferometer for an arm unbalance of 1 mm is shown in Fig. 13 (left) (black curve). In this case, the dispersion in both arms was balanced. In order to simulate sample dispersion, three 0.7 mm thick silicon plates are inserted into the sample arm and the PSF is measured again for the same optical delay. The resulting PSF is depicted in the same graph (red curve). The interference signal was numerically corrected for the losses induced by surface reflection of the plates. For the third PSF, the parameters (phases of the harmonics of the drive waveform) are adjusted by optimizing the width and peak value of the PSF online on an oscilloscope in FFT mode. The PSF resulting from the optimized fringe signal is plotted in Fig. 13 (left) (blue curve). It can be seen that the additional dispersion from the silicon plates leads to a significant degradation of the PSF. By increasing only the third order harmonic phase by approximately 10° , the effect of dispersion is almost perfectly compensated for this particular depth.

To demonstrate partial dispersion compensation over a larger range of imaging depths, a 0.5 mm thick quartz glass plate is inserted into the sample arm of the Michelson interferometer instead of the mirror. Thus, two isolated reflections are detected, one at an imaging depth of 1 mm and one at ~ 1.8 mm. The result is shown in Fig. 13 (right). The black curve represents the PSFs for the k -space linear laser, again with no silicon. The red curve represents the PSF for the same waveform but now with the silicon plates inserted in one arm. Here again, a clear degradation of the PSF can be observed. The blue line shows the PSFs for the re-optimized filter drive waveform. It can be seen that only a partial compensation is possible at two

different depths simultaneously. However, since the amount of added dispersion in this experiment significantly exceeds the typical dispersion imbalance in OCT applications, it can be expected that smaller amounts in real imaging situations can be compensated sufficiently.

7. Conclusion and outlook

In conclusion, a detailed analysis of the problem how to linearize the time-frequency dependence of a high speed, wavelength swept FDML laser source is presented. The required experimental setup to analyze the complex response function of the electrically driven, optical bandpass filter in the laser is described, different methods how to optimize the ideal drive waveform are discussed and an experimental guideline how to generally linearize FDML sources is given. A detailed comparison of the theoretical results and the experimental data is used to discuss in how far the response of the filter can be predicted theoretically. In principle, the presented approach could also be used for linearization of non-FDML laser sources.

Based on this analysis, a wavelength swept FDML laser source is demonstrated with 100 nm sweep range at a center wavelength of 1300 nm, a sweep duration of 3.5 μs and a non-linearity of $2 \cdot 10^{-5}$. The high degree of the linearity enables swept source OCT imaging without the step of resampling or of spectral reshaping prior to FFT. A comparison of image quality shows no difference of k-space linear FDML without recalibration or resampling and standard FDML. Good stability and reproducibility of the system is observed over hours. With the resampling step being obsolete, hardware FFT solutions become feasible, paving the way for future ultrafast real time OCT systems for clinical environments. Furthermore, additional noise generated by the resampling step is avoided. The tuning rate restrictions imposed by the requirement to drive with three harmonics can be solved. In order to improve the speed performance and multiply the effective sweep rate, the technique of buffered FDML [13] can be applied and the image quality can be expected to be similar for identical power levels.

The possibility to dynamically adjust the sweep characteristic to deliberately generate non-linear sweeps in order to compensate for imbalanced dispersion in the interferometer is demonstrated. The technique is analogous to the widely used software based dispersion compensation by resampling; however, again the demonstrated "hardware solution" requires no extra processing power. The technique works well for small amounts of dispersion over the whole imaging range or at a single depth even for high dispersion and may become important for future FDML based OCM systems.

This work demonstrates that the steps of software resampling, numerical apodization and numerical dispersion compensation may become obsolete in future high speed OCT systems. Advantages of k-space linear FDML lasers like no additional noise caused by resampling, reduced speed requirements for the ADC, a factor of 2 reduction in data rate, lower storage capacity requirements for large comprehensive data sets and higher sensitivity due to the avoidance of overexposure of the sample may pave the way for future ultrafast real time OCT systems for clinical environments.

Acknowledgment

We would like to acknowledge support from Prof. Wolfgang Zinth at the LMU Munich, helpful advice from Desmond C. Adler, Vivek J. Srinivasan and James G. Fujimoto from the Massachusetts Institute of Technology and Maciej Wojtkowski from the Nicholas Copernicus University in Torun. This research was sponsored by the Emmy Noether program of the German Research Foundation (DFG) HU 1006/2-1.

3.1.2 Subharmonic Fourier domain mode locking

In case of conventional FDML lasers, light traverses the delay fiber in the cavity completely or partly (higher harmonic operation) during one filter drive period. In subharmonic Fourier domain mode locked (shFDML) lasers, light is recirculated repetitively in the delay line, so that the same delay fiber is passed several times during each round-trip of light in the FDML cavity and within two consecutive passes of the SOA. Therefore, the length of the required fiber can be reduced considerably compared to the case using the same filter drive frequency f_{Filter} but conventional FDML operation. Besides potentially lower costs due to the reduced fiber length, the main advantage of shFDML operation is the possibility to extract a part of the light every time when the light is recirculated and traverses the delay fiber. In this way, the sweep rate can effectively be increased by an adjustable factor. In contrast to typical optical buffering, as described in chapter 2.2.3.3, there is no need for an external optical buffer stage and the multiplication of the sweep rate can be achieved with a minimum of optical fiber required, since the buffer stage is inherently included in the FDML cavity. Within the research reported in this thesis, the first subharmonic FDML laser has been demonstrated in the wavelength range of ~ 1300 nm. A detailed description and analysis of the operation principle of the shFDML laser is presented in the reprint² of the article

C. M. Eigenwillig, W. Wieser, B. R. Biedermann, and R. Huber, "Subharmonic Fourier domain mode locking", *Optics Letters* **34**, 725-727 (2009),

which was written by me jointly with W. Wieser, B. R. Biedermann and R. Huber and which is attached to this chapter. The demonstrated shFDML laser is based on a sigma-ring resonator configuration, as introduced in chapter 2.2.3.1. In order to enable more than two fiber delay passes per round-trip, the tunable bandpass filter is placed in the linear part of the sigma-ring cavity. Since the Fabry-Pérot filter reflects almost all of the non-transmitted light, it can play the role of an adjustable optical switch, defining the number of delay fiber passes per round-trip. The following article analyses drawbacks of shFDML operation, like parasitic lasing in the short fiber ring that currently limits the achievable sweep performance of the shFDML laser. As explained, the use of a polarization maintaining short ring setup, comparable to the PM FDML laser mentioned in chapter 2.2.3.2, can largely suppress this effect. The need to minimize the length of the short ring as well as the feature of power leakage through the filter are mentioned and discussed. High-quality OCT imaging with the shFDML laser is demonstrated at 57 kHz. Extracting a small part of the power of the light in the linear delay line allows for an effective multiplication of the sweep rate by a factor of 10 yielding a sweep rate of 570 kHz. However, in this case, the sweep bandwidth was limited to ~ 40 nm.

² © 2009 Optical Society of America, Inc.

3. New concepts of wavelength-swept light sources in application for OCT

sists of standard SM components, whereas the rest is PM. The FFP-TF is semi-PM; it has a standard SM fiber on one side and a PM fiber on the other side.

Light from the SOA with p polarization is coupled by the polarization beam splitter (PBS) to the tunable FFP-TF. Frequency components matching the instantaneous passband of the filter are transmitted and propagate through a 2×180 m long fiber. A Faraday rotation mirror (FRM) at the end of the cavity rotates the polarization by 90° and the light propagates back to the filter. In contrast to standard FDML operation [8], in a subharmonic configuration the filter does not transmit the light at first arrival but reflects back about 95% of the intensity. If the filter is matched to the $1/n$ th subharmonic of the round trip time in the linear part of the cavity, after n round trips, light of a certain wavelength is transmitted through the FFP-TF back into the short ring. If n is an odd number, the light has s polarization and continues to propagate from the PBS through the short ring. Thus, in this configuration only odd subharmonics are supported. The PM fiber between PBS and SOA is twisted by 90° to couple the light back to the SOA in p polarization.

Parasitic light from an amplified spontaneous emission (ASE) background that did not pass the FFP-TF still has the same polarization state (p -polarization) when it returns to the PBS. Therefore it propagates back to the isolator and is blocked. This way, parasitic lasing in the short ring is suppressed.

The fiber length of the short ring should be minimized to keep the transit time short enough to enable a forward and a backward pass through the FFP-TF. The transit time in our setup is ~ 11 ns (2.3 m fiber length). For high output power, light is coupled out from the short ring (50%, output 1). For high-speed applications, light is extracted from the delay line (5%) in both directions and combined by a 50/50 coupler (output 2). Light from both outputs of the shFDML is postamplified [12] by a booster SOA [see Fig. 1(A), right] after polarization adjustment by the polarization controllers (PCs). For fast SOA current switching in buffered FDML operation [9] and for spectral shaping in hardware [13], a home-built 6 MHz diode driver in combination with an iterative optimization algorithm is used for both SOAs [13].

A characteristic of the presented shFDML configuration is the power leakage during fly-back of the FFP-TF. Figure 1(B) shows the temporal evolution of the transmission wavelength of the filter (solid curve) and the wavelength of the circulating light at the filter over time (dashed curves) in the case of $1/n$ th subharmonic (here $n=3$). For any point in time, light with up to n different wavelengths is present at any point in the delay resonator. The circles indicate the $(n-1)=2$ intersection points per sweep, where light from the stored sweeps can leak through the filter, affecting laser operation and causing a power break-in. This effect can be avoided by extending the filter sweep range compared to the desired wavelength range of the active laser operation, which has to be embedded in between two intersection points.

Figure 2(A) shows the interference signal from the Mach-Zehnder interferometer for one sweep from output 1; operating the laser at the 1/5th subharmonic (56.86 kHz), the corresponding spectrum is plotted in Fig. 2(B). Figure 2(C) demonstrates the spectrum at the 1/3rd subharmonic (94.72 kHz). Owing to the previously discussed leakage (break-in effect), four power modulations are observed in Fig. 2(B) ($n=5$) and 2 in Fig. 2(C) ($n=3$), respectively. For the 1/5th subharmonic a full width of 95 nm centered at 1317 nm is achieved, limited by parasitic lasing in the short ring.

The breakthrough of parasitic lasing in the short ring is due to imperfect suppression of the s polarization state at the reflection of the filter surface. Hence, approximately -17 dB of the incident ASE propagates further in the ring. A dependence of this effect on mechanical bending and stress was observed in the short piece of PM fiber between the PBS and the FFP-TF, probably owing to spectral modulation caused by interference of the two slightly delayed polarization components.

To characterize the instantaneous coherence length of the shFDML (no postamplification, output 1), the measured point-spread functions (PSFs) are plotted against the corresponding ranging depth in OCT. The laser is operated at the 1/5th subharmonic at a full bandwidth of 95 nm. The SOA current was modulated such that only one sweep direction is active and no spectral shaping was applied. The circles indicate the fringe visibility (averaged intensity envelope of interference signal). The absolute scale is chosen such that the peaks of the PSFs represent the sensitivity values of the shFD mode-locked laser in an OCT application. The measured sensitivity at a short ranging depth is ~ 116 dB in very good agreement with the theoretical value of 115.7 dB for an $8.8 \mu\text{s}$ sweep duration and 12 mW of power on the sample averaged over one sweep [4]. The dynamic range was measured to be 50–55 dB at a short ranging depth. The resolution in air is $\sim 12 \mu\text{m}$. The sensitivity roll-off of 11 dB over 4 mm and 25 dB over 10 mm is comparable to conventional FD mode-locked lasers [8,9,11,14]. Figure 3 shows a two-dimensional (2D) and a three-dimensional (3D) OCT data set of a human finger acquired with the shFD mode-locked laser at 9.8 mW on the sample using the booster. The measured performance and the image quality suggest that the observed power break-ins, in cases where they occur, do not have a significant effect on OCT performance.

Besides the reduction in fiber length, shFD mode-locked enables a simplified setup for buffered [9] op-

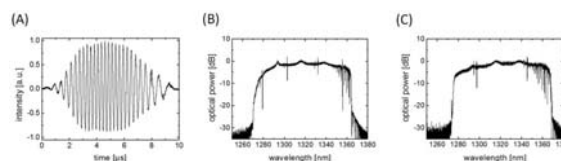


Fig. 2. (A) Measured interference signal at 1/5th subharmonic. (B) Corresponding spectrum. (C) Spectrum for 1/3rd subharmonic.

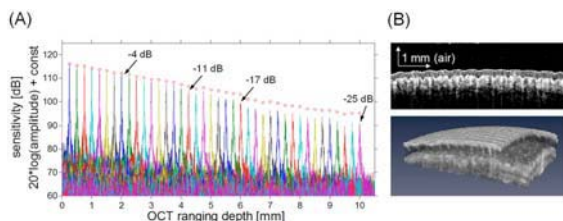


Fig. 3. (Color online) (A) PSFs (curves) and fringe visibility (circles) of the shFD mode-locked laser for different ranging depths. Numbers indicate the corresponding sensitivity roll-off values for several depths. (B) 2D (top) and 3D (bottom) OCT image of human finger.

eration to increase the sweep repetition rate. By coupling light out of the delay resonator (output 2) and modulating the SOA current, a sweep rate multiplication of $2n$ can be achieved. The filter sweep range has to be increased reducing the duration of lasing and avoiding overlap between different parts of a sweep in the delay line. We demonstrate a $10\times$ increased sweep rate (568.6 kHz) at 1/5th subharmonic. Running at a subharmonic and then multiplying is preferable to a shorter FDML cavity because the FFP-TF can be operated near its mechanical resonance. The SOA current is switched on for only $1.58 \mu\text{s}$ (9% of time) during one filter cycle. Figure 4(A) shows the interference signal at output 2. The intensity decreases from the first to the tenth sweep (indicated in the graph) during one filter drive cycle due to loss. This effect can be compensated by modulating the current of the external booster SOA with an approach described previously [13]. This way 10 Hanning shaped waveforms of equal intensity are generated [see Fig. 4(B)]. Owing to the higher sweep speed in this case, the laser bandwidth was limited to 38 nm full width by the propagation time effect through the short ring. A reduction of the fiber length in the short ring will improve this performance.

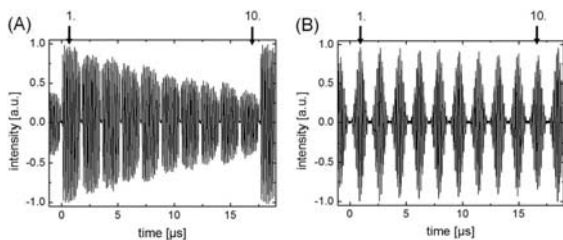


Fig. 4. Interference signal at 568.6 kHz sweep rate. (A) Constant booster current and (B) booster current actively modulated. Numbers indicate the first and the tenth sweep in one filter cycle.

In conclusion, we demonstrate a subharmonically Fourier domain mode-locked (shFD mode-locked) wavelength-swept laser source that uses, compared to an FD mode-locked laser, a substantially reduced fiber length inside the cavity. The delay line of a standard FDML configuration is replaced by a resonator design, where light is recirculating repetitively and the optical bandpass filter is used as an optical switch. The reduced fiber length can enable the application of specialty fibers for future low cost swept laser systems. The source is well suited for OCT imaging and allows for extremely high sweep repetition rates with a simple setup; 568 kHz was demonstrated.

We would like to acknowledge support from W. Zinth at the Ludwig-Maximilians-University Munich. This research was sponsored by the Emmy Noether program of the German Research Foundation (DFG-HU 1006/2-1) and the European Union (EU) project Functional Optical Coherence Tomography (FP7 HEALTH, contract 201880).

References

1. D. Huang, E. A. Swanson, C. P. Lin, J. S. Schuman, W. G. Stinson, W. Chang, M. R. Hee, T. Flotte, K. Gregory, C. A. Puliafito, and J. G. Fujimoto, *Science* **254**, 1178 (1991).
2. A. F. Fercher, C. K. Hitzenberger, G. Kamp, and S. Y. Elzaiat, *Opt. Commun.* **117**, 43 (1995).
3. G. Häusler and M. W. Lindner, *J. Biomed. Opt.* **3**, 21 (1998).
4. M. A. Choma, M. V. Sarunic, C. H. Yang, and J. A. Izatt, *Opt. Express* **11**, 2183 (2003).
5. J. F. de Boer, B. Cense, B. H. Park, M. C. Pierce, G. J. Tearney, and B. E. Bouma, *Opt. Lett.* **28**, 2067 (2003).
6. R. Leitgeb, C. K. Hitzenberger, and A. F. Fercher, *Opt. Express* **11**, 889 (2003).
7. S. H. Yun, G. J. Tearney, J. F. de Boer, N. Iftimia, and B. E. Bouma, *Opt. Express* **11**, 2953 (2003).
8. R. Huber, M. Wojtkowski, and J. G. Fujimoto, *Opt. Express* **14**, 3225 (2006).
9. R. Huber, D. C. Adler, and J. G. Fujimoto, *Opt. Lett.* **31**, 2975 (2006).
10. D. C. Adler, R. Huber, and J. G. Fujimoto, *Opt. Lett.* **32**, 626 (2007).
11. R. Huber, D. C. Adler, V. J. Srinivasan, and J. G. Fujimoto, *Opt. Lett.* **32**, 2049 (2007).
12. R. Huber, M. Wojtkowski, K. Taira, J. G. Fujimoto, and K. Hsu, *Opt. Express* **13**, 3513 (2005).
13. B. Biedermann, W. Wieser, C. Eigenwillig, G. Palte, D. Adler, V. Srinivasan, J. Fujimoto, and R. Huber, *Opt. Lett.* **33**, 2556 (2008).
14. C. M. Eigenwillig, B. R. Biedermann, G. Palte, and R. Huber, *Opt. Lett.* **16**, 8916 (2008).

3. New concepts of wavelength-swept light sources in application for OCT

3.2 Fast wavelength-swept ASE sources - a novel approach

As explained in chapter 2.2.1.3, conventional wavelength-swept lasers have the drawback that the sweep speed is fundamentally limited by the round-trip time of light in the resonator or the laser resonator length due to the fact that lasing continuously has to rebuild from amplified spontaneous emission (ASE) when the spectral transmission window of the tunable filter is shifted over the gain profile. There have been different investigations to solve this problem. On the one hand, there is the possibility to considerably reduce the cavity length and therefore raise the fundamental sweep speed limit. Several short cavity approaches have been introduced in chapter 2.2.1.4. Contrary to this, there is the concept of FDML lasers, where the length of the resonator is increased to several hundreds of meters or to a few kilometers enabling to drive the tunable bandpass filter synchronously to the round-trip time of light in the resonator. In this way, lasing does not continuously has to rebuild from ASE and the fundamental sweep speed limit can be overcome. Note that FDML operation is only possible for discrete filter drive frequencies, which is the fundamental FDML frequency and its higher harmonics.

As already mentioned in chapter 2.2.1.4, another possible solution to avoid the fundamental sweep speed limit is the implementation of a wavelength-swept source with no optical feedback and therefore no build-up time of lasing. However, one single spectral filtering event of ASE cannot yield sufficient output power due to the necessarily narrow spectral width of the filter. A subsequent post-amplification step can raise the overall power, but typically a dominant proportion is unfiltered ASE due to insufficient saturation of the last gain element making such a source unattractive for SS-OCT.

Nevertheless, within the research work reported in this thesis, the concept of a wavelength-swept light source with no optical feedback has been extended, resulting in wavelength-swept ASE sources with high potential for SS-OCT, as presented in this chapter. The key idea is that ASE light alternately passes a cascade of different optical gain elements and different tunable bandpass filters. Optical filtering prior to each amplification step is necessary to prevent excessive amplification of unfiltered ASE background. In this way, just as with swept lasers, a sufficiently high output power can be achieved, while at the same time no fundamental sweep speed limit exists. However, the latter condition is only fulfilled if all bandpass filters are driven slightly out of phase in order to compensate for the transit time of light between the different filters.

This new concept is an alternative way to implement wavelength-swept light sources for high-quality, ultra-high speed SS-OCT, which can have several advantages. Firstly, unlike FDML lasers, the filter drive frequency is not limited to discrete values but can be chosen freely within a continuous frequency range only limited by the electro-mechanical response of the filter [10]. Secondly, in contrast to wavelength-swept lasers, the wavelength-swept ASE source could also be operated with non-periodic filter drive waveforms. Moreover, unlike FDML lasers, a long fiber delay is not required. This can be an advantage at shorter wavelengths necessary for retinal OCT. At 1060 nm, but in

particular at 800 nm, a considerable higher fiber loss, high chromatic dispersion and pronounced polarization effects complicate FDML operation. Thus, the wavelength-swept ASE source could be an attractive alternative. Finally, since wavelength-swept ASE sources have no optical feedback and the instantaneous output spectrum is defined only by the tunable bandpass filters, the temporal sweeps are very repeatable, meaning that the instantaneous center wavelength does not jitter around the mean, time-dependent wavelength evolution. This could be an advantage for applications where an accurate knowledge of center wavelength is important like fiber Bragg grating (FBG) sensing. However, there are also some disadvantages of this approach. On the one hand, a precise phase locked drive of all filters is necessary. On the other hand, the wavelength-swept ASE source usually provides a poorer sensitivity roll-off performance than FDML lasers.

3.2.1 Fast wavelength-swept ASE source at 1300 nm

In this chapter, a wavelength-swept ASE source at ~1300 nm and its applicability for SS-OCT is presented, which has been realized within the research reported in this thesis. A detailed description of this source and a comprehensive analysis of general properties of this new concept of wavelength-swept ASE sources is given in the reprint³ of the article

C. M. Eigenwillig, B. R. Biedermann, W. Wieser, and R. Huber, "Wavelength swept amplified spontaneous emission source", *Optics Express* **17**, 18794-18807 (2009),

which was written by me jointly with B. R. Biedermann, W. Wieser and R. Huber and which is attached to this chapter. In the presented wavelength-swept ASE source, ASE light is amplified in total three times using SOAs where one SOA is passed twice in both directions. Additionally, the light is filtered two times using two tunable Fabry-Pérot filters. Characteristic features occurring due to the double pass of the first SOA are described. The wavelength tuning of both filters is analyzed showing the need for a precise filter drive parameter setting. The knowledge of the instantaneous transmission spectra of both filters allows predicting the required accuracy in phase delay adjustment between both filters as well as the expectable sensitivity roll-off performance due to double filtering. The required phase delay accuracy as well as the sensitivity roll-off performance are measured and compared to the theoretically expected values. Moreover, the following article introduces a model which explains the link between optical filter bandwidth, analog detection bandwidth and incoherent noise background. Relative intensity noise (RIN) of the source is measured and compared to FDML performance. OCT imaging using the wavelength-swept ASE source is demonstrated.

³ © 2009 Optical Society of America, Inc.

Wavelength swept amplified spontaneous emission source

Christoph M. Eigenwillig, Benjamin R. Biedermann, Wolfgang Wieser
and Robert Huber*

*Lehrstuhl für BioMolekulare Optik, Fakultät für Physik, Ludwig-Maximilians-Universität München
Oettingenstr. 67, 80538 Munich, Germany*

** Robert.Huber@Physik.Uni-Muenchen.DE*

Abstract: We present a new, alternative approach to realize a wavelength swept light source with no fundamental limit to sweep speed. Amplified spontaneous emission (ASE) light alternately passes a cascade of optical gain elements and tunable optical bandpass filters. We show that for high sweep speeds, the control signal for the different filters has to be applied with a defined, precise phase delay on the order of nanoseconds, to compensate for the light propagation time between the filters and ensure optimum operation. At a center wavelength of 1300 nm sweep rates of 10 kHz, 100 kHz and 340 kHz over a sweep range of 100 nm full width and an average power of 50 mW are demonstrated. For application in optical coherence tomography (OCT), an axial resolution of 12 μm (air), a sensitivity of 120 dB (50 mW) and a dynamic range of 50 dB are achieved and OCT imaging is demonstrated. Performance parameters like coherence properties and relative intensity noise (RIN) are quantified, discussed and compared to the performance of Fourier Domain Mode Locked (FDML) lasers. Physical models for the observed difference in performance are provided.

©2009 Optical Society of America

OCIS codes: (140.3600) Lasers, tunable; (110.4500) Imaging systems: Optical coherence tomography; (120.3180) Instrumentation, measurement, and metrology: Interferometry; (110.4280) Noise in imaging systems; (120.2230) Instrumentation, measurement, and metrology, Fabry-Perot; (120.2440) Instrumentation, measurement, and metrology: Filters.

References and links

1. D. Huang, E. A. Swanson, C. P. Lin, J. S. Schuman, W. G. Stinson, W. Chang, M. R. Hee, T. Flotte, K. Gregory, C. A. Puliafito, and J. G. Fujimoto, "OPTICAL COHERENCE TOMOGRAPHY," *Science* **254**(5035), 1178–1181 (1991), <http://www.sciencemag.org/cgi/content/abstract/sci;254/5035/1178>.
2. G. Häusler, and M. W. Lindner, "Coherence Radar and Spectral Radar—New Tools for Dermatological Diagnosis," *J. Biomed. Opt.* **3**(1), 21–31 (1998), <http://dx.doi.org/10.1117/1.429899>.
3. A. F. Fercher, C. K. Hitzenberger, G. Kamp, and S. Y. Elzaiat, "MEASUREMENT OF INTRAOCULAR DISTANCES BY BACKSCATTERING SPECTRAL INTERFEROMETRY," *Opt. Commun.* **117**(1-2), 43–48 (1995), [http://dx.doi.org/10.1016/0030-4018\(95\)00119-S](http://dx.doi.org/10.1016/0030-4018(95)00119-S).
4. R. Leitgeb, C. K. Hitzenberger, and A. F. Fercher, "Performance of fourier domain vs. time domain optical coherence tomography," *Opt. Express* **11**(8), 889–894 (2003), <http://www.opticsinfobase.org/oe/abstract.cfm?URI=oe-11-8-889>.
5. J. F. de Boer, B. Cense, B. H. Park, M. C. Pierce, G. J. Tearney, and B. E. Bouma, "Improved signal-to-noise ratio in spectral-domain compared with time-domain optical coherence tomography," *Opt. Lett.* **28**(21), 2067–2069 (2003), <http://www.opticsinfobase.org/ol/abstract.cfm?URI=ol-28-21-2067>.
6. M. A. Choma, M. V. Sarunic, C. H. Yang, and J. A. Izatt, "Sensitivity advantage of swept source and Fourier domain optical coherence tomography," *Opt. Express* **11**(18), 2183–2189 (2003), <http://www.opticsinfobase.org/oe/abstract.cfm?URI=oe-11-18-2183>.
7. S. H. Yun, G. J. Tearney, J. F. de Boer, N. Iftimia, and B. E. Bouma, "High-speed optical frequency-domain imaging," *Opt. Express* **11**(22), 2953–2963 (2003), <http://www.opticsinfobase.org/oe/abstract.cfm?URI=oe-11-22-2953>.
8. S. H. Yun, G. J. Tearney, J. F. de Boer, and B. E. Bouma, "Motion artifacts in optical coherence tomography with frequency-domain ranging," *Opt. Express* **12**(13), 2977–2998 (2004), <http://www.opticsinfobase.org/oe/abstract.cfm?URI=oe-12-13-2977>.

9. S. Moon, and D. Y. Kim, "Ultra-high-speed optical coherence tomography with a stretched pulse supercontinuum source," *Opt. Express* **14**(24), 11575–11584 (2006), <http://www.opticsinfobase.org/oe/abstract.cfm?URI=oe-14-24-11575>.
10. W. Y. Oh, S. H. Yun, B. J. Vakoc, G. J. Tearney, and B. E. Bouma, "Ultrahigh-speed optical frequency domain imaging and application to laser ablation monitoring," *Appl. Phys. Lett.* **88**(10), 103902 (2006), <http://link.aip.org/link/?APPLAB/88/103902/1>.
11. R. Huber, D. C. Adler, and J. G. Fujimoto, "Buffered Fourier domain mode locking: Unidirectional swept laser sources for optical coherence tomography imaging at 370,000 lines/s," *Opt. Lett.* **31**(20), 2975–2977 (2006), <http://www.opticsinfobase.org/ol/abstract.cfm?URI=ol-31-20-2975>.
12. R. Huber, M. Wojtkowski, K. Taira, J. G. Fujimoto, and K. Hsu, "Amplified, frequency swept lasers for frequency domain reflectometry and OCT imaging: design and scaling principles," *Opt. Express* **13**(9), 3513–3528 (2005), <http://www.opticsinfobase.org/oe/abstract.cfm?URI=oe-13-9-3513>.
13. R. Huber, M. Wojtkowski, and J. G. Fujimoto, "Fourier Domain Mode Locking (FDML): A new laser operating regime and applications for optical coherence tomography," *Opt. Express* **14**(8), 3225–3237 (2006), <http://www.opticsinfobase.org/oe/abstract.cfm?URI=oe-14-8-3225>.
14. T. J. Eom, V. A. Tougbaev, B. A. Yu, W. Shin, Y. L. Lee, and D. K. Ko, "Narrowband wavelength selective detector applicable SD-OCT based on Fabry-Perot tunable filter and balanced photoreceiver," in *Coherence Domain Optical Methods and Optical Coherence Tomography in Biomedicine XII*, (SPIE, 2008), 68470R–68471. http://spie.org/x648.html?product_id=766436
15. G. Y. Liu, A. Mariampillai, B. A. Standish, N. R. Munce, X. J. Gu, and I. A. Vitkin, "High power wavelength linearly swept mode locked fiber laser for OCT imaging," *Opt. Express* **16**(18), 14095–14105 (2008), <http://www.opticsinfobase.org/oe/abstract.cfm?URI=oe-16-18-14095>.
16. Y. X. Mao, C. Flueraru, S. Sherif, and S. D. Chang, "High performance wavelength-swept laser with mode-locking technique for optical coherence tomography," *Opt. Commun.* **282**(1), 88–92 (2009), <http://dx.doi.org/10.1016/j.optcom.2008.09.059>.
17. M. Y. Jeon, J. Zhang, and Z. P. Chen, "Characterization of Fourier domain mode-locked wavelength swept laser for optical coherence tomography imaging," *Opt. Express* **16**(6), 3727–3737 (2008), <http://www.opticsinfobase.org/oe/abstract.cfm?URI=oe-16-6-3727>.
18. M. Y. Jeon, J. Zhang, Q. Wang, and Z. P. Chen, "High-speed and wide bandwidth Fourier domain mode-locked wavelength swept laser with multiple SOAs," *Opt. Express* **16**(4), 2547–2554 (2008), <http://www.opticsinfobase.org/oe/abstract.cfm?URI=oe-16-4-2547>.
19. E. J. Jung, C. S. Kim, M. Y. Jeong, M. K. Kim, M. Y. Jeon, W. Jung, and Z. P. Chen, "Characterization of FBG sensor interrogation based on a FDML wavelength swept laser," *Opt. Express* **16**(21), 16552–16560 (2008), <http://www.opticsinfobase.org/oe/abstract.cfm?URI=oe-16-21-16552>.
20. Y. Wang, W. Liu, J. Fu, and D. Chen, "Quasi-distributed fiber Bragg grating sensor system based on a Fourier domain mode locking fiber laser," *Laser Phys.* **19**(3), 450–454 (2009), <http://www.springerlink.com/content/p300147134334266/>.
21. D. Chen, C. Shu, and S. He, "Multiple fiber Bragg grating interrogation based on a spectrum-limited Fourier domain mode-locking fiber laser," *Opt. Lett.* **33**(13), 1395–1397 (2008), <http://www.opticsinfobase.org/ol/abstract.cfm?URI=ol-33-13-1395>.
22. M. J. R. Heck, A. Renault, E. Bente, Y. S. Oei, M. K. Smit, K. S. E. Eikema, W. Ubachs, S. Anantathanasarn, and R. Notzel, "Passively Mode-Locked 4.6 and 10.5 GHz Quantum Dot Laser Diodes Around 1.55 μm With Large Operating Regime," *IEEE J. Sel. Top. Quantum Electron.* **15**, 634–643 (2009), http://ieeexplore.ieee.org/xpl/freeabs_all.jsp?isnumber=5068462&arnumber=4982709&count=68&index=19.
23. D. C. Adler, R. Huber, and J. G. Fujimoto, "Phase-sensitive optical coherence tomography at up to 370,000 lines per second using buffered Fourier domain mode-locked lasers," *Opt. Lett.* **32**(6), 626–628 (2007), <http://www.opticsinfobase.org/ol/abstract.cfm?URI=ol-32-6-626>.
24. D. C. Adler, Y. Chen, R. Huber, J. Schmitt, J. Connolly, and J. G. Fujimoto, "Three-dimensional endomicroscopy using optical coherence tomography," *Nat. Photonics* **1**(12), 709–716 (2007), <http://www.nature.com/nphoton/journal/v1/n12/abs/nphoton.2007.228.html>.
25. D. C. Adler, S. W. Huang, R. Huber, and J. G. Fujimoto, "Photothermal detection of gold nanoparticles using phase-sensitive optical coherence tomography," *Opt. Express* **16**(7), 4376–4393 (2008), <http://www.opticsinfobase.org/oe/abstract.cfm?URI=oe-16-7-4376>.
26. D. C. Adler, J. Stenger, I. Gorczynska, H. Lie, T. Hensick, R. Spronk, S. Wolohojian, N. Khandekar, J. Y. Jiang, S. Barry, A. E. Cable, R. Huber, and J. G. Fujimoto, "Comparison of three-dimensional optical coherence tomography and high resolution photography for art conservation studies," *Opt. Express* **15**(24), 15972–15986 (2007), <http://www.opticsinfobase.org/oe/abstract.cfm?URI=oe-15-24-15972>.
27. P. M. Andrews, Y. Chen, M. L. Onozato, S. W. Huang, D. C. Adler, R. A. Huber, J. Jiang, S. E. Barry, A. E. Cable, and J. G. Fujimoto, "High-resolution optical coherence tomography imaging of the living kidney," *Lab. Invest.* **88**(4), 441–449 (2008), <http://www.nature.com/labinvest/journal/v88/n4/full/labinvest20084a.html>.
28. T. Bajraszewski, M. Wojtkowski, M. Szkulmowska, A. Szkulmowska, R. Huber, and A. Kowalczyk, "Improved spectral optical coherence tomography using optical frequency comb," *Opt. Express* **16**(6), 4163–4176 (2008), <http://www.opticsinfobase.org/oe/abstract.cfm?URI=oe-16-6-4163>.
29. B. R. Biedermann, W. Wieser, C. M. Eigenwillig, G. Palte, D. C. Adler, V. J. Srinivasan, J. G. Fujimoto, and R. Huber, "Real time en face Fourier-domain optical coherence tomography with direct hardware frequency demodulation," *Opt. Lett.* **33**(21), 2556–2558 (2008), <http://www.opticsinfobase.org/ol/abstract.cfm?URI=ol-33-21-2556>.

30. B. R. Biedermann, W. Wieser, C. M. Eigenwillig, T. Klein, and R. Huber, "Dispersion, coherence and noise of Fourier domain mode locked lasers," *Opt. Express* **17**(12), 9947–9961 (2009), <http://www.opticsinfobase.org/oe/abstract.cfm?URI=oe-17-12-9947>.
31. C. M. Eigenwillig, B. R. Biedermann, G. Palte, and R. Huber, "K-space linear Fourier domain mode locked laser and applications for optical coherence tomography," *Opt. Express* **16**(12), 8916–8937 (2008), <http://www.opticsinfobase.org/oe/abstract.cfm?URI=oe-16-12-8916>.
32. C. M. Eigenwillig, W. Wieser, B. R. Biedermann, and R. Huber, "Subharmonic Fourier domain mode locking," *Opt. Lett.* **34**(6), 725–727 (2009), <http://www.opticsinfobase.org/ol/abstract.cfm?URI=ol-34-6-725>.
33. S. W. Huang, A. D. Aguirre, R. A. Huber, D. C. Adler, and J. G. Fujimoto, "Swept source optical coherence microscopy using a Fourier domain mode-locked laser," *Opt. Express* **15**(10), 6210–6217 (2007), <http://www.opticsinfobase.org/oe/abstract.cfm?URI=oe-15-10-6210>.
34. R. Huber, D. C. Adler, V. J. Srinivasan, and J. G. Fujimoto, "Fourier domain mode locking at 1050 nm for ultra-high-speed optical coherence tomography of the human retina at 236,000 axial scans per second," *Opt. Lett.* **32**(14), 2049–2051 (2007), <http://www.opticsinfobase.org/ol/abstract.cfm?URI=ol-32-14-2049>.
35. M. W. Jenkins, D. C. Adler, M. Gargasha, R. Huber, F. Rothenberg, J. Belding, M. Watanabe, D. L. Wilson, J. G. Fujimoto, and A. M. Rollins, "Ultra-high-speed optical coherence tomography imaging and visualization of the embryonic avian heart using a buffered Fourier Domain Mode Locked laser," *Opt. Express* **15**(10), 6251–6267 (2007), <http://www.opticsinfobase.org/oe/abstract.cfm?URI=oe-15-10-6251>.
36. T. Klein, W. Wieser, B. R. Biedermann, C. M. Eigenwillig, G. Palte, and R. Huber, "Raman-pumped Fourier-domain mode-locked laser: analysis of operation and application for optical coherence tomography," *Opt. Lett.* **33**(23), 2815–2817 (2008), <http://www.opticsinfobase.org/ol/abstract.cfm?URI=ol-33-23-2815>.
37. B. R. Biedermann, W. Wieser, C. M. Eigenwillig, and R. Huber, "Recent developments in Fourier Domain Mode Locked lasers for optical coherence tomography: imaging at 1310 nm vs. 1550 nm wavelength," *J. Biophoton.* **2**(6-7), 357–363 (2009), <http://www3.interscience.wiley.com/journal/122473349/abstract>.
38. V. J. Srinivasan, R. Huber, I. Gorczynska, J. G. Fujimoto, J. Y. Jiang, P. Reisen, and A. E. Cable, "High-speed, high-resolution optical coherence tomography retinal imaging with a frequency-swept laser at 850 nm," *Opt. Lett.* **32**(4), 361–363 (2007), <http://www.opticsinfobase.org/ol/abstract.cfm?URI=ol-32-4-361>.
39. J. A. Filipa, J. W. Walewski, and S. T. Sanders, "Optical beating of polychromatic light and its impact on time-resolved spectroscopy. Part II: Strategies for spectroscopic sensing in the presence of optical beating," *Appl. Spectrosc.* **62**(2), 230–237 (2008), <http://www.opticsinfobase.org/as/abstract.cfm?URI=as-62-2-230>.
40. J. W. Walewski, J. A. Filipa, and S. T. Sanders, "Optical beating of polychromatic light and its impact on time-resolved spectroscopy. Part I: Theory," *Appl. Spectrosc.* **62**(2), 220–229 (2008), <http://www.opticsinfobase.org/as/abstract.cfm?URI=as-62-2-220>.

Introduction

Optical Coherence Tomography (OCT) is a novel biomedical imaging technique for visualizing tissue microstructure *in vivo* [1]. While the first OCT systems used the so called time domain detection (TD-OCT), the demand for higher imaging speeds was one of the main reasons for focusing research on frequency domain OCT (FD-OCT) [2, 3]. At equivalent imaging parameters, FD-OCT provides higher sensitivity [4–6]. As an alternative to spectrometer based FD-OCT systems, FD-OCT systems using rapidly wavelength swept narrow-band light sources (swept source – SS-OCT or optical frequency domain imaging – OFDI [7]) offer several potential advantages: (i) The realization of dual balanced detection is easier, suppressing noise and auto-correlation artifacts; (ii) SS-OCT systems often have a longer ranging depth because of the narrow linewidth and long instantaneous coherence length of the applied laser light sources; (iii) SS-OCT/OFDI systems suffer less from fringe washout caused by sample motion or by rapid scanning of structures with high aspect ratio, and so the performance with respect to signal fading, spatial distortion and blurring can be improved [8].

Since the first demonstration of high speed SS-OCT, huge efforts have been made to push the wavelength sweep repetition rate of the OCT light sources [9–11]. For standard wavelength swept lasers, the length of the resonator limits the maximum wavelength sweep speed (and therefore imaging speed), because the number of possible roundtrips of light in the resonator is reduced and the build-up of saturated lasing from amplified spontaneous emission (ASE) is impeded [12]. Minimizing the laser resonator length enables higher sweep speeds but also enlarges the discrete resonator mode spacing [12, 13]. This can increase intensity noise and ultimately limit the maximum OCT ranging depth, if the laser cavity length is reduced down into the millimeter range.

One solution to this problem is the application of optical circuits without feedback. These resonator-less designs can be broadband light sources with a tunable optical bandpass filter

for post-filtering [12]. Although post-filtering is widely used in all kinds of hyperspectral imaging and microscopy applications, the tight instantaneous bandwidth requirement in OCT of ~ 0.1 nm causes a huge power loss due to the high finesse filtering [14]. Therefore an additional post-amplification can be used to provide sufficient levels of output power. The process of post-amplification of filtered ASE was demonstrated in a very rapidly swept laser source [12], where the tuning rate was above the single roundtrip limit and the laser did not have optical feedback anymore. The problem in this setup was the high ASE background of about 2 mW compared to <0.5 mW of the desired wavelength swept narrow-band signal.

With the demonstration of Fourier Domain Mode Locked Lasers (FDML) [13], the physical limitations of the maximum achievable sweep speed could be overcome and additionally, high output power levels at low ASE background can be achieved. In FDML lasers, an optical delay line in the laser resonator enables to drive the tunable optical bandpass filter synchronously to the round trip time of light in the resonator. The optical bandpass filter can be a rotating polygon mirror in combination with an optical grating [15, 16], a tunable fiber Fabry-Perot filter [17–21] or a tunable active gain element [22]. Record imaging speeds of up to 370,000 lines/s [11], high phase stability [23] and long ranging depths [13] have been demonstrated. FDML lasers have successfully been applied for numerous imaging, sensing and ranging applications [11, 13, 15, 19, 23–37].

The presented wavelength swept ASE source is a new, alternative approach to realize a wavelength swept light source with high power, low ASE and rapid sweeping operation. It should be underlined that it is not a real laser, since no resonator and optical feedback exists. In order to achieve a sufficient output power level and sensitivity for OCT imaging, ASE light alternately passes a linear cascade of *multiple* different gain elements and *multiple* different filter elements. The concept is related to post-filtering and amplification. However, in order to prevent excessive amplification of unfiltered ASE background, the light must be filtered prior to *each* new amplification step, so *several different* filters are required. A crucial factor for optimum performance is to drive the different wavelength filters with an accurate phase delay, to compensate for the light transit time between the filters. Using this technique, no fundamental limit to the sweep speed exists, just like in the case of FDML lasers. However, unlike FDML lasers, the demonstrated setup is fundamentally not limited to discrete drive frequencies. It enables high output power over a continuous range of drive frequencies, limited only by the mechanical response of the filter. Furthermore, the concept is not limited to periodic wavelength sweeps as in FDML. Arbitrary sweep functions can be generated. Additionally, no km long, optical delay fiber is required as in FDML. This reduces cost, especially at wavelengths, where expensive specialty fiber has to be used, e.g. for FDML at 1060 nm. Regarding rapidly swept light sources at 800 nm, the high loss of ~ 3 dB/km and large chromatic dispersion in optical fiber make FDML operation difficult. Therefore the wavelength swept ASE source could be a promising alternative for high speed SS-OCT imaging in particular in the 800 nm or 1060 nm wavelength range.

2. Experimental setup and operation

2.1 The optical setup

Figure 1(a) shows the fiber-based setup of the demonstrated wavelength swept ASE source at 1300 nm. ASE from the first semiconductor optical amplifier (SOA 1, Covega Corp.) propagates through an optical circulator (CIR, 2 to 3) and is filtered by a piezo actuated, fiber-based tunable Fabry-Perot filter (FFP-TF 1, Lambda Quest, LLC.). The filtered light is directed back to SOA 1 by the circulator (1 to 2). Therefore SOA 1 is used as source for ASE light and simultaneously as a first amplification stage.

The resulting spectrum has to be filtered again with another fiber-based Fabry-Perot filter (FFP-TF 2, Lambda Quest, LLC.) to remove ASE background before the light can be boosted with SOA 2 (Covega Corp.). The polarization state is adjusted with two polarization controllers (PC1 and PC2) because of the polarization dependent gain in the SOAs. The circulator and several isolators (ISO) prevent an amplification of reflected ASE.

2.2 The filter control drive waveforms

An arbitrary waveform driver generates two sinusoidal, locked AC voltage signals of same frequency $f_{\text{drive}}=\omega/(2\pi)$ with a defined, adjustable phase shift with respect to each other. This phase shifted drive signal is very crucial to account for the light transit time τ_{trans} between FFP-TF 1 and FFP-TF 2. Another effect which has to be compensated is the different phase response $\Delta\phi_R$ of both filters [31] (including contributions of the electronic drivers) at the drive frequency $f_{\text{drive}}=\omega/(2\pi)$. Both signals are amplified and superimposed to two independent controllable DC-voltages $U_{0,1}$ and $U_{0,2}$ determining the center of the wavelength sweep. The resulting waveforms $U_1(t)=U_{0,1}+A_1\cdot\sin(\omega t-\phi_1)$ and $U_2(t)=U_{0,2}+A_2\cdot\sin(\omega t-\phi_2)$ are applied to drive FFP-TF 1 and FFP-TF 2. Because the FFP-TF filters are not identical

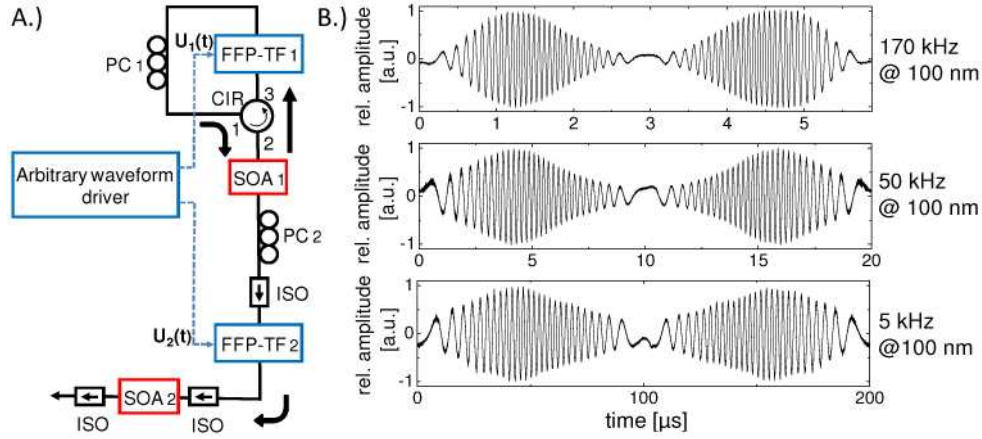


Fig. 1. (a) Setup of the wavelength swept ASE source. The arrows indicate the propagation direction of the light. (b) Interference signal acquired with a Mach-Zehnder interferometer (~ 0.5 mm delay) for 5 kHz, 50 kHz and 170 kHz filter drive frequency (10 kHz, 100 kHz, 340 kHz effective sweep rate) over a sweep range of 100 nm full width each.

with respect to their free spectral range (FSR) at zero voltage and the voltage response of the piezo actuator, we investigate the optimum drive parameter values in the following. To calculate the required drive waveforms, we consider $\lambda_k(m_k, t)$ to be the transmission maximum of FFP-TF(k), i.e. the k th filter in the sequence. The FFP-TF is operated on the m_k th order. Assuming a linear response $\alpha_{\omega, k}$ of the piezo actuator in the filter (filter k at frequency $\omega/(2\pi)$), the refractive index $n=1$ in the FFP-TFs, and the spacing between the mirror surfaces of filter k at zero voltage $d_{0, k}=c/(2\cdot\text{FSR}_k)$, the following two assumptions can be made: (i) The Fabry-Perot resonator length d_k is linearly dependent on the applied piezo voltage $U_k(t)$, yielding $d_k(U_k)=d_{0, k}+\alpha_{0, k}\cdot U_{0, k}+\alpha_{\omega, k}\cdot A_k\cdot\sin(\omega t-\phi_k)$. (ii) The Fabry-Perot condition for constructive interference leads to $\lambda_k(m_k, t)=2d_k/m_k$. Considering the first two filters, $k=1$ and $k=2$, in order to ensure optimum performance of the wavelength swept ASE source, the condition $\lambda_1(m_1, t)=\lambda_2(m_2, t-\tau_{\text{trans}}-\Delta\phi_R/\omega)$ must be fulfilled for all times t . This directly translates to three equations that have to be satisfied simultaneously:

$$\frac{m_2}{m_1} = \frac{d_{0, 2} + \alpha_{0, 2} \cdot U_{0, 2}}{d_{0, 1} + \alpha_{0, 1} \cdot U_{0, 1}}, \quad (1)$$

$$\frac{m_2}{m_1} = \frac{\alpha_{\omega, 2} \cdot A_2}{\alpha_{\omega, 1} \cdot A_1}, \quad (2)$$

$$\Delta\phi = \phi_1 - \phi_2 = \omega \cdot \tau_{\text{trans}} + \Delta\phi_R. \quad (3)$$

Equation (1) is equivalent to the fact that both center wavelengths $\lambda_{c,k}(m_k)=(2/m_k)(d_{0,k}+\alpha_{0,k}\cdot U_{0,k})$ must be matched, Eq. (2) implies equal full sweep ranges $\Delta\lambda_k(m_k)=4\alpha_{0,k}A_k/m_k$ and Eq. (3) describes the condition for the phase delay. Considering only these three equations, for every combination of FFP orders m_1 and m_2 , there is a solution yielding a desired λ_c and $\Delta\lambda$. Nevertheless, since the piezo of the FFP-TF becomes nonlinear for too high input voltages, more conditions emerge that can make the problem unsolvable. Therefore, in order to avoid high $U_{0,k}$ or A_k , it can make sense to choose different orders m_k if the FSRs of both filters at zero voltage are differing considerably. A rough estimation of the required accuracy for the filter parameter adjustment ensuring optimal operation is $\sim 0.2^\circ$ for $\Delta\phi$ and $\sim 0.2\%$ of U_{0k} and A_k .

In our setup, the FSR (zero voltage) of FFP-TF 1 was measured to be 22.2 THz, the FSR (zero voltage) of FFP-TF 2 was 27.2 THz. This difference is mainly compensated by matching the order $m_1=11$ (FFP-TF 1) with the order $m_2=9$ (FFP-TF 2). At a filter drive frequency $f_{drive}=50$ kHz, the DC voltages are $U_{0,1}=11.6$ V and $U_{0,2}=10.5$ V, yielding $\lambda_c\sim 1302$ nm, the AC voltages $A_1=1.4$ V and $A_2=0.9$ V result in $\Delta\lambda=100$ nm.

Due to thermal drift, non-linearity of the PZT and other parasitic effects, it is difficult to exactly predetermine all parameters to operate the source. Therefore, as startup procedure in our experiment, all parameters were optimized by slowly increasing the sweeping bandwidth while monitoring the power output of the source and the symmetry of both sweep directions.

3. Performance of the wavelength swept ASE source

3.1 Spectrum and output power

To demonstrate the good performance of the wavelength swept ASE source over a wide range of filter drive frequencies, we measured the interference signal (Fig. 1(b)) from a Mach-Zehnder interferometer with 0.5 mm arm length mismatch. The signals are plotted over one filter drive cycle (both sweep directions) for 5 kHz, 50 kHz and 170 kHz filter drive frequency at a full sweep range of 100 nm each. This corresponds to sweep rates of 2×5 kHz=10 kHz, 2×50 kHz=100 kHz and 2×170 kHz=340 kHz. The frequencies were chosen close to mechanical resonances of the filter to prevent heating and drift. In all cases, a average output powers of ~ 1.2 mW after FFP-TF 2 and 50 mW after the last isolator have been achieved. In spite of the fact that the wavelength swept ASE source is critically sensitive to the setting of all filter drive parameters (see section 2), a stable operation could be observed for up to half an hour at 2×170 kHz and up to many hours at 2×5 kHz and 2×50 kHz. During this time, the ASE source could be used for imaging until filter drift effects led to a reduction of the output power and the sweeping bandwidth. Then a readjustment, mainly of the DC-voltage, was required. A closed feed-back loop to control the DC-voltage may enable stable, adjustment free operation at any frequency.

Figure 2(a) shows the spectrum of the wavelength swept ASE source at a filter drive frequency of 50 kHz and 100 nm full sweep width (50 mW average output power) measured with an optical spectrum analyzer (OSA). The broad background results from ASE, emitted by SOA 2. The sharp peak features at the edges of the spectrum are due to the non-linear, sinusoidal drive, they do not occur in the time traces (see Fig. 1(b)).

3.2 Required accuracy of the phase delay setting

In order to investigate the required accuracy of the phase delay between the filter drive waveforms, Fig. 2(b) shows the measured relative output power after FFP-TF 2 for different filter phase delay values $\Delta\phi_F=\Delta\phi+\Delta\phi_R$ (red dots), being calculated from the difference in phase of the applied voltage $\Delta\phi$ and the difference in filter phase response $\Delta\phi_R$. The power was averaged over one entire intensity trace, including forward (short to long wavelengths) and backward sweep. The full sweep range was 100 nm, the filter drive frequency 50 kHz. The mechanical phase response of both filters was measured at a drive frequency of 50 kHz with the method described in [31]. We observed a difference in the phase response of $\Delta\phi_R=-1.9^\circ\pm 0.4^\circ$. Figure 2(b) is corrected for the different mechanical response. Thus, the

resulting curve has its maximum at $\Delta\phi_F=1.6^\circ\pm 0.4^\circ$ ($\Delta\phi=3.5^\circ$ phase delay in applied voltage) which is in good agreement with Eq. (3). The transit time τ_{trans} of light between the two filters is 102 ns in the setup, equivalent to 20.8 m of optical fiber or 1.8° phase shift at 50 kHz. This indicates that the phase shifted control of the two filters leads to an efficient operation by compensating light propagation effects. The full width at half maximum (FWHM) of the measured curve in Fig. 2 is 0.95° which implies a temporal width of 52.8 ns at 50 kHz. For a filter drive frequency of 5 kHz, this result translates to a temporal width of 528 ns, at 170 kHz of only 15.5 ns. The axis at the top of the graph shows the corresponding filter wavelength shift for a full sweep width of 100 nm assuming a mean filter sweep speed of 100 nm/10 μ s (triangular, linear sweep). In order to obtain the theoretically expected drop of the average power (Fig. 2(b), black line), the instantaneous transmission spectra of both filters have to be convoluted with each other. For simplification, both spectra were measured only for those

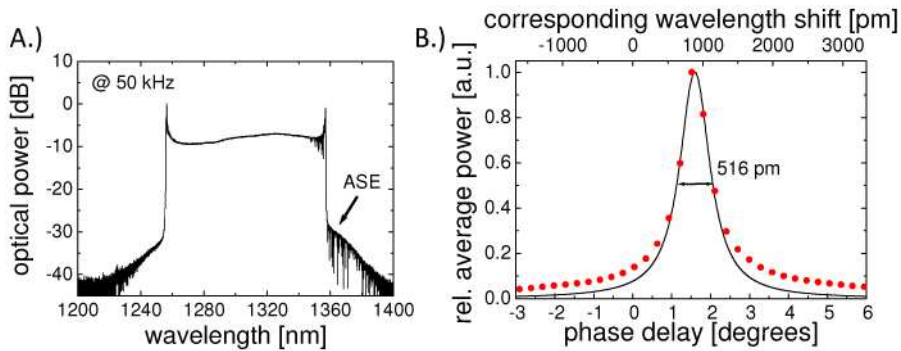


Fig. 2. (a) Output spectrum of the wavelength swept ASE source measured with an OSA at 50 kHz filter drive frequency (100 nm full sweep width) at an output power of ~ 50 mW. (b) Measured relative average power after FFP-TF 2 over the applied filter phase delay at a filter drive frequency of 50 kHz (red dots). The black line represents the relative power drop expected from theory. Additionally, the corresponding wavelength shift (100 nm full sweep range, assuming linear drive) is displayed as second x-axis.

wavelengths providing the smallest instantaneous linewidths in the center of the sweep. The FWHM is 255 pm for FFP-TF 1 at 1330 nm and 284 pm for FFP-TF 2 at 1310 nm, yielding a FWHM of 516 pm (0.93°) after convolution. Good agreement with the measured data is observed. It should be noted that *this is not the* instantaneous linewidth (see chapter 4.3), but the sensitivity with respect to timing. The deviation between measurement and theory in Fig. 2(b), mainly in the wings of the curve, is probably due to an increase of the instantaneous linewidth and a decrease of the filter sweep speed towards the turning points of the filter, making the phase delay adjustment less critical. Thus, the edges of the spectrum make a dominant contribution to the average power in case of large phase detuning.

In summary, directly after FFP-TF 2, the acquired accuracy to set the delay time of the two filter drive signals is only determined by the properties of both filters (instantaneous linewidths) and the filter drive speed. After SOA 2, saturation effects also play a role, making the relative average power less critical to phase delay ($\sim 3^\circ$ FWHM, 50 kHz). Nevertheless, for an optimum performance of the wavelength swept laser source, it is practical to optimize the drive parameters under consideration of the power after FFP-TF 2.

3.3 Instabilities and partial parasitic lasing at low frequencies

One feature of the demonstrated setup is the dual use of SOA 1, on the one hand as ASE source and on the other hand as a first amplification stage. This concept reduces the number of gain elements, no super luminescent diode (SLD) or additional SOA is required as primary broadband light source for seeding the amplification chain. Because of the dual use of SOA 1, saturation must be avoided to prevent a suppression of ASE light. Since in our case the typical average input power P_{in} to SOA 1 is about 10 μ W, the small signal gain G is ~ 30 dB and the

saturation power of the SOA is specified as 68 mW, saturation should be no problem for typical operation. The condition $P_{in} \cdot G \ll P_{sat}$ is fulfilled.

However, at low drive frequencies, we observed a characteristic feature that results from the double pass through SOA 1. The four traces in Fig. 3 show the transient optical power at different sweep frequencies over one filter drive cycle each (after the last isolator, acquired with a 150 MHz photo detector). Each trace corresponds to 100 nm full sweep width and an average output power of ~ 40 mW. In contrast to the filter drive at 50 kHz (Fig. 3(a)), the curve at 5 kHz (Fig. 3(b)) exhibits strong, parasitic modulations and high noise. At 1 kHz filter drive (Fig. 3(d)) the intensity modulation are even worse. In all three cases (A, B, D) the average input power P_{in} to SOA 1 is $\sim 8 \mu\text{W}$. The measurements show that the amplitude of

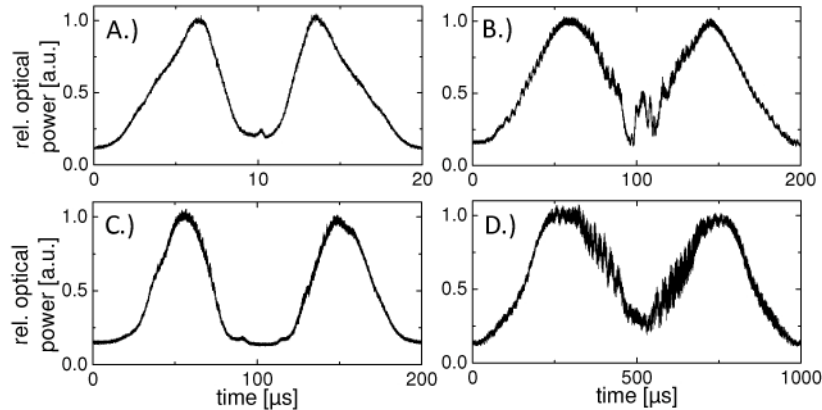


Fig. 3. Relative optical power for forward and backward sweep measured at 100 nm full sweep width and ~ 40 mW output power. The filter drive frequency is 50 kHz (a), 5 kHz (b and c) and 1 kHz (d); the average input power to SOA 1 is $\sim 8 \mu\text{W}$ (a, b and d) and $\sim 4 \mu\text{W}$ (c).

the power modulations is increasing with smaller wavelength sweep speed, slow sweeping causes higher noise. Besides the noise dependence on the filter drive speed, the observed noise also depends on the average input power P_{in} to SOA 1. A considerable reduction of the intensity modulations at 5 kHz drive can be achieved by reducing P_{in} to $\sim 4 \mu\text{W}$ and increasing the amplification of SOA 2, in order to achieve the same output power (compare Fig. 3(c) and Fig. 3(b)). To analyze the origin of the observed instabilities, we calculated the Fourier spectrum of the noise. We observe broad maxima at ~ 10.3 MHz and ~ 11.1 MHz, for sweep rates of 2×1 kHz and 2×5 kHz, respectively. These values correspond very well with the optical path length of 18.4 m, which is the length from SOA 1 to the circulator (port 2), to the FFP-TF 1, to the polarization controller, to the circulator (port 3) and finally back to SOA 1. This observation implies that residual optical feedback from the back facet of SOA 1 causes a resonance. Since in the described circuit light experiences two amplifications by the SOA, the resulting total gain of up to 60 dB is high enough for partial parasitic lasing, considering typical SOA facet reflectivities of 10^{-5} . Since the light passes through the filter, this partial parasitic lasing can only build up for very slow sweep rates of the filter, providing enough round trips. The effect is equivalent to the sweep rate limitation in standard swept laser sources [12]. So, by reducing the gain in SOA 1, this partial parasitic lasing can be avoided. Also, for high sweep rates, the problem does not occur. Increasing the length of the described circuit will also reduce this effect by increasing the transit time. Then, the effect of parasitic lasing will occur at even lower frequencies.

4. Sensitivity and roll-off characteristics

4.1 Coherence and sensitivity

In order to investigate the coherence properties of the wavelength swept ASE source, the roll-off characteristics have been analyzed. We acquired interference signals with a dual balanced

Mach-Zehnder interferometer for different delays at a filter drive frequency of 50 kHz and a full sweep range of 100 nm. The recorded fringe signals were Fourier transformed over forward sweeps (10 μ s) after numerical resampling but without apodization and the resulting point spread functions (PSF) are plotted in Fig. 4(a) (lines) against OCT ranging depth, i.e. 0.5x the arm length mismatch of the Mach Zehnder interferometer. The logarithmic scale was adjusted such that the peak values correspond to the maximum achievable sensitivity in OCT application, assuming a lossless imaging setup and no power attenuation. The maximum sensitivity was determined to be 120.6 dB at a ranging depth of 0.25 mm for an average output power of 48 mW.

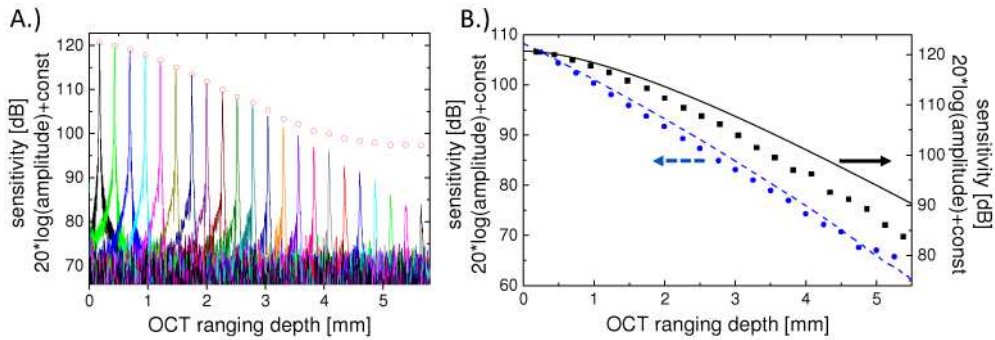


Fig. 4. (a) Logarithmic plot of the measured PSFs (lines) of the wavelength swept ASE source at 50 kHz (100 nm full sweep width), representing the measured sensitivity against different OCT ranging depths. The red circles indicate the drop of fringe contrast. (b) Logarithmic plot of the maxima of the measured PSFs over OCT ranging depth after the second pass through SOA 1 (blue circles, sensitivity left) and at the output of the wavelength swept ASE source after SOA 2 (black squares, sensitivity right). The blue, dashed line and the black, solid line indicate the corresponding drop of sensitivity, expected from theory.

The red circles represent the drop of the interference contrast extracted from the interference signal envelope. No significant difference between forward and backward sweep could be observed. The maximum resolution (3 dB Gaussian fit) was measured to be $\sim 12 \mu$ m in air, the dynamic range was ~ 50 dB.

4.2 Fringe visibility, optical phase noise and incoherent background

There are two remarkable features in Fig. 4(a). First, we can observe that neither the width of the PSFs nor the amount of side lobes change significantly over depth, even though the measurement range covers a total roll-off of ~ 40 dB. All PSFs appear sharp with negligible pedestal, only the amplitude decreases. It should be noted that the calibration signal for time to optical frequency resampling was only recorded once, before all the measurements. The fact that all PSFs are sharp even for long delays indicates that there is no drift, deviation, or low frequency oscillation on the evolution of the instantaneous center wavelength. Each sweep is very repeatable, the instantaneous wavelength does not jitter around the mean time dependent wavelength evolution, which can be the case in standard swept laser sources (random stepwise tuning). This fact may make the source highly suitable for any measurement, where an accurate knowledge of the center wavelength is required, like for fiber Bragg grating (FBG) sensing [20, 21].

The second observation in Fig. 4(a) is that at depths larger than ~ 3 mm, the red dots for the fringe visibility do not lie on the peaks of the PSFs. The roll-off over depth of the fringe visibility is significantly slower than for the PSFs. This is different from the situation found in standard wavelength swept lasers [38] or FDML lasers [31, 32], where over most of the measurement range the roll-off of the fringe visibility and the peaks of the PSFs is similar.

For the situation in the wavelength swept ASE source, we propose the following model. The considerations are similar to the more detailed analysis of *intensity noise* in [39,40], however, here we discuss the influence of *phase noise*. In our case, relative intensity noise is

cancelled out by the dual balanced differential detection. The FWHM of the combined filters is ~ 0.18 nm, i.e. ~ 31 GHz optical linewidth at 1310 nm. This means, over a time of $\sim 1/31$ GHz = 32 ps, phase and amplitude of the optical field are stable and can interfere. The optical field can be split and one part can be delayed by ± 16 ps with respect to the other field. If we consider the situation at a measurement depth of 5 mm (10 mm optical delay), the two optical fields are shifted by 33 ps with respect to each other and interfere. Due to the large temporal shift, there is no well defined phase relation between the two fields, however, the resulting, arbitrary phase difference stays constant for up to about 32 ps. If the dual balanced differential detector would be fast enough, a noise like signal with contributions up to 31 GHz would be observed. We can assume a flat noise spectrum from the SOA, so the measured noise power at the output of our 350 MHz detector will be approximately $31 \text{ GHz}/350 \text{ MHz} = 89$ times smaller, i.e. ~ 19 dB.

In a time domain picture, a signal is generated on the dual balanced differential detector by coherent contributions of the light field, incoherent background is cancelled. The coherence time is ~ 32 ps, i.e. the time over which a stable signal at the photodiode can be generated. After an average time of 32 ps, the phase relation is lost, that means every 32 ps another output value is measured at the photo-receiver. However, since the photodiodes and the detection system have an analog bandwidth of only 350 MHz, ~ 89 of these 32 ps intervals will be averaged incoherently. Because the signals of each of the 32 ps intervals have no phase relation, they add up incoherently and the voltage amplitude will be $\sim \sqrt{89} = 9.4$, i.e. 19 dB lower than a coherent sum, like at short delays. This means a random signal amplitude with -19 dB will always remain at ranging depth longer than the instantaneous coherence length.

If we now compare the roll-off in fringe visibility for 0.25 mm ranging depth and 5.6 mm ranging depth, we observe 120.6 dB and 97.4 dB, respectively. The difference of 23.2 dB has the same order of magnitude than the calculated value above of ~ 19 dB, underlining the link between optical filter bandwidth, analog detection bandwidth and incoherent noise background. This means, applying a more narrowband filter will increase the instantaneous coherence length, but it will also increase the incoherent noise floor. This fact is important for the design of OCT and other coherent ranging systems, operated at the edge of the coherence performance of the applied light source.

The described link between instantaneous optical bandwidth and minimum noise floor should be universal and also applies to FDMML lasers and conventional swept laser sources. However, in the case of lasers, the assumption of a white and flat noise background cannot always be made. Typically, in lasers higher noise at the cavity roundtrip frequency and the harmonics is observed. Even though the observed noise is usually relative intensity noise (RIN), phase noise and coherence properties might also be affected.

4.3 Improved performance by double filtering: reaching the shot noise limit

Another important feature of the wavelength swept ASE source is the advantage of an additional last filtering and amplification step, even though without it, setup and operation of the source would be even less complex. Therefore, in Fig. 4(b) the roll-off performance directly after the second pass through SOA 1 (maxima of PSFs, blue circles) is compared to the one of the wavelength swept ASE-source after FFP-TF 2 and SOA 2 (maxima of PSFs, black squares). The maxima of the PSFs represent the measured sensitivity. The maximum measured sensitivity of the wavelength swept ASE source after FFP-TF 2 and SOA 2 is 120.6 dB (48 mW). It exceeds the value obtained after SOA 1, which is measured to be 106.5 dB (0.25 mm OCT ranging depth) at 12 mW average output power. The shot noise limited sensitivity [6] for the wavelength swept ASE source after FFP-TF 2 and SOA 2 is 121.3 dB which is only 0.7 dB higher than the measured value. The theoretical value after SOA 1 is 115.4 dB which is 8.9 dB larger than the measured value. The observed difference is mainly due to the large ASE background directly after SOA 1, which contributes 80% of the total power, only 20% is coherent signal contribution. This discrepancy is due to the fact that with an input power of ~ 1 mW, SOA 2 is highly saturated, whereas the input power to SOA 1

(typically $\sim 10 \mu\text{W}$ in our setup) is limited by the available power in the ASE spectrum and the narrow FWHM of the FFP-TF 1 transmission, preventing saturation. This means that the shot noise limit can only be reached with 2 SOAs and 2 filters, reducing ASE background.

In addition to higher power and reduced ASE background (yielding higher sensitivity), another advantage of using 2 filters is the improved coherence. At an imaging depth of 4 mm, a 7.5 dB difference in sensitivity is observed (Fig. 4(b)) due to the second filtering event. The blue dashed line (after SOA 1) and black solid line (after FFP-TF 2 and SOA 2) represent the roll-off expected from theory. They are calculated by a fast Fourier transform (FFT) of either the transmission spectrum of FFP-TF 1 (255 pm instantaneous linewidth (FWHM) at 1330 nm) or FFT of the product of both transmission spectra (FFP-TF 1 at 1330 nm and FFP-TF 2 at 1310 nm with an instantaneous linewidth (FWHM) of 180 pm). Good agreement with the measured data is observed, in particular for the operation after SOA 1. The deviation from the solid curve can be caused by a non-perfect drive parameter adjustment. Another possible explanation for the slight deviation of both curves is the increasing transmission bandwidth of the FFP-TFs towards the edges of the spectrum (e.g. 388 pm FWHM at 1250 nm vs. 255 pm FWHM at 1330 pm for FFP-TF 1), degrading the coherence properties. Due to the saturation of SOA 2, the relative power in the edges of the spectrum is increased compared to the spectrum after SOA 1. Thus, a larger instantaneous linewidth at the edges of the spectrum might have a larger influence on the coherence after SOA 2 than after SOA 1, explaining the higher deviation from the expected curve.

In summary, the measurements are indicating that the roll-off characteristics are only determined by the transmission spectra of the filters, if an optimum drive parameter setting is assumed. The roll-off of the demonstrated wavelength swept ASE source cannot match that of FDML operation, where multiple filtering events occur. The R-number (compare [30]) of the wavelength swept ASE source is determined to be 0.13 mm/dB (linear fit from 0.75 mm to 5.5 mm). For FDML lasers with comparable filter specifications and SOA gain media we reported $R \sim 0.3$ mm/dB [31], $R = 1.4$ mm/dB [30] and $R \sim 0.4$ mm/dB [32]. Nevertheless, the coherence properties are comparable to standard wavelength swept laser sources driven at high wavelength tuning speeds, where only the filter bandwidth determines the instantaneous coherence length [12]. It may be sufficient for many applications, like OCT of the human retina, where a ranging depth of ~ 2 mm is sufficient. Furthermore, in order to push the roll-off performance, one or even two filters with a considerably narrower instantaneous transmission spectrum could be used instead, tolerating the resulting drawback of reduced output power. The requirement for the finesse of the filters would be relaxed, if two filters with narrow but slightly different FSR were used in order to achieve very narrow transmission bandwidth (Vernier tuning). Furthermore, the bandwidth of the first or alternatively the second filter may be increased, to make the phase adjustment less critical while still maintaining a narrow linewidth.

5. Relative Intensity Noise (RIN)

The RIN is a very important parameter to characterize light sources. The RIN properties are affecting the dynamic range in OCT application and may influence the image quality. RIN is the ratio of the standard deviation of the optical power δP over the mean optical power P . As described in [30], for periodically swept light sources, it is a reasonable and the most conservative way to analyze the power fluctuations between different sweeps at defined points in time (inter-sweep noise), rather than power fluctuations within one sweep over a sliding time window (intra-sweep noise). For the following measurements the optical power was measured with a photo detector (150 MHz analog bandwidth, Thorlabs), the resulting signal was lowpass filtered at 100 MHz and sampled with a 200 MSamples/s, 12 bit analog to digital converter card (ADC). 100 records, each consisting of 2000 samples, were acquired, each record covers one backward sweep. Thus, RIN (inter sweep noise) can be calculated for every sample in the record and hence assigned to individual wavelengths. The measured inter-sweep noise covers a bandwidth up to the system's 100 MHz analog bandwidth [30].

For a better understanding of the differences, the RIN performance of the presented wavelength swept ASE source is directly compared to the RIN of an FDML laser. Up to now, a quantitative determination of RIN for FDML lasers has only been reported at 1550 nm [30]. The FDML laser used for this comparison (1310 nm) was built in a sigma ring configuration. The complete laser, except for the delay line, consists of polarization maintaining (PM) fiber.

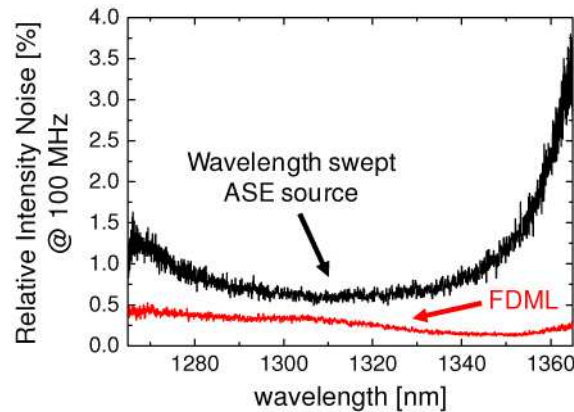


Fig. 5. RIN value versus wavelength at a filter drive frequency of 54.6 kHz and a full sweep range of 100 nm at an analog bandwidth of 100 MHz. The black line represents the RIN of the wavelength swept ASE source, the red line represents the RIN of the FDML laser.

A PM version of the FFP-TF is used (LambdaQuest, LLC.). 30% of the power was coupled out between the SOA (Covega Corp.) and the delay line, 30% after the FFP-TF and the delay line. For the RIN analysis, the output after the SOA was analyzed. In order to match the operation parameters as well as possible, both, the FDML laser and the wavelength swept ASE source were driven at the fundamental FDML frequency of 54.6 kHz (2x bidirectional sweep duration of 9.2 μ s) over a full sweep width of 100 nm and at a center wavelength of 1315 nm. The average output power of \sim 32 mW was attenuated to \sim 1.3 mW on the detector in both cases. For FDML operation, the choice of the accurate drive frequency is important for an optimum RIN performance. Thus, the RIN was measured over a frequency range of 600 Hz with a step size of 1 Hz. The frequency yielding the best RIN performance was chosen. When detuning the wavelength swept ASE source by several 10 Hz, the RIN is almost independent of the drive frequency; small differences are due to frequency dependent differences of the filter phase response (different filter phase delays). Here, the frequency with the highest average output power was chosen.

In Fig. 5, the measured RIN value is plotted versus wavelength. The black line shows the RIN of the wavelength swept ASE source for a frequency of 54.680 kHz, the red line shows the RIN of the FDML laser at 54.574 kHz. The RIN value averaged over all wavelengths is 0.28% for the FDML laser and 1.33% for the wavelength swept ASE source. Obviously, the RIN performance of the FDML laser is exceeding that of the ASE source over the whole sweep spectrum, which is not surprising due to quasi-stationary operation in FDML [13]. The average relative ratio of both RIN values is \sim 4.8, the smallest is found at 1310 nm with 1.7 and the largest value of \sim 14.3 is identified at the long wavelength side of the spectrum at 1365 nm. The reason for the strong increase in RIN of the wavelength swept ASE source at long wavelengths is unclear. It can be assumed that the last saturated amplification step in SOA 2 is considerably improving the RIN performance for the ASE source.

In standard wavelength swept lasers, RIN is considerably increasing with filter sweep speed [12, 30]. The RIN performance of the wavelength swept ASE source is comparable and may be even superior to standard wavelength swept lasers at high imaging speeds, because the lack of optical feedback prevents the appearance of a dominant noise at the laser cavity roundtrip frequency.

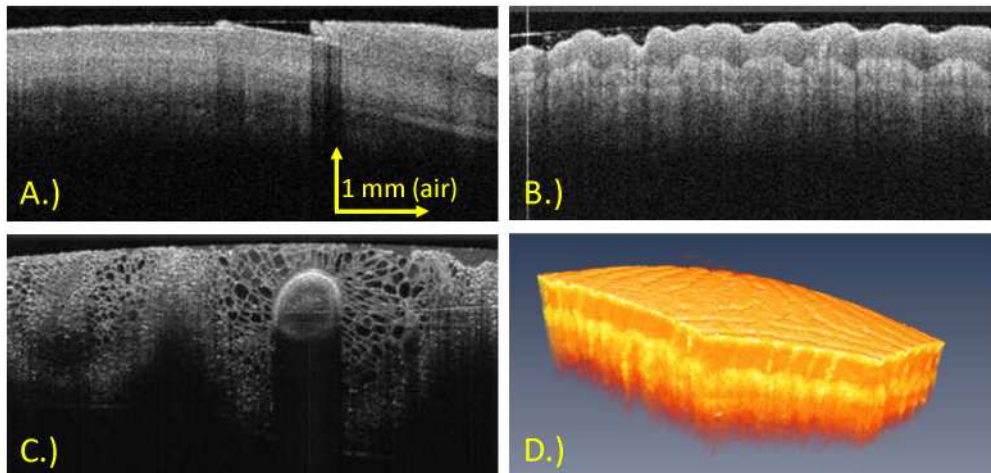


Fig. 6. OCT images acquired with the wavelength swept ASE source at 50 kHz A-line rate and 100 nm full sweep range. (a) human finger (nail fold); (b) human finger; (c) 2D OCT image of a cucumber (10x averaged); (d) Rendered 3D representation of a human finger.

6. OCT imaging

To demonstrate the OCT imaging performance of the wavelength swept ASE source, Fig. 6 shows OCT images at a filter drive frequency of 50 kHz and a full sweep range of 100 nm. The input power into the OCT setup was ~ 30 mW resulting in an average power of 10 mW on the sample. The transversal resolution was ~ 17 μm , the measured sensitivity in the setup was ~ 110 dB. Signals from the detector were sampled at 400 MSamples/s with a 12 bit ADC. The data is numerically resampled for equidistant frequency spacing before the Fourier transform. Figure 6 shows 2D OCT-images (1024 lines, 5.4 mm) of the nail fold of a human finger in vivo (no averaging, Hanning apodized) (A), skin of a human finger (no averaging, Hanning apodized) (B) and a cucumber (10x averaged, Hanning apodized) (C). Figure 6(d) is a 3D reconstruction of an OCT data set of human skin (finger) consisting of 500 frames, 512 lines and 2000 axial pixels. The image quality is comparable to other high speed swept source OCT images. The images exhibit good contrast and penetration.

7. Conclusion and outlook

In conclusion, we presented an alternative approach to realize a rapidly wavelength swept light source for high-speed OCT imaging and sensing. A sequence of optical gain elements and tunable bandpass filters, which are driven with a defined phase delay, represent an optical circuit without feedback, overcoming physical limitations in sweep repetition rate. In analogy to FDML lasers, no fundamental limit to sweep speed exists, but in contrary, an operation over a continuous range of drive frequencies is possible. We demonstrated a wavelength swept ASE source at 1300 nm consisting of two SOA gain elements and two FFP-TF filter elements. We obtained an average output power of 50 mW. A full sweep range of 100 nm at 10 kHz, 100 kHz and 340 kHz sweep rate was achieved.

We showed that two filtering and amplification steps are necessary to achieve shot noise limited detection in OCT, to suppress ASE and to improve the coherence properties of the light source. We present a physical model for the connection between the optical filter bandwidth, the analog detection bandwidth and the observed incoherent background noise in OCT application. OCT imaging was demonstrated at 50 kHz line rate with good image quality, contrast and penetration.

In the future, the demonstrated technique may be attractive for swept light sources at 800 nm and 1060 nm, where high fiber loss and dispersion impede the realization of FDML lasers. Since no km long delay fiber is required, the wavelength swept ASE source might be very promising for ophthalmic high-speed SS-OCT. By optimizing the bandwidth of the

different optical bandpass filters, the performance of the source may be further optimized. Non-equal values may be chosen to achieve good coherence properties and robust operation. Since the source appears to have extremely repeatable temporal tuning characteristics, it may be very suitable for sensing applications where a highly accurate measurement of spectral features is required, e.g. for fiber bragg grating sensors.

Acknowledgments

We would like to acknowledge support from Prof. W. Zinth at the Ludwig-Maximilians-University Munich. This research was sponsored by the Emmy Noether program of the German Research Foundation (DFG - HU 1006/2-1) and the European Union project FUN-OCT (FP7 HEALTH, contract no. 201880).

3.2.2 Fast wavelength-swept ASE source for retinal OCT at 1060 nm

Chapter 3.2.1 addressed a wavelength-swept ASE source which was operated at ~ 1300 nm and enabled OCT imaging of the human skin. However, one of the most important medical applications of OCT is medical diagnostics in the human eye, which is not possible at ~ 1300 nm due to high absorption in water. Consequently, there is the need for ultra-high speed wavelength-swept light sources operated at ~ 1060 nm or at ~ 800 nm. Compared to ~ 1300 nm, FDML operation at ~ 1060 nm is considerably more complicated due to higher dispersion, higher loss and more emphasized polarization effects in the long delay fiber [74]. At ~ 800 nm, these drawbacks are even more pronounced and FDML operation has not been demonstrated until now. All in all, the application of wavelength-swept ASE sources in these wavelength ranges could be an attractive alternative. Therefore, a wavelength-swept light source operated at ~ 1060 nm was investigated during the research work presented in this thesis and ultra-high speed retinal OCT imaging has been demonstrated. A detailed description and analysis of the wavelength-swept ASE source at ~ 1060 nm can be found in the reprint⁴ of the article

C. M. Eigenwillig, T. Klein, W. Wieser, B. R. Biedermann, and R. Huber, "Wavelength swept amplified spontaneous emission source for high speed retinal optical coherence tomography at 1060nm", *J. Biophotonics* **4**, 552-558 (2011),

which was written by me jointly with T. Klein, W. Wieser, B. R. Biedermann and R. Huber and which is attached to this chapter. Here, two different implementations of a wavelength-swept ASE source are utilized and the results are compared to each other. The first implementation is similar to the source at ~ 1300 nm, as introduced in chapter 3.2.1. However, one disadvantage is that the achievable output power is smaller due to a reduced ASE power and gain of the available SOAs and due to an increased loss of all optical components at ~ 1060 nm compared to ~ 1300 nm. Similar performance could be expected if the setup would be extended by an additional tunable filter and an additional SOA. However, the second implementation that is presented in this article is different. An Ytterbium (Yb)-doped fiber amplifier (YDFA) is used replacing the last SOA. In this way, a very high average output power exceeding 40 mW is achieved. Since forward and backward sweeps are almost identical, bidirectional operation is considerably simplified compared to other swept light sources and optical buffering is not mandatory in order to double the sweep rate. Retinal OCT imaging at 170 kHz, corresponding to an effective, bidirectional sweep rate of 340 kHz, is demonstrated. To the best of our knowledge, this has been the highest sweep rate reported for retinal SS-OCT until the date of submission of this article.

⁴ © 2011 Wiley-VCH Verlag GmbH&Co. KGaA, Weinheim.

3. New concepts of wavelength-swept light sources in application for OCT

Journal of

www.biophotonics-journal.org

BIOPHOTONICS

 WILEY-VCH

REPRINT

FULL ARTICLE

Wavelength swept amplified spontaneous emission source for high speed retinal optical coherence tomography at 1060 nm

*Christoph M. Eigenwillig, Thomas Klein, Wolfgang Wieser, Benjamin R. Biedermann, and Robert Huber**

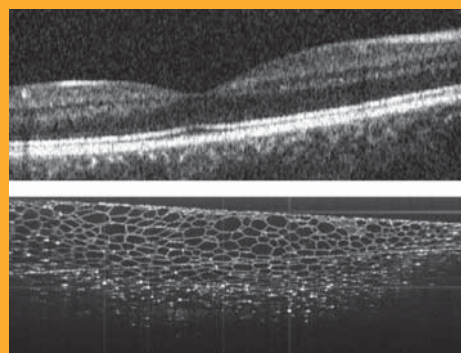
Lehrstuhl für BioMolekulare Optik, Fakultät für Physik, Ludwig-Maximilians-Universität München, Oettingenstr. 67, 80538 Munich, Germany

Received 23 September 2010, revised 28 October 2010, accepted 1 November 2010
Published online 15 November 2010

Key words: optical coherence tomography, tunable lasers, optical frequency domain imaging, ophthalmology

➔ **Supporting information** for this article is available free of charge under <http://dx.doi.org/10.1002/jbio.201000104>

The wavelength swept amplified spontaneous emission (ASE) source presented in this paper is an alternative approach to realize a light source for high speed swept source optical coherence tomography (OCT). ASE alternately passes a cascade of different optical gain elements and tunable optical bandpass filters. In this work we show for the first time a wavelength swept ASE source in the 1060 nm wavelength range, enabling high speed retinal OCT imaging. We demonstrate ultra-rapid retinal OCT at a line rate of 170 kHz, a record sweep rate at 1060 nm of 340 kHz with 70 nm full sweep width, enabling an axial resolution of 11 μm . Two different implementations of the source are characterized and compared to each other. The last gain element is either a semiconductor optical amplifier or an Ytterbium-doped fibre amplifier enabling high average output power of >40 mW. Various biophotonic imaging examples provide a wide range of quality benchmarks achievable with such sources.



OCT images of human retina and cucumber with 1060 nm wavelength swept ASE light source.

1. Introduction

Optical Coherence Tomography (OCT) is a high-resolution optical imaging technique with many different clinical applications [1]. In ophthalmology, OCT

can successfully visualize pathologies of the retina [2]. The introduction of frequency domain OCT (FD-OCT) [3, 4] led to a significant increase in sensitivity [5–7] and imaging speed compared to time-domain based systems. Besides spectrometer based

* Corresponding author: e-mail: Robert.Huber@LMU.DE, Phone: +49 89 2180 9235, Fax: +49 89 2180 9202

FD-OCT, research focuses on OCT using rapidly wavelength swept, narrow band light sources [8] (swept source OCT (ss-OCT) or optical frequency domain imaging (OFDI)). Advantages like dual balanced detection, potentially enhanced ranging depth, higher imaging speed and simple implementation of multi-spot detection [9–11] could be demonstrated. The potentially improved imaging speed is highly desirable for in vivo OCT of the human retina in ophthalmology, since patient eye motion and blinking complicate the acquisition of large, densely sampled data sets.

A key parameter for ss-OCT systems, especially for the maximum achievable acquisition speed, is the wavelength sweep rate of the light source. In standard wavelength swept lasers this speed is fundamentally limited by the build-up time of lasing from fluorescence during sweep operation [12]. Currently standard wavelength swept laser sources at 1060 nm for retinal OCT imaging achieve up to 200 kHz sweep rate [13]. This sweep speed has been achieved by using a commercially available light source with a very short cavity to reduce the sweep speed limitation described above. The light source was operated at a sweep rate of 100 kHz which was subsequently doubled to 200 kHz by applying the technique of optical buffering, a technique to time-multiplex individual wavelength sweeps demonstrated previously [14, 15].

The invention of Fourier domain mode locking (FDML) [16] for ss-OCT has overcome the physical limitations to sweep speed [12], yielding record sweep rates of >5 MHz [11]. In the 1060 nm wavelength regime, FDML operation has already been demonstrated at up to 249 kHz [15, 17–19]. However, the large dispersion, high loss and pronounced polarization effects at 1060 nm in the km long delay fibre of FDML lasers complicate FDML operation at 1060 nm compared to 1310 nm.

Another approach, which also overcomes the physical limitations set by the build-up time for las-

ing from fluorescence, is the wavelength swept amplified spontaneous emission (ASE) source, also exhibiting no fundamental sweep speed limit and additionally providing operation over a continuous range of sweep frequencies [20]. However, up to now, the wavelength swept amplified spontaneous emission (ASE) source has only been demonstrated at 1300 nm, a wavelength range that cannot be used for imaging the human retina due to high water absorption. Since, compared to 1300 nm wavelength, the lower optical performance of active and passive fibre components at 1060 nm considerably complicate operation of the source, the most important aim of this work is to investigate if sufficient performance can be achieved for high quality, ultra-fast OCT imaging of the human retina in vivo. In this paper, we investigate two different implementations of the wavelength swept amplified spontaneous emission (ASE) source at 1060 nm and investigate the image quality at record sweep rates of up to 340 kHz.

In the configuration here, ASE light alternately passes a linear cascade of (a) two different gain elements for sufficient output power and (b) two different optical bandpass filters to prevent amplification of unfiltered ASE. The filters have to be driven in a precise, phase shifted way to compensate for light propagation time between the filters.

2. Experimental setup

Figure 1 illustrates the setup of the wavelength swept ASE source at 1060 nm. All components are pigtailed with Corning Hi1060 fiber. ASE light emitted from a semiconductor optical amplifier (SOA 1, Covega Corp.) passes an optical circulator (CIR) is filtered by the first fibre-based, tunable Fabry-Perot filter (FFP-TF 1, Lambda Quest, LLC.) and is redirected back to SOA 1 by the circulator. SOA 1 is

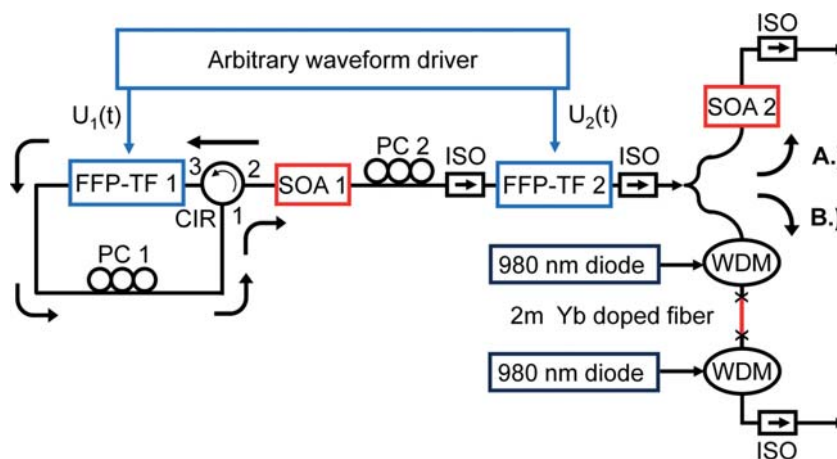


Figure 1 (online color at: www.biophotonics-journal.org) Setup of the two different implementations of the wavelength swept ASE source: The last gain element is either a semiconductor optical amplifier (SOA) (A) or an Ytterbium-doped fiber amplifier (B).

used as both, ASE source and first booster stage. In order to prevent subsequent amplification of unfiltered ASE, light has to be filtered again by the second FFP-TF 2 (Lambda Quest, LLC). Two precisely set, sinusoidal voltage signals $U_1(t)$ and $U_2(t)$ are applied to both filters to ensure optimal operation [20]. Due to thermal drifts in the filter slight corrections of the filter drive parameters can be necessary to maintain optimal operation over a time scale larger than ~ 30 min. For a potential commercial product active feedback control will be required. We did not observe problems with different non-linear response characteristics of the filters. In the first configuration of the source, a second SOA (SOA 2 – Alphion Corp.) serves as final amplification step (configuration A).

However, since the fiber components and SOAs at 1060 nm exhibit higher loss and lower gain compared to 1310 nm devices, the average output power of configuration A is rather small compared to the source at 1300 nm. Hence, a second, alternative approach using an Ytterbium (Yb)-doped fiber amplifier (YDFA) (configuration B) is investigated. YDFAs have been demonstrated to increase the output power in other types of swept light sources before [18, 21]. Pump light from two diodes (Bookham Inc.) is coupled to ~ 2 m of Yb-doped fibre (Liekki Yb1200-4/125) via two wavelength division multiplexers (WDM) enabling forward and backward pumping. The fibre length was optimized for a compromise between maximum output power efficiency and minimum unfiltered ASE background.

Polarization controllers (PC) are required to maximize the polarization dependent gain of both SOAs,

whereas the YDFA is polarization independent. Optical isolators (ISO) are necessary preventing that back-reflected light affects the SOA amplification or causes potential Q-switching in the Yb-doped fiber. High optical isolation (>30 dB) is required prior to FFP-TF 2 and after the last WDM.

Operation over a continuous drive frequency range is possible and only limited by the filter response function [22]. Since for ASE swept light sources both sweep directions have almost identical properties [20], the bidirectional operation of the filter leads to $2 \times$ higher effective sweep rate without any additional optical setup. So unlike standard wavelength swept lasers which often require external buffering to achieve ultra-high sweep rates [13, 14, 23], with wavelength swept ASE sources both sweep directions of the bidirectional sweep can directly be used.

For characterization two filter drive frequencies were chosen, 55 kHz (110 kHz effective sweep rate) and 170 kHz (340 kHz effective sweep rate), which are close to two dominant mechanical resonance peaks of both filters.

3. Spectrum and output power

Figure 2(A1) shows the time integrated spectrum of configuration A, measured with an optical spectrum analyzer (OSA) at 55 kHz. Figure 2(A2) presents the dual balanced interference signal (both sweep directions) acquired with a Mach-Zehnder interferom-

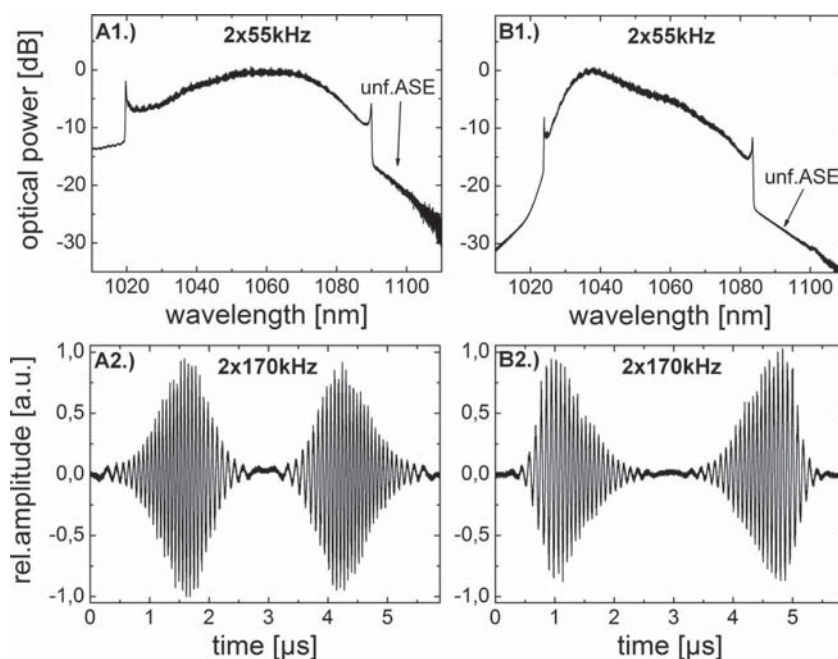


Figure 2 Time integrated spectra acquired at 2×55 kHz sweep rate (**A1** and **B1**) and dual balanced interference signals measured at 2×170 kHz sweep rate (**A2** and **B2**) characterizing the source in case of amplification with an SOA (A1, B1) and an YDFA (A2, B2).

eter (MZI) at 170 kHz. Both measurements are performed using SOA amplification featuring 70 nm full sweep range. The average seed power prior to SOA 2 is $\sim 130 \mu\text{W}$ which is much lower compared to the corresponding power of $\sim 1.2 \text{ mW}$ for the source at 1300 nm. Thus, SOA 2 is not saturated to the same degree leading to a higher background of unfiltered ASE (determined to be $\sim 18\%$ of the total power, see Figure 2(A1)). The achievable average output power after SOA 2 is $\sim 4 \text{ mW}$. The measured axial resolution (FWHM of Gaussian fit in point spread function (PSF) in OCT application) is $\sim 15 \mu\text{m}$ (in air) and $\sim 11 \mu\text{m}$ in tissue. The results for configuration B using an YDFA for higher output power are shown in Figure 2(B1) and Figure 2(B2). Here, very high average output power of 40 mW can easily be realized ($\sim 20\%$ is unfiltered ASE).

The high level of available pump power enables considerably higher output power. Limiting factors may be damage of the WDMs or potential Q-switching in the Yb-fiber. Since the YDFA exhibits a reduced spectral gain width compared to SOA amplification, the axial resolution is slightly reduced and measured to be $\sim 19 \mu\text{m}$ in air ($\sim 14 \mu\text{m}$ in tissue) at a full sweep width of 60 nm.

The differences in spectral shape and output power at 55 kHz and 170 kHz are negligible, independent of the applied amplification scheme. It should be underlined that the high output power may enable hardware spectral shaping for better axial resolution [24].

4. Coherence properties

In order to characterize the instantaneous coherence length, figure 3 shows the PSFs for different OCT ranging depths in case of SOA amplification at $2 \times 55 \text{ kHz}$ sweep rate (A) and YDFA at $2 \times 55 \text{ kHz}$ (B) and $2 \times 170 \text{ kHz}$ (C) sweep rate. In order to be able to compare roll-off performance, the R-numbers (see [25], here: linear fit over 5 mm) are determined to be 0.17 mm/dB (Figure 3(A)), 0.18 mm/dB (Figure 3(B)) and 0.15 mm/dB (Figure 3(C)) which is sufficient for most retinal imaging applications and is close to the theoretical limit ($\sim 0.19 \text{ mm/dB}$ @5 mm) given only by the transmission widths of both filters (here: $\sim 160 \text{ pm}$ FWHM). For a sweep rate of $2 \times 170 \text{ kHz}$, the R-number is slightly smaller, probably since a precise filter drive is more difficult.

The dynamic range was measured to be $\sim 50 \text{ dB}$ in all cases. Another important parameter is relative intensity noise (RIN) [25]. In the case of the SOA amplification, the ortho RIN [25] was measured to be 3.9% (average over one sweep) at an analog bandwidth of 100 MHz ($2 \times 55 \text{ kHz}$ sweep rate, 60 nm full sweep width, $\sim 4 \text{ mW}$ output power). In-

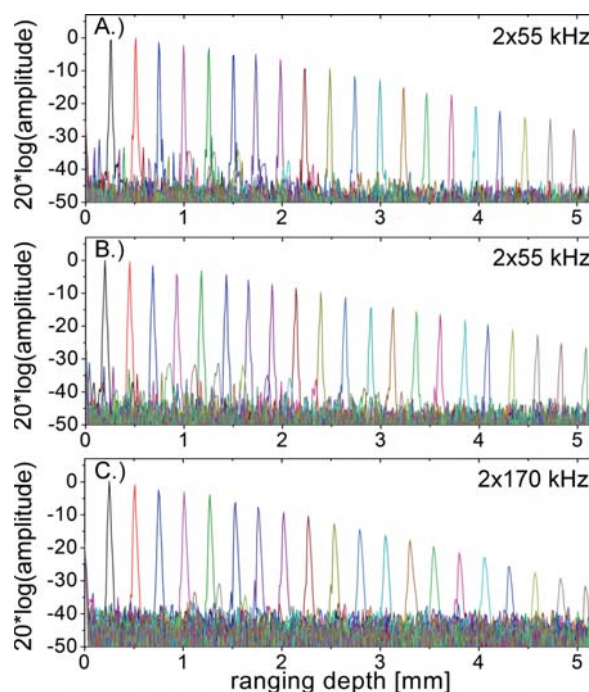


Figure 3 (online color at: www.biophotonics-journal.org) PSFs for different OCT ranging depths acquired with SOA amplification at $2 \times 55 \text{ kHz}$ sweep rate (A) and with YDFA at $2 \times 55 \text{ kHz}$ (B) and $2 \times 170 \text{ kHz}$ (C).

terestingly the mean ortho RIN measured in case of YDFA ($2 \times 55 \text{ kHz}$ sweep rate, 60 nm full sweep width, $\sim 32 \text{ mW}$ output power, 100 MHz analog bandwidth) was 3.7% which is very similar to the result for SOA post-amplification in spite of a ~ 8 times higher amplification factor.

5. OCT imaging and sensitivity

For OCT imaging, a standard Michelson interferometer with two 50/50 couplers for dual balancing is used. The dispersion in reference and sample arm was physically matched best possible. At $2 \times 55 \text{ kHz}$ sweep rate (using YDFA) the sensitivity is determined to be $\sim 98 \text{ dB}$ at an average sample power of $\sim 4.5 \text{ mW}$ (shot noise limit 109 dB [5]). Accounting for an interferometer loss of $\sim 6 \text{ dB}$, the discrepancy of 5 dB compared to the shot noise limit is probably due to unfiltered ASE background and larger excess noise [26]. In the case of the SOA booster stage (configuration A), the power on the sample was $\sim 650 \mu\text{W}$ and the sensitivity ($2 \times 55 \text{ kHz}$) was measured to be $\sim 89 \text{ dB}$.

Figure 4(A), (B) and (C) show OCT images of human nail fold (no averaging), human finger ($5 \times$

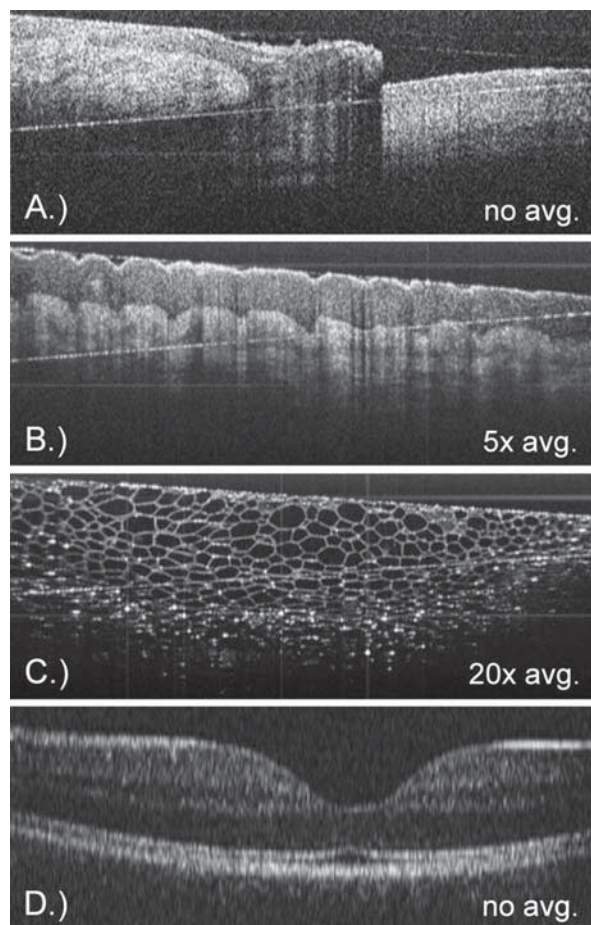


Figure 4 2D-OCT images of human nail fold ((A), $\sim 5.4 \text{ mm} \times 2.6 \text{ mm}$ in air), human finger ((B), $\sim 5 \text{ mm} \times 2.6 \text{ mm}$ in air) and a cucumber ((C), $\sim 4.6 \text{ mm} \times 2.6 \text{ mm}$ in air) acquired with YDFA at $2 \times 170 \text{ kHz}$. 2D-OCT image of the fovea ($\sim 9 \text{ mm} \times 0.7 \text{ mm}$ in air) acquired with SOA amplification and associated media file showing a fly-through animation (slowed down from 166 frames/s to 30 frames/s) at $2 \times 170 \text{ kHz}$ (D).

averaging) and a cucumber ($20 \times$ averaging), respectively, acquired with the YDFA ($\sim 4.5 \text{ mW}$ on sample). OCT imaging of the human retina was demonstrated (no averaging) with the SOA based amplification ($\sim 650 \mu\text{W}$ on sample, Figure 4(D)). The OCT line rate was 170 kHz because only one sweep direction was used, identical imaging performance at $2 \times 770 = 340 \text{ kHz}$ is expected without additional hardware. The associated media file (Figure 4(D), see Supporting Material online) shows a fly-through animation, slowed down from 166 frames/s to 30 frames/s. The promising image quality clearly demonstrates the high potential of the wavelength swept ASE source for high-speed OCT.

6. Conclusion and outlook

In conclusion we presented for the first time a wavelength swept ASE source in the 1060 nm wavelength range, relevant for ophthalmology, and presented OCT imaging of human retina in vivo with this source. To the best of our knowledge, the bidirectional wavelength sweep rate of $2 \times 170 \text{ kHz} = 340 \text{ kHz}$ is the highest achieved by wavelength swept light sources for retinal OCT reported to this date.

Ultra high speed retinal imaging at 170 kHz was demonstrated at a full sweep range of 70 nm . To overcome problems with the, compared to 1300 nm , higher losses and lower performance of 1060 nm fibre components, an YDFA amplification scheme was implemented and analyzed, yielding an average output power in excess of 40 mW .

Like most of the presented 1060 nm ss-OCT setups to date, the sensitivity is slightly below the theoretical shot noise limit, but this might be improved by more sophisticated detection electronics in the future. However, the achieved good OCT image quality in combination with sufficient output power to enable multi-spot scanning makes the presented light source very attractive for future high speed retinal OCT imaging setups. Unlike to all other swept light sources used for retinal OCT imaging, no external buffering lines of km-long fibers [13, 15, 17] are required to achieve $>200 \text{ kHz}$ sweep rate, which makes this source potentially cheaper and simpler than the alternative approaches of FDML or short cavity lasers.

Acknowledgements We would like to acknowledge support from Prof. W. Zinth at the Ludwig-Maximilians-University Munich. This research was sponsored by the Emmy Noether program of the German Research Foundation (DFG-HU 1006/2-1) and the European Union project FUN OCT (FP7 HEALTH, contract no. 201880).



Christoph Martin Eigenwillig studied physics at the LMU Munich, Germany, where he received his Diploma in 2007. During his diploma thesis he worked on ultracold atoms, Bose-Einstein condensates and degenerate fermionic gases at the chair of Prof. Theodor Hänsch. Since 2007 he is a

Ph.D. student in the Emmy Noether group of Robert Huber at the Chair for BioMolecular Optics (Prof. Zinth) at the LMU.



Thomas Klein studied physics in Karlsruhe, Southampton and at the LMU Munich, Germany. In 2008, he joined the Emmy Noether group of Robert Huber at the chair for BioMolecular Optics (Prof. Zinth) at the LMU. He received his Diploma in 2009 and is now a Ph.D. student in the same group.



Wolfgang Wieser studied physics at the LMU Munich, Germany, where he received his Diploma in 2007. During his diploma thesis he worked on ultracold atoms, Bose-Einstein condensates and degenerate fermionic gases at the chair of Prof. Theodor Hänsch. In 2008 he joined the Emmy Noether

group of Robert Huber as Ph.D. student at the Chair for BioMolecular Optics (Prof. Zinth) at the LMU.



Benjamin Robert Biedermann studied physics at the Ruprecht-Karls-Universität in Heidelberg and the LMU Munich, Germany, where he received his Diploma in 2007. During his diploma thesis he worked on optical spin initialization and laser spectroscopy on single quantum dots in the group of

Prof. Khalid Karrai. Since 2007 he is a Ph.D. student in the Emmy Noether group of Robert Huber at the Chair for BioMolecular Optics (Prof. Zinth) at the LMU.



Robert Huber studied physics at the LMU Munich, Germany, where he received his Ph.D. in 2002 for work on ultrafast electron transfer processes. In 2003 he worked as Postdoc at the University of Frankfurt on protein dynamics and molecular switches. From 2003 to 2006 he joined the group of

Prof. J. Fujimoto at the Massachusetts Institute of Technology. Since 2007 he has been leading an independent junior research group in the Emmy Noether programme of the German research foundation at the LMU.

References

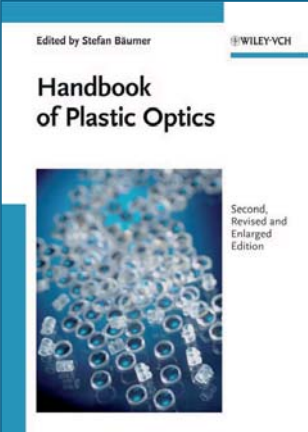
- [1] D. Huang, E. A. Swanson, C. P. Lin, J. S. Schuman, W. G. Stinson, W. Chang, M. R. Hee, T. Flotte, K. Gregory, C. A. Puliafito, and J. G. Fujimoto, *Science* **254**, 1178–1181 (1991).
- [2] C. A. Puliafito, M. R. Hee, C. P. Lin, E. Reichel, J. S. Schuman, J. S. Duker, J. A. Izatt, E. A. Swanson, and J. G. Fujimoto, *Ophthalmology* **102**, 217–229 (1995).
- [3] A. F. Fercher, C. K. Hitzenberger, G. Kamp, and S. Y. Elzaiat, *Opt. Commun.* **117**, 43–48 (1995).
- [4] G. Häusler and M. W. Lindner, *J. Biomed. Opt.* **3**, 21–31 (1998).
- [5] M. A. Choma, M. V. Sarunic, C. H. Yang, and J. A. Izatt, *Opt. Express* **11**, 2183–2189 (2003).
- [6] J. F. de Boer, B. Cense, B. H. Park, M. C. Pierce, G. J. Tearney, and B. E. Bouma, *Opt. Lett.* **28**, 2067–2069 (2003).
- [7] R. Leitgeb, C. K. Hitzenberger, and A. F. Fercher, *Opt. Express* **11**, 889–894 (2003).
- [8] S. H. Yun, G. J. Tearney, J. F. de Boer, N. Iftimia, and B. E. Bouma, *Opt. Express* **11**, 2953–2963 (2003).
- [9] M. K. K. Leung, A. Mariampillai, B. A. Standish, K. K. C. Lee, N. R. Munce, I. A. Vitkin, and V. X. D. Yang, *Opt. Lett.* **34**, 2814–2816 (2009).
- [10] K. Koenig, M. Speicher, R. Bueckle, J. Reckfort, G. McKenzie, J. Welzel, M. J. Koehler, P. Elsner, and M. Kaatz, *J. Biophotonics* **2**, 389–397 (2009).
- [11] W. Wieser, B. R. Biedermann, T. Klein, C. M. Eigenwillig, and R. Huber, *Opt. Express* **18**, 14685–14704 (2010).
- [12] R. Huber, M. Wojtkowski, K. Taira, J. G. Fujimoto, and K. Hsu, *Opt. Express* **13**, 3513–3528 (2005).
- [13] B. Potsaid, B. Baumann, D. Huang, S. Barry, A. E. Cable, J. S. Schuman, J. S. Duker, and J. G. Fujimoto, *Opt. Express* **18**, 20029–20048 (2010).
- [14] R. Huber, D. C. Adler, and J. G. Fujimoto, *Opt. Lett.* **31**, 2975–2977 (2006).
- [15] V. J. Srinivasan, D. C. Adler, Y. L. Chen, I. Gorczynska, R. Huber, J. S. Duker, J. S. Schuman, and J. G. Fujimoto, *Invest. Ophthalmol. Vis. Sci.* **49**, 5103–5110 (2008).
- [16] R. Huber, M. Wojtkowski, and J. G. Fujimoto, *Opt. Express* **14**, 3225–3237 (2006).
- [17] R. Huber, D. C. Adler, V. J. Srinivasan, and J. G. Fujimoto, *Opt. Lett.* **32**, 2049–2051 (2007).
- [18] M. K. Harduar, A. Mariampillai, B. Vuong, K. H. Y. Cheng, L. R. Chen, X. Gu, B. A. Standish, and V. X. D. Yang, in: *Fiber Lasers VII: Technology, Systems, and Applications* (SPIE, Photonics West, San Francisco 2010), 75802S.

- [19] S. Marschall, T. Klein, W. Wieser, B. R. Biedermann, K. Hsu, K. P. Hansen, B. Sumpf, K. H. Hasler, G. Erbert, O. B. Jensen, C. Pedersen, R. Huber, and P. E. Andersen, *Opt. Express* **18**, 15820–15831 (2010).
- [20] C. M. Eigenwillig, B. R. Biedermann, W. Wieser, and R. Huber, *Opt. Express* **17**, 18794–18807 (2009).
- [21] F. D. Nielsen, L. Thrane, K. Hsu, A. Bjarklev, and P. E. Andersen, *Proc. SPIE* **6429**, J4291 (2007).
- [22] C. M. Eigenwillig, B. R. Biedermann, G. Palte, and R. Huber, *Opt. Express* **16**, 8916–8937 (2008).
- [23] W. Y. Oh, B. J. Vakoc, M. Shishkov, G. J. Tearney, and B. E. Bouma, *Opt. Lett.* **35**, 2919–2921.
- [24] B. Biedermann, W. Wieser, C. Eigenwillig, G. Palte, D. Adler, V. Srinivasan, J. Fujimoto, and R. Huber, *Opt. Lett.* **33**, 2556–2558 (2008).
- [25] B. R. Biedermann, W. Wieser, C. M. Eigenwillig, T. Klein, and R. Huber, *Opt. Express* **17**, 9947–9961 (2009).
- [26] Y. L. Chen, D. M. de Bruin, C. Kerbage, and J. F. de Boer, *Opt. Express* **15**, 16390–16399 (2007).

Edited by **STEFAN BÄUMER**
Philipps Eindhoven

Handbook of Plastic Optics

2nd revised and enlarged edition



Edited by Stefan Bäumer
WILEY-VCH
Handbook of Plastic Optics
Second, Revised and Enlarged Edition

A coherent overview of the current status of injection molded optics, describing in detail all aspects of plastic optics, from design issues to production technology and quality control.

This updated second edition is supplemented by a chapter on the equipment and process of injection wells as well as a look at recent applications.

The contributors, each one a leading expert in their discipline, have either a background in or strong ties to the industry, thus combining a large amount of practical experience.

With its focus firmly set on practical applications, this is an indispensable reference for all those working in optics research and development.

2010. XII, 296 pages,
approx. 80 figures, 60 in color.
Hardcover.
€ 109.- /£ 90.- /US\$ 175.-
ISBN: 978-3-527-40940-2

WILEY-VCH • P.O. Box 10 11 61 • 69451 Weinheim, Germany
Fax: +49 (0) 62 01 - 60 61 84
e-mail: service@wiley-vch.de • http://www.wiley-vch.de

Register now for the free
WILEY-VCH Newsletter!
www.wiley-vch.de/home/pas



4 Picosecond pulse generation with an FDML laser

Chapter 3 focused on investigating and analyzing new concepts of wavelength-swept light sources (including new operation modes of FDML lasers) with the aim of improving application for SS-OCT. However, the subject of this chapter is quite different, since it deals with a completely novel approach of short pulse generation using FDML lasers and a subsequent temporal compressor stage. The goal of this chapter is to introduce and motivate this new technique (chapter 4.1), explain the experimental setup (chapter 4.2) and present and discuss the latest results (chapter 4.3). These experiments give an insight into the coherence properties of the FDML laser and point out important FDML parameters that influence the performance of pulse generation. Additionally, similar pulse generation experiments using incoherent wavelength-swept light sources (comparable to those introduced in chapter 3.2) are demonstrated and compared to the results obtained with the FDML laser.

4.1 Motivation and overview of the work

As already described in chapter 2.2.2.1, the ideal FDML laser can be seen as a new mode of stationary laser operation, where there exists a definite phase and amplitude relation in the electric field evolution between different sweeps and within each sweep (high coherence). In the frequency domain, this results in longitudinal modes which are coupled and exhibit a definite phase relation. Therefore, the idea to temporally compress the sweeps (or equivalently the highly chirped, very long pulses) after the output of the FDML laser is an interesting new approach for short pulse generation, since, under previous assumptions, the generation of almost time-bandwidth limited pulses should be possible. The typical bandwidth of FDML lasers using SOAs can exceed 100 nm at ~ 1300 nm or ~ 1550 nm. Thus, the perfect FDML laser principally should enable the generation of sub 100 fs pulses, assuming an ideal compression. Moreover, this technique can provide several advantages compared to standard mode locked semiconductor lasers [9], which suffer from short carrier relaxation times of ~ 100 ps impeding high pulse energies. This problem can be overcome using FDML lasers, where the whole wavelength sweep and thus the total energy per sweep, which can be as high as several 100 nJ, is stored optically in the long fiber delay line and not as population inversion in the gain medium. This approach therefore principally allows for very high pulse energies at repetition rates of several 100 kHz generated directly from the oscillator. Note that, benefitting from the same advantage, high pulse energies have been real-

ized using semiconductor chirped pulse amplification concepts [232-234]. Another potential advantage of the FDML approach is that this novel technique could provide direct access to the phase, i.e. the chirp of the pulses and direct access to the intensity shape of the pulses via control of the tunable bandpass filter and via current modulation of the SOA, respectively. This means that short pulse generation with FDML lasers inherently provides a pulse shaping mechanism.

However, the experimental implementation is challenging since the subsequent temporal compression of the sweeps requires a very large amount of dispersion that has to be added after the FDML laser, resulting in loss in optical power and reduced pulse energy. Since optimal temporal compression over a large spectral bandwidth is not easily achievable, the optical bandwidth of the pulses can be limited. This can additionally reduce the optical pulse energy. In the experiments performed within the framework of this thesis, temporal compression was enabled by light passing at least 15 km of highly dispersive fiber (dispersion compensation fiber (DCF), see chapter 2.2.2.2). Experimental restrictions of this compressor stage are discussed in chapter 4.2.2. One finding of the experiments, described in chapter 4.3.3, is that bandwidth limited pulses cannot be achieved under currently given experimental conditions. The reason is that the FDML laser dynamics does not provide a fully coherent evolution of the electric field and optimal mode-locking. However, as explained in chapter 4.3.5, the obtained results demonstrate that the different wavelength components of the sweeps must exhibit at least partially coherence. Furthermore, they show that the achievable temporal pulse width strongly depends on characteristic internal FDML parameters which influence the coherence properties of the laser but currently cannot be modified as desired due to experimental restrictions. Besides the fact that this new concept might be an attractive candidate for future semiconductor pulse lasers, it also provides a good opportunity to gain an insight into the FDML laser coherence properties.

Based on a theoretical model of the FDML laser, numerical simulations have been performed and used to describe FDML laser dynamics [15]. The simulations were conducted by Sebastian Todor and Dr. Christian Jirauschek, who is the supervisor of the junior research group “Modeling of Quantum Cascade Devices” at the Institute of Nanoelectronics at Technische Universität München (TU). They work in close collaboration with our group, which is responsible for the experimental input. The simulations are based on numerically solving a generalized nonlinear Schrödinger equation using a split-step Fourier method. An important step was the introduction of a swept filter reference frame moving along with the center transmission wavelength. This allows for a considerably smaller number of grid points in the numerical simulation and therefore a reduced computational effort. The theoretical model comprises chromatic dispersion and self phase modulation in the delay fiber, coupling between the gain and the refractive index as well as saturation effects in the SOA and the spectral filtering of the bandpass filter [15, 228]. Several comparative studies showed good agreement between experiment and theory in terms of, for example, output power or instantaneous

linewidth [15, 228]. The interaction of different effects with regard to stationary operation in FDML lasers was examined [210].

On the basis of this numerical model, Sebastian Todor and Dr. Christian Jirauschek also performed numerical simulations in order to describe the generation of short pulses with FDML lasers. The chromatic dispersion required for temporal compression was introduced by adding one smooth phase trajectory to the phase evolutions of the electric field of all sweeps resulting from numerical simulations. Important experimental parameters have been measured by our group and used as input for the simulations. These are the wavelength dependent gain or saturation power of the SOA, the residual dispersion in the fiber delay, the wavelength dependent cavity loss and the filter drive properties and the spectral transmission function of the bandpass filter. The results of the simulation have been compared to the pulse compression experiments (see chapter 4.3.3). The theoretical description is in particular interesting since it provides the possibility to analyze parameter regimes which are currently not accessible in the experiment.

4.2 Experimental setup

4.2.1 FDML cavity at 390 kHz and optical switching

The all fiber based FDML resonator (see Figure 4.1) used for these experiments is based on a polarization independent SOA (Covega-SOA1117), which has a maximum gain at ~ 1550 nm. This wavelength range has the advantage that the addition of a large amount of negative dispersion required for temporal compression can be realized in a comparably easy way using dispersion compensation fiber (DCF), providing a maximum negative dispersion at ~ 1570 nm (see Figure 2.9). The cavity is arranged in a sigma-ring configuration, reducing polarization effects in the delay line (see chapter 2.2.3.1). The isolator and the circulator in the cavity ensure unidirectional lasing.

Since the achievable temporal pulse widths are highly dependent on the coherence properties of the FDML laser, the chromatic dispersion in the FDML cavity must be minimized [14, 185]. Thus, the linear delay line consists of 246 m of standard single mode fiber (Corning SMF 28) and 16m of dispersion compensation fiber (OFS-HFDK) (see chapter 2.2.2.2 and Figure 2.9). This results in a minimum residual dispersion of the fiber delay close to ~ 1555 nm. The residual dispersion is considerably smaller than 0.25 ps/nm within a spectral window of ~ 40 nm.

A crucial element of the FDML cavity is the home-built, bulk-optic tunable Fabry-Pérot filter (BFP-TF) [8], since it allows for FDML operation with very high sweep speeds ($v_{Sweep} \sim 250$ nm/ μ s) at a very high filter drive frequency $f_{Filter} \sim 390$ kHz. This is of high importance for pulse generation due to several reasons: On the one hand, the most important reason is the fact that the magnitude of the dispersion that has to be added for temporal compression is equal to the filter sweep speed ($D = -1/v_{Sweep}$). Conse-

4. Picosecond pulse generation with an FDML laser

quently, v_{Sweep} should be as large as possible in order to minimize the required length of the DCF in the temporal compressor stage and therefore the fiber loss. On the other hand, a higher filter drive frequency f_{Filter} is advantageous regarding the coherence properties of the FDML laser. The reason is as follows: Assuming a predefined filter sweep speed v_{Sweep} determined by the amount of the added dispersion, FDML operation at a higher filter drive frequency f_{Filter} results in a reduced filter sweep bandwidth $\Delta\lambda_{FilterSweep}$. According to the simple model introduced in chapter 2.2.2.1, the ratio of the filter gate time to the round-trip time mismatch $\Delta\tau_G/\Delta\tau_M$ is therefore higher. Another advantage of the home-built BFP-TF is the possibility to easily vary the filter bandwidth $\Delta\lambda_{Filter}$ by changing the free spectral range of the filter.

In order to extract optical power from the FDML laser, a fused 50/50 fiber coupler (FC) is used. The light is directed to a second polarization dependent booster SOA (Covega-BOA1004) (see Figure 4.1), which amplifies the light but also plays the role of an optical switch using a fast current modulator (Wieser Labs-WL-LDC10D). In this way, a definite part of each forward sweep can be extracted, defining the temporal sweep width ΔT , the sweep bandwidth $\Delta\lambda$ and the center sweep wavelength λ_C , which are relevant for temporal compression (see Figure 4.3a, red line). Light is either amplified from ~ 10 mW average power before the booster SOA to ~ 47 mW instantaneous power (SOA on) after the booster SOA or suppressed by a factor >10 dB (SOA off). Polarization controllers (PC) (see chapter 2.2.2.2) enable adjustment of the polarization state in the fiber.

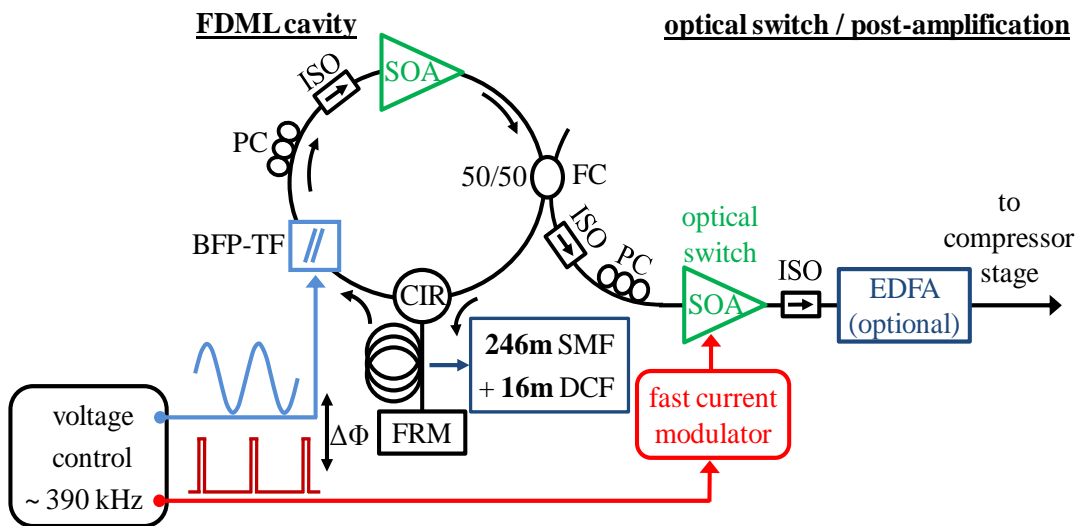


Figure 4.1: FDML cavity in sigma-ring configuration operated at ~ 1560 nm with a filter drive frequency of 390 kHz. The fiber delay line, arranged in a sigma-ring configuration, is dispersion compensated using DCF. An additional SOA is used for post-amplification and as optical switch via fast current modulation. Two locked and phase shifted ($\Delta\Phi$) voltage signals are generated for the sinusoidal filter drive and for the control of the SOA current switching. Optionally, erbium doped fiber amplification (EDFA) is applied to increase the power of the truncated sweeps. (SOA: Semiconductor optical amplifier, BFP-TF: Bulk optic Fabry-Pérot tunable filter, ISO: Optical isolator, PC: Polarization controller, FRM: Faraday rotation mirror, CIR: Optical circulator, FC: Fused fiber coupler, BFP-TF: Bulk Fabry-Pérot tunable filter, SMF: Standard single-mode fiber, DCF: Dispersion compensation fiber)

A two channel voltage control generates, on the one hand, the sinusoidal filter drive signal enabling sinusoidal wavelength tuning of the BFP-TF (Channel 1) and, on the other hand, the control signal for the fast current modulation (Channel 2). Both channels are phase locked at a repetition rate of 390 kHz with an adjustable phase difference $\Delta\Phi$. Additionally, a DC-voltage signal determines the filter sweep offset wavelength of the bandpass filter. An active feedback loop is implemented, controlling the DC-voltage, in order to keep the center sweep wavelength λ_C constant at a certain value. This is realized using an optical spectrum analyzer (OSA).

4.2.2 Temporal compressor stage and filter drive parameters

The temporal compressor stage is graphically sketched in Figure 4.2. Temporal compression is achieved with light passing a ~ 15 km long DCF spool (Corning HFDK) either a single time (1x pass, black) or, optionally, four times (4x pass, blue). In the latter case a quadruple pass of the fiber is possible since light passes the fiber in two directions and in each direction two times with orthogonal polarization states. This can be realized using an optical circulator, a polarization beam splitter (one output not connected), a Faraday rotation mirror and a conventional fiber mirror (see Figure 4.2).

For all experiments a center wavelength of $\lambda_C=1560$ nm is chosen, since this wavelength range is a good trade-off between a large amount of negative dispersion (-4 ns/nm), a limited fiber loss (~ 8.5 dB) in the compressor stage and a good dispersion compensation in the FDML cavity.

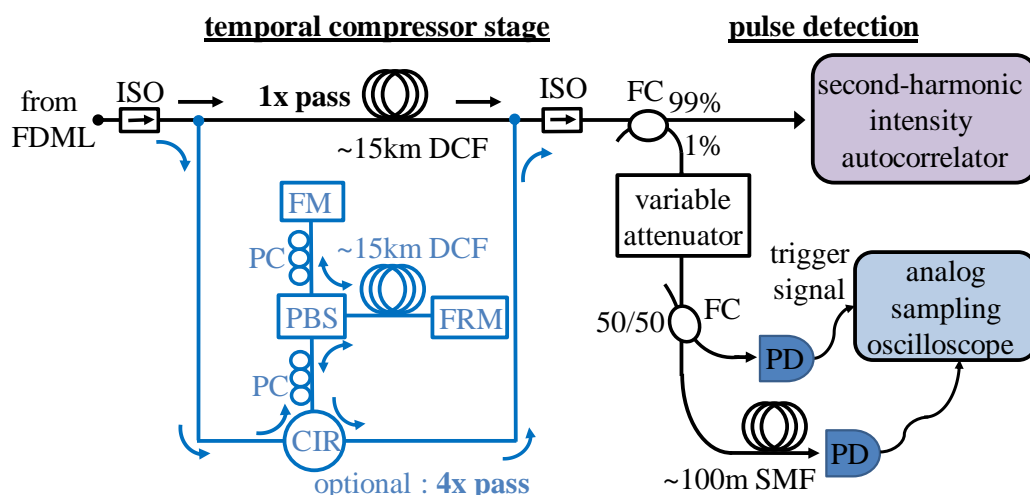


Figure 4.2: Temporal compressor stage and pulse detection. Temporal compression is realized by a single pass (1x pass) of the light through ~ 15 km of dispersion compensation fiber (DCF) (black) or, optionally, by a quadruple pass (4x pass) of the light through ~ 15 km long DCF under two directions and two orthogonal polarization states (blue). The pulses are either analyzed with a second-harmonic intensity autocorrelator or using a fast photodiode and a fast analog sampling oscilloscope. The optical power is split by a fiber coupler, where one output is used as trigger for the sampling oscilloscope. (ISO: Optical isolator, CIR: Optical circulator, PBS: Polarization beam splitter, FRM: Faraday rotation mirror, FM: Fiber mirror, PC: Polarization controller paddles, FC: Fused fiber coupler, PD: Photodiode)

4. Picosecond pulse generation with an FDML laser

Typically, temporal compression is realized with a single pass of the 15 km long DCF. In this case, the negative dispersion equals $D \sim -4$ ns/nm (@1560 nm) and the fiber loss is ~ -8.5 dB (@1560 nm). Since the magnitude of the filter sweep speed v_{Sweep} must be equal to the inverse of the added dispersion ($v_{Sweep} = -1/D \sim 250$ nm/ μ s, see Figure 4.3b), the filter sweep range $\Delta\lambda_{FilterSweep}$ has to be chosen appropriately ($\Delta\lambda_{FilterSweep} \sim 211$ nm), as sketched in Figure 4.3a. In case of a quadruple pass of the 15 km long DCF, as used for some experiments, the situation is different. The added dispersion is increased by a factor of 4 ($D \sim -16$ ns/nm @1560 nm) and, consequently, the required sweep speed $v_{Sweep} \sim 62.5$ nm/ μ s and the filter sweep range $\Delta\lambda_{FilterSweep} \sim 53$ nm are reduced accordingly. However, the fiber loss is increased as well (~ -39 dB). Due to the dispersion slope of the DCF (see Figure 2.9) and the sinusoidal drive of the optical filter, the temporal compressor stage is not perfect (uncompensated higher order chirp). Thus, there exists a limit to the temporal compressibility (τ_{com}). Understandably, this limit τ_{com} is considerably depending on the chosen sweep bandwidth $\Delta\lambda$. Besides accurate adjustment of the filter sweep range $\Delta\lambda_{FilterSweep}$, a reasonable choice of the phase difference $\Delta\Phi$ (between the filter drive and the current modulation signal) is important. In this way, the part of the forward sweep which is extracted by the optical switch can be chosen slightly displaced from the inflection point of the sinusoidal filter drive. Thus, the curvature of the filter drive can partly compensate for the dispersion slope of the DCF. In the case of the compressor stage used for these experiments, τ_{com} (full width half maximum (FWHM)) was estimated. On the basis of the measured dispersion of the DCF [221] (see Figure 2.9), this was achieved by calculating the residual wavelength dependent time delay (sum of red and blue curve in Figure 4.3b) for differ-

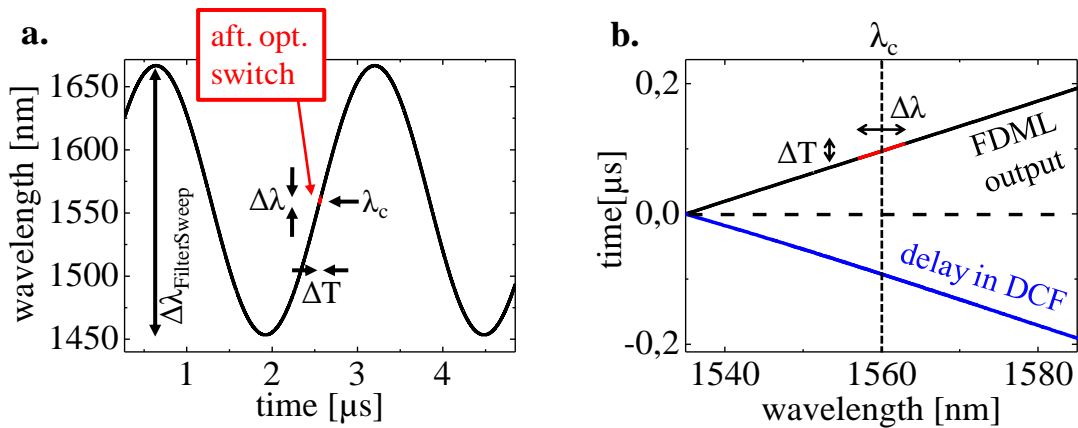


Figure 4.3: **a.** Wavelength tuning of the bandpass filter over time (black) and the corresponding time-wavelength characteristic of light which is extracted by the optical switch and is temporally compressed subsequently (red). The resulting temporal sweep width ΔT and the sweep bandwidth $\Delta\lambda$ (centered at $\lambda_c \sim 1560$ nm within each forward sweep) are indicated in the graph. **b.** Calculated time delay for different wavelengths of the forward sweep after the FDML laser (black) and after the optical switch (red) as well as the measured wavelength dependent time delay induced due to the compressor stage (blue). In case of ideal compression, the sum of the black and the blue curve gives a wavelength independent constant time delay. Both graphs represent the case of pulse generation using a single pass through the 15km long dispersion compensation fiber.

ent parameter combinations of $\Delta\lambda$, $\Delta\lambda_{FilterSweep}$ and $\Delta\Phi$. Results predict $\tau_{com} < 10$ ps for sweep bandwidths of $\Delta\lambda \sim 6$ nm (1x pass of the DCF) and $\Delta\lambda \sim 1.5$ nm (4x pass of the DCF). However, in case of increased sweep bandwidth ($\Delta\lambda \gg 6$ nm (1x pass of the DCF) or $\Delta\lambda \gg 1.5$ nm (4x pass of the DCF)), τ_{com} is considerably longer ($\tau_{com} > 10$ ps). This limitation of the sweep bandwidth is a drawback of the currently used pulse compressor stage. Consequently, the sweep bandwidth for all experiments has been set to $\Delta\lambda \sim 6$ nm ($\Delta T \sim 24$ ns) in case of a single pass of the 15 km long DCF (see Figure 4.3a and Figure 4.3b) and $\Delta\lambda \sim 1.5$ nm ($\Delta T \sim 24$ ns) in case of a quadruple pass of the 15 km long DCF.

4.2.3 Erbium-doped fiber amplification

Optionally, the truncated sweeps after the booster SOA can be amplified using erbium-doped fiber amplification (EDFA) (see Figure 4.1). EDFA is realized using ~ 6 m of erbium-doped fiber (MetroGain-M12-980-125) which is placed between two wavelength division multiplexers. Narrowband light from a pump diode (JDSU-S34) at 1457 nm is used as optical pump in forward direction. Assuming typical experimental conditions ($\Delta T \sim 24$ ns, $\Delta\lambda \sim 6$ nm, 1x pass of the DCF), amplification by at least 22 dB is easily possible.

4.2.4 Pulse detection: Sampling oscilloscope or autocorrelation

The pulses generated from the FDML laser are measured either using an analog sampling oscilloscope or a second-harmonic intensity autocorrelator (see Figure 4.2). A fused fiber coupler splits the optical power, directing 99% to the autocorrelator and 1% towards the sampling oscilloscope, where a further attenuation is achieved using a bulk optic variable attenuator. In order to guarantee proper triggering of the fast analog sampling oscilloscope (Tectronix 7603, 25 ps rise time), the pulse train is split (50/50 fiber coupler). One output of the coupler directs the light to a photodiode (WieserLabs WL-PD1GA), whose signal is used to trigger the oscilloscope. Light from the other output is optically delayed (~ 100 m single mode fiber) and monitored with a fast photodiode (Kyosemi Corporation-KPDX10GV3). In order to evaluate the measurements, the analog oscilloscope screen is photographed and the pulse traces are digitized. One prerequisite for correct evaluation of the signals measured with the oscilloscope is the knowledge of the apparatus function of the detection unit comprising the fast photodiode and the sampling oscilloscope. For the purpose of a correct determination of the apparatus function, short pulses (several ps) from the amplified output of a 74 MHz titanium sapphire oscillator (Femtolasers Integral, 975 nm part post-amplified by an Ytterbium-doped fiber amplifier, see [235]) were measured in the same manner yielding a FWHM of ~ 127 ps (see Figure 4.5). Assuming Gaussian pulse shapes, the actual pulse width τ_{pulse} (FWHM) can then be estimated from the measured pulse

width τ_{meas} (FWHM) using deconvolution: $\tau_{pulse} = \sqrt{\tau_{meas}^2 - (127 \text{ ps})^2}$. Note that the sampling oscilloscope cannot show several different pulses individually, but that the displayed intensity trace always reflects an average over multiple pulses.

The pulses can also be measured with a second-harmonic autocorrelator. However, current restrictions in optical pulse energy require an EDFA post-amplification. The home-built second-harmonic autocorrelator capable for automated pulse measurement of up to 500 ps pulse length (~ 15 cm delay) is based on a non-collinear geometry (bismuth borate crystal - BIBO). In this way, a background free signal is generated. The frequency doubled signal is detected with a very sensitive silica photodiode integrator (Wieser Labs-WL LPD4A) adjusted to 250 μs integration time and a read out rate of ~ 900 Hz. Each data point is an average of 100 read-out events.

4.3 Results and discussion

In this chapter, the results of the pulse generation experiments with the FDML laser are presented and discussed. Furthermore, pulse generation experiments using a fully incoherent wavelength-swept ASE source are shown. The chapter begins with the introduction of a theoretical model describing the expected temporal pulse width.

4.3.1 Theoretical model: Achievable pulse width for two special cases

The temporal width of pulses generated by temporal compression of the sweeps of wavelength-swept light sources inevitably depends on the coherence properties of the source. In order to be able to judge the results obtainable with an FDML laser, it is reasonable to consider the two special cases of fully incoherent⁵ and fully coherent wavelength-swept light sources.

4.3.1.1 Fully incoherent case

In the following, for the sake of simplicity, we assume a fully incoherent wavelength-swept light source that sweeps with a constant sweep speed $v_{Sweep} = \Delta\lambda/\Delta T$. The light source is expected to have a constant instantaneous linewidth $\Delta\lambda_{inst}$. The minimum achievable pulse width τ_{inc} after optimal temporal compression then is determined by two effects:

On the one hand, the pulse width is defined due to the time-bandwidth limitation regarding the instantaneous linewidth $\Delta\lambda_{inst}$. The latter directly determines the instantaneous coherence time which corresponds to a minimum potential pulse width τ_{TB} , defined as:

⁵ Note that, in the context of this thesis, the terminology “fully incoherent” is used for wavelength-swept light sources that have no optical feedback (narrowband filtering of spectrally broadband incoherent light, no lasing).

$\tau_{TB} = 0.44 \cdot \lambda_c^2 / (c \cdot \Delta\lambda_{inst})$. Here, a Gaussian spectral shape of the instantaneous spectrum is assumed and c is the speed of light in vacuum. The reason is as follows: Since the phase relation of the electric field of the spectral contributions within each sweep and between different sweeps is arbitrary, an optimal temporal compression equally applied to each forward sweep increases the instantaneous power but cannot yield a reduction of the pulse widths below τ_{TB} . In Figure 4.4a, b and c, τ_{TB} is plotted against the instantaneous linewidth $\Delta\lambda_{inst}$ (black dashed curve).

On the other hand, the minimum achievable pulse width τ_{inc} is influenced by the wavelength sweep speed v_{Sweep} . Due to wavelength sweeping, the resolvable spectral window of the instantaneous linewidth $\Delta\lambda_{inst}$ directly translates to a resolvable temporal window $\tau_{Switch} = \Delta\lambda_{inst} / v_{Sweep}$. In the fully incoherent case and assuming $\tau_{Switch} \gg \tau_{TB}$, there is a random phase relation in the electric field evolution within each time interval τ_{Switch} , as well as between different adjacent time intervals τ_{Switch} . An optimal temporal compression equally applied to each forward sweep increases the instantaneous power but cannot yield a reduction of the pulse width below τ_{Switch} . In Figure 4.4a, b and c, τ_{Switch} is sketched for two distinct wavelength sweep speeds corresponding to 4x pass of the DCF (cyan dashed line) and 1x pass of the DCF (pink dashed line).

Consequently, on the one hand, the minimum achievable pulse width τ_{inc} equals τ_{TB} if the instantaneous linewidth $\Delta\lambda_{inst}$ is very small and/or the sweep speed v_{Sweep} is very high. On the other hand, τ_{inc} equals τ_{Switch} if the instantaneous linewidth $\Delta\lambda_{inst}$ is very large and/or the sweep speed v_{Sweep} is very small. A more general solution, including both effects, can be obtained by convolution (assuming Gaussian shape). The minimum

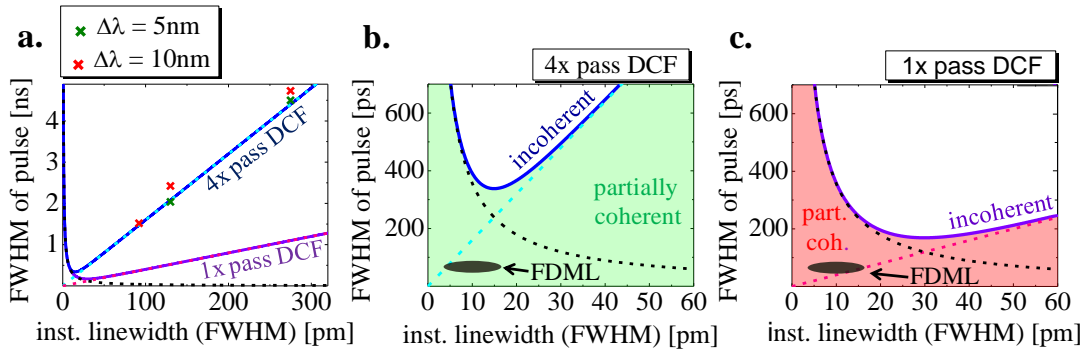


Figure 4.4: **a.** Results of a theoretical model describing temporal compression of the wavelength-swept output of fully incoherent wavelength-swept light sources: Minimum achievable pulse width against the instantaneous linewidth $\Delta\lambda_{inst}$ of the swept light source in case of two different filter sweep speeds corresponding to 4x pass of the DCF (blue curve) and 1x pass of the DCF (violet curve). Both curves are defined on the basis of two contributions: due to time-bandwidth limitation (black dashed line) and due wavelength sweeping (4x pass of the DCF: cyan dashed line and 1x pass of the DCF: pink dashed line). The crosses show experimental results obtained with an incoherent wavelength-swept ASE source (4x pass of the DCF) for different sweep bandwidths $\Delta\lambda$. **b. and c.** Zoomed views of a, corresponding to two different filter sweep speeds. The green area (4x pass of the DCF) and the red area (4x pass of the DCF) show the parameter range corresponding to partially coherent superposition of the different spectral components within the sweeps. Black ovals indicate the approximate parameter range currently achievable with FDML lasers, clearly included in the area representing partially coherent superposition.

achievable pulse width in the fully incoherent case can then be estimated to:

$$\tau_{inc} = \sqrt{\left(\frac{\Delta\lambda_{inst}}{v_{sweep}}\right)^2 + \left(0.44 \cdot \frac{\lambda_c^2}{c \cdot \Delta\lambda_{inst}}\right)^2} \quad 4.1$$

This limit is illustrated in Figure 4.4a, b and c in case of sweep speeds corresponding to 4x pass of the DCF (blue curve) and 1x pass of the DCF (violet curve). Consequently, one can draw the following conclusion: If the temporal compression of the sweeps from a wavelength-swept laser with a distinct instantaneous linewidth $\Delta\lambda_{inst}$ enables a pulse width $\tau_{pulse} < \tau_{inc}(\Delta\lambda_{inst})$, there must occur at least partially coherent superposition of the different spectral components of the sweeps within the temporal compression process. The parameter range of partial coherence is illustrated in Figure 4.4b (green area) in case of 4x pass of the DCF and in Figure 4.4c (red area) in case of 1x pass of the DCF.

4.3.1.2 Fully coherent case

In the fully coherent case, the minimum temporal pulse width τ_{coh} is only determined by the sweep bandwidth $\Delta\lambda$. The electric field within the each sweep and between adjacent sweeps is optimally coherent resulting in perfect mode locked laser operation. In this case, all longitudinal laser modes exhibit a defined phase relation. Assuming a Gaussian spectral shape, i.e. a time-bandwidth product of 0.44, the minimum pulse width τ_{coh} reads:

$$\tau_{coh} = 0.44 \cdot \frac{\lambda_c^2}{c \cdot \Delta\lambda} \quad 4.2$$

With regard to the sweep bandwidths $\Delta\lambda = 6$ nm (1x pass of the DCF) and $\Delta\lambda = 1.5$ nm (4x pass of the DCF), as chosen for the experiments within the framework of this thesis, the corresponding minimum pulse widths in the fully coherent case are $\tau_{coh} \sim 600$ fs and $\tau_{coh} \sim 2.4$ ps, respectively (assuming a time-bandwidth product of 0.44).

4.3.2 Pulse generation with an incoherent wavelength-swept source

Besides temporal compression of the wavelength-swept output of the FDML laser, comparable experiments have been performed investigating the compressibility of a swept light source which is very similar to the wavelength-swept ASE sources presented in chapter 3.2. The wavelength-swept light source utilized here is based on only one spectral filter followed by several amplification steps using SOAs. The disadvantage compared to the two filter approach, as explained in chapter 3.2, is an increased amount of unfiltered ASE background. However, this does not affect the compression experiments. The spectral filter is identical to the one which is used in the FDML laser and is driven in the same way to enable temporal compression by a 4x pass of the DCF. A very important point is that the wavelength-swept ASE source is a fully incoherent

swept source since there is no optical feedback. This results in a random phase relation of the electric field of the spectral contributions within each sweep and between different sweeps. Thus, this source is optimal for comparison with the theoretical model introduced in chapter 4.3.1.1. As described in chapter 3.2.1, the instantaneous linewidth $\Delta\lambda_{inst}$ of wavelength-swept light sources is identical to the spectral filter width $\Delta\lambda_{Filter}$ and can therefore easily be changed. Unlike FDML lasers (see Figure 4.5c), no measurable filter drive frequency dependence has been observed. The crosses in Figure 4.4a show the experimental results achieved with different sweep bandwidths ($\Delta\lambda\sim 5$ nm (green) and $\Delta\lambda\sim 10$ nm (red)). Discrepancies at a given spectral filter width are most probably due to the imperfect temporal compressor stage. Obviously, the results are in very good agreement with the theoretical model. Reducing the instantaneous linewidth clearly results in shorter pulses. Unfortunately, experimental restrictions prevented a further reduction of the filter width $\Delta\lambda_{Filter}$. Therefore, the increase of the pulse width for very small instantaneous linewidths, as would be expected from the incoherent wavelength-swept ASE source, has not yet been confirmed experimentally.

4.3.3 Pulse generation with an FDML laser

The following chapter describes current results of temporal compression of the FDML laser. All results presented in Figure 4.5 were obtained with light passing the 15 km long DCF a single time (1x pass), with a sweep bandwidth $\Delta\lambda$ set to ~ 6 nm (FWHM) (corresponding to a sweep time of $\Delta T\sim 24$ ns) and with a spectral filter width $\Delta\lambda_{Filter}$ of the BFP-TF adjusted to ~ 315 pm (FWHM). Figure 4.5a shows the measured apparatus function of the photodiode and the sampling oscilloscope (orange dots), as described in chapter 4.2.4. The temporal width (FWHM) of the apparatus function is determined to ~ 127 ps. Additionally, the slightly broader, optimum pulse obtained from the FDML laser is plotted (black dots) yielding a measured temporal width $\tau_{meas}\sim 144$ ps (FWHM). Using deconvolution (see chapter 4.2.4), the actual pulse width τ_{pulse} can be estimated to ~ 68 ps (FWHM). The same experiments were performed with larger sweep bandwidths $\Delta\lambda \gg 6$ nm. However, in this case the achievable pulse considerably broadens and develops long, asymmetric shoulders. Due to the dispersion slope of the DCF and the sinusoidal filter drive, the achievable compressibility is limited to a value τ_{com} , which is depending on $\Delta\lambda$. Therefore, these findings are not surprising and agree with estimations of τ_{com} (see chapter 4.2.2). However, the same estimation also predicts a compressibility $\tau_{com} < 10$ ps at a sweep bandwidth $\Delta\lambda\sim 6$ nm. Therefore, the imperfect temporal compression cannot explain the limited pulse width of $\tau_{pulse}\sim 68$ ps. Since the sweep bandwidth principally should allow for sub-ps pulses, the current limitations in pulse width must be caused by internal properties of the FDML laser that directly influence the coherence of the laser. One parameter that deserves particular attention is the filter drive frequency $f_{Filter}\sim 390$ kHz. Figure 4.5b shows the measured pulses in case of optimum frequency ($\Delta f_{Filter} = 0$, black dots) and two slightly detuned frequencies ($\Delta f_{Filter} = -0.5$ Hz, red dots and $\Delta f_{Filter} = +0.3$ Hz, blue dots), whereas Figure 4.5c

4. Picosecond pulse generation with an FDML laser

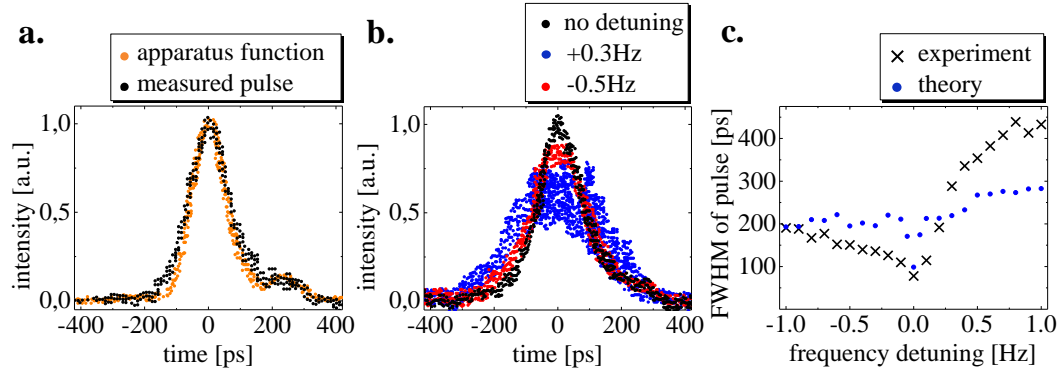


Figure 4.5: **a.** Optimum pulse measured with the sampling oscilloscope in case of 1x pass of the DCF and $\Delta\lambda \sim 6$ nm (black dots) and the measured apparatus function of the sampling oscilloscope and the photodiode (orange dots). The effective pulse duration (FWHM) can be determined to $\tau_{pulse} \sim 68$ ps using deconvolution. **b.** Corresponding pulses measured for slightly detuned filter drive frequencies f_{Filter} . The presented graphs in a and b are created from digitizing photographs of the analog sampling oscilloscope. **c.** Measured pulse widths τ_{pulse} (FWHM) against the filter drive frequency detuning (black crosses) and the corresponding results obtained from numerical simulations (blue dots). Clear broadening is observed for relative detunings of $\sim 3 \cdot 10^{-7}$.

shows the measured pulse width τ_{pulse} (FWHM) plotted against Δf_{Filter} (black crosses). Obviously, already a minimal detuning $\Delta f_{Filter} \sim 0.1$ Hz (relative frequency change of $3 \cdot 10^{-7}$) causes an increase of τ_{pulse} by $\sim 50\%$. This broadening is clearly not due to the negligible change of temporal compression in the DCF caused by frequency detuning since, in this case, τ_{pulse} would be expected to increase only by ~ 200 ppm. Thus, this effect must result from a degradation of coherence in the FDML laser. Obviously, the experimental results show an asymmetry with regard to the sign of the frequency detuning. A positive frequency detuning results in a more emphasized pulse broadening and blurring of the oscilloscope signal, potentially due to differing intensity shapes of successive pulses. Additionally, Figure 4.5c presents the corresponding results obtained from numerical simulations, which are based on a theoretical model of the FDML laser (blue dots) (see chapter 4.1). As can be seen, the simulations show an even more critical dependence on the filter drive frequency f_{Filter} . Though they predict smaller pulse widths for large positive frequency detunings, both, experiments, as well as simulations show the same asymmetry with respect to the sign of frequency detuning. Differences might be caused by the fact that the underlying theory, as basis for the simulations, considers only one polarization state, whereas the experiment allows for arbitrary polarizations, due to the polarization independent SOA.

Figure 4.6a is a summary of different measurements showing the optimum achievable pulse width τ_{pulse} for different filter widths $\Delta\lambda_{Filter}$ and in case of different filter drive parameters corresponding to a single pass of the DCF ($v_{Sweep} \sim 250$ nm/ μ s, $\Delta\lambda \sim 6$ nm, $\Delta T \sim 24$ ns, black crosses) and a quadruple pass of the DCF ($v_{Sweep} \sim 62.5$ nm/ μ s, $\Delta\lambda \sim 1.5$ nm, $\Delta T \sim 24$ ns, violet crosses). The measurements indicate that τ_{pulse} to a certain extent correlates with $\Delta\lambda_{Filter}$ and with the sweep speed v_{Sweep} : Smaller filter widths $\Delta\lambda_{Filter}$ yield smaller pulse widths τ_{pulse} and higher sweep

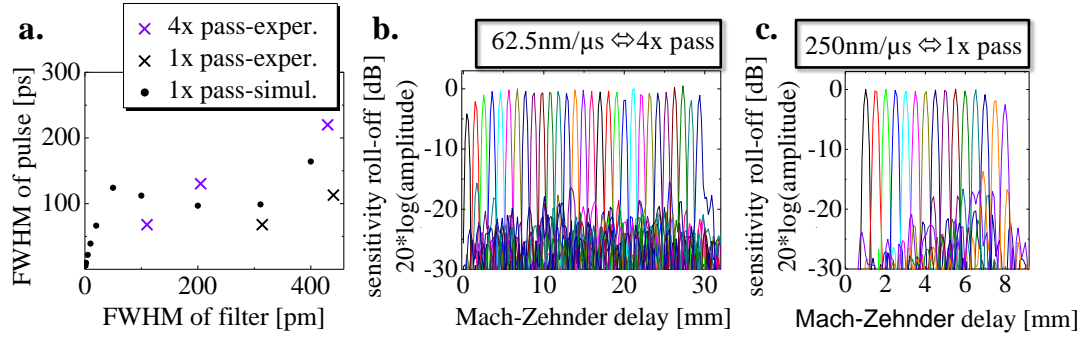


Figure 4.6: **a.** Measured optimum pulse width τ_{pulse} for different spectral widths of the optical bandpass filter $\Delta\lambda_F$ in case of 4x pass of the DCF ($\Delta\lambda \sim 1.5$ nm, $\Delta T \sim 24$ ns, violet crosses) and 1x pass of the DCF ($\Delta\lambda \sim 6$ nm, $\Delta T \sim 24$ ns, black crosses) and the corresponding results obtained from numerical simulation in case of 1x pass of the DCF (black dots). **b. and c.** Measured sensitivity roll-off performance of the FDML laser plotted against the Mach-Zehnder delay (twice the equivalent OCT imaging range) at filter drive parameters equivalent to temporal compression experiments with 4x pass of the DCF and 1x pass of the DCF. The emphasized drop of the PSF maxima at large delays is due to limited electronic response of the 1 GHz dual balanced photo detector. The increase at very small delays is due to AC-coupling of the photo detector.

speeds v_{Sweep} enable smaller pulse widths τ_{pulse} at constant filter width $\Delta\lambda_{Filter}$. Note that these findings resemble the dependency of the achievable pulse width in case of using a fully incoherent wavelength-swept light source, such as the wavelength-swept ASE source. The observed dependency of the pulse width in the measurements of Figure 4.6a can therefore in part be attributed to the fact that the FDML laser currently does not provide fully coherent sweeps. Due to a limited finesse and mechanical restrictions of the home-built BFP-TF, the spectral filter width $\Delta\lambda_{Filter}$ was not reduced below ~ 110 pm (4x pass of the DCF) and ~ 315 pm (1x pass of the DCF), respectively. In both cases, a minimum pulse width $\tau_{pulse} \sim 68$ ps has been achieved. Additionally, the corresponding results of the numerical simulations (see chapter 4.1) are included in case of a single pass through the DCF (Figure 4.6a, black dots). In spite of a pronounced plateau, the simulations predict that considerably smaller pulse widths can be obtained by reducing the spectral filter width $\Delta\lambda_{Filter}$ ($\Delta\lambda_{Filter} \ll 50$ pm). The experimentally achieved pulse widths are slightly smaller than predicted by the simulations, which might again be due to the fact that the underlying theory only considers one single polarization state.

4.3.4 Sensitivity roll-off performance of the FDML laser

Additionally to pulse generation experiments, the sensitivity roll-off performance (see chapter 2.1.4.2 and chapter 2.2.2.3) of the dispersion compensated FDML laser was measured using a Mach-Zehnder interferometer, a dual balanced photo detector (WieserLabs WL-BPD1GA) and a 1 GHz Tektronix real time oscilloscope (type DPO 7104). The filter drive frequency f_{Filter} was optimized for best roll-off performance in each case [14]. Figure 4.6b and Figure 4.6c show the roll-off measurements acquired with the same filter drive parameters as used for optimal pulse generation in

4. Picosecond pulse generation with an FDML laser

case of 4x pass of the DCF ($v_{Sweep} \sim 62.5 \text{ nm}/\mu\text{s}$, $\Delta\lambda_{Filter} \sim 110 \text{ pm}$) and in case of 1x pass of the DCF ($v_{Sweep} \sim 250 \text{ nm}/\mu\text{s}$, $\Delta\lambda_{Filter} \sim 315 \text{ pm}$). Besides learning about potential OCT imaging range, the sensitivity roll-off measurement allows for a determination of the mean instantaneous linewidth $\Delta\lambda_{inst}$ of the FDML laser (average over the sweep), which is directly connected to coherence [227]. In the measurements presented here, the sensitivity roll-off is comparably small. Due to a limited electrical bandwidth of the photo detector and the oscilloscope ($\sim 1 \text{ GHz}$), the roll-off was only measurable up to a Mach-Zehnder delay of $\sim 6.5 \text{ mm}$ ($v_{Sweep} \sim 250 \text{ nm}/\mu\text{s}$) and $\sim 27 \text{ mm}$ ($v_{Sweep} \sim 62.5 \text{ nm}/\mu\text{s}$). Since a roll-off measurement including the 6 dB roll-off point would require a considerably higher electrical bandwidth, the determination of the instantaneous linewidth is considerably complicated, in particular in the case of Figure 4.6c. In Figure 4.6b as well as in Figure 4.6c the pronounced decrease of the maxima of the PSFs at very large delays is caused by the limited electrical response of the photodiode and the oscilloscope, whereas the increase at small delays (see Figure 4.6b) can be attributed to AC-coupling of the photo-detector. Nevertheless, an extrapolation of the maxima of the PSFs allows giving the rough estimation that for both cases the mean instantaneous linewidth $\Delta\lambda_{inst}$ is most probably larger than a few pm and smaller than $\sim 15 \text{ pm}$. This finding is used to highlight the approximate operation regime of the FDML laser in Figure 4.4b and Figure 4.4c (black ovals).

4.3.5 Evaluation of the results: Partially coherent superposition

Since the current limitations of pulse widths ($\tau_{pulse} \sim 68 \text{ ps}$) cannot be attributed to the imperfectness of the temporal compressor stage and the utilized sweep bandwidths of $\Delta\lambda \sim 6 \text{ nm}$ or $\Delta\lambda \sim 1.5 \text{ nm}$ should principally allow for pulse widths $\tau_{coh} \sim 600 \text{ fs}$ or $\tau_{coh} \sim 2.4 \text{ ps}$ (see equation 4.2), it is obvious that the FDML dynamics does not provide a fully coherent evolution of the electric field. However, there are several considerations that indicate and demonstrate that there exists at least partial coherence under the currently given experimental conditions. At first, one has to notice that temporal compression using a fully incoherent wavelength-swept ASE source, operated with the same filter drive parameters and the same filter width $\Delta\lambda_F$, generates pulses which are considerably broader compared to the results achieved with the FDML laser (factor ~ 26 for $\Delta\lambda_F \sim 110 \text{ pm}$ and 4x pass of the DCF, see Figure 4.4a). Another indication is the strong dependence of the pulse width τ_{pulse} from the filter drive frequency f_{Filter} (required relative accuracy of $3 \cdot 10^{-7}$), which is directly linked to the internal coherence properties of the FDML laser. Furthermore, Figure 4.4b and Figure 4.4c clearly demonstrate partial coherence of the FDML sweeps. Without considering the instantaneous linewidth $\Delta\lambda_{inst}$ of the FDML laser, one can state that τ_{pulse} is at least a factor of 5 (4x pass of the DCF) and at least a factor of 2.5 (1x pass of the DCF) smaller than the expected pulse width τ_{inc} in the fully incoherent case. Therefore, FDML operation can clearly be attributed to the parameter regime representing partial coherence (green area (4x pass of the DCF) and red area (1x pass of the DCF)). Under consideration of the

approximate, measured instantaneous linewidth $\Delta\lambda_{\text{inst}}$ ($\sim 10 \text{ pm} \pm 5 \text{ pm}$) of the FDML laser, the corresponding parameter range for FDML operation can be sketched in Figure 4.4b and Figure 4.4c (black ovals), underlining the previous findings.

4.3.6 Pulse generation with an FDML laser and EDFA amplification

Due to loss in the dispersion compensation fiber and limited spectral bandwidth due to imperfect temporal compression, the achievable pulse energies obtainable from the FDML oscillator and the booster SOA are currently limited to $\sim 140 \text{ pJ}$. The corresponding peak power is $\sim 2 \text{ W}$. In order to enable pulse detection with a second-harmonic autocorrelator, erbium-doped fiber amplification (EDFA) has been applied prior to temporal compression. The results will be discussed in this chapter. Note that EDFA amplification of the truncated wavelength-swept output of the FDML laser has been demonstrated to show nonlinear broadening in a dispersion shifted fiber (DSF) (no temporal compression) [236]. In the following, light passes the DCF a single time (1x pass of the DCF), the filter width is set to $\Delta\lambda_{\text{Filter}} \sim 315 \text{ pm}$ and the sweep bandwidth is chosen to be $\Delta\lambda \sim 6 \text{ nm}$ ($\Delta T \sim 24 \text{ ns}$). In case of an amplification of $\sim 16 \text{ dB}$ (factor of ~ 40), an optimum pulse width τ_{pulse} of $\sim 59 \text{ ps}$ has been determined with the sampling oscilloscope. The corresponding intensity autocorrelation, measured with the home-build second-order intensity autocorrelator, is sketched in Figure 4.7a showing two features. A narrow coherence spike (consistent with the bandwidth limit of $\sim 600 \text{ fs}$) is centered on top of a broad pedestal (FWHM, $\tau_{\text{AC}} \sim 89 \text{ ps}$) (contrast ratio $\sim 1:1$). This implies a pulse width of $\tau_{\text{pulse}} \sim 63 \text{ ps}$ (FWHM, assuming a Gaussian envelope), con-

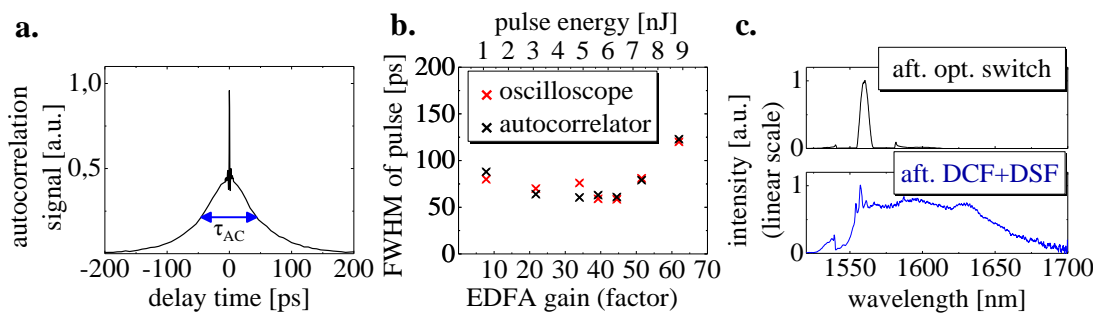


Figure 4.7: **a.** Optimum autocorrelation signal acquired with the intensity autocorrelator at $\sim 5.6 \text{ nJ}$ pulse energy (1x pass of the DCF) after EDFA. A narrow coherence spike ($\sim 600 \text{ fs}$ temporal width) is centered upon a broad pedestal of temporal width $\tau_{\text{AC}} \sim 89 \text{ ps}$, which corresponds to a pulse width τ_{pulse} of $\sim 63 \text{ ps}$. **b.** Pulse width τ_{pulse} derived from measurements with the autocorrelator and the sampling oscilloscope depending on the gain factor of the erbium doped fiber amplification prior to the DCF (1x pass of the DCF). The upper x-axis shows the corresponding pulse energy after temporal compression. **c.** Time averaged spectrum acquired with an optical spectrum analyzer (OSA) directly after the optical switch with $\Delta\lambda \sim 6 \text{ nm}$ (FWHM) (upper graph) and the broad and very flat (linear scale!) continuum spectrum generated with $\sim 11 \text{ nJ}$ pulses passing additionally $\sim 1700 \text{ m}$ of dispersion shifted fiber (DSF) (lower graph). The small satellite peaks result from adjacent Fabry-Pérot modes, remaining after suppression by the booster SOA.

sistent with the result obtained with the sampling oscilloscope. However, the coherence spike in the intensity autocorrelation indicates the existence of an intensity substructure [237, 238], which most probably can be attributed to not fully coherent superposition during temporal compression resulting in intensity fluctuations. Figure 4.7b shows the achievable pulse width τ_{pulse} for different amplification factors of the EDFA determined either with the sampling oscilloscope (red crosses) or with the intensity autocorrelator (black crosses). Figure 4.7b demonstrates very good agreement between both pulse detection methods. Obviously, τ_{pulse} seems to increase slightly when decreasing the amplification factor and the minimum pulse width is marginally smaller than the corresponding result obtained without EDFA. Whereas these findings remain rather unclear, the considerable pulse broadening for amplification factors >40 is clearly due to nonlinear effects in the DCF, most probably dominated by self phase modulation (SPM), setting an upper limit to the EDFA amplification factor. The optimal EDFA amplification corresponds to a pulse energy of ~ 5.6 nJ after temporal compression, as indicated by the upper x-axis of Figure 4.7b. The corresponding average power and peak power after the DCF are ~ 2.2 mW and ~ 96 W, respectively.

Figure 4.7c (top) shows the time averaged spectrum measured with an optical spectrum analyzer directly after the optical switch (booster SOA), exhibiting a FWHM of ~ 6 nm. The shape of the spectrum after temporal compression does not change without using EDFA amplification. However, in the case of optimum EDFA amplification (factor of ~ 40), slight modification of the spectral shape can be observed caused by nonlinear effects in the DCF. Increasing the amplification factor considerably changes the shape and broadens the spectrum. The time averaged spectrum presented in Figure 4.7c (bottom) is the result of the pulses passing additionally ~ 1700 m of dispersion shifted fiber (DSF) (see chapter 2.2.2.2) and using pulse energies after the DCF of ~ 11 nJ. This demonstrates the potential of continuum generation. Remarkable is the flatness of the continuum over a spectral range of more than 100 nm (linear scale).

4.3.7 Conclusion

With the experimental work presented in chapter 4, a completely new approach of short pulse generation has been demonstrated. Temporal compression of the wavelength-swept output of the FDML laser using at least 15 km of DCF enabled pulses with a FWHM of ~ 60 -70 ps at a repetition rate of 390 kHz and pulse energies of ~ 5.6 nJ (using EDFA). The dependence of the achievable pulse width from internal FDML parameters like the filter bandwidth or the filter drive frequency has been investigated. Very strong dependence on the filter drive frequency (relative accuracy of $3 \cdot 10^{-7}$) is observed, indicating the high dependence on coherence properties of the FDML laser. A theoretical model was introduced describing the expectable pulse width in case of temporally compressing the output of fully incoherent swept light sources. Compression experiments have been performed with an incoherent wavelength-swept ASE source, where the results agreed with the theoretical model. Although time-bandwidth limited

pulses have not been achieved with the FDML laser, it was demonstrated that that there must occur at least partially coherent superposition of the different spectral components of the FDML sweep within the temporal compression process.

Based on a theoretical model of the FDML laser [15], the research group of Dr. Christian Jirauschek performed simulations which are in good agreement with the experiments, showing similar parameter dependencies. The simulations also included parameter ranges which are currently not accessible in the experiment. Interestingly, for smaller spectral filter widths ($\ll 50$ pm), the simulations showed considerably smaller pulse widths of <10 ps. Moreover, by setting the residual dispersion in the FDML cavity to zero and assuming very small filter widths, simulations resulted in a further reduction of the temporal pulse width, reaching almost time-bandwidth limited pulses. Therefore, there is justified hope that experimental improvements like an even better dispersion compensation in the cavity and an improved tunable bandpass filter performance (increased finesse) could considerably reduce the achievable temporal pulse widths and might enable almost time-bandwidth limited pulses in the future. Due to the high requirements in accuracy of the filter drive frequency and thermal drifts of the FDML cavity, accurate active frequency feed-back stabilization will certainly simplify short pulse generation and will be required for future experiments.

Another problem is uncompensated higher order chirp using the DCF, which currently limits the spectral bandwidth and thus the achievable pulse energy. However, improvements like the additional application of chirped fiber Bragg gratings [185] for arbitrary dispersion compensation might allow for temporal compression of several tens of nm pushing the achievable pulse energy to several nJ without using EDFA amplification.

4. Picosecond pulse generation with an FDML laser

5 Conclusion and outlook

The research work presented in this thesis focused on the investigation and characterization of different novel concepts of fast semiconductor-based wavelength-swept light sources, which are characterized by a very high wavelength sweep speed, a large spectral sweep range and a narrowband instantaneous spectrum. The most prominent and successful application is swept source based optical coherence tomography (SS-OCT), where the demand for high imaging speed drove the research in the field of wavelength-swept light sources in the last years. Conventional semiconductor-based wavelength-swept lasers suffer from a fundamental sweep speed limit [5] which is determined by the laser cavity length and caused by the finite build-up time of lasing from amplified spontaneous emission (ASE). The most obvious solution to this problem is a minimization of the cavity length. In this way, ultra-high OCT imaging speeds have been achieved with optically pumped MEMS-based tunable vertical-cavity surface-emitting lasers (VCSEL) [183, 184], providing single line operation at sweep rates approaching the MHz range. However, the fastest high-quality OCT imaging up to now was realized with a completely different approach, overcoming the fundamental sweep speed limitation. In Fourier domain mode locked (FDML) lasers [6], the laser cavity length is extended up to a few kilometers by inserting optical fiber enabling a repetitive wavelength tuning synchronous to the round-trip time of light in the laser cavity. In this way, SS-OCT imaging at sweep rates exceeding several MHz [7, 8] has been demonstrated. One main objective of this thesis was the research on novel concepts of wavelength-swept light sources improving performance and applicability for SS-OCT. Regarding this, an important issue was the investigation of two novel modes of operation in FDML lasers.

Almost all wavelength-swept light sources utilized for SS-OCT exhibit non-linear time-frequency sweep characteristics, which has several disadvantages in the application for OCT. Since equidistant frequency sampling is required prior to Fourier transformation, additional numerical resampling is usually applied complicating data processing. Apart from that, a non-linear sweep characteristic can result in a slightly reduced sensitivity or dynamic range. Within the framework of this thesis, the first k-space linear FDML laser has been demonstrated at ~ 1300 nm with a sweep rate of ~ 57 kHz, overcoming these drawbacks. As shown, a very high linearity, i.e. an integrated relative optical frequency error on the order of 10^{-5} or smaller, is required to enable high-quality OCT imaging without numerical resampling. The crucial point to achieve k-space linear operation is the correct drive of the piezo-actuated tunable Fabry-Pérot filter. Based on numerical simulations, different strategies were introduced to determine

the suitable control waveform comprising the fundamental FDML frequency and several higher harmonics. Here, the consideration of the frequency-dependent electro-mechanical amplitude and phase response of the Fabry-Pérot filter played an important role. Adapting the filter drive waveform, the k-space linear FDML laser has also been used to compensate for unbalanced chromatic dispersion in the OCT setup, which worked very well within at least a small imaging range. Moreover, k-space linear operation was the prerequisite for a new approach of en-face OCT, which was introduced by our group [231] and enabled real-time visualization of en-face images without the need for Fourier transformation. In the future, k-space linear FDML operation at considerably higher imaging speeds could be achieved using the technique of optical buffering. The gained knowledge about k-space linear FDML operation could also be transferred to other non-FDML swept sources facilitating the linearization of the wavelength sweeps. The second introduced novel mode of operation is subharmonic FDML (shFDML), which was demonstrated at ~ 1300 nm. A reflective tunable Fabry-Pérot filter is placed at the beginning of the linear delay line of a sigma-ring cavity and thus can play the role of an optical switch. In this way, light is recirculated in the delay line a preselected number of times yielding multiple passes through the same delay fiber during each round-trip in the cavity. The main advantage is that shFDML lasers provide the inherent possibility to multiply the sweep rate and increase OCT imaging speed with a minimum of optical fiber required and without the need for an additional optical buffer stage. This can be accomplished by extracting a part of the optical power within each pass of the fiber delay in combination with appropriate gain switching. In this way, a multiplication by a factor of 10 has been achieved reaching a sweep rate of 570 kHz. However, there are currently two main drawbacks which limited the achievable spectral sweep bandwidth. On the one hand, there is parasitic lasing, which was suppressed best possibly using a polarization maintaining setup. On the other hand, the double pass of light through the Fabry-Pérot filter during each cavity round-trip increasingly complicates shFDML operation when raising the sweep speed due to the finite length of the short ring. Future improvements, like the application of an one-sided reflective filter in order to avoid parasitic lasing and a further reduction of the short ring length, will be necessary. Alternatively, an extension of this length, making the short ring resonant, in combination with a suitable gain modulation could have the potential to overcome both drawbacks. In the future, shFDML lasers could become an attractive alternative for ultra-high speed OCT, in particular if high filter drive frequencies are not feasible requiring a high sweep rate multiplication factor.

Besides advances in FDML laser technology, the research work presented in this thesis also included the introduction and characterization of a novel concept of ultrafast wavelength-swept light sources, referred to as wavelength-swept ASE sources. This approach can overcome the fundamental sweep speed limit and, unlike other swept sources, is based on a setup with no optical feedback. In order to guarantee a sufficiently high output power, ASE light alternately passes a cascade of different gain elements and different optical filters, which are required to prevent the amplification of unfiltered ASE

background. As verified experimentally, optimum operation can only be achieved if the different spectral filters are driven with a precisely adjusted phase delay in order to compensate for the transit time of light between the filters. It was demonstrated that the required phase accuracy and the sensitivity roll-off are mainly determined by the spectral transmission functions of the filters. Within the framework of this thesis, different implementations of wavelength-swept ASE sources have been investigated enabling in-vivo OCT imaging of the human finger at ~ 1300 nm and, additionally, of the human retina at ~ 1060 nm, where very high average output powers exceeding 40 mW were achieved using Yb-doped fiber post-amplification. The effective sweep rate of 340 kHz, which has been realized with this novel approach, was the highest sweep rate demonstrated for retinal OCT imaging at this time. Wavelength-swept ASE sources provide several advantages compared to other swept light sources, like highly repeatable temporal tuning characteristics or equal performance of forward and backward sweep. Since no long optical fiber delay is required, this technique could be an attractive alternative for future high speed SS-OCT systems in wavelength ranges where high dispersion, high loss or large polarization effects in the fiber complicate FDML operation. Each setup was based on a cascade of two filtering and three amplification steps, however, for future applications the number of elements could be extended, if necessary. An automated regulation of the filter drive parameters will be required. Furthermore, an optimization of the spectral bandwidths of the different filters, using non-equal values, could improve the roll-off performance and relax the required filter drive accuracy.

In summary, the introduced novel approaches, which were investigated within the framework of this thesis, have the potential to facilitate and improve SS-OCT in the future. From today's perspective, it is highly probable that swept source based technology will become the technique of choice for all future OCT systems, however, it remains exciting to see which swept source technique will prevail.

The second main objective of this thesis was the demonstration of a completely novel approach of short pulse generation based on subsequent temporal compression of the sweeps from an FDML laser. This has been accomplished using a 15 km long dispersion compensation fiber (DCF) placed after a dispersion compensated FDML laser, which was operated at ~ 1560 nm and 390 kHz. Moreover, this approach offered the possibility to gain an insight into the coherence properties of the FDML laser. This new concept is of high interest due to different reasons. On the one hand, this technique has the potential to enable considerably higher pulse energies compared to conventionally mode locked semiconductor lasers, since energy is stored optically in the laser cavity and not as population inversion in the gain medium. On the other hand, the generation of almost time-bandwidth limited pulses might become possible in the future, since ideal FDML operation can be seen as a new mode of stationary laser operation, where sequential sweeps are mutually coherent and the laser modes are phase locked [6].

In the research work presented in this thesis, temporal pulse widths of ~ 60 -70 ps at a repetition rate of 390 kHz have been demonstrated. Due to uncompensated higher order chirp, the bandwidth was limited to ~ 6 nm. Therefore and due to loss in the DCF, the

pulse energies were restricted to ~ 140 pJ. Erbium-doped fiber amplification (EDFA) prior to temporal compression enabled pulse energies of ~ 5.6 nJ at a peak power of ~ 96 W. In the future, the additional application of chirped fiber Bragg gratings [185] could enable temporal compression of several tens of nm, which would raise the achievable pulse energy to several nJ without using EDFA amplification.

The minimum achievable temporal pulse width of ~ 60 - 70 ps, as realized under currently given experimental conditions, is limited by the internal coherence properties of the laser and not due to imperfect temporal compression. The crucial role of coherence in the laser has been impressively demonstrated by the strong dependence of the pulse width on the drive frequency of the tunable filter, requiring a relative accuracy of $\sim 3 \cdot 10^{-7}$. Moreover, equivalent pulse compression experiments have been performed with a per se incoherent wavelength-swept ASE source, showing considerably longer pulse widths. The experimental results were in good agreement with a theoretical model, which was introduced describing pulse generation with fully incoherent swept light sources. On the basis of this model, it has been shown that there occurs at least partially coherent superposition of the different spectral components of the FDML sweeps within the temporal compression process.

Analyzing the interference signal, obtained by superposing one sweep with a delayed copy, high intra-sweep coherence of the FDML laser has been observed. Moreover, these measurements indicate an ultra-stable operation similar as presented in [239] and suggest that the FDML sweeps show sections with a very high coherence which are interrupted by wavelength/phase discontinuities. Further investigations using a considerably higher detection bandwidth will be required. Moreover, different studies which were performed in our research group and were based on superposing different successive wavelength sweeps showed mutual inter-sweep coherence [222].

In collaboration with the research group of Dr. Jirauschek, pulse generation with FDML lasers has been described using numerical simulations based on a theoretical model of the FDML laser [15]. The simulations have largely reflected the dependencies of the different parameters that were observed in the experiment and predicted significantly narrower pulses in case of considerably reduced spectral filter widths, which are currently not feasible in the experiment due to restrictions of the filter performance. Moreover, using zero residual cavity dispersion and very small filter widths, the simulations yielded almost time-bandwidth limited pulses. In the future, an extension of the underlying theory, considering different polarization states, can become reasonable since the polarization in the fiber seems to play a non-negligible role for FDML dynamics.

All these findings give justified hope that the generation of considerably shorter, or even almost bandwidth-limited pulses might become possible in the future by improving the coherence properties of the FDML laser. Active frequency feed-back stabilization, improved tunable filter performance or reduced residual dispersion in the cavity could be important steps on this way. A deeper understanding of FDML laser physics will play a crucial role. Therefore, this field provides many exciting challenges remaining for the future.

Bibliography

- [1] D. Huang, E. A. Swanson, C. P. Lin, J. S. Schuman, W. G. Stinson, W. Chang, M. R. Hee, T. Flotte, K. Gregory, C. A. Puliafito, and J. G. Fujimoto, "Optical coherence tomography", *Science* **254**, 1178-1181 (1991).
- [2] M. Choma, M. Sarunic, C. Yang, and J. Izatt, "Sensitivity advantage of swept source and Fourier domain optical coherence tomography", *Optics Express* **11**, 2183-2189 (2003).
- [3] J. F. de Boer, B. Cense, B. H. Park, M. C. Pierce, G. J. Tearney, and B. E. Bouma, "Improved signal-to-noise ratio in spectral-domain compared with time-domain optical coherence tomography", *Optics Letters* **28**, 2067-2069 (2003).
- [4] R. Leitgeb, C. Hitzenberger, and A. Fercher, "Performance of fourier domain vs. time domain optical coherence tomography", *Optics Express* **11**, 889-894 (2003).
- [5] R. Huber, M. Wojtkowski, K. Taira, J. G. Fujimoto, and K. Hsu, "Amplified, frequency swept lasers for frequency domain reflectometry and OCT imaging: design and scaling principles", *Optics Express* **13**, 3513-3528 (2005).
- [6] R. Huber, M. Wojtkowski, and J. G. Fujimoto, "Fourier Domain Mode Locking (FDML): A new laser operating regime and applications for optical coherence tomography", *Optics Express* **14**, 3225-3237 (2006).
- [7] T. Klein, W. Wieser, R. André, T. Pfeiffer, C. M. Eigenwillig, and R. Huber, "Multi-MHz FDML OCT: snapshot retinal imaging at 6.7 million axial-scans per second", in *Optical Coherence Tomography and Coherence Domain Optical Methods in Biomedicine XVI*, (SPIE, 2012), 82131E.
- [8] W. Wieser, B. R. Biedermann, T. Klein, C. M. Eigenwillig, and R. Huber, "Multi-Megahertz OCT: High quality 3D imaging at 20 million A-scans and 4.5 GVoxels per second", *Optics Express* **18**, 14685-14704 (2010).
- [9] J. E. Bowers, P. A. Morton, A. Mar, and S. W. Corzine, "Actively mode-locked semiconductor-lasers", *Ieee Journal of Quantum Electronics* **25**, 1426-1439 (1989).
- [10] C. M. Eigenwillig, B. R. Biedermann, G. Palte, and R. Huber, "K-space linear Fourier domain mode locked laser and applications for optical coherence tomography", *Optics Express* **16**, 8916-8937 (2008).
- [11] C. M. Eigenwillig, W. Wieser, B. R. Biedermann, and R. Huber, "Subharmonic Fourier domain mode locking", *Optics Letters* **34**, 725-727 (2009).
- [12] C. M. Eigenwillig, B. R. Biedermann, W. Wieser, and R. Huber, "Wavelength swept amplified spontaneous emission source", *Optics Express* **17**, 18794-18807 (2009).
- [13] C. M. Eigenwillig, T. Klein, W. Wieser, B. R. Biedermann, and R. Huber, "Wavelength swept amplified spontaneous emission source for high speed retinal optical coherence tomography at 1060 nm", *Journal of Biophotonics* **4**, 552-558 (2011).

- [14] B. R. Biedermann, W. Wieser, C. M. Eigenwillig, T. Klein, and R. Huber, "Dispersion, coherence and noise of Fourier domain mode locked lasers", *Optics Express* **17**, 9947-9961 (2009).
- [15] C. Jirauschek, B. Biedermann, and R. Huber, "A theoretical description of Fourier domain mode locked lasers", *Optics Express* **17**, 24013-24019 (2009).
- [16] J. S. Schuman, Puliafito C.A., Fujimoto J.G., *Optical Coherence Tomography of Ocular Diseases*, 2nd ed. (Slack Inc., Thorafare, 2004).
- [17] I. K. Jang, B. E. Bouma, D. H. Kang, S. J. Park, S. W. Park, K. B. Seung, K. B. Choi, M. Shishkov, K. Schlendorf, E. Pomerantsev, S. L. Houser, H. T. Aretz, and G. J. Tearney, "Visualization of coronary atherosclerotic plaques in patients using optical coherence tomography: Comparison with intravascular ultrasound", *Journal of the American College of Cardiology* **39**, 604-609 (2002).
- [18] G. J. Tearney, M. E. Brezinski, B. E. Bouma, S. A. Boppart, C. Pitris, J. F. Southern, and J. G. Fujimoto, "In vivo endoscopic optical biopsy with optical coherence tomography", *Science* **276**, 2037-2039 (1997).
- [19] M. A. Duguay and A. T. Mattick, "Ultrahigh Speed Photography of Picosecond Light Pulses and Echoes", *Applied Optics* **10**, 2162-2170 (1971).
- [20] A. P. Bruckner, "Picosecond light scattering measurements of cataract microstructure", *Applied Optics* **17**, 3177-3183 (1978).
- [21] J. G. Fujimoto, S. De Silvestri, E. P. Ippen, C. A. Puliafito, R. Margolis, and A. Oseroff, "Femtosecond optical ranging in biological systems", *Optics Letters* **11**, 150-152 (1986).
- [22] H. H. Gilgen, R. P. Novak, R. P. Salathe, W. Hodel, and P. Beaud, "Submillimeter optical reflectometry", *Journal of Lightwave Technology* **7**, 1225-1233 (1989).
- [23] K. Takada, I. Yokohama, K. Chida, and J. Noda, "New measurement system for fault location in optical waveguide devices based on an interferometric technique", *Applied Optics* **26**, 1603-1606 (1987).
- [24] R. C. Youngquist, S. Carr, and D. E. N. Davies, "Optical coherence-domain reflectometry: a new optical evaluation technique", *Optics Letters* **12**, 158-160 (1987).
- [25] A. F. Fercher, K. Mengedoht, and W. Werner, "Eye-length measurement by interferometry with partially coherent light", *Optics Letters* **13**, 186-188 (1988).
- [26] X. Clivaz, F. Marquis-Weible, R. P. Salathé, R. P. Novák, and H. H. Gilgen, "High-resolution reflectometry in biological tissues", *Optics Letters* **17**, 4-6 (1992).
- [27] J. M. Schmitt, A. Knüttel, and R. F. Bonner, "Measurement of optical properties of biological tissues by low-coherence reflectometry", *Applied Optics* **32**, 6032-6042 (1993).
- [28] J. Beutel, H. L. Kundel, and R. L. Van Metter, *Handbook of Medical Imaging* (SPIE Society of Photo-Optical Instrumentation, 2000).
- [29] G. Muehllehner and J. S. Karp, "Positron emission tomography", *Physics in Medicine and Biology* **51**, R117-R137 (2006).
- [30] T. Wilson, *Confocal Microscopy* (Academic Press Inc., 1990).
- [31] M. Gu, C. J. R. Sheppard, and X. Gan, "Image-formation in a fiberoptic confocal scanning microscope", *Journal of the Optical Society of America a-Optics Image Science and Vision* **8**, 1755-1761 (1991).

-
- [32] W. Drexler and J. G. Fujimoto, *Optical Coherence Tomography: Technology and Applications*, Biological and Medical Physics, Biomedical Engineering (Springer, 2008).
- [33] W. R. Hedrick, D. L. Hykes, and D. E. Starchmann, *Ultrasound Physics and Instrumentation 4th edition* (Mosby, 2005).
- [34] T. L. Szabo, *Diagnostic Ultrasound Imaging-Inside Out* (Academic Pr. Inc, 2004).
- [35] W. Drexler, U. Morgner, R. K. Ghanta, F. X. Kartner, J. S. Schuman, and J. G. Fujimoto, "Ultrahigh-resolution ophthalmic optical coherence tomography", *Nature Medicine* **7**, 502-507 (2001).
- [36] G. M. Hale and M. R. Querry, "Optical Constants of Water in the 200-nm to 200- μ m Wavelength Region", *Applied Optics* **12**, 555-563 (1973).
- [37] A. N. Bashkatov, E. A. Genina, V. I. Kochubey, and V. V. Tuchin, "Optical properties of human skin, subcutaneous and mucous tissues in the wavelength range from 400 to 2000 nm", *Journal of Physics D-Applied Physics* **38**, 2543-2555 (2005).
- [38] M. E. Brezinski, G. J. Tearney, B. E. Bouma, J. A. Izatt, M. R. Hee, E. A. Swanson, J. F. Southern, and J. G. Fujimoto, "Optical coherence tomography for optical biopsy - Properties and demonstration of vascular pathology", *Circulation* **93**, 1206-1213 (1996).
- [39] J. G. Fujimoto, M. E. Brezinski, G. J. Tearney, S. A. Boppart, B. Bouma, M. R. Hee, J. F. Southern, and E. A. Swanson, "Optical biopsy and imaging using optical coherence tomography", *Nature Medicine* **1**, 970-972 (1995).
- [40] J. M. Schmitt, A. Knuttel, M. Yadlowsky, and M. A. Eckhaus, "Optical coherence tomography of a dense tissue - Statistics of attenuation and backscattering", *Physics in Medicine and Biology* **39**, 1705-1720 (1994).
- [41] B. R. Biedermann, W. Wieser, C. M. Eigenwillig, and R. Huber, "Recent developments in Fourier Domain Mode Locked lasers for optical coherence tomography: Imaging at 1310 nm vs. 1550 nm wavelength", *Journal of Biophotonics* **2**, 357-363 (2009).
- [42] B. Povazay, K. Bizheva, B. Hermann, A. Unterhuber, H. Sattmann, A. F. Fercher, W. Drexler, C. Schubert, P. K. Ahnelt, M. Mei, R. Holzwarth, W. J. Wadsworth, J. C. Knight, and P. S. Russel, "Enhanced visualization of choroidal vessels using ultrahigh resolution ophthalmic OCT at 1050 nm", *Optics Express* **11**, 1980-1986 (2003).
- [43] Y. Chen, D. L. Burnes, M. de Bruin, M. Mujat, and J. F. de Boer, "Three-dimensional pointwise comparison of human retinal optical property at 845 and 1060 nm using optical frequency domain imaging", *Journal of Biomedical Optics* **14**, 024016 (2009).
- [44] B. Povazay, B. Hermann, A. Unterhuber, B. Hofer, H. Sattmann, F. Zeiler, J. E. Morgan, C. Falkner-Radler, C. Glittenberg, S. Blinder, and W. Drexler, "Three-dimensional optical coherence tomography at 1050 nm versus 800 nm in retinal pathologies: enhanced performance and choroidal penetration in cataract patients", *Journal of Biomedical Optics* **12**, 041211 (2007).
- [45] A. Unterhuber, B. Povazay, B. Hermann, H. Sattmann, A. Chavez-Pirson, and W. Drexler, "In vivo retinal optical coherence tomography at 1040 nm-enhanced penetration into the choroid", *Optics Express* **13**, 3252-3258 (2005).
- [46] M. Brezinski, *Optical Coherence Tomography-Principles and Application* (Academic Press, 2006).

- [47] H. A. Haus, *Waves and Fields in Optoelectronics*, Solid state physical electronics (Prentice-Hall, Inc., New Jersey, 1984).
- [48] E. A. Swanson, D. Huang, M. R. Hee, J. G. Fujimoto, C. P. Lin, and C. A. Puliafito, "High-speed optical coherence domain reflectometry", *Optics Letters* **17**, 151-153 (1992).
- [49] A. F. Fercher, C. K. Hitzenberger, G. Kamp, and S. Y. Elzaiat, "Measurement of Intraocular Distances by Backscattering Spectral Interferometry", *Optics Communications* **117**, 43-48 (1995).
- [50] M. Wojtkowski, R. Leitgeb, A. Kowalczyk, T. Bajraszewski, and A. F. Fercher, "In vivo human retinal imaging by Fourier domain optical coherence tomography", *Journal of Biomedical Optics* **7**, 457-463 (2002).
- [51] H. Barfuss and E. Brinkmeyer, "Modified optical frequency-domain reflectometry with high spatial-resolution for components of integrated optic systems", *Journal of Lightwave Technology* **7**, 3-10 (1989).
- [52] W. Eickhoff and R. Ulrich, "Optical frequency-domain reflectometry in single-mode fiber", *Applied Physics Letters* **39**, 693-695 (1981).
- [53] U. Glombitza and E. Brinkmeyer, "Coherent frequency-domain reflectometry for characterization of single-mode integrated-optical waveguides", *Journal of Lightwave Technology* **11**, 1377-1384 (1993).
- [54] S. R. Chinn, E. A. Swanson, and J. G. Fujimoto, "Optical coherence tomography using a frequency-tunable optical source", *Optics Letters* **22**, 340-342 (1997).
- [55] B. Golubovic, B. E. Bouma, G. J. Tearney, and J. G. Fujimoto, "Optical frequency-domain reflectometry using rapid wavelength tuning of a Cr⁴⁺:forsterite laser", *Optics Letters* **22**, 1704-1706 (1997).
- [56] S. H. Yun, G. J. Tearney, J. F. de Boer, N. Ifimia, and B. E. Bouma, "High-speed optical frequency-domain imaging", *Optics Express* **11**, 2953-2963 (2003).
- [57] S. H. Yun, G. J. Tearney, J. F. de Boer, and B. E. Bouma, "Removing the depth-degeneracy in optical frequency domain imaging with frequency shifting", *Optics Express* **12**, 4822-4828 (2004).
- [58] E. Gotzinger, M. Pircher, R. A. Leitgeb, and C. K. Hitzenberger, "High speed full range complex spectral domain optical coherence tomography", *Optics Express* **13**, 583-594 (2005).
- [59] R. A. Leitgeb, C. K. Hitzenberger, A. F. Fercher, and T. Bajraszewski, "Phase-shifting algorithm to achieve high-speed long-depth-range probing by frequency-domain optical coherence tomography", *Optics Letters* **28**, 2201-2203 (2003).
- [60] M. Wojtkowski, A. Kowalczyk, R. Leitgeb, and A. F. Fercher, "Full range complex spectral optical coherence tomography technique in eye imaging", *Optics Letters* **27**, 1415-1417 (2002).
- [61] Y. Yasuno, S. Makita, T. Endo, G. Aoki, M. Itoh, and T. Yatagai, "Simultaneous B-M-mode scanning method for real-time full-range Fourier domain optical coherence tomography", *Applied Optics* **45**, 1861-1865 (2006).
- [62] J. Zhang, J. S. Nelson, and Z. P. Chen, "Removal of a mirror image and enhancement of the signal-to-noise ratio in Fourier-domain optical coherence tomography using an electro-optic phase modulator", *Optics Letters* **30**, 147-149 (2005).

-
- [63] R. A. Leitgeb, R. Michaely, T. Lasser, and S. C. Sekhar, "Complex ambiguity-free Fourier domain optical coherence tomography through transverse scanning", *Optics Letters* **32**, 3453-3455 (2007).
- [64] M. Szkulmowski, I. Grulkowski, D. Szlag, A. Szkulmowska, A. Kowalczyk, and M. Wojtkowski, "Flow velocity estimation by complex ambiguity free joint Spectral and Time domain Optical Coherence Tomography", *Optics Express* **17**, 14281-14297 (2009).
- [65] M. A. Choma, C. H. Yang, and J. A. Izatt, "Instantaneous quadrature low-coherence interferometry with 3 x 3 fiber-optic couplers", *Optics Letters* **28**, 2162-2164 (2003).
- [66] M. V. Sarunic, M. A. Choma, C. H. Yang, and J. A. Izatt, "Instantaneous complex conjugate resolved spectral domain and swept-source OCT using 3x3 fiber couplers", *Optics Express* **13**, 957-967 (2005).
- [67] M. V. Sarunic, B. E. Applegate, and J. A. Izatt, "Real-time quadrature projection complex conjugate resolved Fourier domain optical coherence tomography", *Optics Letters* **31**, 2426-2428 (2006).
- [68] B. Hofer, B. Povazay, B. Hermann, A. Unterhuber, G. Matz, and W. Drexler, "Dispersion encoded full range frequency domain optical coherence tomography", *Optics Express* **17**, 7-24 (2009).
- [69] G. L. Abbas, V. W. S. Chan, and T. K. Yee, "Local-oscillator excess-noise suppression for homodyne and heterodyne detection", *Optics Letters* **8**, 419-421 (1983).
- [70] A. G. Podoleanu, "Unbalanced versus balanced operation in an optical coherence tomography system", *Applied Optics* **39**, 173-182 (2000).
- [71] A. M. Rollins and J. A. Izatt, "Optimal interferometer designs for optical coherence tomography", *Optics Letters* **24**, 1484-1486 (1999).
- [72] M. W. Jenkins, D. C. Adler, M. Gargsha, R. Huber, F. Rothenberg, J. Belding, M. Watanabe, D. L. Wilson, J. G. Fujimoto, and A. M. Rollins, "Ultrahigh-speed optical coherence tomography imaging and visualization of the embryonic avian heart using a buffered Fourier Domain Mode Locked laser", *Optics Express* **15**, 6251-6267 (2007).
- [73] D. C. Adler, Y. Chen, R. Huber, J. Schmitt, J. Connolly, and J. G. Fujimoto, "Three-dimensional endomicroscopy using optical coherence tomography", *Nature Photonics* **1**, 709-716 (2007).
- [74] T. Klein, W. Wieser, C. M. Eigenwillig, B. R. Biedermann, and R. Huber, "Megahertz OCT for ultrawide-field retinal imaging with a 1050nm Fourier domain mode-locked laser", *Optics Express* **19**, 3044-3062 (2011).
- [75] F. Lexer, C. K. Hitzenberger, W. Drexler, S. Molebny, H. Sattmann, M. Sticker, and A. F. Fercher, "Dynamic coherent focus OCT with depth-independent transversal resolution", *Journal of Modern Optics* **46**, 541-553 (1999).
- [76] S. H. Yun, G. J. Tearney, J. F. de Boer, and B. E. Bouma, "Motion artifacts in optical coherence tomography with frequency-domain ranging", *Optics Express* **12**, 2977-2998 (2004).
- [77] H. C. Hendargo, R. P. McNabb, A.-H. Dhalla, N. Shepherd, and J. A. Izatt, "Doppler velocity detection limitations in spectrometer-based versus swept-source optical coherence tomography", *Biomedical Optics Express* **2**, 2175-2188 (2011).
- [78] J. M. Schmitt and G. Kumar, "Optical scattering properties of soft tissue: a discrete particle model", *Applied Optics* **37**, 2788-2797 (1998).

- [79] J. A. Izatt, M. R. Hee, G. M. Owen, E. A. Swanson, and J. G. Fujimoto, "Optical coherence microscopy in scattering media", *Optics Letters* **19**, 590-592 (1994).
- [80] Z136-Committee, *American National Standard for Safe Use of Lasers: ANSI Z136.1-2000* (Laser Institute of America, 2007).
- [81] I. Grulkowski, M. Gora, M. Szkulmowski, I. Gorczynska, D. Szlag, S. Marcos, A. Kowalczyk, and M. Wojtkowski, "Anterior segment imaging with Spectral OCT system using a high-speed CMOS camera", *Optics Express* **17**, 4842-4858 (2009).
- [82] E. L. Dereniak and G. D. Boreman, *Infrared Detectors and Systems* (John Wiley&Sons, 1996).
- [83] B. M. Oliver, "Thermal and quantum noise", *Proceedings of the Institute of Electrical and Electronics Engineers* **53**, 436-454 (1965).
- [84] L. K. Anderson and B. J. McMurtry, "High-speed photodetectors", *Applied Optics* **5**, 1573-1587 (1966).
- [85] M. O. Scully and M. S. Zubairy, *Quantum Optics*, 1 ed. (Cambridge University Press, 1997).
- [86] B. Saleh, *Photoelectron Statistics : With applications to Spectroscopy and Optical Communication*, Springer series in Optical Sciences (Springer, 1978).
- [87] H. Hodara, "Statistics of Thermal and Laser Radiation", *Proceedings of the Institute of Electrical and Electronics Engineers* **53**, 696-704 (1965).
- [88] P. R. Morkel, R. I. Laming, and D. N. Payne, "Noise characteristics of high-power doped-fiber superluminescent sources", *Electronics Letters* **26**, 96-98 (1990).
- [89] S. S. Sherif, C. C. Rosa, C. Fluerau, S. Chang, Y. Mao, and A. G. Podoleanu, "Statistics of the depth-scan photocurrent in time-domain optical coherence tomography", *Journal of the Optical Society of America A-Optics Image Science and Vision* **25**, 16-20 (2008).
- [90] M. Blazek, S. Hartmann, A. Molitor, and W. Elsaesser, "Unifying intensity noise and second-order coherence properties of amplified spontaneous emission sources", *Optics Letters* **36**, 3455-3457 (2011).
- [91] G. Palte, "Diplomarbeit: Fourierdomänen modengekoppelte Laser für polarisationssensitive optische Kohärenztomographie", *Diplomarbeit* (Ludwig-Maximilians-Universität München, 2008).
- [92] T. Klein, "Diploma thesis: Fourier Domain Mode Locked Lasers for Optical Coherence Tomography", *Diplomarbeit* (Ludwig-Maximilians-Universität München, 2009).
- [93] R. H. Webb, G. W. Hughes, and O. Pomerantzeff, "Flying spot TV ophthalmoscope", *Applied Optics* **19**, 2991-2997 (1980).
- [94] A. F. Fercher, C. K. Hitzenberger, W. Drexler, G. Kamp, and H. Sattmann, "in-vivo Optical Coherence Tomography", *American Journal of Ophthalmology* **116**, 113-115 (1993).
- [95] E. A. Swanson, J. A. Izatt, M. R. Hee, D. Huang, C. P. Lin, J. S. Schuman, C. A. Puliafito, and J. G. Fujimoto, "In vivo retinal imaging by optical coherence tomography", *Optics Letters* **18**, 1864-1866 (1993).
- [96] J. A. Goldsmith, Y. Li, M. R. Chalita, V. Westphal, C. A. Patil, A. M. Rollins, J. A. Izatt, and D. Huang, "Anterior chamber width measurement by high speed optical coherence tomography", *Ophthalmology* **112**, 238-244 (2005).
- [97] H. Hoerauf, C. Wirbelauer, C. Scholz, R. Engelhardt, P. Koch, H. Laqua, and R. Birngruber, "Slit-lamp-adapted optical coherence tomography of the anterior

- segment", Graefes Archive for Clinical and Experimental Ophthalmology **238**, 8-18 (2000).
- [98] S. Radhakrishnan, A. M. Rollins, J. E. Roth, S. Yazdanfar, V. Westphal, D. S. Bardenstein, and J. A. Izatt, "Real-time optical coherence tomography of the anterior segment at 1310 nm", Archives of Ophthalmology **119**, 1179-1185 (2001).
- [99] B. E. Bouma, G. J. Tearney, H. Yabushita, M. Shishkov, C. R. Kauffman, D. D. Gauthier, B. D. MacNeill, S. L. Houser, H. T. Aretz, E. F. Halpern, and I. K. Jang, "Evaluation of intracoronary stenting by intravascular optical coherence tomography", Heart **89**, 317-320 (2003).
- [100] B. E. Bouma and G. J. Tearney, "Power-efficient nonreciprocal interferometer and linear-scanning fiber-optic catheter for optical coherence tomography", Optics Letters **24**, 531-533 (1999).
- [101] A. M. Rollins, R. Ung-arunyawee, A. Chak, R. C. K. Wong, K. Kobayashi, M. V. Sivak, and J. A. Izatt, "Real-time in vivo imaging of human gastrointestinal ultrastructure by use of endoscopic optical coherence tomography with a novel efficient interferometer design", Optics Letters **24**, 1358-1360 (1999).
- [102] B. E. Bouma, G. J. Tearney, C. C. Compton, and N. S. Nishioka, "Endoscopic optical coherence tomography of the gastrointestinal tract", Gastrointestinal Endoscopy **49**, AB152-AB152 (1999).
- [103] A. V. Shakhov, A. B. Terentjeva, V. A. Kamensky, L. B. Snopova, V. M. Gelikonov, F. I. Feldchtein, and A. M. Sergeev, "Optical coherence tomography monitoring for laser surgery of laryngeal carcinoma", Journal of Surgical Oncology **77**, 253-258 (2001).
- [104] A. G. Bibas, A. G. Podoleanu, R. G. Cucu, M. Bonmarin, G. M. Dobre, V. M. M. Ward, E. Odell, A. Boxer, M. J. Gleeson, and D. A. Jackson, "3-D optical coherence tomography of the laryngeal mucosa", Clinical Otolaryngology **29**, 713-720 (2004).
- [105] N. Hanna, D. Saltzman, D. Mukai, Z. Chen, S. Sasse, J. Milliken, S. Guo, W. Jung, H. Colt, and M. Brenner, "Two-dimensional and 3-dimensional optical coherence tomographic imaging of the airway, lung, and pleura", Journal of Thoracic and Cardiovascular Surgery **129**, 615-622 (2005).
- [106] C. Pitris, M. E. Brezinski, B. E. Bouma, G. J. Tearney, J. F. Southern, and J. G. Fujimoto, "High resolution imaging of the upper respiratory tract with optical coherence tomography - A feasibility study", American Journal of Respiratory and Critical Care Medicine **157**, 1640-1644 (1998).
- [107] A. Sergeev, V. Gelikonov, G. Gelikonov, F. Feldchtein, R. Kuranov, N. Gladkova, N. Shakhova, L. Snopova, A. Shakhov, I. Kuznetzova, A. Denisenko, V. Pochinko, Y. Chumakov, and O. Streltzova, "In vivo endoscopic OCT imaging of precancer and cancer states of human mucosa", Optics Express **1**, 432-440 (1997).
- [108] G. J. Tearney, M. E. Brezinski, J. F. Southern, B. E. Bouma, S. A. Boppart, and J. G. Fujimoto, "Optical biopsy in human urologic tissue using optical coherence tomography", Journal of Urology **157**, 1915-1919 (1997).
- [109] S. A. Boppart, M. E. Brezinski, B. E. Bouma, G. J. Tearney, and J. G. Fujimoto, "Investigation of developing embryonic morphology using optical coherence tomography", Developmental Biology **177**, 54-63 (1996).

- [110] M. W. Jenkins, O. Q. Chughtai, A. N. Basavanhally, M. Watanabe, and A. M. Rollins, "In vivo gated 4D imaging of the embryonic heart using optical coherence tomography", *Journal of Biomedical Optics* **12**, 030505 (2007).
- [111] A. Baumgartner, S. Dichtl, C. K. Hitzenberger, H. Sattmann, B. Robl, A. Moritz, Z. F. Fercher, and W. Sperr, "Polarization-sensitive optical coherence tomography of dental structures", *Caries Research* **34**, 59-69 (2000).
- [112] B. W. Colston, U. S. Sathyam, L. B. DaSilva, M. J. Everett, P. Stroeve, and L. L. Otis, "Dental OCT", *Optics Express* **3**, 230-238 (1998).
- [113] J. Welzel, "Optical coherence tomography in dermatology: a review", *Skin Research and Technology* **7**, 1-9 (2001).
- [114] Z. Chen, T. E. Milner, S. Srinivas, X. Wang, A. Malekafzali, M. J. C. van Gemert, and J. S. Nelson, "Noninvasive imaging of in vivo blood flow velocity using optical Doppler tomography", *Optics Letters* **22**, 1119-1121 (1997).
- [115] J. A. Izatt, M. D. Kulkarni, S. Yazdanfar, J. K. Barton, and A. J. Welch, "In vivo bidirectional color Doppler flow imaging of picoliter blood volumes using optical coherence tomography", *Optics Letters* **22**, 1439-1441 (1997).
- [116] Z. H. Ding, Y. H. Zhao, H. W. Ren, J. S. Nelson, and Z. P. Chen, "Real-time phase-resolved optical coherence tomography and optical Doppler tomography", *Optics Express* **10**, 236-245 (2002).
- [117] J. S. Nelson, K. M. Kelly, Y. H. Zhao, and Z. P. Chen, "Imaging blood flow in human port-wine stain in situ and in real time using optical Doppler tomography", *Archives of Dermatology* **137**, 741-744 (2001).
- [118] Y. H. Zhao, Z. P. Chen, C. Saxer, Q. M. Shen, S. H. Xiang, J. F. de Boer, and J. S. Nelson, "Doppler standard deviation imaging for clinical monitoring of in vivo human skin blood flow", *Optics Letters* **25**, 1358-1360 (2000).
- [119] Y. H. Zhao, Z. P. Chen, C. Saxer, S. H. Xiang, J. F. de Boer, and J. S. Nelson, "Phase-resolved optical coherence tomography and optical Doppler tomography for imaging blood flow in human skin with fast scanning speed and high velocity sensitivity", *Optics Letters* **25**, 114-116 (2000).
- [120] B. Baumann, B. Potsaid, M. F. Kraus, J. J. Liu, D. Huang, J. Hornegger, A. E. Cable, J. S. Duker, and J. G. Fujimoto, "Total retinal blood flow measurement with ultrahigh speed swept source/Fourier domain OCT", *Biomedical Optics Express* **2**, 1539-1552 (2011).
- [121] R. A. Leitgeb, L. Schmetterer, W. Drexler, A. F. Fercher, R. J. Zawadzki, and T. Bajraszewski, "Real-time assessment of retinal blood flow with ultrafast acquisition by color Doppler Fourier domain optical coherence tomography", *Optics Express* **11**, 3116-3121 (2003).
- [122] S. Makita, Y. Hong, M. Yamanari, T. Yatagai, and Y. Yasuno, "Optical coherence angiography", *Optics Express* **14**, 7821-7840 (2006).
- [123] B. J. Vakoc, S. H. Yun, J. F. de Boer, G. J. Tearney, and B. E. Bouma, "Phase-resolved optical frequency domain imaging", *Optics Express* **13**, 5483-5493 (2005).
- [124] B. R. White, M. C. Pierce, N. Nassif, B. Cense, B. H. Park, G. J. Tearney, B. E. Bouma, T. C. Chen, and J. F. de Boer, "In vivo dynamic human retinal blood flow imaging using ultra-high-speed spectral domain optical Doppler tomography", *Optics Express* **11**, 3490-3497 (2003).
- [125] S. Zotter, M. Pircher, T. Torzicky, M. Bonesi, E. Goetzinger, R. A. Leitgeb, and C. K. Hitzenberger, "Visualization of microvasculature by dual-beam phase-

- resolved Doppler optical coherence tomography", *Optics Express* **19**, 1217-1227 (2011).
- [126] M. R. Hee, D. Huang, E. A. Swanson, and J. G. Fujimoto, "Polarization-Sensitive Low-Coherence Reflectometer for Birefringence Characterization and Ranging", *Journal of the Optical Society of America B-Optical Physics* **9**, 903-908 (1992).
- [127] J. F. deBoer, T. E. Milner, M. J. C. vanGemert, and J. S. Nelson, "Two-dimensional birefringence imaging in biological tissue by polarization-sensitive optical coherence tomography", *Optics Letters* **22**, 934-936 (1997).
- [128] J. F. de Boer, T. E. Milner, and J. S. Nelson, "Determination of the depth-resolved Stokes parameters of light backscattered from turbid media by use of polarization-sensitive optical coherence tomography", *Optics Letters* **24**, 300-302 (1999).
- [129] C. K. Hitzenberger, E. Gotzinger, M. Sticker, M. Pircher, and A. F. Fercher, "Measurement and imaging of birefringence and optic axis orientation by phase resolved polarization sensitive optical coherence tomography", *Optics Express* **9**, 780-790 (2001).
- [130] M. C. Pierce, B. H. Park, B. Cense, and J. F. de Boer, "Simultaneous intensity, birefringence, and flow measurements with high-speed fiber-based optical coherence tomography", *Optics Letters* **27**, 1534-1536 (2002).
- [131] C. E. Saxer, J. F. de Boer, B. H. Park, Y. Zhao, Z. Chen, and J. S. Nelson, "High-speed fiber based polarization-sensitive optical coherence tomography of in vivo human skin", *Optics Letters* **25**, 1355-1357 (2000).
- [132] Y. Yasuno, S. Makita, Y. Sutoh, M. Itoh, and T. Yatagai, "Birefringence imaging of human skin by polarization-sensitive spectral interferometric optical coherence tomography", *Optics Letters* **27**, 1803-1805 (2002).
- [133] E. Gotzinger, M. Pircher, and C. K. Hitzenberger, "High speed spectral domain polarization sensitive optical coherence tomography of the human retina", *Optics Express* **13**, 10217-10229 (2005).
- [134] B. H. Park, M. C. Pierce, B. Cense, S. H. Yun, M. Mujat, G. J. Tearney, B. E. Bouma, and J. F. de Boer, "Real-time fiber-based multi-functional spectral-domain optical coherence tomography at 1.3 μm ", *Optics Express* **13**, 3931-3944 (2005).
- [135] M. Yamanari, S. Makita, V. D. Madjarova, T. Yatagai, and Y. Yasuno, "Fiber-based polarization-sensitive Fourier domain optical coherence tomography using B-scan-oriented polarization modulation method", *Optics Express* **14**, 6502-6515 (2006).
- [136] E. Goetzinger, M. Pircher, B. Baumann, T. Schmoll, H. Sattmann, R. A. Leitgeb, and C. K. Hitzenberger, "Speckle noise reduction in high speed polarization sensitive spectral domain optical coherence tomography", *Optics Express* **19**, 14568-14584 (2011).
- [137] E. Goetzinger, B. Baumann, M. Pircher, and C. K. Hitzenberger, "Polarization maintaining fiber based ultra-high resolution spectral domain polarization sensitive optical coherence tomography", *Optics Express* **17**, 22704-22717 (2009).
- [138] J. Zhang, W. G. Jung, J. S. Nelson, and Z. P. Chen, "Full range polarization-sensitive Fourier domain optical coherence tomography", *Optics Express* **12**, 6033-6039 (2004).

- [139] M. Yamanari, S. Makita, and Y. Yasuno, "Polarization-sensitive swept-source optical coherence tomography with continuous source polarization modulation", *Optics Express* **16**, 5892-5906 (2008).
- [140] M. Yamanari, Y. Lim, S. Makita, and Y. Yasuno, "Visualization of phase retardation of deep posterior eye by polarization-sensitive swept-source optical coherence tomography with 1- μm probe", *Optics Express* **17**, 12385-12396 (2009).
- [141] J. M. Schmitt, S. H. Xiang, and K. M. Yung, "Differential absorption imaging with optical coherence tomography", *Journal of the Optical Society of America a-Optics Image Science and Vision* **15**, 2288-2296 (1998).
- [142] R. Leitgeb, M. Wojtkowski, C. K. Hitzenberger, A. F. Fercher, M. Sticker, and A. Kowalczyk, "Depth resolved spectroscopy by frequency domain optical coherence tomography", in *Photon Migration, Diffuse Spectroscopy and Optical Coherence Tomography: Imaging and Functional Assessment*, (SPIE, 2000), 57-62.
- [143] U. Morgner, W. Drexler, F. X. Kartner, X. D. Li, C. Pitris, E. P. Ippen, and J. G. Fujimoto, "Spectroscopic optical coherence tomography", *Optics Letters* **25**, 111-113 (2000).
- [144] P. Koch, G. Huttman, H. Schleiermacher, J. Eichholz, and E. Koch, "Linear OCT system with down conversion of the fringe pattern", in *Coherence Domain Optical Methods and Optical Coherence Tomography in Biomedicine VIII*, (SPIE, 2004), 260-267.
- [145] P. Koch, V. Hellemanns, and G. Huettmann, "Linear optical coherence tomography system with extended measurement range", *Optics Letters* **31**, 2882-2884 (2006).
- [146] A. Dubois, K. Grieve, G. Moneron, R. Lecaque, L. Vabre, and C. Boccara, "Ultrahigh-resolution full-field optical coherence tomography", *Applied Optics* **43**, 2874-2883 (2004).
- [147] A. Dubois, J. Moreau, and C. Boccara, "Spectroscopic ultrahigh-resolution full-field optical coherence microscopy", *Optics Express* **16**, 17082-17091 (2008).
- [148] A. Dubois, L. Vabre, A. C. Boccara, and E. Beaurepaire, "High-resolution full-field optical coherence tomography with a Linnik microscope", *Applied Optics* **41**, 805-812 (2002).
- [149] T. Bonin, G. Franke, M. Hagen-Eggert, P. Koch, and G. Huettmann, "In vivo Fourier-domain full-field OCT of the human retina with 1.5 million A-lines/s", *Optics Letters* **35**, 3432-3434 (2010).
- [150] B. Bouma, G. J. Tearney, S. A. Boppart, M. R. Hee, M. E. Brezinski, and J. G. Fujimoto, "High-resolution optical coherence tomographic imaging using a mode-locked Ti-Al₂O₃ laser source", *Optics Letters* **20**, 1486-1488 (1995).
- [151] W. Drexler, U. Morgner, F. X. Kartner, C. Pitris, S. A. Boppart, X. D. Li, E. P. Ippen, and J. G. Fujimoto, "In vivo ultrahigh-resolution optical coherence tomography", *Optics Letters* **24**, 1221-1223 (1999).
- [152] M. Wojtkowski, V. J. Srinivasan, T. H. Ko, J. G. Fujimoto, A. Kowalczyk, and J. S. Duker, "Ultrahigh-resolution, high-speed, Fourier domain optical coherence tomography and methods for dispersion compensation", *Optics Express* **12**, 2404-2422 (2004).
- [153] W. Drexler, H. Sattmarin, B. Hermann, T. H. Ko, M. Stur, A. Unterhuber, C. Scholda, O. Findl, M. Wirtitsch, J. G. Fujimoto, and A. F. Fercher, "Enhanced

- visualization of macular pathology with the use of ultrahigh-resolution optical coherence tomography", *Archives of Ophthalmology* **121**, 695-706 (2003).
- [154] T. H. Ko, J. G. Fujimoto, J. S. Duker, L. A. Paunescu, W. Drexler, C. R. Baumal, C. A. Puliafito, E. Reichel, A. H. Rogers, and J. S. Schuman, "Comparison of ultrahigh- and standard-resolution optical coherence tomography for imaging macular hole pathology and repair", *Ophthalmology* **111**, 2033-2043 (2004).
- [155] S. L. Jiao, R. Knighton, X. R. Huang, G. Gregori, and C. A. Puliafito, "Simultaneous acquisition of sectional and fundus ophthalmic images with spectral-domain optical coherence tomography", *Optics Express* **13**, 444-452 (2005).
- [156] N. Nassif, B. Cense, B. Park, M. Pierce, S. Yun, B. Bouma, G. Tearney, T. Chen, and J. de Boer, "In vivo high-resolution video-rate spectral-domain optical coherence tomography of the human retina and optic nerve", *Optics Express* **12**, 367-376 (2004).
- [157] Y. Zhang, B. Cense, J. Rha, R. S. Jonnal, W. Gao, R. J. Zawadzki, J. S. Werner, S. Jones, S. Olivier, and D. T. Miller, "High-speed volumetric imaging of cone photoreceptors with adaptive optics spectral-domain optical coherence tomography", *Optics Express* **14**, 4380-4394 (2006).
- [158] B. Potsaid, J. Liu, V. Manjunath, I. Gorczynska, V. J. Srinivasan, J. Jiang, S. Barry, A. Cable, J. S. Duker, and J. G. Fujimoto, "Ultrahigh speed volumetric ophthalmic OCT imaging at 850nm and 1050nm", in *Ophthalmic Technologies XX*, (SPIE, 2010), 75501K.
- [159] T. Schmoll, E. Goetzinger, M. Pircher, C. K. Hitzenberger, and R. A. Leitgeb, "Single-camera polarization-sensitive spectral-domain OCT by spatial frequency encoding", *Optics Letters* **35**, 241-243 (2010).
- [160] B. Potsaid, I. Gorczynska, V. J. Srinivasan, Y. Chen, J. Jiang, A. Cable, and J. G. Fujimoto, "Ultrahigh speed Spectral/Fourier domain OCT ophthalmic imaging at 70,000 to 312,500 axial scans per second", *Optics Express* **16**, 15149-15169 (2008).
- [161] L. An, H. M. Subhash, and R. K. Wang, "Full range complex spectral domain optical coherence tomography for volumetric imaging at 47 000 A-scans per second", *Journal of Optics* **12**, 084003 (2010).
- [162] S. Makita, T. Fabritius, and Y. Yasuno, "Full-range, high-speed, high-resolution 1- μ m spectral-domain optical coherence tomography using BM-scan for volumetric imaging of the human posterior eye", *Optics Express* **16**, 8406-8420 (2008).
- [163] P. Puvanathan, P. Forbes, Z. Ren, D. Malchow, S. Boyd, and K. Bizheva, "High-speed, high-resolution Fourier-domain optical coherence tomography system for retinal imaging in the 1060 nm wavelength region", *Optics Letters* **33**, 2479-2481 (2008).
- [164] R. K. Wang and L. An, "Multifunctional imaging of human retina and choroid with 1050-nm spectral domain optical coherence tomography at 92-kHz line scan rate", *Journal of Biomedical Optics* **16**, 050503 (2011).
- [165] L. An, G. Guan, and R. K. Wang, "High-speed 1310 nm-band spectral domain optical coherence tomography at 184,000 lines per second", *Journal of Biomedical Optics* **16**, 060506 (2011).

- [166] L. An, P. Li, T. T. Shen, and R. Wang, "High speed spectral domain optical coherence tomography for retinal imaging at 500,000 A-lines per second", *Biomedical Optics Express* **2**, 2770-2783 (2011).
- [167] D. Choi, H. Hiro-Oka, H. Furukawa, R. Yoshimura, M. Nakanishi, K. Shimizu, and K. Ohbayashi, "Fourier domain optical coherence tomography using optical demultiplexers imaging at 60,000,000 lines/s", *Optics Letters* **33**, 1318-1320 (2008).
- [168] D. M. de Bruin, D. L. Burnes, J. Loewenstein, Y. L. Chen, S. Chang, T. C. Chen, D. D. Esmaili, and J. F. de Boer, "In vivo three-dimensional imaging of neovascular age-related macular degeneration using optical frequency domain imaging at 1050 nm", *Investigative Ophthalmology & Visual Science* **49**, 4545-4552 (2008).
- [169] E. C. Lee, J. F. de Boer, M. Mujat, H. Lim, and S. H. Yun, "In vivo optical frequency domain imaging of human retina and choroid", *Optics Express* **14**, 4403-4411 (2006).
- [170] H. Lim, J. F. de Boer, B. H. Park, E. C. W. Lee, R. Yelin, and S. H. Yun, "Optical frequency domain imaging with a rapidly swept laser in the 815-870 nm range", *Optics Express* **14**, 5937-5944 (2006).
- [171] H. Lim, M. Mujat, C. Kerbage, E. C. W. Lee, Y. Chen, T. C. Chen, and J. F. de Boer, "High-speed imaging of human retina in vivo with swept-source optical coherence tomography", *Optics Express* **14**, 12902-12908 (2006).
- [172] V. J. Srinivasan, R. Huber, I. Gorczynska, J. G. Fujimoto, J. Y. Jiang, P. Reisen, and A. E. Cable, "High-speed, high-resolution optical coherence tomography retinal imaging with a frequency-swept laser at 850 nm", *Optics Letters* **32**, 361-363 (2007).
- [173] S. H. Yun, C. Boudoux, G. J. Tearney, and B. E. Bouma, "High-speed wavelength-swept semiconductor laser with a polygon-scanner-based wavelength filter", *Optics Letters* **28**, 1981-1983 (2003).
- [174] W. Y. Oh, S. H. Yun, G. J. Tearney, and B. E. Bouma, "115 kHz tuning repetition rate ultrahigh-speed wavelength-swept semiconductor laser", *Optics Letters* **30**, 3159-3161 (2005).
- [175] W. Y. Oh, S. H. Yun, B. J. Vakoc, G. J. Tearney, and B. E. Bouma, "Ultrahigh-speed optical frequency domain imaging and application to laser ablation monitoring", *Applied Physics Letters* **88**, 103902 (2006).
- [176] S. Moon and D. Y. Kim, "Ultra-high-speed optical coherence tomography with a stretched pulse supercontinuum source", *Optics Express* **14**, 11575-11584 (2006).
- [177] R. Huber, D. C. Adler, and J. G. Fujimoto, "Buffered Fourier domain mode locking: unidirectional swept laser sources for optical coherence tomography imaging at 370,000 lines/s", *Optics Letters* **31**, 2975-2977 (2006).
- [178] R. Huber, D. C. Adler, V. J. Srinivasan, and J. G. Fujimoto, "Fourier domain mode locking at 1050 nm for ultra-high-speed optical coherence tomography of the human retina at 236,000 axial scans per second", *Optics Letters* **32**, 2049-2051 (2007).
- [179] S. Marschall, T. Klein, W. Wieser, B. R. Biedermann, K. Hsu, K. P. Hansen, B. Sumpf, K.-H. Hasler, G. Erbert, O. B. Jensen, C. Pedersen, R. Huber, and P. E. Andersen, "Fourier domain mode-locked swept source at 1050 nm based on a tapered amplifier", *Optics Express* **18**, 15820-15831 (2010).

- [180] M. Kuznetsov, W. Atia, B. Johnson, and D. Flanders, "Compact Ultrafast Reflective Fabry-Perot Tunable Lasers For OCT Imaging Applications", in *Optical Coherence Tomography and Coherence Domain Optical Methods in Biomedicine Xiv*, (SPIE, 2010), 75541F.
- [181] B. Potsaid, B. Baumann, D. Huang, S. Barry, A. E. Cable, J. S. Schuman, J. S. Duker, and J. G. Fujimoto, "Ultrahigh speed 1050nm swept source / Fourier domain OCT retinal and anterior segment imaging at 100,000 to 400,000 axial scans per second", *Optics Express* **18**, 20029-20048 (2010).
- [182] W.-Y. Oh, B. J. Vakoc, M. Shishkov, G. J. Tearney, and B. E. Bouma, ">400 kHz repetition rate wavelength-swept laser and application to high-speed optical frequency domain imaging", *Optics Letters* **35**, 2919-2921 (2010).
- [183] V. Jayaraman, J. Jiang, H. Li, P. J. S. Heim, G. D. Cole, B. Potsaid, J. G. Fujimoto, and A. Cable, "OCT Imaging up to 760 kHz Axial Scan Rate Using Single-Mode 1310nm MEMS-Tunable VCSELs with >100nm Tuning Range", in *Conference on Lasers and Electro-Optics*, (Optical Society of America, 2011), PDPB2.
- [184] V. Jayaraman, J. Jiang, B. Potsaid, G. D. Cole, J. G. Fujimoto, and A. Cable, "Design and performance of broadly tunable, narrow line-width, high repetition rate 1310nm VCSELs for swept source optical coherence tomography", in *Vertical-Cavity Surface-Emitting Lasers XVI*, (SPIE, 2012), 82760D.
- [185] D. C. Adler, W. Wieser, F. Trepanier, J. M. Schmitt, and R. A. Huber, "Extended coherence length Fourier domain mode locked lasers at 1310 nm", *Optics Express* **19**, 20930-20939 (2011).
- [186] J. A. Giordmaine and R. C. Miller, "Tunable Coherent Parametric Oscillation in LiNbO₃ at Optical Frequencies", *Physical Review Letters* **14**, 973 (1965).
- [187] H. Walther and J. L. Hall, "Tunable dye-laser with narrow spectral output", *Applied Physics Letters* **17**, 239-242 (1970).
- [188] D. J. Taylor, S. E. Harris, S. T. K. Nieh, and T. W. Hansch, "Electronic Tuning of a Dye Laser Using the Acousto-Optic Filter", *Applied Physics Letters* **19**, 269-271 (1971).
- [189] J. M. Telle and C. L. Tang, "Direct absorption spectroscopy using a rapidly tunable cw dye laser", *Optics Communications* **11**, 251-253 (1974).
- [190] J. M. Telle and C. L. Tang, "New method for electrooptical tuning of tunable lasers", *Applied Physics Letters* **24**, 85-87 (1974).
- [191] J. M. Telle and C. L. Tang, "Very rapid tuning of cw dye laser", *Applied Physics Letters* **26**, 572-574 (1975).
- [192] B. Mroziewicz, "External cavity wavelength tunable semiconductor lasers - a review", *Opto-Electronics Review* **16**, 347-366 (2008).
- [193] G. A. Coquin and K. W. Cheung, "Electronically Tunable External-Cavity Semiconductor-Laser", *Electronics Letters* **24**, 599-600 (1988).
- [194] J. R. Andrews, "Electronically tunable single-mode external-cavity diode-laser", *Optics Letters* **16**, 732-734 (1991).
- [195] W. R. Trutna and L. F. Stokes, "Continuously tuned external-cavity semiconductor-laser", *Journal of Lightwave Technology* **11**, 1279-1286 (1993).
- [196] T. Suzuki, R.-i. Nagai, O. Sasaki, and S. Choi, "Rapid wavelength scanning based on acousto-optically tuned external-cavity laser diode", *Optics Communications* **284**, 4615-4618 (2011).

- [197] P. Wang, L. K. Seah, V. M. Murukeshan, and Z. X. Chao, "Electronically tunable external-cavity laser diode using a liquid crystal deflector", *Ieee Photonics Technology Letters* **18**, 1612-1614 (2006).
- [198] A. Bilenca, S. H. Yun, G. J. Tearney, and B. E. Bouma, "Numerical study of wavelength-swept semiconductor ring lasers: the role of refractive-index nonlinearities in semiconductor optical amplifiers and implications for biomedical imaging applications", *Optics Letters* **31**, 760-762 (2006).
- [199] A. Q. Liu and X. M. Zhang, "A review of MEMS external-cavity tunable lasers", *Journal of Micromechanics and Microengineering* **17**, R1-R13 (2007).
- [200] K. Totsuka, K. Isamoto, T. Sakai, A. Morosawa, and C. Chong, "MEMS scanner based swept source laser for optical coherence tomography", in *Optical Coherence Tomography and Coherence Domain Optical Methods in Biomedicine Xiv*, (SPIE, 2010), 75542Q.
- [201] L. A. Coldren, G. A. Fish, Y. Akulova, J. S. Barton, L. Johansson, and C. W. Coldren, "Tunable semiconductor lasers: A tutorial", *Journal of Lightwave Technology* **22**, 193-202 (2004).
- [202] R. Passy, N. Gisin, J. P. Vonderweid, and H. H. Gilgen, "Experimental and theoretical investigations of coherent OFDR with semiconductor-laser sources", *Journal of Lightwave Technology* **12**, 1622-1630 (1994).
- [203] D. Derickson, M. Bemacil, A. DeKelaita, B. Maher, S. O'Connor, M. N. Sysak, and L. Johanssen, "SGDBR single-chip wavelength tunable lasers for swept source OCT", in *Coherence Domain Optical Methods and Optical Coherence Tomography in Biomedicine Xii*, (SPIE, 2008), P8472-P8472.
- [204] M. P. Minneman, J. Ensher, M. Crawford, and D. Derickson, "All-Semiconductor High-Speed Akinetic Swept-Source for OCT", in *Optical Sensors and Biophotonics Iii*, (SPIE, 2011), 831116.
- [205] E. C. Vail, G. S. Li, W. Yuen, and C. J. ChangHasnain, "High performance micromechanical tunable vertical cavity surface emitting lasers", *Electronics Letters* **32**, 1888-1889 (1996).
- [206] Y. Nakazaki and S. Yamashita, "Fast and wide tuning range wavelength-swept fiber laser based on dispersion tuning and its application to dynamic FBG sensing", *Optics Express* **17**, 8310-8318 (2009).
- [207] S. Yamashita and M. Asano, "Wide and fast wavelength-tunable mode-locked fiber laser based on dispersion tuning", *Optics Express* **14**, 9299-9306 (2006).
- [208] S. E. Harris and O. P. McDuff, "Theory of FM laser oscillation", *Ieee Journal of Quantum Electronics* **1**, 245-262 (1965).
- [209] S. Longhi and P. Laporta, "Time-domain analysis of frequency modulation laser oscillation", *Applied Physics Letters* **73**, 720-722 (1998).
- [210] S. Todor, B. Biedermann, R. Huber, and C. Jirauschek, "Balance of physical effects causing stationary operation of Fourier domain mode-locked lasers", *JOSA B* **29**, 656-664 (2012).
- [211] D. C. Adler, R. Huber, and J. G. Fujimoto, "Phase-sensitive optical coherence tomography at up to 370,000 lines per second using buffered Fourier domain mode-locked lasers", *Optics Letters* **32**, 626-628 (2007).
- [212] L. A. Kranendonk, X. An, A. W. Caswell, R. E. Herold, S. T. Sanders, R. Huber, J. G. Fujimoto, Y. Okura, and Y. Urata, "High speed engine gas thermometry by Fourier-domain mode-locked laser absorption spectroscopy", *Optics Express* **15**, 15115-15128 (2007).

-
- [213] S.-W. Huang, A. D. Aguirre, R. A. Huber, D. C. Adler, and J. G. Fujimoto, "Swept source optical coherence microscopy using a Fourier domain mode-locked laser", *Optics Express* **15**, 6210-6217 (2007).
- [214] E. J. Jung, C. S. Kim, M. Y. Jeong, M. K. Kim, M. Y. Jeon, W. Jung, and Z. P. Chen, "Characterization of FBG sensor interrogation based on a FDML wavelength swept laser", *Optics Express* **16**, 16552-16560 (2008).
- [215] B. C. Lee and M. Y. Jeon, "Remote fiber sensor based on cascaded Fourier domain mode-locked laser", *Optics Communications* **284**, 4607-4610 (2011).
- [216] B. C. Lee, E.-J. Jung, C.-S. Kim, and M. Y. Jeon, "Dynamic and static strain fiber Bragg grating sensor interrogation with a 1.3 μm Fourier domain mode-locked wavelength-swept laser", *Measurement Science & Technology* **21**, 094008 (2010).
- [217] J. Zhang, G. Liu, and Z. Chen, "Ultra broad band Fourier domain mode locked swept source based on dual SOAs and WDM couplers", in *Optical Coherence Tomography and Coherence Domain Optical Methods in Biomedicine Xiv*, (SPIE, 2010), 75541I.
- [218] M. K. Harduar, A. Mariampillai, B. Vuong, K. H. Y. Cheng, L. R. Chen, X. Gu, B. A. Standish, and V. X. D. Yang, "Dual Core Ytterbium Doped Fiber Ring Laser in Fourier Domain Mode Locked Operation for Swept-Source Optical Coherence Tomography", in *Fiber Lasers Vii: Technology, Systems, and Applications*, (SPIE, 2010), 75802S.
- [219] T. Klein, W. Wieser, B. R. Biedermann, C. M. Eigenwillig, G. Palte, and R. Huber, "Raman-pumped Fourier-domain mode-locked laser: analysis of operation and application for optical coherence tomography", *Optics Letters* **33**, 2815-2817 (2008).
- [220] K. H. Y. Cheng, B. A. Standish, V. X. D. Yang, K. K. Y. Cheung, X. Gu, E. Y. Lam, and K. K. Y. Wong, "Wavelength-swept spectral and pulse shaping utilizing hybrid Fourier domain modelocking by fiber optical parametric and erbium-doped fiber amplifiers", *Optics Express* **18**, 1909-1915 (2010).
- [221] W. Wieser, B. R. Biedermann, T. Klein, C. M. Eigenwillig, and R. Huber, "Ultra-rapid dispersion measurement in optical fibers", *Optics Express* **17**, 22871-22878 (2009).
- [222] B. Biedermann, "Fourierdomänen modengekoppelte Laser: Aufklärung der Funktionsweise und Erschließung neuer Anwendungsgebiete", Dissertation (Ludwig-Maximilians-Universität München, 2010).
- [223] G. Y. Liu, A. Mariampillai, B. A. Standish, N. R. Munce, X. Gu, and I. A. Vitkin, "High power wavelength linearly swept mode locked fiber laser for OCT imaging", *Optics Express* **16**, 14095-14105 (2008).
- [224] Y. Mao, C. Flueraru, S. Sherif, and S. Chang, "High performance wavelength-swept laser with mode-locking technique for optical coherence tomography", *Optics Communications* **282**, 88-92 (2009).
- [225] A. Ghatak and K. Thyagaraja, *Introduction to fiber optics* (Cambridge University Press, 1998).
- [226] W. Wieser, G. Palte, C. M. Eigenwillig, B. Biedermann, T. Pfeiffer, and R. Huber, "Chromatic polarization effects of swept waveforms in FDML lasers and fiber spools", *Optics Express* **20**, 9819-9832 (2012).
- [227] B. R. Biedermann, W. Wieser, C. M. Eigenwillig, T. Klein, and R. Huber, "Direct measurement of the instantaneous linewidth of rapidly wavelength-swept lasers", *Optics Letters* **35**, 3733-3735 (2011).

- [228] S. Todor, B. Biedermann, W. Wieser, R. Huber, and C. Jirauschek, "Instantaneous lineshape analysis of Fourier domain mode-locked lasers", *Optics Express* **19**, 8802-8807 (2011).
- [229] J. Zhang, J. Jing, P. Wang, and Z. Chen, "Polarization-maintaining buffered Fourier domain mode-locked swept source for optical coherence tomography", *Optics Letters* **36**, 4788-4790 (2011).
- [230] J. Noda, K. Okamoto, and Y. Sasaki, "Polarization-maintaining fibers and their applications", *Journal of Lightwave Technology* **4**, 1071-1089 (1986).
- [231] B. R. Biedermann, W. Wieser, C. M. Eigenwillig, G. Palte, D. C. Adler, V. J. Srinivasan, J. G. Fujimoto, and R. Huber, "Real time en face Fourier-domain optical coherence tomography with direct hardware frequency demodulation", *Optics Letters* **33**, 2556-2558 (2008).
- [232] K. Kim, S. Lee, and P. J. Delfyett, "1.4kW high peak power generation from an all semiconductor mode-locked master oscillator power amplifier system based on eXtreme Chirped Pulse Amplification(X-CPA)", *Optics Express* **13**, 4600-4606 (2005).
- [233] K. Kim, S. Lee, and P. J. Delfyett, "eXtreme chirped pulse amplification - Beyond the fundamental energy storage limit of semiconductor optical amplifiers", *Ieee Journal of Selected Topics in Quantum Electronics* **12**, 245-254 (2006).
- [234] S. Lee, D. Mandridis, and P. J. Delfyett, Jr., "eXtreme chirped pulse oscillator operating in the nanosecond stretched pulse regime", *Optics Express* **16**, 4766-4773 (2008).
- [235] E. Ploetz, B. Marx, T. Klein, R. Huber, and P. Gilch, "A 75 MHz Light Source for Femtosecond Stimulated Raman Microscopy", *Optics Express* **17**, 18612-18620 (2009).
- [236] R. Leonhardt, B. R. Biedermann, W. Wieser, and R. Huber, "Nonlinear optical frequency conversion of an amplified Fourier Domain Mode Locked (FDML) laser", *Optics Express* **17**, 16801-16808 (2009).
- [237] M. Horowitz, Y. Barad, and Y. Silberberg, "Noiselike pulses with a broadband spectrum generated from an erbium-doped fiber laser", *Optics Letters* **22**, 799-801 (1997).
- [238] W. L. Nighan, T. Gong, L. Liou, and P. M. Fauchet, "Self-diffraction - A new method for characterization of ultrashort laser-pulses", *Optics Communications* **69**, 339-344 (1989).
- [239] T. Kraetschmer and S. T. Sanders, "Ultrastable Fourier Domain Mode Locking Observed in a Laser Sweeping 1363.8-1367.3 nm", in *Conference on Lasers and Electro-Optics/International Quantum Electronics Conference*, (Optical Society of America, 2009), CFB4.

List of publications

Journal Papers

- 1 B. R. Biedermann, W. Wieser, **C. M. Eigenwillig**, G. Palte, D. C. Adler, V. J. Srinivasan, J. G. Fujimoto, and R. Huber, "Real time en face Fourier-domain optical coherence tomography with direct hardware frequency demodulation", *Optics Letters* **33**, 2556-2558 (2008).
- 2 B. R. Biedermann, W. Wieser, **C. M. Eigenwillig**, and R. Huber, "Recent developments in Fourier Domain Mode Locked lasers for optical coherence tomography: Imaging at 1310 nm vs. 1550 nm wavelength", *Journal of Biophotonics* **2**, 357-363 (2009).
- 3 B. R. Biedermann, W. Wieser, **C. M. Eigenwillig**, T. Klein, and R. Huber, "Dispersion, coherence and noise of Fourier domain mode locked lasers", *Optics Express* **17**, 9947-9961 (2009).
- 4 B. R. Biedermann, W. Wieser, **C. M. Eigenwillig**, T. Klein, and R. Huber, "Direct measurement of the instantaneous linewidth of rapidly wavelength-swept lasers", *Optics Letters* **35**, 3733-3735 (2010).
- 5 C. Blatter, B. Grajciar, **C. M. Eigenwillig**, W. Wieser, B. R. Biedermann, R. Huber, and R. A. Leitgeb, "Extended focus high-speed swept source OCT with self-reconstructive illumination", *Optics Express* **19**, 12141-12155 (2011).
- 6 **C. M. Eigenwillig**, B. R. Biedermann, G. Palte, and R. Huber, "K-space linear Fourier domain mode locked laser and applications for optical coherence tomography", *Optics Express* **16**, 8916-8937 (2008).
- 7 **C. M. Eigenwillig**, B. R. Biedermann, W. Wieser, and R. Huber, "Wavelength swept amplified spontaneous emission source", *Optics Express* **17**, 18794-18807 (2009).
- 8 **C. M. Eigenwillig**, W. Wieser, B. R. Biedermann, and R. Huber, "Subharmonic Fourier domain mode locking", *Optics Letters* **34**, 725-727 (2009).
- 9 **C. M. Eigenwillig**, T. Klein, W. Wieser, B. R. Biedermann, and R. Huber, "Wavelength swept amplified spontaneous emission source for high speed retinal optical coherence tomography at 1060 nm", *Journal of Biophotonics* **4**, 552-558 (2011).
- 10 T. Klein, W. Wieser, B. R. Biedermann, **C. M. Eigenwillig**, G. Palte, and R. Huber, "Raman-pumped Fourier-domain mode-locked laser: analysis of operation and application for optical coherence tomography", *Optics Letters* **33**, 2815-2817 (2008).
- 11 T. Klein, W. Wieser, **C. M. Eigenwillig**, B. R. Biedermann, and R. Huber, "Megahertz OCT for ultrawide-field retinal imaging with a 1050nm Fourier domain mode-locked laser", *Optics Express* **19**, 3044-3062 (2011).

- 12 W. Wieser, B. R. Biedermann, T. Klein, **C. M. Eigenwillig**, and R. Huber, "Ultra-rapid dispersion measurement in optical fibers", *Optics Express* **17**, 22871-22878 (2009).
- 13 W. Wieser, B. R. Biedermann, T. Klein, **C. M. Eigenwillig**, and R. Huber, "Multi-Megahertz OCT: High quality 3D imaging at 20 million A-scans and 4.5 GVoxels per second", *Optics Express* **18**, 14685-14704 (2010).
- 14 W. Wieser, B. R. Biedermann, T. Klein, **C. M. Eigenwillig**, and R. Huber, "High-Quality 3-D Imaging with Multimegahertz OCT", *Optics and Photonics News* **21**, 28 (2010).
- 15 W. Wieser, G. Palte, **C. M. Eigenwillig**, B. Biedermann, T. Pfeiffer, and R. Huber, "Chromatic polarization effects of swept waveforms in FDML lasers and fiber spools", *Optics Express* **20**, 9819-9832 (2012).

Conference Papers

- 1 C. Blatter, B. Grajciar, **C. M. Eigenwillig**, W. Wieser, B. R. Biedermann, R. Huber, and R. A. Leitgeb, "High-Speed Functional OCT with Self-Reconstructive Bessel Illumination at 1300nm", in *Optical Coherence Tomography and Coherence Techniques V*, (SPIE, 2011), 809104.
- 2 **C. M. Eigenwillig**, B. R. Biedermann, and R. Huber, "Optical Coherence Tomography Imaging with k-Space Linear Fourier Domain Mode Locked Lasers", in *Conference on Lasers and Electro-Optics / Quantum-Electronics and Laser Science Conference*, (Optical Society of America, 2008), CFM2.
- 3 **C. M. Eigenwillig**, B. R. Biedermann, W. Wieser, and R. Huber, "Wavelength swept ASE source", in *Optical Coherence Tomography and Coherence Techniques IV* (SPIE, 2009), 737200.
- 4 **C. M. Eigenwillig**, W. Wieser, B. Biedermann, T. Klein, and R. Huber, "Picosecond pulses from an FDML laser", in *Conference on Lasers and Electro-Optics Europe / European Quantum Electronics Conference*, (Optical Society of America, 2011), CF_P27.
- 5 **C. M. Eigenwillig**, S. Todor, W. Wieser, B. Biedermann, T. Klein, C. Jirauschek, and R. Huber, "Picosecond pulses from an FDML laser", in *Conference on Lasers and Electro-Optics*, (Optical Society of America, 2012), CF1N.1.
- 6 C. Jirauschek, **C. M. Eigenwillig**, B. Biedermann, and R. Huber, "Fourier Domain Mode Locking Theory", in *Conference on Lasers and Electro-Optics/Quantum-Electronics and Laser Science Conference* (Optical Society of America, 2008), CTuFF2.
- 7 T. Klein, W. Wieser, B. R. Biedermann, **C. M. Eigenwillig**, and R. Huber, "FDML laser for megahertz retinal OCT imaging", in *Conference on Lasers and Electro-Optics*, (Optical Society of America, 2011), CWB1.
- 8 T. Klein, W. Wieser, R. André, T. Pfeiffer, **C. M. Eigenwillig**, and R. Huber, "Multi-MHz FDML OCT: snapshot retinal imaging at 6.7 million axial-scans per second", in *Optical Coherence Tomography and Coherence Domain Optical Methods in Biomedicine XVI*, (SPIE, 2012), 82131E.

- 9 G. Palte, W. Wieser, B. R. Biedermann, **C. M. Eigenwillig**, and R. Huber, "Fourier Domain Mode Locked (FDML) Lasers for Polarization Sensitive OCT", in *Optical Coherence Tomography and Coherence Techniques IV*, (SPIE, 2009), 73720M.

Patent applications

- 1 R. A. Huber, **C. M. Eigenwillig**, B. R. Biedermann, "Wavelength-tunable light source", DE102008045634-A1(2010); CA2735792-A1(2010); AU2009289223-A1(2010); WO2010026197-A2/A3(2010); US2011157686-A1(2011); EP2364106-A2(2011); JP2012502456-A(2012); US2012075691-A1(2012).
- 2 R. A. Huber, T. Klein, W. Wieser, B. R. Biedermann, **C. M. Eigenwillig**, D. Müllner, M. Eder, "Dynamischer Dreikomponenten-Filter", DE102011109971(2012).

Curriculum Vitae

Christoph Martin Eigenwillig

Date of Birth: 28.12.1981
Place of Birth: Landsberg am Lech

- 1992 - 2001** Dominikus-Zimmermann-Gymnasium (grammar school) in Landsberg am Lech
- 2001** Abitur
- 2001 - 2007** **Studies of physics**, Ludwig-Maximilians-Universität, Munich
- 2006 - 2007** **Diploma thesis** in the research group of Prof. Kai Dieckmann at the chair of Prof. Hänsch (Faculty of Physics, Ludwig-Maximilians-Universität, Munich)
Title: *“Optimierte Herstellung einer ultrakalten Bose-Fermi-Mischung in der Magnetfalle“*
- 2007** **Diploma in physics** (Physik-Diplom)
- 2007 - 2012** **PHD student** in the research group of Dr. Robert Huber at the chair of Prof. Zinth (Faculty of Physics, Ludwig-Maximilians-Universität, Munich)

Danksagung

An dieser Stelle möchte ich all denjenigen Menschen meinen herzlichen Dank aussprechen, die direkt oder indirekt zum Gelingen dieser Arbeit beigetragen haben.

Zunächst gilt mein besonderer Dank meinem Gruppenleiter und Doktorvater Robert, der mich als ersten Doktoranden in seine neue Forschungsgruppe aufgenommen hat. Ich danke ihm für die Aufrechterhaltung eines kontinuierlichen Mittelzuflusses, der sich in einer sehr umfangreichen Laborausstattung manifestiert hat. Besonders schätze ich, dass Robert sich immer sehr viel Zeit für die Diskussion von experimentellen Resultaten oder die gemeinsame Planung neuer Projekte genommen hat. Ich bin ihm sehr dankbar, dass er seine vielfachen experimentalphysikalischen Erfahrungen und sein weitreichendes physikalisches und technisches Wissen immer gerne mit anderen geteilt hat und ich somit sehr viel von ihm lernen konnte.

Bei Prof. Zinth möchte ich mich dafür bedanken, dass ich an seinem Lehrstuhl promovieren durfte und von der sehr guten Ausstattung und den umfangreichen optischen Erfahrungen am Lehrstuhl profitieren konnte. Die sehr kollegiale Atmosphäre und große Hilfsbereitschaft unter den Mitarbeitern habe ich immer als sehr positiv empfunden.

Herrn Prof. Kleineberg danke ich für seine Bereitschaft, das Zweitgutachten für meine Doktorarbeit zu erstellen.

Der gesamten Arbeitsgruppe Huber möchte ich für die durchwegs sehr gute bis freundschaftliche Atmosphäre danken, die das wissenschaftliche Arbeiten sehr angenehm gestaltet hat.

Bei allen meinen Mitdoktoranden möchte ich mich für fruchtbare Zusammenarbeit bedanken. Meinem langzeitigen Büronachbarn Benjamin, der kurz nach mir mit seiner Doktorarbeit begonnen hat, danke ich für die tatkräftige Unterstützung bei der Neuausstattung des Labors und seine wertvollen Vorschläge zur Lösung experimenteller Probleme. Wolfgang, dessen physikalische Fähigkeiten ich im Labor sehr zu schätzen gelernt habe, hat mit seinem hervorragenden Fachwissen in Elektronik für die Gruppe eine Vielzahl an elektronischen Schaltungen entwickelt. Dadurch hat er zu vielen meiner Projekte wichtige Beiträge geliefert. Hierfür bin ich ihm sehr dankbar. Thomas danke ich, dass er mit mir zusammen seinen von ihm gerade neu entwickelten OCT-Aufbau zur Augenhintergrund-Untersuchung mit der von mir gebauten sehr schnell abstimmbaren Lichtquelle eingeweiht hat. Natürlich möchte ich mich auch bei den beiden neuesten Doktoranden Nino und Tom für ihre Hilfsbereitschaft bedanken. Auch das gelegentliche gemeinsame Fußballspielen mit den beiden, zusammen mit weiteren Kollegen, hat mir immer große Freude bereitet. Nino danke ich außerdem, dass er sich die Mühe gemacht hat, diese Arbeit Korrektur zu lesen.

Dank gebührt selbstverständlich auch allen anderen, die in der AG-Huber mitgearbeitet haben oder immer noch mitarbeiten und mit ihrer Begeisterungsfähigkeit für die Physik oft sehr wichtige Beiträge für die Gruppe geliefert haben. Hierzu zählen Gesa, Raphael und Matthias, die sich entschlossen haben bei uns ihre Diplom- oder Masterarbeit anzufertigen. Außerdem möchte ich auch die Werkstudenten/Bachelorstudenten Simon, Rainer, Corinna, Kathrin, Markus P., Korbinian, Tobias, Dieter, Michael, Hajrullah, Leonhard, Andi, Mathias, Markus S. und Björn nicht unerwähnt lassen.

Den Mitarbeitern der mechanischen und optischen Werkstatt des Lehrstuhls Rudi, Alfons, Christian und Harald danke ich für das schnelle Anfertigen oder die Abänderung von Bauteilen. Dies hat die Forschung im Labor sehr oft erleichtert und viel Zeit gespart.

Dr. Christian Jirauschek und Sebastian Todor von der Technischen Universität München möchte ich für die fruchtbare Zusammenarbeit und die erkenntnisbringenden Diskussionen danken. Auf Basis der von ihnen durchgeführten numerischen Simulationen gelang es, die Erzeugung kurzer Pulse mit FDML-Lasern auch von der theoretischen Seite zu beleuchten.

Meiner Familie und insbesondere meinen Eltern möchte ich sehr herzlich danken, dass sie mich auf meinem Lebensweg in jeglicher Hinsicht immer unterstützt und bekräftigt haben. Für die Förderung meiner naturwissenschaftlichen Interessen und die finanzielle Unterstützung während meines Physik-Studiums bin ich ihnen sehr dankbar.